Strong field single ionization of atoms and small molecules:

a hybrid anti-symmetrized coupled channels approach

Naga Venkata Vinay Pramod Majety

Munich 2015

Strong field single ionization of atoms and small molecules:
a hybrid anti-symmetrized coupled channels approach

Naga Venkata Vinay Pramod Majety

PhD thesis
Faculty of Physics
Ludwig Maximilians University
Munich

Presented by
Naga Venkata Vinay Pramod Majety
from Vijayawada

Munich, 25.08.2015

First examiner: Prof. Dr. Armin Scrinzi
Second examiner: Prof. Dr. Regina de Vivie-Riedle
Date of the examination: 06.10.2015

Contents

Summary **vii**

Zussamenfassung **ix**

1 Introduction **1**
1.1 Background 1
1.2 Re-collision imaging 4
1.3 Photoionization 6
1.4 Ab-inito modeling 8
1.4.1 Simple models 9
1.4.2 Popular ab-initio techniques 10
1.5 Goal of the current work 13

2 Cumulative thesis **15**
2.1 The haCC approach 16
2.1.1 Computation of observables 23
2.2 Benchmarking tests 25
2.3 Strong field ionization of small molecules 27
2.3.1 Polarization effects 28
2.3.2 Role of exchange interaction 30

3 Full articles **33**
3.1 Photoionization of few electron systems: a hybrid coupled channels approach, New J. Phys. 17 (2015) 063002. 35
3.2 Mixed gauge in strong laser-matter interaction, J. Phys. B: At. Mol. Opt. Phys. 48 (2015) 025601. 53
3.3 Photoionization of noble gases: a demonstration of hybrid coupled channels approach. Photonics 2015, 2, 93-103. 63
3.4 Static field ionization rates for multi-electron atoms and small molecules. Submitted to J Phys B. 75
3.5 Dynamic exchange in the strong field ionization of molecules. Phys. Rev. Lett. 115, 103002 (2015) 93

4 Conclusions and outlook **99**

5 Technical appendices **103**
5.1 Derivation of matrix elements . . . 103
5.1.1 Overlap . . . 104
5.1.2 Single particle operators . . . 105
5.1.3 Two particle operators . . . 109
5.2 Two electron integrals . . . 113
5.2.1 Hartree term . . . 114
5.2.2 Standard exchange term . . . 115
5.2.3 Non-standard two-electron integral: $\langle\alpha\phi_b|V^{\{2\}}|\phi_c\phi_d\rangle\rho^{IJ}_{abcd}$ . . . 116
5.2.4 Non-standard two-electron integral: $\langle\phi_a\phi_b|V^{\{2\}}|\phi_d\beta\rangle\eta^{NJ}_{abd}$ . . . 117
5.3 Interfacing with quantum chemistry . . . 118
5.4 The haCC code . . . 119
5.4.1 tRecX: a general pde solver . . . 120
5.4.2 Reconstructing the CI wavefunctions . . . 122

Bibliography **123**

Acknowledgements **130**

Summary

In this thesis, strong field single ionization (SFI) of multi-electron atoms and small molecules is studied by developing a new non-perturbative multi-electron Schrödinger equation solver called the hybrid anti-symmetrized coupled channels (haCC) approach.

SFI is the basis for several ultra-fast imaging techniques like molecular orbital tomography, high harmonic spectroscopy and laser induced electron diffraction. Analyzing these new techniques theoretically needs solving the non-perturbative multi-electron Schrödinger equation which in practice cannot be solved in full generality. Hence, for a long time these techniques were understood using single electron models. Recent experimental studies on angle dependent SFI of molecules CO and CO_2 could not be explained by single electron models opening up a fundamental question on the role of multi-electron effects in SFI.

In this context, a viable numerical method that goes beyond single electron models and that can systematically include multi-electron effects to examine their role is essential. For this purpose, the haCC technique was formulated and implemented in the form of a new `C++` code. The method tackles the two important problems of solving the many electron Schrödinger equation: the multi-dimensionality by using a coupled channels formalism and the complexity arising from the multi-centered nature of a molecule by describing the ionizing electron with a hybrid single particle basis that consists of atom centered and origin centered functions. The method brings together a host of techniques in electronic structure theory and strong field physics: configuration interaction theory implemented in `COLUMBUS` quantum chemistry package, finite element technology, infinite range exterior complex scaling absorption technique, mixed gauge representations and the time dependent surface flux spectral analysis method.

The key observables studied here are photo-electron spectra, angle dependent static field ionization rates and yields. The results obtained for the inert gas atoms conform with the existing knowledge that they behave as effective single electron systems. The new findings are in the case of molecules. The haCC calculations show that dynamic exchange and polarization are the important multi-electron effects in SFI of molecules. They also helped resolve long standing discrepancies between experiments and theory in angle dependent SFI of O_2, CO and CO_2. The calculations show that polarization at moderate intensities can be modeled using a few channel ansatz which is reassuring for further theoretical development. In the case of CO molecule it turns out that core polarization effects can reverse the maximum emission direction based on the intensity. Treating dynamic exchange, which refers to exchange interaction in the system beyond the initial and final states, accurately leads to a perfect agreement between theory and the experiment for the peak emission angles of O_2 and CO_2.

Zussamenfassung

In dieser Arbeit wird die Einfachionisation von Multielektronatomen und kleinen Molekülen durch starke Felder studiert. Zu diesem Zweck wurde ein neuartiger Ansatz namens "hybrid anti-symmetrized coupled channels" (haCC) für die Lösung der Multielektron-Schrödingergleichung entwickelt.

Ionisation durch starke Felder (Strong Field Ionization - SFI) ist die Basis für einige neuartige Verfahren zur Abbildung von ultraschneller Kern- und Elektronenbewegung, wie zum Beispiel die Molekülorbitaltomografie (molecular orbital tomography), Spektroskopie mittels Frequenzvervielfachung (high harmonic spectroscopy) und laserinduzierte Elektronenbeugung (laser induced electron diffraction). Die Analyse dieser Techniken erfordert die Lösung der nicht-perturbativen Multielektron-Schrödingergleichung, was in der Praxis nicht im vollen Umfang möglich ist. Daher wurden die Experimente bisher nur im Rahmen von Einelektronmodellen beschrieben. Neue winkelauflösende Experimente zur SFI von CO und CO_2 Molekülen konnten jedoch so nicht erklärt werden, was grundlegende Fragen über die Rolle von Multielektroneffekten in SFI aufwarf.

In diesem Zusammenhang ist eine praktikable numerische Methode unerlässlich, die über das Einelektronmodel hinausgeht, systematisch Multielektroneffekte einschließt, und somit deren gezielte Untersuchung ermöglicht. Zu diesem Zweck wurde die haCC Methode formuliert und in Form eines neuen `C++` Codes implementiert. Die Methode löst die beiden wichtigsten Probleme, welche sich bei der Lösung der Multielektron-Schrödingergleichung stellen: die Hochdimensionalität durch einen Formalismus für gekoppelte Ionisations-Kanäle und die fehlende sphärische Symmetrie eines Moleküls durch Verwendung einer hybriden Einelektron-Basis bestehend aus ursprungszentrierten und atomzentrierten Funktionen. Das Verfahren vereint mehrere Techniken aus den Bereich der Elektronenstruktur und der Physik starker Felder: Konfigurationswechselwirkung aus dem Quantenchemiepaket `COLUMBUS`, die Finite Elemete Methode, "komplexe Skalierung" (infinite range exterior complex scaling) als aborbierende Randbedingungen, nicht-standard gemischte Feldkopplung (mixed gauge) und die Berechnung von Elektronspektren aus Oberflächenflüssen (time dependent surface flux).

Als Observable betrachten wir Photoelektronenspektren, winkelabhängige statische Feldionisationsraten und totale Ionisationswahrscheinlichkeiten. Es konnte bestätigt werden, dass Edelgasatome sich wie effektive Einelektronsysteme verhalten. Neue Erkenntnisse gibt es bei Molekülen: die lange bestehenden Diskrepanzen zwischen Experiment und Theorie bei winkelabhängiger SFI von O_2, CO und CO_2 konnte erklärt und beseitigt werden. Dynamische Austauschwechselwirkung (dynamic exchange) und Polarisationseffekte wurden als die wichtigsten Mehrelektroneffekte in SFI von Molekülen identifiziert. Zur Modellierung von Polarisationseffekten bei moderaten Intensitäten genügen wenige Kanäle, was beruhigend für die weitere theoretische Entwicklung ist. Im Fall des CO-Moleküls können Polarisationseffekte bei gewissen Intensitäten die Richtung maximaler Emission umkehren.

Berücksichtigung dynamischen Austauschwechselwirkung bei der Berechnung von winkelabhängigen Ionisationsprofilen von CO_2 und O_2 bringt Theorie und Experiment in perfekte Übereinstimmung.

1

Introduction

1.1 Background

Understanding motion of atoms and electrons on their natural time scales is the goal of ultrafast science. The time scales of motion associated with various degrees of freedom in a molecular system are related to their respective energies. Broadly, the rotational dynamics happen on the picosecond ($1ps = 10^{-12}s$) timescale, the vibrational motion in few tens to hundreds of femtoseconds ($1fs = 10^{-15}s$) and electron motion in attoseconds ($1as = 10^{-18}s$) to a few femtoseconds. Taking snapshots of these dynamics on their natural time scales requires probes whose duration is smaller than these timescales [1].

Typical probes are light pulses, electron pulses or ion pulses. Charged particles repel each other and this makes it difficult to achieve very short duration pulses with them. Hence, for a number of applications in the femtosecond and attosecond domain, the preferred choice is light probes. From the time the first laser was constructed in 1960, a number of technical advancements have led to shortening of laser pulses. These include mechanical choppers that provided microsecond pulses, Q-switching which provided picosecond pulses to mode-locking and dispersion engineering which reduced the pulse durations in the optical regime to few femtoseconds. However, these optical techniques could not help surpass the few femtosecond duration barrier [2].

In the last two decades new ideas evolved like Fourier synthesis in optical domain, high harmonic generation and cascaded stimulated Raman scattering to beat the femtosecond barrier in the near optical domain [2, 3]. This has provided stimulus to extending concepts of time resolved spectroscopy to attosecond domain [1, 4]. In Fourier synthesis technique, optical pulses produced independently in different spectral windows are overlapped and their spectral phases are appropriately controlled to obtain a desired pulse profile. In the high harmonic generation technique, a gaseous system is driven by a strong laser pulse that induces a highly nonlinear time dependent dipole response that inturn generates high harmonic radiation. In the cascaded stimulated Raman scattering, a Raman medium is used to generate a series of Stokes and anti-Stokes lines which have a specific phase relation and the broad frequency comb generated implies generation of an ultrashort pulse.

High harmonic generation received significant attention from the first measurements due to a conspicuous structure in its spectral profile [5, 6, 7]. It does not follow the expectations from the perturbation theory, that is, the intensities of the generated harmonics do not follow a power law. The high harmonic spectra instead exhibit a distinct plateau structure. These findings also coincided with the observation of high energy above threshold ionization (ATI) peaks [8] in photo-electron spectra from strong field ionization of Xenon atom which also exhibited a plateau structure [9, 10].

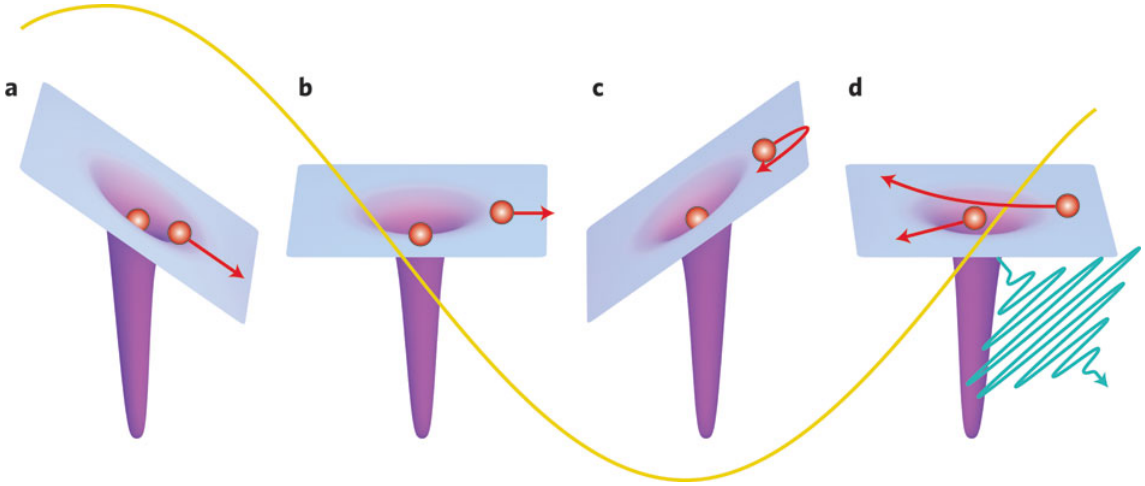

Figure 1.1: Schematic describing the three step model. The yellow curve is the driving laser electric field. a) An electron is emitted at the peak of the electric field, b) and is driven away from the parent system. c) When the electric field reverses, the electron is redirected, d) and the ionized electron re-collides with the parent system emitting radiation or scatters off the system. Figure reproduced from [11].

In early 1990s, these structures were successfully understood using a classical three-step model [7]. The underlying process can be understood in terms of the following three steps:

1. A strong driving laser pulse ionizes the system releasing an electron at a time t_i, with a certain initial momentum, $p(t_i)$.

2. The electron is accelerated away from the parent system by the laser field and is re-directed back when the laser field reverses its direction. In the process, the electron picks up additional momentum from the laser field and its momentum at a time $t > t_i$, is $p(t) = p(t_i) - A(t_i) + A(t)$ where $A(t)$ is the vector potential.

3. At a time t_f, when the position $(\vec{r}(t))$ of the electron is same as its initial position $(\vec{r}(t_f) = \vec{r}(t_i))$, the returning electron interacts with the parent ion. The interaction of the returning electron leads to partly rescattering and partly recombination emitting radiation.

This is depicted in the schematic 1.1. This phenomenological explanation predicts accurate estimates for the different cut-offs in the ATI spectra and the high harmonic spectra. The

high harmonic cut-off is given by

$$\hbar\omega_{cut-off} = I_p + 3.17U_p$$

where I_p is the ionization potential of the system and U_p is the pondermotive energy given by the relation:

$$U_p = \frac{e^2 E_0^2}{4m_e\omega^2}$$

where ω is the frequency of the driving laser, E_0 is the peak electric field and m_e, e are the mass and the charge of the electron respectively. The pondermotive energy gives the average energy that an electron picks up in one cycle of the driving laser field. While the three-step model is classical, the ionization and recombination steps need to be understood using a quantum mechanical approach.

The highest frequency generated in a high harmonic generation process is proportional to the square of the driving laser wavelength and the conversion efficiency is inversely proportional to the fifth-sixth power of the wavelength due to the spreading of the continuum wavepacket [12]. Traditionally, due to the wide availability of the Ti:Sapphire lasers, high harmonic generation experiments were performed in the near infra-red regime ($\lambda \approx 800nm$). More recently they are being extended to few micron wavelength driving laser fields [13]. At these long wavelengths, ionization occurs via tunneling, multi-photon ionization, or a "combination" of both [14]. Both these processes are highly non-linear with respect to the driving field strength. While tunneling has an exponential dependence, multi-photon ionization has a power law dependence. (See section 1.3.) If we consider tunnel ionization, a requirement for the process to occur is that the laser field must be strong relative to the Coulomb potential of the atom or the molecule under consideration. For example, the Coulomb field felt by an electron in the ground state of hydrogen atom is $E_a \approx 5.1\times10^9$ V cm^{-1} which translates to an intensity of $I_a = 3.51\times10^{16}$ W cm^{-2}. The laser field strength needs to be strong enough to bend the Coulomb potential of the system to form a barrier through which the electron can tunnel as shown in the figure 1.2.

As a result, the birth times t_i at which the driving laser field is at its maximum and the electron trajectories that follow are the most important contributors to the whole process. This implies that the high harmonic bursts obtained in this three step process are generated on a narrow time window smaller than the quarter cycle period of the driving laser field. For a 800 nm laser, these radiation bursts happen on time scales of less than 0.65 fs thereby producing attosecond radiation bursts with central wavelengths in the ultra-violet regime [15]. This establishes a relation between the research areas of "Strong field physics" and "attosecond physics" and understanding strong field ionization processes is an important aspect of attosecond physics.

A standard technique to study dynamics using these ultra-short high harmonic light sources is to perform pump-probe experiments. In a pump-probe study, a first pulse called the pump pulse is used to initiate a process in the system, and the second pulse which arrives after a certain time delay probes the instantaneous state of the system. By varying the time delay between the pump and the probe pulses, it is possible to study the system's

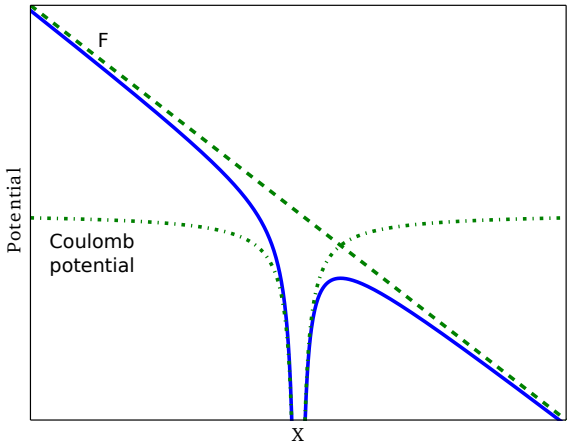

Figure 1.2: Schematic showing the potential barrier formed when a strong laser field of strength comparable to the Coulomb potential is superimposed on the Coulomb potential. Dash-dotted line: Plot of Coulomb potential $-\frac{1}{|x|}$. Dashed line: Plot of the dipole interaction term $-Ex$ for a constant field strength of 0.1 a.u (corresponding intensity, $I = 3.5 \times 10^{14}$ W cm^{-2}). Solid line: Sum of the field and the Coulomb potential.

time evolution. However, due to the low conversion efficiency of the high harmonic generation (HHG) process the XUV pulses generated are weak making it technically challenging to perform XUV pump-probe experiments with them. Such experiments have been realized only recently [16]. Alternatively, these pulses are also currently being used in two-color schemes like XUV-IR pump probe experiments [17] and streaking experiments [18].

1.2 Re-collision imaging

While increasing the intensity of high harmonic radiation is a work in progress, our understanding of the HHG process based on the three step model, has opened up new avenues to image electron and nuclear dynamics. According to the classical analysis based on electron trajectories, for different ionization times t_i, the electron follows a different trajectory and leads to emission of harmonics of different compositions or diffraction from the residual system at a different instant of time. It implies a possibility to extract signatures of ultrafast dynamics from the emitted radiation or from the re-scattered electrons. This has led to the conceptualization of a new class of imaging techniques called the self-imaging or recollision imaging techniques [19, 20]. Two of the popular techniques are the laser induced electron diffraction and high harmonic spectroscopy.

- **Laser induced electron diffraction (LIED):**

  Diffraction by the re-directed electron wavepacket is superior to the conventional electron diffraction for two reasons [3, 21, 22, 23]. The current density easily exceeds 10^{10} A cm^{-2}. Such current densities are only available from large accelerators. The

electron wavepacket duration is on the order of few femtoseconds that provides an unprecedented time resolution for electron diffraction experiments.

In a tunnel ionization process, the maximum ionization occurs when the electric field is at its maximum. The emitted wavepacket re-collides with the parent system after about half a laser cycle period. The time difference between the ionization and the re-collision events has the correspondence to the pump-probe time delay which can be tuned by varying wavelength of the driving laser field. Assuming that the dependence of the initial ionization on wavelength is fully known, tuning the wavelength would amount to probing the ionized system at different instants of time after the ionization.

In recent works reported in Refs [22, 23], proof of principle experiments were performed using N_2 and O_2 molecules. From the re-scattered photo-electron distributions, time dependence of the bond length was measured. In the case of N_2, the residual ion is left in the ground state of the ion whose bond length is the same as the neutral. As a result, the system is left in the ground vibrational state. The extracted bond lengths were nearly independent of the wavelength. In the case of the O_2 molecule, there is a significant variation in the equilibrium bond lengths of the ground states of the neutral and singly charged ion. The extracted bond lengths varied with the wavelength as expected, demonstrating that the vibrational dynamics can be probed using this technique.

- **High harmonic spectroscopy (HHS):**

  Alternatively, the emitted radiation or the high harmonic spectra can be used to image dynamics. The central idea again is that the electron trajectories map the transit time (time between the ionization and the recombination events) to the high harmonic photon energies with less than a femtosecond resolution.

  The concept was initially tested using numerical studies. Lein *et. al* in [24], showed that in diatomic molecules H_2^+ and H_2, two-center interference effects lead to a distinct minimum in the high harmonic spectra. It was shown that it is possible to back calculate the bond length from the minimum. In [25], this concept was further extended to show that high harmonic spectra are sensitive to vibrational dynamics and can be used to probe them.

  An application of the HHS called the molecular orbital tomography was demonstrated with N_2 molecule in Refs [26, 27]. In these experiments high harmonic spectra were measured with different orientations of the laser field with respect to the molecular axis and they were used to reconstruct the three dimensional image of the ionizing orbital.

  In 2009, Smirnova et. al [28] studied high harmonic spectra of CO_2 molecule where an intensity dependent minimum was observed. As the minimum was dependent on the driving laser parameters, it cannot be a feature of the field-free electronic structure but some thing induced by the laser. It was shown that this minimum is related to interference between two ionizing channels and this shows that HHS can

be used to observe channel coupling dynamics. Similar experiments were performed for SF_6 recently [29].

1.3 Photoionization

Photoionization is at the heart of re-collision imaging techniques. Photoionization of a multi-electron system can be broadly divided in to perturbative and non-perturbative regimes.

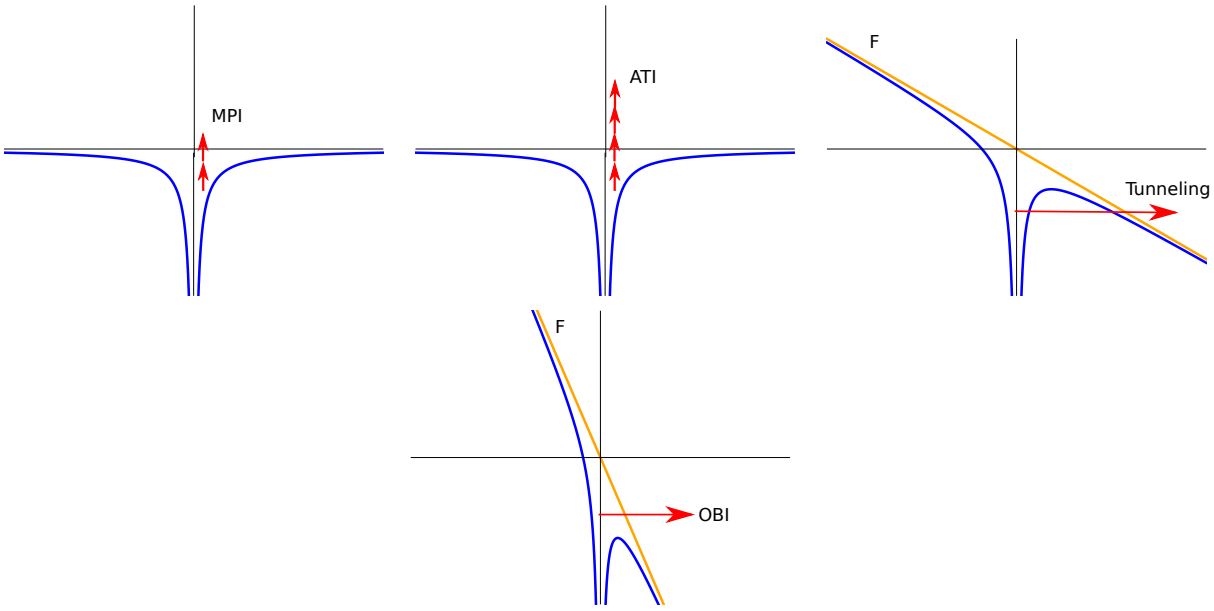

Figure 1.3: Schematic showing four different ionization mechanisms in the following order: multi-photon ionization (MPI), above threshold ionization (ATI), tunneling ionization and over the barrier ionization or the above barrier ionization.

Perturbative regime: When the influence of the external field is small compared to the field-free Hamiltonian, the interaction with the external field can be accounted by adding correction terms to the solutions of the field-free Hamiltonian. This is called the perturbation theory. In this approach, an N-photon ionization process can be treated by using the lowest non-vanishing order term in the perturbation series [30] where, the N-photon ionization rate ($\Gamma^{(N)}$) for example is calculated as

$$\Gamma^{(N)} = \left(\frac{I}{\hbar\omega}\right)^N \sigma^N(\omega) \tag{1.1}$$

where $\left(\frac{I}{\hbar\omega}\right)^N$ is the photon flux and $\sigma^N(\omega)$ is the cross-section which is related to the N^{th} order transition matrix element, $M_{fg}^{(N)}$, between the initial state $|g\rangle$ and the final state

$|f\rangle$:

$$M_{fg}^{(N)} = \sum_{s} \cdots \sum_{n} \sum_{m} \frac{\langle f|\hat{E}\cdot\vec{r}|s\rangle}{(E_s - E_g - (N-1)\hbar\omega)} \cdots \frac{\langle n|\hat{E}\cdot\vec{r}|m\rangle}{(E_n - E_g - 2\hbar\omega)} \frac{\langle m|\hat{E}\cdot\vec{r}|g\rangle}{(E_m - E_g - \hbar\omega)}. \tag{1.2}$$

Here, $|s\rangle$,$|n\rangle$,$|m\rangle$ indicate intermediate states and E_s,E_m and E_n their corresponding energies. An ionization process where the minimum number of photons are absorbed to overcome the ionization threshold is referred to as multi-photon ionization (MPI). When the number of photons absorbed is larger than the minimum requirement, the ionization process is called the above threshold ionization (ATI). A schematic of these processes is shown in figure 1.3. The main challenge in this approach is to obtain all the necessary intermediate states needed to evaluate the required transition matrix elements.

As the name suggests, the theory is suitable only at low intensities where the influence of the external field can be treated as a perturbation. As the intensity is increased, higher order terms start to contribute and the perturbation expansion may not converge.

Non-perturabative regime: In this regime, the external field is strong and cannot be treated by adding a few correction terms to the field-free solutions. In this case, the time dependent Schrödinger equation (TDSE) needs to be completely solved after the inclusion of all the required interaction terms into the Hamiltonian.

- **Quasi-static limit:** A special case in the non-perturbative regime is the low frequency limit. In the presence of a strong low frequency laser field ionization occurs by tunneling or by above the barrier ionization process. See schematics in figure 1.3. Here, it can be assumed that the ionizing system adjusts adiabatically to the external field and the ionization yield ($Y(t)$) can be computed using static field ionization rates as:

$$Y(t) = 1 - \exp\left(-\int_0^t dt' \Gamma_{stat}(F(t'))\right) \tag{1.3}$$

  where $\Gamma_{stat}(F)$ is the static ionization rate for a field strength F. Hence, it suffices to solve a time independent problem.

In 1965, Landau and Lifshitz first derived the tunnel ionization rate for hydrogen atom [31]. This formula was generalized for complex atoms, in single electron approximation by Ammosov, Delone and Krainov in 1986 [32]. which is widely using in this field and is popularly known as the ADK formula. According to this formula the static field ionization rate for an atom at a field strength F is given as:

$$\Gamma_{ADK}(F) = \frac{C_l^2}{2^{|m|}|m|!} \frac{(2l+1)(l+|m|)!}{2(l-|m|)!} \frac{1}{\kappa^{2Z_c/\kappa-1}} \left(\frac{2\kappa^3}{F}\right)^{2Z_c/\kappa-|m|-1} e^{-2\kappa^3/3F}. \tag{1.4}$$

Here l and m are the angular momentum quantum numbers of the outermost electron of the atom, C_l is the amplitude of the electron wavefunction in the tunneling region, $\kappa = \sqrt{2I_p}$

with I_p being the ionization potential and Z_c is the effective nuclear charge. This formula was extended to account for the multi-centered nature of molecules by Tong et. al [33] in 2002 and this formula is referred to as the MO-ADK formula.

Comparison with numerical studies showed that ADK formula over-estimates ionization rates at high field strengths. An empirical correction to the formula was presented in 2005 [34] which works well for inert gas atoms also at high field strengths:

$$\Gamma_{corr} = \Gamma_{ADK}\ e^{-\alpha\left(Z_c^2/I_p\right)\left(F/\kappa^3\right)} \tag{1.5}$$

Here α is a fitting parameter.

A seminal work by Keldysh in 1965 [35] presented solutions of the non-perturbative Schrödinger equation using an approximation that is now known as the strong field approximation (SFA). In SFA, the influence of the Coulomb potential is neglected for the electron continuum states and they are represented using Volkov states. An important conclusion of this work is that a parameter γ known as the Keldysh parameter identifies the limits of pure tunnel ionization and multi-photon ionization.

$$\gamma = \sqrt{\frac{I_p}{2U_p}} = \omega\tau_T \tag{1.6}$$

where I_p is the ionization potential, U_p is the pondermotive energy, ω the driving laser frequency and τ_T is the characteristic tunneling time. Computing ionization rate showed that when $\gamma \ll 1$, the ionization rate has an exponential dependence on the field strength, which corresponds to a pure tunneling type of ionization and when $\gamma \gg 1$ the rate has a power law dependence on the field strength which indicates multi-photon type of ionization. In the intermediate regime, ionization mechanism is a "combination" of both [14]. Different formulations of the Keldysh theory were also presented by Faisal [36] and Reiss [37] and hence this theory is also often referred to as the Keldysh-Faisal-Reiss (KFR) theory.

1.4 Ab-inito modeling

The central difficulty in giving a general utility to the promising re-collision imaging ideas is the large number of coupled degrees of freedom that are present in a general multi-electron system. The response of a system to an ultra-short (broadband) light probe is a convolution of the different processes that the laser pulse initiates. This makes it complicated to control and extract the required dynamical information.

Ab-initio theoretical modeling is essential to fully understand the role of the different degrees of freedom which in turn may help gain control over the dynamics. This implies solving the non-perturbative multi-electron Schrödinger equation. But, solving it in full generality is an impossible task.

Quoting from Agostini et. al.[19]: *Strong-field ionization is a field of research which has, all along, been driven by experiments while the theory has followed, often painstakingly.*

The three important difficulties of solving a general non-perturbative TDSE are:

1. The exponential dependence of the required discretization points on the number of electrons: also popularly called the "curse of dimensionality". Consider an N-electron system and each electron wavefunction discretized by 'k' basis functions, $f_{i_n}(\vec{r}_n)$. The wavefunction can be written as:

$$\psi(\vec{r}_1, ..., \vec{r}_N) = \sum_{i_1, \dots, i_N=1}^{k} c_{i_1, \dots, i_N}(t) f_{i_1}(\vec{r}_1) \dots f_{i_N}(\vec{r}_N) \tag{1.7}$$

   with the constraint that the coefficients, $c_{i_1, \dots, i_N}(t)$, satisfy the required anti-symmetry property. The number of discretization coefficients is $k^N/N!$.

2. Atoms have spherical symmetry which helps in reducing the dimensionality of the problem. With molecules, this advantage is lost and their multi-centered nature leads to large angular expansions when treated in spherical coordinates.

3. Unfavorable scaling with wavelength (λ) for solving TDSE: solving full TDSE is the only choice available while dealing with photo-ionization regimes where using perturbation theory or employing quasi-static approximation is not an option. Studying single ionization problem scales as λ^4 [38]. This comes from 3 factors, the required time propagation scales as λ, the required momentum to be resolved scales as λ and the required box size scales as λ^2. At long wavelengths the ionized part of the wavefunction can spread over several orders of magnitude larger space compared to the spatial extent of a typical parent system. This leads to large numerical box requirements making even single electron calculations expensive.

The unfavorable scaling of the box size with wavelength can be circumvented for computation of those observables that do not need asymptotic information by imposing absorbing boundary conditions. Even for photo-electron spectra that need analysis of asymptotic part of the wavefunction, a recent technique called the time dependent surface flux method allows computation with minimal box sizes [38, 39].

In the case of the first two difficulties, approximation is the only remedy. As of today, obtaining numerical solutions with more that 6 degrees of freedom has not been possible [40, 41] from general solvers. Hence, since inception of this field, strong field ionization based processes have been understood using simple models.

1.4.1 Simple models

Simple models include single electron numerical calculations with effective core potentials [42, 43], electron density based methods: density functional theory (DFT) [44, 45] and analytical formula like the ADK, MO-ADK formula. Two of the popular models that are used to interpret the HHS and LIED experiments are the Lewenstein model [46] and its improved version called the quantitative rescattering method (QRS) [47]. These models are

considered as the quantum mechanical analogs of the classical three-step model due to the three distinct terms in the dipole matrix element that can be interpreted as the ionization, propagation and recombination steps. Both the approaches are essentially single electron approaches and are based on the strong field approximation. While QRS has an option of computing the recombination matrix elements with continuum states from multi-electron methods, it treats the ionization process in single electron approximation.

The obvious drawback of the effective single electron methods is the absence of multi-electron dynamics. DFT based approaches include multi-electron effects through exchange correlation functionals but these functionals cannot be systematically improved to perform convergence studies. Also, the electron density based approaches do not provide direct access to the wavefunction to compute observables like photo-electron spectra.

Evidence of multi-electron effects

Single electron models were successful in the case of inert gas atoms to a large extent [34]. However, in the recent past a number of examples have been reported where the single electron methods fail indicating the presence of multi-electron effects. Examples include, inter-channel coupling effects in high harmonic spectroscopy of Xenon [48], CO_2 [28] and SF_6 [29]; the failure of ADK to explain angle dependent ionization of H_2 [49]; and the failure of most single electron methods to even qualitatively explain angle dependent strong field ionization of molecules CO [50, 51] and CO_2 [42, 44, 45, 52, 53].

In this scenario, there are two approaches possible: The first approach would be to refine the single electron models further to include multi-electron effects. But this can mostly be done in an ad-hoc way and the validity of a particular approximation can be only established through comparison with experiments which in the first place include a number of averaging effects. The second approach would be to develop ab-initio methods which are self-consistent. In this work the second approach is followed. There exist in literature several ab-initio techniques that work for atomic systems but in the case of molecules the application of these techniques has been minimal due to the difficulty 2 listed above. The following section presents a list of popular techniques.

1.4.2 Popular ab-initio techniques

In order to handle the problem of multi-dimensionality, several methods have been developed in past decades. The central strategy in all the methods is to discretize the wavefunction using only that part of the total N-electron Hilbert space which is seemingly required for electron dynamics. A brief description of popular methods is given below.

- **Time dependent Hartree-Fock method**

  Time dependent Hartree Fock (TDHF) theory [54], which is the simplest of all, is an extension of the standard Hartree-Fock theory to time dependent problems. Here, the wavefunction is expressed as a single Slater determinant. Each single particle orbital

that compose the Slater determinant evolves in the mean potential or the Hartree-Fock potential created by the nuclei and the remaining electrons. Let $\phi_i(\vec{r}_i, t)$ denote a single particle orbital, then the wavefunction is written as:

$$\begin{aligned}\psi(\vec{r}_1, ..., \vec{r}_N) &= \mathcal{A}\left[\phi_1(\vec{r}_1, t) \; ... \; \phi_N(\vec{r}_N, t)\right] \\ &= c_{i_1}(t) \; .... \; c_{i_N}(t) \; \mathcal{A}\left[f_{i_1}(\vec{r}_1) \; ... \; f_{i_N}(\vec{r}_N)\right]\end{aligned} \tag{1.8}$$

where f_{i_j} are discretization functions for single particle orbitals. The ansatz has only kN discretization points which is much smaller compared to the general ansatz 1.7. Being a very simple ansatz, it has several limitations. It is only suitable for situations where the system's response is linear or in other words, where the response of a system can be written in terms of product states. Being a single determinant approach, it does not include correlation in a true state. As a result, it cannot describe auto-ionizing states accurately and underestimates their decay rates for example [54].

- **Multi-configuration time dependent Hartree-Fock method**

  A systematic extension of TDHF method is the multi-configuration time-dependent Hartree-Fock (MCTDHF) approach [55, 56]. It discretizes the N-electron wavefunction in terms of several Slater determinants each composed of time dependent single particle orbitals.

$$\psi(\vec{r}_1, ..., \vec{r}_N) = \sum_{i_1, \; ... \; , i_N} c_{i_1, \; ... \; , i_N}(t) \mathcal{A}\left[\phi_{i_1}(\vec{r}_1, t) \; ... \; \phi_{i_N}(\vec{r}_N, t)\right] \tag{1.9}$$

  This is a complete basis in principle and can include correlation needed to describe any state of the system. As the orbitals and coefficients are time dependent, this ansatz allows for a very compact representation of the wavefunction. However, the non-linear equations involved in solving the TDSE with this ansatz lead to an unfavorable scaling with the number of electrons. It has been so far applied to 10 electron systems in one dimensional problems [56] and upto four electron systems in three dimensions [55].

- **Time dependent configuration interaction method**

  The time dependence of the single particle orbitals leads to non-linear equations of motion in the previous two methods. In time dependent configuration interaction method, the time dependence is restricted to the coefficients and the single particle orbitals are chosen to be field-free Hartree-Fock orbitals (includes both "occupied" and "virtual" orbitals). Denoting creation and annihilation operators acting on a Hartree-Fock orbital ϕ_k as $a_k^\dagger$, a_k, the time dependent configuration interaction wavefunction can be written as:

$$|\psi\rangle = c_0(t) \; |\Phi_0\rangle + \sum_{ip} c_i^p(t) \; a_p^\dagger a_i \; |\Phi_0\rangle + \sum_{ijpq} c_{ij}^{pq}(t) \; a_q^\dagger a_p^\dagger a_i a_j \; |\Phi_0\rangle + ... \tag{1.10}$$

where $|\Phi_0\rangle$ is the Hartree-Fock determinant.

The expansion consists of the HF determinant and determinants created by exciting a fixed number of electrons to virtual orbitals with respect to the HF determinant, for example, the second term consists of the single excitations, the third term consists of double excitations and so on.

If there are n_{hf} Hartree-Fock orbitals, then the size of such an expansion is $\frac{n_{hf}!}{(n_{hf}-N)!N!}$, which grows very quickly with the number of HF orbitals and the number of electrons. Typically, truncation schemes are employed. If the expansion includes only up to single excitations, the method is referred to as the time dependent configuration interaction singles (TD-CIS) [57, 58].

- **Coupled channels formalism**

  In a coupled channels formalism [59, 60], the wavefunction is discretized using a set of neutral bound states and single ionic channel functions.

$$\psi(\vec{r}_1, ..., \vec{r}_N) = \sum_{i,I} c_{i,I}(t)\mathcal{A}\left[\phi_i(\vec{r}_1)\Phi_I(\vec{r}_2, \ ... \ , \vec{r}_N)\right] + \sum_{\mathcal{N}} c_{\mathcal{N}}(t)\mathcal{N}_I(\vec{r}_1, \ ... \ , \vec{r}_N) \quad (1.11)$$

  This kind of discretization is suitable for the cases where (N-1) electron dynamics can be restricted to few bound states. The advantage of the approach is that the size of discretization is independent of the exact number of electrons and hence can be easily applied to larger problems.

- **Other wavefunction methods**

  There are a number of other methods which can be considered as variants of the above methods. Some of them include the time dependent complete active space self-consistent field method (TD-CASSCF) [61], time dependent restricted active space self-consistent field method (TD-RASSCF) [62, 63] which are variations of MCTDHF[64, 65]. Each method applies different restrictions and flexibilities in the form of orbital partitioning schemes and can be advantageous to specific problems at hand.

  Another popular method in the context of atomic physics is the R-matrix method [66]. It is similar in spirit to the coupled channel formalism but employs an additional spatial partitioning scheme. The physical space is divided in to inner and outer regions. In the inner region, all the terms in the Hamiltonian are treated exactly, where as in the outer region approximations are made. The solutions in the two regions are appropriately matched to satisfy the conditions of continuity and the derivative continuity of the wavefunction.

All the above mentioned methods barring the coupled channels method have been applied only to atomic systems in the context of strong field physics. The lack of spherical

symmetry leads to large angular momentum expansions and the Hamiltonian couples a large number of basis functions unlike in atoms imposing severe bottle-neck to these methods.

1.5 Goal of the current work

The goal of the current work is three fold:

1. To develop an *ab-initio* technique to study strong field ionization of atoms and small molecules: For this purpose a coupled channels formalism was chosen.

2. In the process, make use of the well established techniques in the fields of quantum chemistry and one-, two-electron strong field physics. The techniques put together in this work are configuration interaction theory from quantum chemistry, finite element methods, infinite range exterior complex scaling technique, mixed gauge representations and the time dependent surface flux spectral analysis technique.

3. Apply the method to strong field ionization of molecules where several discrepancies between experiments and theory surfaced in the recent past which would help advance the larger field of imaging dynamics using strong field ionization processes.

There exists an earlier work with coupled channels approach by Spanner et. al [59]. They however approximate exchange interaction during dynamics which simplifies the problem by a great deal. Here, such an approximation is not made and all the technical issues resulting are dealt with. It is shown that approximating exchange can be a severe approximation while studying strong field ionization of molecules and can lead to misleading interpretation of the physics behind the ionization process.

2

Cumulative thesis

The new ab-initio computational technique developed in this thesis is called the hybrid anti-symmetrized coupled channels approach (haCC). The current work contributes to its formulation, implementation in the form of a new `C++` code, benchmarking and its application to strong field ionization of small molecules. The work done for this thesis is presented in the following articles which are reproduced after this chapter.

1. *V. P. Majety, A. Zielinski and A. Scrinzi*, Photoionization of few electron systems: a hybrid coupled channels approach, **New J. Phys.** 17 (2015) 063002.

2. *V. P. Majety, A. Zielinski and A. Scrinzi*, Mixed gauge in strong laser-matter interaction, **J. Phys. B**: At. Mol. Opt. Phys. 48 (2015) 025601.

3. *V. P Majety and A. Scrinzi*, Photoionization of noble gases: a demonstration of hybrid coupled channels approach. **Photonics** (2015), 2, 93-103.

4. *V. P Majety and A. Scrinzi*, Static field ionization rates for multi-electron atoms and small molecules. **Submitted to J Phys B.**

5. *V. P Majety and A. Scrinzi*, Dynamic exchange in the strong field ionization of molecules. **Phys. Rev. Lett.** 115, 103002 (2015)

This chapter provides a brief account of these articles. An overview of the code that implements the method is provided in the appendix. The haCC method was also employed in the following work:

6. *A. Zielinski, V.P. Majety, S. Nagele, R. Pazourek, J. Burgdörfer, A. Scrinzi.* Anomalous Fano profiles in external fields. **arXiv:1405.4279, Submitted to Phys. Rev. Lett.**.

which studies the influence of external fields on Fano resonances in Helium atom. This however is not a part of this thesis and is not discussed.

2.1 The haCC approach

The mathematical formulation of the haCC method and its benchmarking is dealt in detail in *articles 1 and 2*. This section provides an overview of these articles. The haCC technique solves the multi-electron Schrödinger equation

$$i\frac{\partial}{\partial t}\Psi(\vec{r}_1,\cdots,\vec{r}_N,t) = \hat{H}(\vec{r}_1,\cdots,\vec{r}_N,t)\Psi(\vec{r}_1,\cdots,\vec{r}_N,t) \tag{2.1}$$

numerically using the following basis ansatz for the N-electron wavefunction:

$$|\Psi(\vec{r}_1,\cdots,\vec{r}_N)\rangle = \sum_{\mathcal{I}} c_{\mathcal{I}}(t)|\mathcal{I}(\vec{r}_1,\cdots,\vec{r}_N)\rangle + \sum_{\mathcal{N}} c_{\mathcal{N}}(t)|\mathcal{N}(\vec{r}_1,\cdots,\vec{r}_N)\rangle. \tag{2.2}$$

Here $\hat{H}$ is the time dependent Hamiltonian, $c_{\mathcal{I}}, c_{\mathcal{N}}$ are the time dependent expansion coefficients, $|\mathcal{N}\rangle$ are the neutral bound states and $|\mathcal{I}\rangle$ are ionic channel functions defined as:

$$|\mathcal{I}(\vec{r}_1,\cdots,\vec{r}_N)\rangle = \mathcal{A}\left[|i(\vec{r}_1)\rangle|I(\vec{r}_2,\cdots,\vec{r}_N)\rangle\right] \tag{2.3}$$

where $|I\rangle$ are single ionic functions, $|i\rangle$ are numerical one-electron basis functions and $\mathcal{A}$ denotes anti-symmetrization.

Approximations

Along with the basis set discretization of the wavefunction, Eq. 2.2, the following approximations are made:

- **Fixed nuclei approximation:** Atoms have only electronic degrees of freedom, but molecules possess additional rotational and vibrational degrees of freedom. Usually, the motion associated with these degrees of freedom is a few orders of magnitude slower than the electronic motion. By Born-Oppenheimer approximation [68], it can be assumed under these circumstances that the electronic wavefunction adapts adiabatically to the changes in the nuclear configuration. As a result, the electronic part of the Schrödinger equation can be solved separately for each nuclear configuration. Here, such a fixed nuclei approximation is made and only the electronic Schrödinger equation is solved with equilibrium nuclear configurations.

- **(N-1) electrons are restricted to their bound states.** As solving the Schrödinger equation in full generality is not possible, the multi-electron basis set must be restricted. As this work concentrates on single ionization problems, the ionic and the neutral states in the basis, Eq. 2.2, are restricted to bound states. Note, the indistinguishability of electrons is however correctly imposed through the anti-symmetrization.

- **Non-relativistic approximation:** The Schrödinger equation is non-relativistic. Hence, spin dynamics are not allowed and spin quantum number enters the scheme only as a parameter. Spin-orbit couplings are also neglected. The mass of the electron

is taken to be its rest mass which is a good approximation for photo-ionization by extreme ultraviolet or longer wavelength radiation where the ionized electron energies do not exceed a hundred eV.

- **Dipole approximation:** The electromagnetic field is treated classically and under dipole approximation. When the wavelength of the ionizing radiation is larger than the spatial extent of the system, the field can be considered to be spatially independent. Using the Taylor's series for a plane wave, a linearly polarized time-varying electric field can be approximated as follows:

$$E(\vec{r},t) = E_0 e^{i\left(\vec{k}\cdot\vec{r}-\omega t\right)} \tag{2.4}$$

$$= E_0 e^{-i\omega t}\left(1 + i\vec{k}\cdot\vec{r} + \frac{\left(i\vec{k}\cdot\vec{r}\right)^2}{2!} + \cdots\right) \tag{2.5}$$

$$\approx E_0 e^{-i\omega t} \tag{2.6}$$

By Faraday's law, the neglect of the spatial dependence of the time varying electric field also implies the neglect of the magnetic field.

The basis, Eq. 2.2

The ionic and the neutral states needed in the basis are computed using Multi-reference Configuration Interaction (MRCI) theory implemented in `COLUMBUS` quantum chemistry package [69]. For this purpose an interface to this package was written with the support of the `COLUMBUS` authors (See appendix 5.3). The MRCI wavefunctions are based on Hartree-Fock orbitals (ϕ_k) that are constructed from a set of atom centered Gaussian orbitals. In the current work, MRCI singles and MRCI singles, doubles schemes are used. The general interface also implies that, in principle, more advanced orbital partition schemes that are available in quantum chemistry codes can be used.

The single electron basis, $|i\rangle$ is a single centered expansion (centered on the origin) with finite element discretization [70], $|f_i\rangle$, for the radial coordinate and spherical harmonics, $|Y_{l_i m_i}\rangle$, for angular coordinates.

$$|i(\vec{r}_1)\rangle = |f_i(r_1)\rangle|Y_{l_i m_i}(\Omega_1)\rangle \tag{2.7}$$

In principle, $|i\rangle$ can be any complete basis. Instead of finite-elements, other types of discretizations like B-splines [71] or finite difference schemes [59] could be used. The specific choice of finite-elements is motivated by the fact that, finite-elements being local basis sets, lead to blocked matrices when various operators are evaluated with them. This is a useful property to perform operations like matrix-vector multiplications, inverting matrices and so on.

The haCC discretization allows a compact representation of strong field ionization processes mainly for two reasons:

- Correlated states that need a large number of channel functions to be well represented can be explicitly included in the basis. For example, in the strong field ionization of Helium, correlation plays a role only in the initial state and the ionization problem can be described by a single channel ansatz [72]. The explicit inclusion of the ground state (or other neutral states) keeps the basis compact.

- When dealing with a single center expansion, the representation of a molecular (multi-centered) wavefunction needs large number of angular momenta. The hybrid nature of the single particle basis - atom centered Gaussians and a single centered expansion mitigates this problem to some extent and keeps the basis compact.

A technical complication with the basis is that it is over-complete. The single electron basis, $|i\rangle$ being complete can represent the Gaussian orbitals that constitute ionic and neutral functions. This problem is dealt by solving the Schrödinger equation in a subspace that does not include the zero vectors.

Time propagation

Substituting the ansatz 2.2 into the TDSE gives a set of coupled ordinary differential equations (ODE) for the time dependent expansion coefficients:

$$i\left[\langle\mathcal{G}|\mathcal{G}\rangle\frac{dC_{\mathcal{G}}}{dt}+\langle\mathcal{G}|\mathcal{I}\rangle\frac{dC_{\mathcal{I}}}{dt}\right]=\langle\mathcal{G}|\hat{H}|\mathcal{G}\rangle C_{\mathcal{G}}+\langle\mathcal{G}|\hat{H}|\mathcal{I}\rangle C_{\mathcal{I}} \tag{2.8}$$

$$i\left[\langle\mathcal{I}|\mathcal{G}\rangle\frac{dC_{\mathcal{G}}}{dt}+\langle\mathcal{I}|\mathcal{I}\rangle\frac{dC_{\mathcal{I}}}{dt}\right]=\langle\mathcal{I}|\hat{H}|\mathcal{G}\rangle C_{\mathcal{G}}+\langle\mathcal{I}|\hat{H}|\mathcal{I}\rangle C_{\mathcal{I}} \tag{2.9}$$

These equations are solved using standard fourth order Runge-Kutta scheme with an adaptive step size control. These equations can be cast into the form:

$$iS\frac{d\vec{c}}{dt}=H\vec{c} \tag{2.10}$$

where $\vec{c}$ is the vector of all the time dependent coefficients, S is the overlap matrix and H is the matrix corresponding to the Hamiltonian operator in the haCC basis. (Detailed derivation of the matrix elements in appendix 5.1)

In order to solve the equations 2.10, the overlap matrix needs to be inverted. The overlap matrix has a useful structure: it is a banded matrix to which a low rank correction term is added. This property is used to efficiently apply the inverse overlap using the Woodbury formula [73]. However, in general this is more complicated as the over-completeness of the basis 2.2 can make the overlap matrix ill-conditioned. In order to solve this problem, a generalization of the Woodbury formula has been formulated (See *Article 1*) and this allows for the computation of the inverse in a chosen subspace, here the subspace being the space of the non-zero eigenvectors of the overlap matrix.

Two-electron repulsion integrals

The evaluation of the electron-electron repulsion integrals forms the computationally most intensive part of obtaining the Hamiltonian matrix that is required to setup the coupled ODE's 2.10. This is the case for any multi-electron technique. In quantum chemistry, where Gaussian basis sets are used these integrals can be computed analytically, but with general basis sets these integrals need to be evaluated numerically. Here a multi-pole expansion method is used. The single particle functions are projected on to a single center expansion and the integrals are computed using the expansion:

$$\frac{1}{|\vec{r}_1 - \vec{r}_2|} = \sum_{L=0}^{\infty} \sum_{M=-L}^{L} \frac{4\pi}{2L+1} \frac{r_<^L}{r_>^{L+1}} Y_{LM}(\theta_1, \phi_1) Y_{LM}^*(\theta_2, \phi_2) \tag{2.11}$$

where $r_< = \min(r_1, r_2)$ and $r_> = \max(r_1, r_2)$. The limits of the expansion are set automatically by the angular momentum truncation in the single center expansions. No other truncation schemes for the L, M expansion are used here.

A number of two electron integrals arise with the haCC basis: the standard Hartree and the exchange terms, and other kinds of exchange terms due to non-orthogonality of the Gaussians with the finite elements. As computation of these integrals is expensive, sufficient care has been taken to keep the operations count to minimum. There exists a trade-off between the storage requirements and the number of floating point operations. The algorithms used to evaluate each of these integrals is presented in appendix 5.2.

Absorption at box boundaries: infinite range exterior complex scaling

During the time propagation parts of the wavefunction can spread to large distances compared to the spatial extent of the initial state of the system due to the population of the continuum states that extend to infinity. In order to avoid numerical reflections from the box boundaries due to this spreading wavefunction, the numerical box sizes need to be large. This makes computations expensive. Several observables like the ionization yields, cross-sections do not need the asymptotic information. When such observables are of interest, it is more efficient to absorb the wavefunction beyond a certain distance from the origin by imposing absorbing boundary conditions. An essential property of such an absorber is that it should preserve dynamics in the region before absorption.

Exterior complex scaling is robust way to impose these absorbing boundary conditions. In this technique, the outgoing waves are transformed into exponentially decaying functions [74] using the coordinate transformation:

$$r_\theta = \begin{cases} r & \text{for } r \leq R_c \\ e^{i\theta}(r - R_c) + R_c. & \text{for } r > R_c. \end{cases} \tag{2.12}$$

Here θ is the complex scaling angle that can be any value in the interval $[0, \pi/2]$ and R_c is the coordinate value beyond which the transformation starts. In order for this transformation

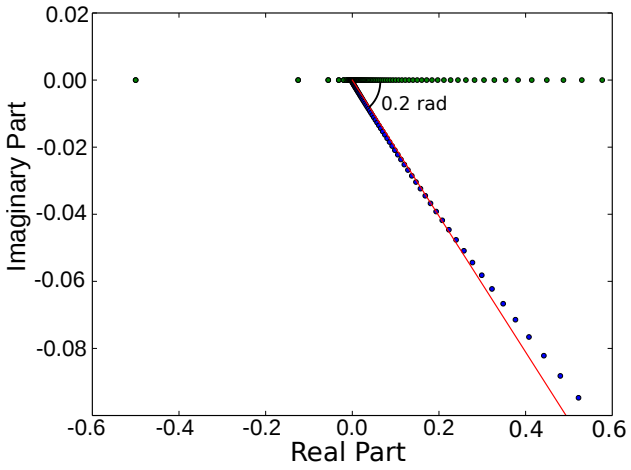

Figure 2.1: Eigenvalue spectra (in a.u.) of the field-free Hamiltonian for hydrogen atom. Scatter in green is the spectra without complex scaling and the scatter in blue is with complex scaling. A complex scaling angle of 0.1 radians was used. The red line has a slope of 0.2 radians and it fits the continuum spectra rotated in to the lower complex plane.

to act as an absorption technique, the Hamiltonian must satisfy a mathematical property called "Dilation analyticity" which one comes across in advanced functional analysis [75]. In this thesis, this is used as a well established black box approach which has certain properties and no effort has been made to look into the underlying mathematical theorems.

The complex scaling transformation has the following influence on "Dilation analytic" Hamiltonians: It leaves the bound state spectrum intact and transforms the continuum states into exponentially decaying waves [74]. This entails to imposing the required absorbing boundary conditions.

Figure 2.1 demonstrates these properties with the example of the hydrogen atom. The numerically computed eigenvalue spectra for the field-free Hamiltonian with and without complex scaling angle ($\theta = 0.1$ rad) are shown. The bound states remain unchanged where as the continuum states are rotated by an angle 2θ. The negative imaginary part in the eigenvalues implies that these functions decay during the time propagation. A finite discretization cannot represent continuum spectra. As a result, from the point where the continuum states become inaccurate (seen through the sparsity of points) the complex scaled eigenvalues deviate from the analytical expectations.

Another useful property of this complex scaling transformation is the uncovering of the semi-bound states or the resonant states from the continuum spectra. The resonant states like the doubly excited states in Helium have a strongly bound nature. As a result these states are not rotated by angle 2θ like the continuum states. The complex scaling transformation converts the eigenvalues of these states into the form $E_f = r_f - i\hbar\frac{\Gamma_f}{2}$ where Γ_f is the decay width of the state. These eigenvalues are also not effected by the exact complex scaling angle.

Here, a recent version of its implementation called the infinite range exterior complex scaling (irECS) [70] is used. The trick used in irECS version is to use exponentially decaying basis functions in the complex scaled region to represent the decaying waves (See schematic 2.2). This improves the numerical efficiency of the method. The actual implementation of the method involves the imposition of a "non-intuitive" discontinuity at the scaling radius (R_c) [70]. Radial discontinuities in solutions can be easily imposed with a finite element basis, if an element boundary is chosen at the discontinuity.

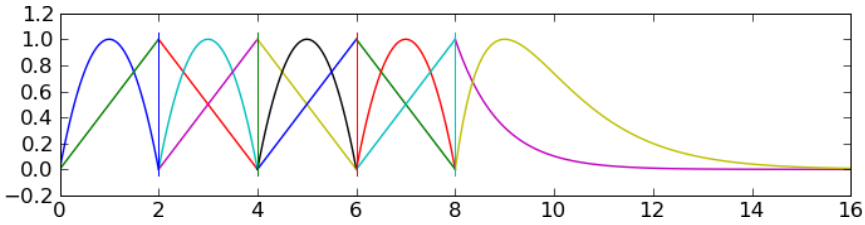

Figure 2.2: Schematic showing finite element radial discretization for irECS absorption scheme. The last set of polynomials extend to infinity. In practice, high order polynomials are used.

Mixed gauge representation

The gauge freedom that the scalar (ϕ) and vector potentials ($\vec{A}$) possess in classical electrodynamics translates into our context as a local unitary transformation of the form [76, 77]:

$$\Psi_2(\vec{r},t) = U_g(\vec{r},t)\Psi_1(\vec{r},t) \quad \text{with} \quad U_g = e^{ig(\vec{r},t)}. \tag{2.13}$$

In *Article 2*, it is shown that while all gauge representations are equally "correct" (they are all related by unitary transformations), the choice of gauge defines the convergence properties with a particular discretization, defines the properties of the Hamiltonian and hence the properties of time evolution. The choice of gauge is not an important question when basis sets used can be pushed to the limit of completeness. However, this is not possible with multi-electron systems and all methods make approximations in terms of basis set restrictions. With the example of the haCC discretization, it is shown that instead of the length and the velocity gauges that are popularly used in this field, using a mixed gauge representation can be numerically efficient. This concept is of general importance to other approximate methods as well, where analyzing the numerical properties with different gauge representations can help improve their numerical efficiency.

The wavefunctions in length (Ψ_L) and velocity (Ψ_V) gauges are related as follows:

$$\Psi_L(\vec{r},t) = e^{-i\vec{A}(t)\cdot\vec{r}}\Psi_V(\vec{r},t). \tag{2.14}$$

In the short wavelength regime, the wavefunctions in the two gauges are identical. For example, with 20 nm wavelength laser pulse and with a peak intensity 10^{14} W cm^{-2} (peak

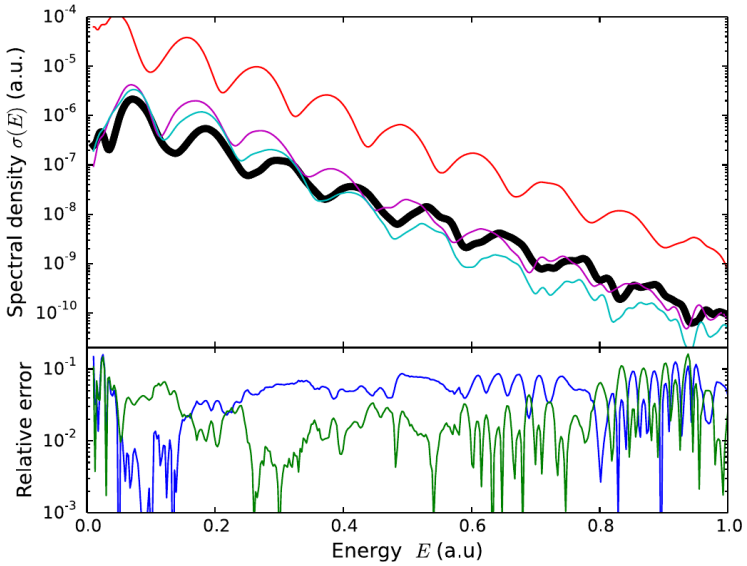

Figure 2.3: Photo-electron spectra from Helium with a 400nm, 3-cycle, $\cos^2$ envelope pulses with a peak intensity of 1.0×10^{14} W cm^{-2}. The solid line in the top panel shows full dimensional calculations. The mixed gauge computations with one (blue) and five (green) channels overlap with the solid line and hence a plot of relative difference is shown in the lower panel. The remaining red, magenta and cyan curves are velocity gauge computations with one, five and nine ionic channels respectively. All the haCC calculations include the neutral ground state in the basis.

vector potential = 0.023 a.u), the gauge factor at 1 a.u distance is 0.9997+0.023i, where as with the same intensity at 800nm the peak vector potential is 0.937a.u that leads to a gauge factor of 0.592+0.806i. At short wavelengths and at low intensities, the length and velocity gauge wavefunctions do not differ significantly. But when this is not the case the effect of a particular gauge choice can be dramatic.

In the context of the haCC method both the velocity and length gauges have certain advantages and disadvantages. The Hamiltonian in the velocity gauge satisfies the required properties for the ECS absorption to work, requires lesser number of angular momenta for convergence, but is not suitable for modeling ionic dynamics in terms of a few bound states. This is because, in velocity gauge the mechanical momentum in the presence of the external laser field is time dependent and different from the field-free case. As a result, the ionic states in the basis loose their physical meaning. On the other hand, the Hamiltonian in the length gauge representation is suitable when modeling in terms of a few ionic bound states, but needs larger number of angular momenta for convergence and is not compatible with the ECS absorption technique. The length gauge Hamiltonian is not "dilation analytic", or in practical terms, the Hamiltonian has eigenvalues with both positive and negative imaginary values. This means some eigenstates are exponentially growing functions and the ECS does not act as an absorption technique.

In order to combine the advantages of both, a mixed gauge formalism is used. In this

scheme, length gauge is used in the region that encompasses the ionic bound states, and the region thereafter where the absorption starts an "asymptotic velocity gauge" is used. This is obtained by the "continuous gauge transformation"[77] defined as:

$$\Psi(\vec{r},t) = \begin{cases} \Psi_L(\vec{r},t) & \text{for } r \leq r_g \\ \exp\left[i\vec{A}(t)\cdot(\vec{r}-\vec{r}_g)\right]\Psi_L(\vec{r},t) & \text{for } r > r_g. \end{cases} \tag{2.15}$$

where r_g is the gauge boundary at which the gauge transition happens. Note that with this gauge transformation, the wavefunction at r_g remains continuous at all times. Other forms of mixed gauge transformations are also possible [77] . But Eq. 2.15 is the easiest to implement as it does not involve imposition of any time dependent discontinuities.

Figure 2.3 demonstrates the efficiency of the mixed gauge representation over the pure velocity gauge. The pure length gauge computations could not be done as the irECS absorption which is needed for the overall scheme does not work here. The figure shows that, with mixed gauge, a single channel computation can produce spectra comparable to full dimensional calculations on the level of 10% accuracy, where as with velocity gauge even a 9 channel computation could not produce the correct result.

2.1.1 Computation of observables

The different observables considered in this work are static field ionization rates, ionization yields, cross-sections and photo-electron spectra. They are computed as follows:

- **Static field ionization rates:**

  Computation of static field ionization rates only needs solving the time independent problem. Exterior complex scaling of a Hamiltonian [74, 75] has the useful property that the semi-bound states like the field-free ground state in the presence of a static field acquires an imaginary part that is related to the ionization rate. The eigenvalue is of the form $E_f = r_f - i\hbar\frac{\Gamma_f}{2}$ where Γ_f in the imaginary part of the eigenvalue is the ionization rate. The ionization rate as a function of field strength is calculated by adiabatically following the field-free ground state with respect to the field strength.

- **Ionization yields** are computed from the drop in the norm of the wavefunction in the unscaled region. The ionized part of the wavefunction irrespective of the energy content travels away from the parent system to "infinity". Hence for any given size of the unscaled region propagating long enough allows us to compute the yields.

- **Cycle averaged ionization rates** are obtained by calculating the rate at which the norm dropped in the unscaled region for a sufficiently long continuous wave with an initial ramp up and ramp down at the end.

- **Multi-photon ionization cross-sections** ($\sigma^{(n)}$) are computed from the cycle averaged ionization rates using the formula [66]:

$$\sigma^{(n)} = (8\pi\alpha)^n \left(\frac{3.5\times10^{16}}{I}\right)^n \omega^n \Gamma a_0^{2n} t_0^{n-1} \tag{2.16}$$

where $\sigma^{(n)}$ is the n photon ionization cross-section in units cm^{2n}/s^{n-1}, I is the intensity in Wcm^{-2}, ω is the laser frequency in a.u, α is the fine structure constant and a_0, t_0 are atomic units of length and time respectively in cms. Γ is the total ionization rate in a.u.

- **Photoelectron spectra:**

  Computation of the photo-electron spectra needs analysis of the asymptotic part of the wavefunction unlike the previous observables like yields or cross-sections. This means that the wavefunction cannot be absorbed and large simulation box sizes are needed. The traditional way to compute photo-electron spectra is to time propagate using a large simulation box and project the wavefunction on to single continuum states.

  This implies two difficulties: (i) Large simulation boxes that make computations expensive and (ii) computation of single continuum states. Single continuum states are analytically known for the Hydrogen atom, but beyond that these states can only be computed using approximate numerical methods like effective single electron calculations, DFT based methods [71], iterative Schwinger variational method with a frozen core or a few channel ansatz [78] and so on. As these methods approximate the influence of the complicated electron-electron interactions, the continuum states are approximate in the vicinity of the nucleus. They are accurate only in the asymptotic region where the residual system because of screening can be effectively treated as a hydrogen like system. As a consequence, in the traditional method, the time propagation has to be done long enough until the ionized wavepacket has traveled far enough for the projection onto the approximate continuum state to be accurate.

  These two problems are circumvented in a recently developed technique called the time dependent surface flux method (tSURFF) [38, 39]. The tSURFF method approximates the various potentials in the Hamiltonian by smoothly turning them off before a radius called the tSURFF radius (R_c) which is a convergence parameter for the method. This implies that the solutions beyond R_c can be approximated as Volkov states (χ_k), which are the solutions of a free particle in an external field. If $\Theta_N(R_c)$ is a Heaviside function that characterizes the Nth coordinate space $r_N > R_c$, the channel resolved single ionization spectra, $\sigma_{c,k}$, can be computed as:

$$\begin{aligned}\sigma_{c,k} &= |\langle\chi_k(\vec{r}_N,t)|\Theta_N(R_c)|\zeta_c(\vec{r}_N,t)\rangle|^2 \\ &= |i\int_0^T dt\langle\chi_k(\vec{r}_N,t)|\left[-\frac{1}{2}\triangle_N + i\vec{A}(t)\cdot\vec{\nabla}_N,\Theta_N(R_c)\right]|\zeta_c(\vec{r}_N,t)\rangle|^2,\end{aligned} \tag{2.17}$$

where T is some large time after the laser pulse, $\chi_k(\vec{r}_N,t)$ are single particle Volkov states corresponding to momentum k and $\zeta_c(\vec{r}_N,t)$ is the Dyson orbital corresponding to the ionization channel, c defined as:

$$\zeta_c(\vec{r}_n,t) := \langle\kappa_c(\vec{r}_1,...,\vec{r}_{N-1},t)|\Psi(\vec{r}_1,...,\vec{r}_N,t)\rangle. \tag{2.18}$$

Here κ_c is the ionic channel function at time t. As the integrand in Eq. 2.17 is the expectation value of the commutator with a Heaviside function, it is sufficient to have the values of the wavefunction on the surface characterized by radius $r_N = R_c$ to evaluate it.

As computation of the spectra needs only the wavefunction on the surface defined by the tSURFF radius, the wavefunction thereafter can be absorbed. This leads to dramatic reduction of the required simulation box sizes [38, 39] making the computations less expensive. The limitation is that the threshold spectra are not produced accurately due to the truncation of the Coulomb potential.

2.2 Benchmarking tests

The Schrödinger equation can be solved in full dimensionality for two-electron systems: helium and the hydrogen molecule and hence are the typical benchmarking systems. Below are a few benchmarking results presented in *Articles 1,3 and 4* [79, 60]. Unless mentioned otherwise, the following labeling scheme is used below to represent haCC calculations: The neutral ground state is always included in the basis. A basis labeled haCC(n) indicates that the lowest n ionic channels are included in the basis. Degeneracies are counted separately.

Table 2.1 presents static field ionization rates for helium from the haCC method at selected field strengths compared to rates from full dimensional calculations reported in [80, 81]. The haCC(1) and haCC(5) basis schemes refer to one and five channel calculations respectively. The haCC calculations agree with the literature values on the range of 5-10%.

F (a.u)	haCC(1)	haCC(5)	Ref [80]	Ref [81]
0.06	$< 10^{-10}$	$< 10^{-10}$	7.8936×10^{-11}	
0.09	5.131×10^{-7}	5.243×10^{-7}	5.3387×10^{-7}	5.09×10^{-7}
0.12	3.533×10^{-5}	3.613×10^{-5}	3.6829×10^{-5}	3.62×10^{-5}
0.15	4.115×10^{-4}	4.209×10^{-4}	4.2913×10^{-4}	4.23×10^{-4}
0.20	4.144×10^{-3}	4.308×10^{-3}	4.3347×10^{-3}	4.31×10^{-3}

Table 2.1: Static field ionization rates (a.u) at fields, F (a.u), for Helium atom with haCC(1) and haCC(5) schemes compared to full dimensional calculations in literature.

Figures 2.4 and 2.5 present photo-electron spectra from the haCC method with different number of ionic channels for Helium atom and H_2 molecule respectively with 400 nm laser pulses compared to full dimensional calculations [82]. The exact pulse parameters are mentioned in the figure captions. The upper panels of the plots present spectra and the lower panels the relative difference from the full dimensional calculations. In either case the spectra agree on the level of 10% with respect to the full dimensional calculations. Notably, the haCC calculations can also reproduce the small peak around 0.62 a.u photo-electron energy in the H_2 spectra.

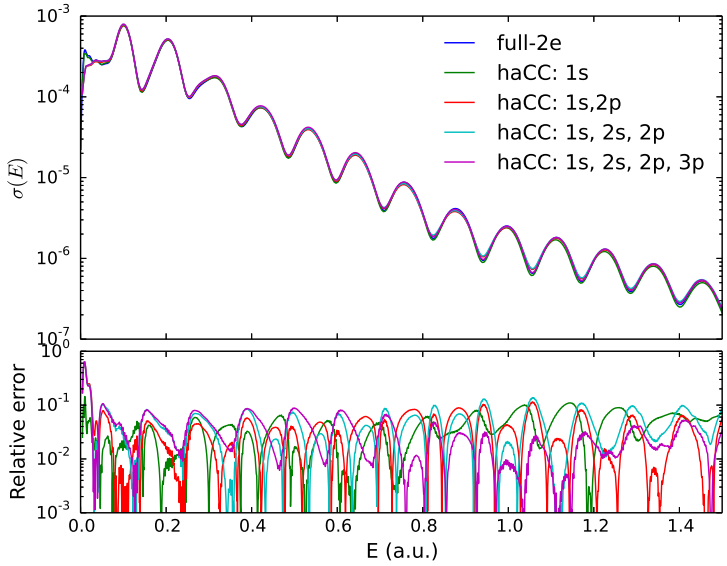

Figure 2.4: Photo-electron spectra for Helium from haCC calculations with different number of ionic channels as indicated in the legend and full dimensional calculations (full-2e). The upper panel shows spectra (in a.u.) and the lower panel shows the relative difference between the haCC calculations and the full-2e calculations. Pulse parameters: 3-cycle, $\cos^2$ pulse, 400nm, 3×10^{14} W/cm^2 peak intensity.

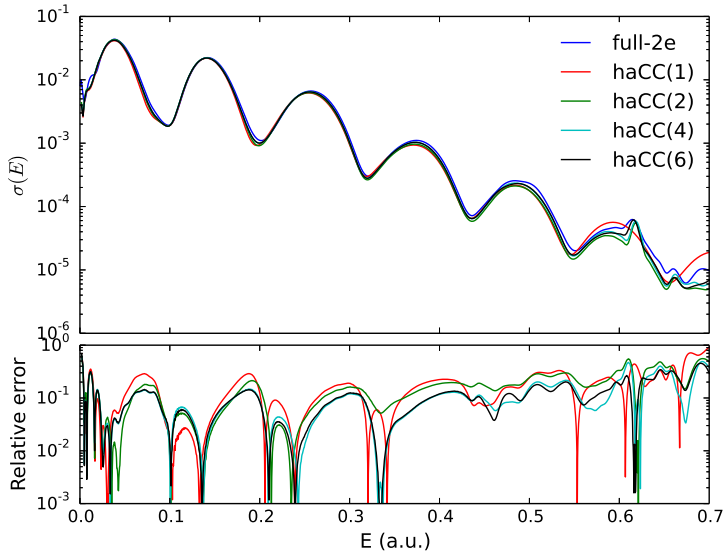

Figure 2.5: Photo-electron spectra for H_2 molecule at the equilibrium inter-nuclear distance 1.4 a.u from haCC calculations with different number of ionic channels as indicated in the legend and full dimensional calculations (full-2e). The upper panel shows spectra and the lower panel shows the relative difference between the haCC calculations and the full-2e calculations. Pulse parameters: 3-cycle, $\cos^2$ pulse, 400nm, 1×10^{14} W/cm^2 intensity.

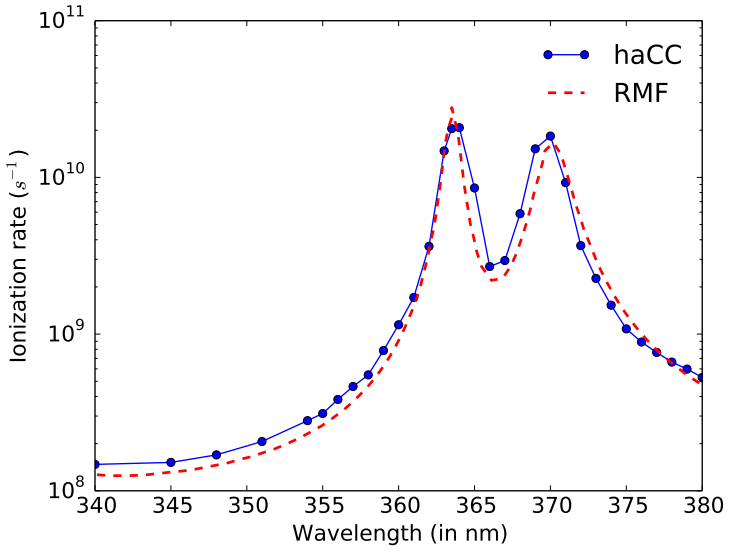

Figure 2.6: Five photon ionization rates as a function of wavelength for Argon from R-matrix Floquet (RMF) theory and from the haCC(4) scheme [79].

In addition to two electron systems, inert gas atoms have been well studied using various techniques of atomic physics listed in the introduction. In *Article 3* [83], a few comparisons of multi-photon ionization cross-sections and rates from the haCC and the R-matrix method have been presented. Figure 2.6 is a sample plot from this work which presents a comparison of the five photon ionization rates obtained from the R-matrix theory and the haCC technique.

The various benchmarking tests presented in *Articles 1,3 and 4* [60, 83, 79] demonstrate the correctness of the method. The lower computational cost involved with this method compared to full dimensional calculations implies that it can be applied to more complex systems where solutions cannot be obtained in full generality. The largest computations presented in the thesis took less that 48 hours on a standard 8-core machine.

2.3 Strong field ionization of small molecules

In this section, the application of the haCC approach to study angle dependent strong field ionization of small molecules: N_2, O_2, CO and CO_2 presented in *Articles 4 and 5* [79, 84] is summarized. The central observable chosen for this purpose is the angle dependent static field ionization rates, though angle dependent yields were also computed under single channel approximation by solving TDSE.

This is motivated by the following reasons. Firstly, static field ionization rates which are important inputs in Lewenstein and QRS models used to interpret recollision imaging experiments have been accessible only from single electron models prior to this work. Secondly, in the recent past a number of experiments [50, 51, 52, 85] performed to measure

the angle dependent strong field ionization of small molecules have remained unexplained or their interpretation remained ambiguous due to the failure of simple single electron models or due to the contradictory results obtained from different models. Two of these striking examples are CO and CO_2 molecules. At the outset, this may seem surprising as these are relatively simple systems for quantum chemistry. But the current realm of study is outside the scope of standard quantum chemistry which pre-dominantly deals with bound state dynamics.

CO is a heteronuclear, diatomic, linear molecule. Experiments measuring angle dependent SFI [51, 50] for this molecule showed that the direction of maximum emission is the carbon atom end. However, the catalog of the many single electron models is divided in their predictions. While the stark corrected MO-ADK and the Weak field asymptotic theory theories predict maximum emission from O atom end, the standard MO-ADK, strong field approximation (SFA), stark-corrected SFA, adiabatic SFA predict the preferred direction to be the C end [86]. Also, only the adiabatic SFA could predict an asymmetry parameter close to the one measured in the experiment so far [86]. A work done using the time dependent Hartree-Fock method [87] showed that polarization effects play an important role in SFI of CO.

The angle dependent ionization of CO_2 was measured in [52, 85] and the maximum emission angle was found to be 45° with respect to the molecular axis. A number of theoretical methods were employed to reproduce this result with little success: Calculations were performed using MO-ADK [52], DFT [44] ,TD-DFT [45], single electron TDSE with DFT based potential [42], semi-classical analysis [53] and adiabatic SFA [86]. The only calculation that reproduced the experimental result is the single electron calculation with the DFT based potential in Ref. [42]. But being an ad-hoc approach (the DFT potential cannot be systematically varied), the calculation could not help in correctly identifying the reason behind its success or the reason behind the failure of other methods.

The results presented in the articles *Articles 4 and 5* have two aspects to them:

- The haCC approach allowed for the first time computation of static field ionization rates from a multi-electron method where a systematic convergence study in terms of ionic channel functions is possible.

- The calculations reveal that two important multi-electron effects: polarization and exchange are needed to described accurately the strong field ionization of small molecules. Including these two aspects accurately resolves discrepancies between experiment and theory for the molecules studied here.

2.3.1 Polarization effects

Figure 2.7 shows angle dependent static field ionization rates for N_2 at selected field strengths from haCC(1) to haCC(5) computations. Inclusion of excited ionic states improves the description of core electron polarization and this leads to an effective increase

in the ionization potential through DC Stark shifts. This leads to a general reduction of ionization rates.

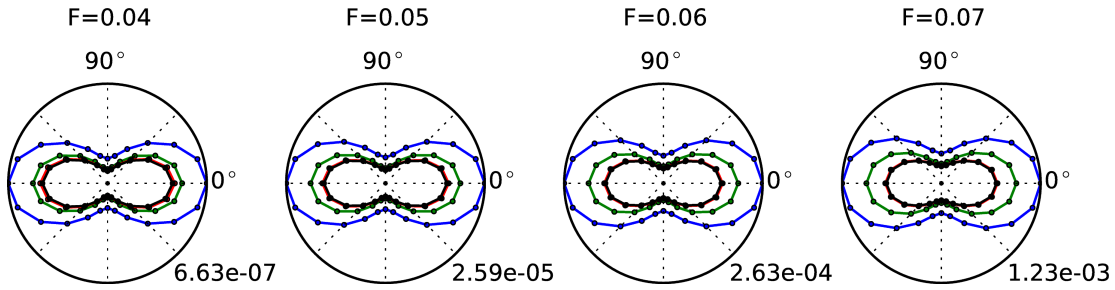

Figure 2.7: Angle dependent ionization rates of N_2 with different number of ionic channels included at various field strengths (F) in atomic units. The angle is defined with respect to the molecular axis. Blue: haCC(1). Green: haCC(3). Red: haCC(4). Black: haCC(5).

The effect of polarization on CO is more dramatic. Improvement in the description of core polarization by including excited ionic channels leads to a change in the maximum emission direction. Figure 2.8 shows the asymmetry parameter for the ionization rates defined as $(\Gamma_{0^\circ} - \Gamma_{180^\circ})/(\Gamma_{0^\circ} + \Gamma_{180^\circ})$ with different number of ionic states in the basis. The angle is defined as 0° when field points from O atom to C atom. The converged calculation shows that the preferred direction of emission is the C atom end which is consistent with the experiments. The single channel computations however predict an incorrect emission direction at low intensities. This shows that not describing the core polarization sufficiently would lead to even qualitatively incorrect results for CO.

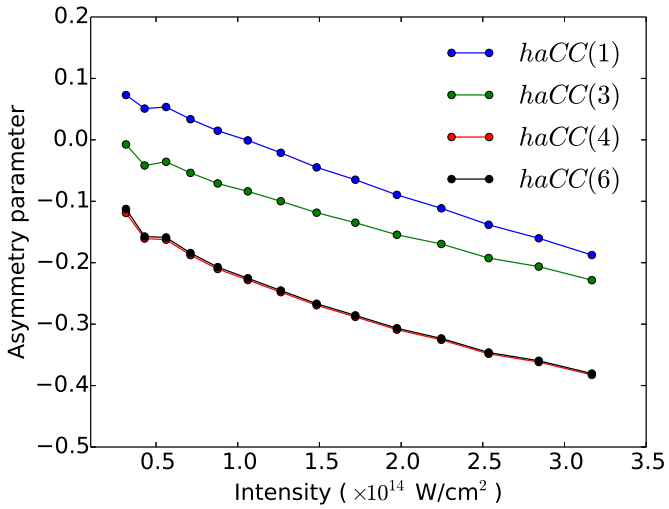

Figure 2.8: Asymmetry parameter for CO molecule defined as $(\Gamma_{0^\circ} - \Gamma_{180^\circ})/(\Gamma_{0^\circ} + \Gamma_{180^\circ})$. The single channel computation even predicts incorrect maximum emission direction at low intensities. The angle is defined as 0° when the field points from O atom to C atom.

A common finding in these calculations is that polarization in small molecules can be described using a few channel ansatz. This is a result of the exponential dependence of ionization rate on the ionization potential (for example see ADK formula 1.4). This is reassuring for future theoretical developments.

2.3.2 Role of exchange interaction

An important revelation from the haCC calculations is the importance of the exchange. Exchange symmetry imposed by anti-symmetrizing the wavefunction is a fundamental property when studying fermionic systems. However, the long tradition of studying strong field physics with single electron models has often led to the neglect of this fundamental property. The haCC calculations show that exchange interaction plays a very decisive role in determining the angle dependent strong field emission profiles of molecules. CO_2 is a system where this is dramatically manifested. This is presented in detail in *Article 5* [84]. Imposing dynamic exchange, that is exchange symmetry beyond just the initial and final states, resolves all the confusion behind the angle dependent emission of CO_2 which was studied in a number of works [52, 44, 45, 42, 53, 86].

Figure 2.9 presents a comparison of experimentally measured angle dependent ionization yields with a single electron theory MO-ADK for N_2, O_2 and CO_2 molecules at 800 nm wavelength from Ref [52]. Figure 2.10 shows normalized ionization rates for the same molecules computed under ground ionic channel approximation with and without anti-symmetrization imposed in the channel functions in the haCC ansatz 2.2. Exchange interaction has a dramatic qualitative effect for CO_2. It changes the maximum emission direction by 15° and it explains the experimental observation. The angle dependent emission profile is maintained also in the time dependent problem, that is, when yields are computed from TDSE (See *Article 5*). In the case of N_2 molecule, dynamic exchange broadens the emission profile. Finally in the case of O_2, it explains the 5° discrepancy between experiment and theory. The reason for the failure of MO-ADK and other single electron models is the neglect or insufficient description of exchange interaction during the dynamics.

Anti-symmetrization in the haCC basis, Eq. 2.2, has two effects: it orthogonalizes the single electron basis with respect to the orbitals in the ionic states and it leads to a non-local exchange interaction term in the Hamiltonian. By performing time dependent Hartree-Fock calculations with and without explicit orthogonalization of the single electron basis with respect to the Hartree-Fock orbitals, it is shown in *article 5*, that the dominant effect in this context is indeed the non-local exchange term.

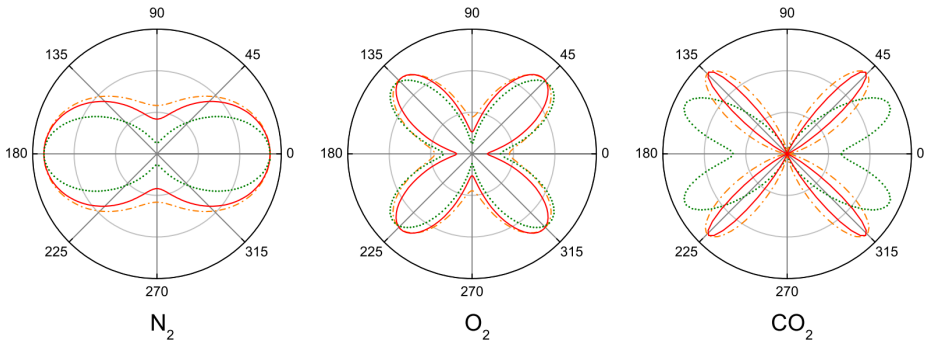

Figure 2.9: Angle dependent ionization profiles from experiment and MO-ADK theory for N_2, O_2 and CO_2 molecules with 800nm, 40fs laser pulses. The peak intensities used are 1.5×10^{14} W cm^{-2}, 1.3×10^{14} W cm^{-2} and 1.1×10^{14} W cm^{-2} respectively. The figure is reproduced from [52]. The red and orange curves are experimental results. The green curve gives the predictions from MO-ADK theory.

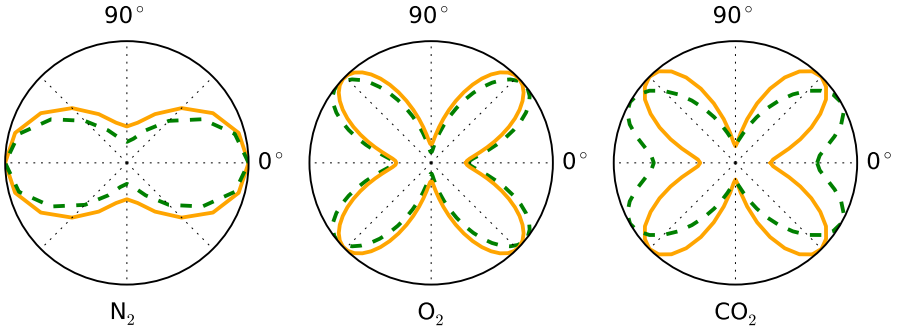

Figure 2.10: Normalized angle dependent ionization rates for N_2, O_2 and CO_2 with (orange) and without (green) anti-symmetrization (exchange) in the channel function in the haCC basis. The computations are performed only with the ground state neutral and the ground ionic channel. The results are with field strengths: 0.07 (1.7×10^{14} W cm^{-2}), 0.06, 0.06 (1.25×10^{14} W cm^{-2}) a.u respectively.

3

Full articles

New Journal of Physics
The open access journal at the forefront of physics

Deutsche Physikalische Gesellschaft DPG
IOP Institute of Physics

Published in partnership with: Deutsche Physikalische Gesellschaft and the Institute of Physics

PAPER

OPEN ACCESS

RECEIVED
27 December 2014

REVISED
31 March 2015

ACCEPTED FOR PUBLICATION
5 May 2015

PUBLISHED
1 June 2015

Content from this work may be used under the terms of the Creative Commons Attribution 3.0 licence.

Any further distribution of this work must maintain attribution to the author(s) and the title of the work, journal citation and DOI.

Photoionization of few electron systems: a hybrid coupled channels approach

Vinay Pramod Majety, Alejandro Zielinski and Armin Scrinzi

Physics Department, Ludwig Maximilians Universität, D-80333 Munich, Germany

E-mail: armin.scrinzi@lmu.de

Keywords: strong field physics, photoelectron spectra, coupled channels method, tSURFF

Abstract

We present the hybrid anti-symmetrized coupled channels method for the calculation of fully differential photo-electron spectra of multi-electron atoms and small molecules interacting with strong laser fields. The method unites quantum chemical few-body electronic structure with strong-field dynamics by solving the time dependent Schrödinger equation in a fully anti-symmetrized basis composed of multi-electron states from quantum chemistry and a one-electron numerical basis. Photoelectron spectra are obtained via the time dependent surface flux (tSURFF) method. Performance and accuracy of the approach are demonstrated for spectra from the helium and beryllium atoms and the hydrogen molecule in linearly polarized laser fields at wavelengths from 21 to 400 nm. At long wavelengths, helium and the hydrogen molecule at equilibrium inter-nuclear distance can be approximated as single channel systems whereas beryllium needs a multi-channel description.

1. Introduction

Understanding laser-atom/molecule interaction has become an important research pursuit with the introduction of many versatile light probes over the past decade. Experimental techniques like re-collision imaging [1] and attosecond streaking [2] are being pursued to study time resolved electron dynamics. One of the factors that always creates a certain amount of vagueness in interpreting these strong field ionization experiments is the possible presence of multi-electron effects. An accurate interpretation of the experiments needs solutions of the multi-electron time dependent Schrödinger equation (TDSE). As perturbation theory is not valid in the strong field regime, one resorts to direct numerical solutions of the TDSE.

While simple single electron models or low dimensional models have been partially successful in explaining laser matter interactions, there have been several cases reported where a more elaborate description of electronic structure becomes important. Some of the examples include inter-channel coupling leading to an enhancement in high harmonic generation (HHG) from xenon [3], modification of angle resolved ionization yield of CO_2 [4] and photoionization cross-sections in SF_6 [5], enhancement in HHG due to participation of doubly excited states in beryllium [6], influence of nuclear motion [7], presence of conical intersections [8] and so on. All these instances need a more involved description of the electronic structure.

With one and two electron systems, a full dimensional numerical treatment is possible in linearly polarized laser fields. For systems with more than 6 degrees of freedom a full dimensional calculation is infeasible. There have been several efforts in the past decade to overcome this barrier of dimensionality for few electron systems by choosing only a part of the Hilbert space that is seemingly important for the dynamics. Some of the approaches that are being employed are time dependent configuration interaction methods [9], different variants of multi-configuration methods [10–17], the time-dependent R-matrix method [18], and coupled channel methods [4].

One of the observables that is typically measured in strong laser-atom/molecule interaction experiments are photoelectron spectra. While the methods listed above [4, 9–18] have tried to include multi-electron effects in photoionization studies, calculation of photoelectron spectra from multi-electron systems, especially at long

© 2015 IOP Publishing Ltd and Deutsche Physikalische Gesellschaft

wavelengths has remained out of computational reach. The particular difficultly arises from the fact that, in order to compute photoelectron spectra the asymptotic part of the wavefunction is required. This needs large simulation box volumes and access to exact single continuum states to project the wavefunction onto at the end of time propagation. Having large simulation boxes and computing single continuum states of a multi-electron system are expensive tasks, making these kind of computations costly or outright impossible.

In this respect, a recently developed method called the time dependent surface flux (tSURFF) method [19, 20] has turned out to be an attractive solution. In the tSURFF approach, the wavefunction outside a certain simulation box is absorbed, and the electron flux through the box surface is used to obtain photoelectron spectra. This way photoelectron spectra can be computed with minimal box sizes.

We deal with the difficulties of the few body problem and computation of photoelectron spectra by combining quantum chemical structure with tSURFF for single electron systems through a coupled channels approach. The ansatz is similar in spirit to the one presented in [4]. However, unlike in [4], we deal with anti-symmetrization exactly. We discretize our multi-electron wavefunctions with the neutral ground state of the system and with anti-symmetrized products of the system's single ionic states and a numerical one-electron basis. This ansatz is suitable to study single ionization problems. The ionic and neutral states are computed by the COLUMBUS code [21] giving us the flexibility to treat the ionic states at various levels of quantum chemistry. While the fully flexible active electron basis describes the ionizing electron, the ionic basis describes the core polarization and the exact anti-symmetrization ensures indistinguishability of the electrons. The inclusion of the field-free neutral helps us to get the right ionization potential and start with the correct initial state correlation without much effort. We call our method hybrid fully anti-symmetrized coupled channels method and use the acronym haCC to refer to it in this work. Using tSURFF with haCC, we compute photoelectron spectra with minimal box sizes.

We intend to communicate in this article the mathematical formulation of our method, and demonstrate its usefulness by computing photoelectron spectra of He, H_2 and Be in linearly polarized 21–400 nm wavelength laser fields and compare them with fully numerical two electron results. We discuss the advantages and limitations of such an approach through suitable examples.

2. Mathematical formulation

In this section, we describe our mathematical setup to solve the N-electron TDSE in the presence of an external laser field. We solve

$$\mathrm{i}\frac{\partial}{\partial t}\Psi = \hat{H}\Psi \tag{1}$$

with fixed nuclei approximation and with dipole approximation which implies neglecting the spatial dependence of the laser field. Atomic units $m_e = \hbar = e^2 = 1$ are used unless specified otherwise. The non-relativistic N-electron field-free Hamiltonian can be written as:

$$\hat{H} = \sum_i \left[-\frac{1}{2}\nabla_i^2 - \sum_p \frac{Z_p}{\left|\vec{r}_i - \vec{a}_p\right|} \right] + \sum_{i<j} \frac{1}{\left|\vec{r}_i - \vec{r}_j\right|}, \tag{2}$$

where Z_p is the nuclear charge and $\vec{a}_p$ are the nuclear coordinates of the pth nucleus. The interaction with the external laser field in length gauge is given by:

$$\hat{D}_L = -\sum_j \vec{E}(t) \cdot \vec{r}_j \tag{3}$$

and in velocity gauge by

$$\hat{D}_V = \sum_j \mathrm{i}\vec{A}(t) \cdot \vec{\nabla}_j. \tag{4}$$

We describe our multi-electron discretization in detail in 2.1, present the time propagation equations in 2.2 and the matrix elements in 2.3. As the basis is non-orthogonal, an overlap matrix appears in the computation, whose efficient inversion by low rank updates will be presented in 2.4. Treating anti-symmetrization exactly and including neutrals introduces a technical difficulty in the form of linear dependencies in our basis. This is handled by performing a generalized inverse of the overlap matrix which will be presented in 2.5. We work in mixed gauge for the reasons detailed in [22] and briefed in 2.6. Finally, we present tSURFF for our coupled channels setup in section 2.7.

2.1. Multi-electron discretization

We discretize our N-electron wavefunction by channel wave functions chosen as anti-symmetrized products of ionic states with a numerical one-electron basis. To this we add the wave function of the neutral ground state, resulting in the expansion

$$|\Psi(t)\rangle \approx \sum_{\mathcal{I}} |\mathcal{I}\rangle C_{\mathcal{I}}(t) + |\mathcal{G}\rangle C_{\mathcal{G}}(t), \tag{5}$$

where

$$|\mathcal{I}\rangle = \mathcal{A}[\,|i\rangle|I\rangle\,]. \tag{6}$$

Here, $\mathcal{A}$ indicates anti-symmetrization, $|i\rangle$ are functions from a numerical one-electron basis, $|I\rangle$ and $|\mathcal{G}\rangle$ are (N-1) and N particle functions respectively and $C_{\mathcal{I}}(t)$, $C_{\mathcal{G}}(t)$ are the time dependent coefficients.

For the single electron basis $|i\rangle$ we use a finite element representation on the radial coordinate times spherical harmonics on the angular coordinates

$$|i(\vec{r})\rangle = \left|f_i(r)\right\rangle \left|Y_{l_i m_i}(\hat{r})\right\rangle. \tag{7}$$

On each finite element we use high order scaled Legendre polynomials as basis functions. The typical orders we use are 10–14. The details of the finite element approach used here can be found in [23, 24]. A brief description is given in appendix for the convenience of the reader. We refer to this basis as the active electron basis.

We choose $|I\rangle$ to be the eigenstates of the single ionic Hamiltonian obtained from the multi-reference configuration interaction singles doubles (MR-CISD) level of quantum chemistry. $|\mathcal{G}\rangle$ is chosen as the ground state of the system, also obtained from the MR-CISD level of quantum chemistry. These quantum chemistry wavefunctions are constructed with an atom centered primitive Gaussian basis as the starting point. While $|\mathcal{G}\rangle$ is the lowest eigenvector of the N particle Hamiltonian as obtained from COLUMBUS, it is not the ground state of the Hamiltonian in our basis: by treating one of the electrons with the active electron basis that is superior to the Gaussian basis one further improves the ground state energy.

The wavefunctions $|\mathcal{G}\rangle$ and $|I\rangle$ can be represented in a general form as sums of determinants:

$$|I\rangle = \sum_{p_1,p_2,\ldots,p_{n-1}} d_{p_1,p_2,\ldots,p_{n-1}} \left|\mathcal{A}\left[\phi_{p_1}\phi_{p_2}\ldots\phi_{p_{n-1}}\right]\right\rangle \tag{8}$$

$$|\mathcal{G}\rangle = \sum_{p_1,p_2,\ldots,p_n} d_{p_1,p_2,\ldots,p_n} \left|\mathcal{A}\left[\phi_{p_1}\phi_{p_2}\ldots\phi_{p_n}\right]\right\rangle, \tag{9}$$

where ϕ_k are the Hartree–Fock orbitals of the neutral system. The same set of Hartree–Fock orbitals are used to construct both ionic and neutral CI functions. This allows us to use simple Slater–Condon rules to compute any matrix elements between them.

The explicit inclusion of the neutral ground state is motivated by the fact that, while the ionization process itself may be well described by one or a few ionic channels, the initial ground state may be more strongly correlated. In order to avoid inclusion of many ionic states just to describe the initial state, we include the neutral ground state explicitly, thereby reducing the number of basis functions needed. This idea can be easily extended to include any specific correlated state that is of importance to a particular process.

2.2. Time propagation equations

Substituting the ansatz (5) into the TDSE (1) yields a set of coupled ordinary differential equations for the time dependent coefficients:

$$i\left[\langle\mathcal{G}|\mathcal{G}\rangle\frac{dC_{\mathcal{G}}}{dt} + \langle\mathcal{G}|\mathcal{I}\rangle\frac{dC_{\mathcal{I}}}{dt}\right] = \langle\mathcal{G}|\,\hat{H}\,|\mathcal{G}\rangle C_{\mathcal{G}} + \langle\mathcal{G}|\,\hat{H}\,|\mathcal{I}\rangle C_{\mathcal{I}} \tag{10}$$

$$i\left[\langle\mathcal{I}|\mathcal{G}\rangle\frac{dC_{\mathcal{G}}}{dt} + \langle\mathcal{I}|\mathcal{I}\rangle\frac{dC_{\mathcal{I}}}{dt}\right] = \langle\mathcal{I}|\,\hat{H}\,|\mathcal{G}\rangle C_{\mathcal{G}} + \langle\mathcal{I}|\,\hat{H}\,|\mathcal{I}\rangle C_{\mathcal{I}}. \tag{11}$$

The time-derivative of the coefficient vector is multiplied by an overlap matrix composed of the blocks $\langle\mathcal{G}|\mathcal{G}\rangle$, $\langle\mathcal{G}|\mathcal{I}\rangle$, $\langle\mathcal{I}|\mathcal{G}\rangle$ and $\langle\mathcal{I}|\mathcal{I}\rangle$.

We time propagate the coefficients using an explicit fourth order Runge–Kutta method with adaptive step size. In order to absorb the wavefunction at the box boundaries we use infinite range exterior complex scaling (irECS) [23]. We typically choose simulation boxes larger than the spatial extent of the Hartree–Fock orbitals and start absorption after the Hartree–Fock orbitals vanish. This implies that it suffices to complex scale only one of the N coordinates.

The cost of time propagation scales with the number of ionic states (say n_I) as n_I^2 and it is independent of the exact number of electrons. This makes basis sets of the kind (5) attractive for treating many electron systems.

2.3. Matrix elements

In order to solve the TDSE we need to evaluate various operators. Firstly, we introduce several generalized reduced density matrices with the help of creation ($a_k^\dagger$) and annihilation (a_k) operators on the single particle state ϕ_k. A pth order generalized reduced density matrix between the (N-1) particle ionic functions is given by:

$$\rho^{IJ}_{k_1,\ldots,k_p,l_1,\ldots,l_p} = \langle I|\ a^\dagger_{k_1}\ldots a^\dagger_{k_p} a_{l_1}\ldots a_{l_p}\ |J\rangle. \tag{12}$$

Similarly, we define generalized Dyson coefficients between the N-particle neutral wavefunctions and (N-1) particle ionic wavefunctions as

$$\eta^{\mathcal{GJ}}_{k_1,\ldots,k_p,l_1,\ldots,l_{p-1}} = \langle \mathcal{G}|\ a^\dagger_{k_1}\ldots a^\dagger_{k_p} a_{l_1}\ldots a_{l_{p-1}}\ |J\rangle. \tag{13}$$

With the help of these objects, we can present the final form of the matrix elements. The overlap matrix blocks have the form

$$\begin{aligned}
\langle \mathcal{G}|\mathcal{G}\rangle &= 1\\
\langle \mathcal{G}|\mathcal{I}\rangle &= \eta^{\mathcal{GI}}_k \left\langle \phi_k \middle| i\right\rangle\\
\langle \mathcal{I}|\mathcal{J}\rangle &= \langle i|j\rangle\langle I|J\rangle - \left\langle i\middle|\phi_l\right\rangle \rho^{IJ}_{kl}\left\langle \phi_k\middle|j\right\rangle\\
&= \langle i|j\rangle\delta_{IJ} - \left\langle i\middle|\phi_l\right\rangle \rho^{IJ}_{kl}\left\langle \phi_k\middle|j\right\rangle,
\end{aligned} \tag{14}$$

where $\eta^{\mathcal{GI}}_k$ can be identified with the Dyson orbital coefficients with respect to the Hartree–Fock orbitals and ρ^{IJ}_{kl} are the one particle reduced density matrices.

Any exchange-symmetric single particle operator can be written as

$$\hat{T} = \hat{t}\,(1) + \hat{t}\,(2) + \ldots + \hat{t}\,(N), \tag{15}$$

where $\hat{t}\,(u)$ is the single particle operator corresponding to the coordinate u. Matrix elements of $\hat{T}$ are

$$\begin{aligned}
\langle \mathcal{G}|\ \hat{T}\ |\mathcal{G}\rangle &= \rho^{\mathcal{GG}}_{kl}\left\langle \phi_k\middle|\ \hat{t}\ \middle|\phi_l\right\rangle\\
\langle \mathcal{G}|\ \hat{T}\ |\mathcal{I}\rangle &= \eta^{\mathcal{GI}}_k\left\langle \phi_k\middle|\ \hat{t}\ |i\right\rangle + \eta^{\mathcal{GI}}_{klm}\left\langle \phi_k\middle|\ \hat{t}\ \middle|\phi_m\right\rangle\left\langle \phi_l\middle|i\right\rangle\\
\langle \mathcal{I}|\ \hat{T}\ |\mathcal{J}\rangle &= \langle i|j\rangle\langle I|\ \hat{t}\ |J\rangle + \langle i|\ \hat{t}\ |j\rangle\langle I|J\rangle - \langle i|\ \hat{t}\ \middle|\phi_l\right\rangle\rho^{IJ}_{kl}\left\langle \phi_k\middle|j\right\rangle\\
&\quad - \left\langle i\middle|\phi_l\right\rangle\rho^{IJ}_{kl}\left\langle \phi_k\middle|\ \hat{t}\ |j\right\rangle - \left\langle i\middle|\phi_c\right\rangle\left\langle \phi_a\middle|j\right\rangle\left\langle \phi_b\middle|\ \hat{t}\ \middle|\phi_d\right\rangle\rho^{IJ}_{abcd},
\end{aligned} \tag{16}$$

where $\eta^{\mathcal{GI}}_{klm}$ are the three index generalized Dyson coefficients, equation (13), and ρ^{IJ}_{abcd} are the two particle reduced density matrices, equation (12).

Finally, the two particle operators

$$\hat{V}^{(2)} = \sum_{i<j}\hat{v}\,(ij) \tag{17}$$

have the matrix elements

$$\begin{aligned}
\langle \mathcal{G}|\ \hat{V}^{(2)}|\mathcal{G}\rangle &= \frac{1}{2}\rho^{\mathcal{GG}}_{abcd}\left\langle \phi_a\phi_b\middle|\ \hat{v}\ \middle|\phi_c\phi_d\right\rangle\\
\langle \mathcal{G}|\ \hat{V}^{(2)}|\mathcal{I}\rangle &= \eta^{\mathcal{GI}}_{klm}\left\langle \phi_k\phi_l\middle|\ \hat{v}\ \middle|\phi_m i\right\rangle + \frac{1}{2}\eta^{\mathcal{GI}}_{abcde}\left\langle \phi_a\phi_b\middle|\ \hat{v}\ \middle|\phi_d\phi_e\right\rangle\left\langle \phi_c\middle|i\right\rangle\\
\langle \mathcal{I}|\ \hat{V}^{(2)}|\mathcal{J}\rangle &= \frac{1}{2}\rho^{\mathcal{IJ}}_{abcd}\left\langle \phi_a\phi_b\middle|\ \hat{v}\ \middle|\phi_c\phi_d\right\rangle\langle i|j\rangle + \underbrace{\rho^{IJ}_{kl}\left\langle \phi_k i\middle|\ \hat{v}\ \middle|\phi_l j\right\rangle}_{\text{Direct term}} - \underbrace{\rho^{IJ}_{kl}\left\langle \phi_k i\middle|\ \hat{v}\ \middle|j\phi_l\right\rangle}_{\text{Standard exchange term}}\\
&\quad \underbrace{- \rho^{IJ}_{abcd}\left\langle \phi_a i\middle|\ \hat{v}\ \middle|\phi_c\phi_d\right\rangle\left\langle \phi_b\middle|j\right\rangle - \rho^{IJ}_{abcd}\left\langle \phi_a\phi_b\middle|\ \hat{v}\ \middle|\phi_c j\right\rangle\left\langle i\middle|\phi_d\right\rangle - \frac{1}{2}\rho^{IJ}_{abcdef}\left\langle \phi_a\phi_b\middle|\ \hat{v}\ \middle|\phi_d\phi_e\right\rangle\left\langle i\middle|\phi_f\right\rangle\left\langle \phi_c\middle|j\right\rangle}_{\text{Other exchange terms due to non-orthogonality}},
\end{aligned} \tag{18}$$

where $\eta^{\mathcal{GI}}_{abcde}$ are the five index generalized Dyson coefficients, equation(13) and ρ^{IJ}_{abcdef} are the three particle reduced density matrices, equation (12). Although it appears from equation (18) that the necessity of ρ^{IJ}_{abcdef}, $\eta^{\mathcal{GI}}_{abcde}$ leads to large memory requirements, we must point out that the contractions $\rho^{IJ}_{abcdef}\langle\phi_a\phi_b|\hat{v}|\phi_d\phi_e\rangle$ and $\eta^{\mathcal{GI}}_{abcde}\langle\phi_a\phi_b|\hat{v}|\phi_d\phi_e\rangle$ can be made while computing ρ^{IJ}_{abcdef} and $\eta^{\mathcal{GI}}_{abcde}$ itself, thereby storing only simple matrices and vectors.

In order to compute the two-electron integrals, we first project the Hartree–Fock orbitals onto a single center expansion:

$$\phi_k(\vec{r}) = \sum_{q_k l_k m_k} d_{q_k l_k m_k} Y_{l_k m_k}(\theta, \phi), \tag{19}$$

where q_k are radial quadrature points, l_k, m_k refer to the angular momentum functions and use these expansions with the multi-pole expansion:

$$\frac{1}{|\vec{r}_1 - \vec{r}_2|} = \sum_{LM} \frac{4\pi}{2L+1} \frac{r_<^L}{r_>^{L+1}} Y_{LM}(\theta_1, \phi_1) Y^*_{LM}(\theta_2, \phi_2) \tag{20}$$

with $r_< = \min(r_1, r_2)$ and $r_> = \max(r_1, r_2)$.The limits for the multi-pole expansion are determined by the angular momenta in the one-electron numerical basis and the single center expansion for the molecular orbitals ϕ_k. No other truncation schemes are employed. These two particle operators pose a challenge for efficient computation. While the direct term is relatively easy to handle, the exchange terms consume a major portion of the Hamiltonian setup time.

2.4. Inverse of the overlap matrix

The overlap matrix (14) is not a standard finite element overlap matrix, which would be banded and would allow for efficient application of the inverse. Rather, non-orthogonality between the active electron basis and the Hartree–Fock orbitals leads to extra cross terms that destroy the banded structure in general and complicate the computation of the inverse. However, the inverse of the overlap can still be computed efficiently using low rank updates. We use here the Woodbury formula [25], according to which the inverse of a modified matrix of the form $(S_0 - U\Lambda U^\dagger)$ can be computed as:

$$\begin{aligned} S^{-1} &= (S_0 - U\Lambda U^\dagger)^{-1} \\ &= S_0^{-1} - S_0^{-1} U (U^\dagger S_0^{-1} U - \Lambda^{-1})^{-1} U^\dagger S_0^{-1}. \end{aligned} \tag{21}$$

As an example, with 2 ionic states and 1 neutral the overlap matrix (14) can be cast in the form:

$$S = \underbrace{\begin{pmatrix} s_0 & 0 & 0 \\ 0 & s_0 & 0 \\ 0 & 0 & 1 \end{pmatrix}}_{S_0} - \underbrace{\begin{pmatrix} u & 0 & 0 \\ 0 & u & 0 \\ 0 & 0 & 1 \end{pmatrix}}_{U} \underbrace{\begin{pmatrix} \rho^{11} & \rho^{12} & \eta^{\mathcal{G}1} \\ \rho^{21} & \rho^{22} & \eta^{\mathcal{G}2} \\ [\eta^{\mathcal{G}1}]^T & [\eta^{\mathcal{G}2}]^T & 0 \end{pmatrix}}_{\Lambda} U^\dagger \tag{22}$$

which is suitable for the Woodbury formula (21). Here, $(s_0)_{ij} = \langle i|j\rangle$ and $u_{ik} = \langle i|\phi_k\rangle$. Let n_a denote the number of active electron basis functions $|i\rangle$ and n_{hf} be the number of Hartree–Fock orbitals ϕ_k that is much smaller that n_a. The overlap matrix s_0 has dimensions $n_a \times n_a$ but is narrowly banded, and the dimensions of matrix u are $n_a \times n_{hf}$.

Let n_I be the number of ionic states. Then the overlap S and S_0 are $(n_I n_a + 1) \times (n_I n_a + 1)$ matrices, where the inverse of S_0 can be easily applied. The matrix U is $(n_I n_a + 1) \times (n_I n_{hf} + 1)$ and Λ is $(n_I n_{hf} + 1) \times (n_I n_{hf} + 1)$. This low rank structure of the correction terms can be utilized to compute the inverse efficiently by using the Woodbury formula.

2.5. Handling linear dependencies

Anti-symmetrization and non-orthogonality of the active electron basis with respect to the Hartree–Fock orbitals may render our basis linearly dependent. If the $\{|i\rangle\}$-basis is near-complete w.r.t. the HF-orbital basis

$$\left\langle \phi_k \middle| i \right\rangle \; [s_0^{-1}]_{ij} \; \left\langle j \middle| \phi_l \right\rangle \approx \delta_{kl}, \tag{23}$$

it is possible to find coefficients $c_{i,I}$ such that

$$\sum_{i,I} c_{i,I} \mathcal{A}[|i\rangle |I\rangle] \approx 0. \tag{24}$$

An obvious case where this happens is when one and the same HF orbital ϕ_{k_0} appears in all the ionic determinants. For a linear combination $\sum_i c_{i,I}|i\rangle \approx \phi_{k_0}$ anti-symmetrization renders equation (24) near zero. As a result, the overlap matrix becomes non-invertible. A possible solution would be to orthogonalize the active electron basis with respect to the Hartree–Fock orbitals. But this is not an easily implementable solution with a CI ionic basis. For each determinant, the set of Hartree–Fock orbitals with respect to which the active electron basis must be orthogonal is different.

As an alternative solution we use a generalization of the Woodbury formula (21) to compute the inverse of a matrix only on the subspace of the non-zero eigenvectors of the matrix. Let Z denote the $n_0 \times n_z$ matrix of eigenvectors with near-zero eigenvalues $z_p < \epsilon$, $p = 1, \ldots, n_z$ of the generalized eigenvalue problem

$$SZ = S_0 Z d_z, \tag{25}$$

with d_z denoting the diagonal matrix of the eigenvalues z_p and Z satisfying the orthonormality relation $Z^\dagger S_0 Z = \mathbf{1}$. In general, there will be comparatively few such eigenvectors $n_z \ll n_0$ and these can be easily determined by an iterative solver. We can remove these singular vectors from our calculation by the projector

$$Q = 1 - ZZ^\dagger S_0. \tag{26}$$

The projector property $Q^2 = Q$ can be easily verified. As the projector refers to the generalized eigenvalue problem with $S_0 \neq \mathbf{1}$, Q is not an orthogonal projector, that is $Q^\dagger \neq Q$. We define a pseudo-inverse $\tilde{S}^{-1}$ of S on the subspace of generalized eigenvectors with non-zero eigenvalues with the property

$$\tilde{S}^{-1} S Q = Q. \tag{27}$$

One can verify directly that the generalized Woodbury formula

$$\tilde{S}^{-1} = Q S_0^{-1} \left[1 - U \left(U^\dagger Q S_0^{-1} U - \Lambda \right)^{-1} U^\dagger Q S_0^{-1} \right] \tag{28}$$

satisfies the definition (27). The matrix $(U^\dagger Q S_0^{-1} U - \Lambda)$ is invertible on all vectors appearing in $U^\dagger Q$ to its right, as exactly the singular vectors are removed by the projector Q. Apart from the necessity to determine Z during setup, the correction does not significantly increase the operations count for the inverse overlap.

2.6. Choice of gauge

In [22], we had shown that when an electron is treated with a restricted basis, for example, in terms of a few bound states, the length gauge is a more natural gauge. Compared to pure velocity gauge, the coupled channel computations converge quickly in mixed gauge with length gauge spanning the region of the ionic states and velocity gauge thereafter for asymptotics. In this current work, we use continuous gauge switching, detailed in [22], for its easy implementation. Starting from the length-gauge, we solve the TDSE after applying the gauge transformation

$$U_c = \begin{cases} 1 & \text{for } r \leqslant r_g, \\ \exp\left[i\vec{A}(t) \cdot \sum_{j=1}^{N} \hat{r_j} (r_j - r_g) \right] & \text{for } r > r_g. \end{cases} \tag{29}$$

Here, r_g is the gauge radius that separates the length gauge and velocity gauge regions.

2.7. Computation of photoelectron spectra

The computation of photoelectron spectra is expensive for two reasons. (1) The asymptotic part of the wavefunction is needed to extract photoelectron spectra, which means large simulation boxes to preserve the asymptotic part and to avoid any numerical reflections that may corrupt the wavefunction. (2) Single continuum states are needed into which the wavefunction must be decomposed, in order to obtain photoelectron spectra. These two problems are circumvented in a recently developed method tSURFF [19, 20]: one computes the spectra by a time integration of electron flux through a surface defined by a radius R_c called the tSURFF radius. The Coulomb potential is smoothly turned off before R_c, which implies that the scattering solutions thereafter are the well known Volkov solutions. R_c becomes a convergence parameter, and by varying this radius, one can compute spectra to a given accuracy. This method has been explained in detail in previous works for single ionization in [19] and for double ionization in [20]. A proposal for extension of this method for single ionization of multi-electron systems has been outlined in [20]. We describe here the application of the method with our coupled channels setup.

Let χ_k be the scattering solutions which take the form of Volkov solutions beyond R_c and $\Psi(T)$ be the wavefunction at some large time T. According to tSURFF for single electron systems, photoelectron spectra can be computed as $\sigma_k = |b_k|^2$ with b_k defined as:

$$\begin{aligned} b_k &= \langle \chi_k(T) | \, \Theta(R_c) | \Psi(T) \rangle \\ &= i \int_0^T dt \, \langle \chi_k(t) | \left[-\frac{1}{2}\triangle + i\vec{A}(t) \cdot \vec{\nabla}, \Theta(R_c) \right] | \Psi(t) \rangle. \end{aligned} \tag{30}$$

Here $\Theta(R_c)$ is a Heaviside function that is unity for $r > R_c$ and 0 elsewhere.

This formulation can be easily extended to the N electron problem in a coupled channels setup. In the present setup, we mostly take a set of ionic bound states for the ionic basis. These states have a finite extent. We may choose R_c such that the electrons described by the ionic basis vanish by R_c which means all the exchange terms in the Hamiltonian vanish after R_c. The remaining direct potential can be smoothly turned off just as the Coulomb potential. This implies that the wavefunction beyond R_c evolves by the Hamiltonian:

$$H(r > R_c) = H_{\text{ion}} \otimes \hat{1} + \hat{1}_{\text{ion}} \otimes \left[-\frac{1}{2}\triangle + \mathrm{i}\vec{A}(t) \cdot \vec{\nabla} \right] \tag{31}$$

that allows for a complete set of solutions of the form:

$$\xi_{c,k}(\vec{r}_1, \ldots, \vec{r}_n, t) = \mathcal{A}\left[\kappa_c(\vec{r}_1, \ldots, \vec{r}_{n-1}, t) \otimes \chi_k(\vec{r}_n, t) \right], \tag{32}$$

where H_{ion} is the single ionic Hamiltonian and $\kappa_c(t)$ are time dependent ionic channel functions solving the TDSE

$$\mathrm{i}\frac{\partial \kappa_c(t)}{\partial t} = \hat{H}_{\text{ion}}\kappa_c(t) \tag{33}$$

within the ansatz in terms of field-free ionic states

$$|\kappa_c(t)\rangle = \sum_I |I\rangle d_{cI}(t). \tag{34}$$

With the help of the $\xi_{c,k}$, channel resolved photoelectron spectra can be computed as

$$\sigma_{c,k} = \left| \left\langle \xi_{c,k}(\vec{r}_1, \ldots, \vec{r}_n, T) \right| \Theta(R_c) |\Psi(\vec{r}_1, \ldots, \vec{r}_n, T)\right\rangle \right|^2 \tag{35}$$

and the asymptotic decomposition of Ψ in terms of $\xi_{c,k}$ is obtained as

$$\begin{aligned} &\left\langle \xi_{c,k}(\vec{r}_1, \ldots, \vec{r}_n, T) \right| \Theta(R_c) |\Psi(\vec{r}_1, \ldots, \vec{r}_n, T)\rangle \\ &\quad = \mathrm{i}\int_0^T \mathrm{d}t \left\langle \mathcal{A}\left[\kappa_c(\vec{r}_1, \ldots, \vec{r}_{n-1}, t) \otimes \chi_k(\vec{r}_n, t) \right] \right| \left[-\frac{1}{2}\triangle_n + \mathrm{i}\vec{A}(t) \cdot \vec{\nabla}_n, \Theta_n(R_c) \right] |\Psi(\vec{r}_1, \ldots, \vec{r}_n, t)\rangle \\ &\quad = \mathrm{i}\int_0^T \mathrm{d}t \left\langle \chi_k(\vec{r}_n, t) \right| \left[-\frac{1}{2}\triangle_n + \mathrm{i}\vec{A}(t) \cdot \vec{\nabla}_n, \Theta_n(R_c) \right] |\zeta_c(\vec{r}_n, t)\rangle, \end{aligned} \tag{36}$$

where we introduced the time-dependent Dyson orbitals

$$\zeta_c(\vec{r}_n, t) := \langle \kappa_c(\vec{r}_1, \ldots, \vec{r}_{n-1}, t) | \Psi(\vec{r}_1, \ldots, \vec{r}_n, t)\rangle. \tag{37}$$

The commutator of the derivatives with the Heaviside function Θ gives δ-like terms involving values and derivatives of Ψ at the surface $|\vec{r}| = R_c$. As we choose R_c such that the Hartree–Fock orbitals vanish by then, we do not need to consider the exchange terms in computing ζ_c. Along with time propagating the N electron problem, one needs to also time propagate the ionic problem (33).

A detailed discussion of performance and intrinsic limitations of the tSURFF method is contained in [19, 20]. We here summarize the main points of this discussion. The strength of tSURFF lies (a) in a dramatic reduction of the required numerical box sizes to compute accurate spectra and (b) in the fact that no scattering states are needed for spectral analysis. As the asymptotic scattering information is generated during time-propagation rather than by solving an independent stationary problem, propagation times must be long enough for all relevant processes to terminate and for all electrons to pass through the surface. This favors the application of the method for fast processes. For slow processes like emission at near zero electron energy or the decay of long-lived resonances purely stationary methods or methods that combine solutions of the TDSE during pulse with a stationary analysis after the end of the pulse may become advantageous. Also, if small boxes are used, the capability for representing very extended objects like Rydberg states is limited by the box size. We will illustrate these points below when discussing photo-emission from the helium atom at short wave length.

2.8. Spin symmetry

As we solve the non-relativistic TDSE, the total spin of the system is conserved during the time evolution. We can therefore remove the spin degree of freedom through suitable linear combinations of the anti-symmetrized products in the basis (5) to enforce a particular spin symmetry. This reduces the size of our basis. We consider only singlet spin symmetric systems in this work. As an example, we show how singlet spin symmetry can be enforced. Let $\uparrow$ and $\downarrow$ indicate the spin states $\pm\frac{1}{2}$ associated with a spatial function. Choosing linear combinations of the kind:

$$\mathcal{A}[|I\rangle|i\rangle] := \frac{\mathcal{A}\left[|I^{\uparrow}\rangle|i^{\downarrow}\rangle\right] - \mathcal{A}\left[|I^{\downarrow}\rangle|i^{\uparrow}\rangle\right]}{\sqrt{2}} \tag{38}$$

enforces singlet symmetry. This can be extended to creating linear combinations that enforce an arbitrary spin symmetry.

3. Two-electron benchmark calculations

We use two-electron full dimensional calculations (full-2e) as benchmark for our haCC computations. We solve the two-electron TDSE using an independent particle basis of the form:

$$\Psi(\vec{r}_1, \vec{r}_2, t) = \sum_{k_1 k_2 l_1 l_2 m} c_{k_1 k_2 l_1 l_2 m}(t) f_{k_1}(r_1) f_{k_2}(r_2) Y_{l_1 m}(\theta_1, \phi_1) Y_{l_2 - m}(\theta_2, \phi_2), \tag{39}$$

where $c_{k_1 k_2 l_1 l_2 m}(t)$ are the time dependent coefficients, $f_{k_1}(r_1)$, $f_{k_2}(r_2)$ are functions from a finite element discretization of the same type as for our active electron basis and Y_{lm} are spherical harmonics. We use the same type of single center expansion for all the benchmark computations. A complete description of this method will be presented elsewhere [24]. Solving the TDSE with the expansion (39) needs much larger computational resources compared to the haCC approach.

The purpose of the two-electron calculations is to demonstrate to which extent these fully correlated calculations are reproduced by the haCC approach. For that we use the same tSURFF propagation times and identical box sizes when comparing the two types of calculations. Full convergence of the two-electron calculation in propagation time and box size is not discussed in the present paper.

4. Single photoelectron spectra

In this section, we present photoelectron spectra from helium and beryllium atoms and from the hydrogen molecule with linearly polarized laser fields computed with the above described coupled channels formalism. We also present the single photon ionization cross-sections for the beryllium atom and the wavelength dependence of the ionization yield for the hydrogen molecule to compare with other existing calculations. We use $\cos^2$ envelope pulses for all the calculations and the exact pulse shape is given as

$$A_z(t) = A_0 \cos^2\left(\frac{\pi t}{2cT}\right) \sin\left(\frac{2\pi t}{T} + \beta\right) \tag{40}$$

$$E_z(t) = -\frac{\mathrm{d}A_z(t)}{\mathrm{d}t}, \tag{41}$$

where T is the single cycle duration, $A_0 = E_0 T/(2\pi)$ for a peak field strength E_0, c is the number of laser cycles and β is the carrier envelope phase. We compare our results for helium and the hydrogen molecule with full-2e calculations [24] and for beryllium with effective two electron model calculations.

The convergence of the full-2e benchmark calculations and the haCC calculations were done systematically and independently. All the spectra presented here were computed with simulation box sizes on the scale of $R_c \sim 30$–50 a.u. The radial finite element basis consisted of high order polynomials with typical orders 10–14 and the total number of radial basis functions was such that there were 2–3 functions per atomic unit. The angular momenta requirement strongly depends on the wavelength. The longer wavelengths needed larger number of angular momenta for convergence. For the examples considered below, the angular momenta range from $L_{\max} = 5$ at 21 nm to $L_{\max} = 30$ at 400 nm. All the calculations presented are converged with respect to the single electron basis parameters like the order and the box size, well below the differences caused by inclusion of ionic states. Hence, we only present various observables as a function of the number of ionic states.

The storage requirements with the algorithms that we use are dictated by the two particle reduced density matrices. For the largest problem considered here, with 11 ionic states (n_I) and about 50 molecular orbitals (n_{hf}), the number of doubles that had to be stored is given by the formula: $\frac{n_I(n_I+1)}{2}\frac{n_{hf}^2(n_{hf}+1)^2}{4}$, which yields a storage requirement of 1.7 GB. This is not a large requirement in the context of the currently available computational resources. In order to avoid replication, these objects were stored in shared memory. The computation times vary widely depending on the wavelength and the number of ionic states in the basis. They scale with the square of the number of ionic states. For the cases presented here, the required times range from 0.25–30 h on an eight core machine. These times also have a strong dependence on the exact time propagators used and a discussion on the suitable time propagators is out of the scope of this work.

4.1. Helium

Helium is the largest atom that can be numerically treated in full dimensionality. With linearly polarized laser fields, the symmetry of the system can be used to reduce the problem to five-dimensions. The energies of the helium ionic states are $-2/n^2$ for principal quantum number n. The first two ionic states are separated by 1.5 a.u. in energy, which is large, for example, compared to a photon energy of 0.456 a.u. at 100 nm. This has been a motivation to treat helium as an effective single electron system with XUV and longer wavelengths in some

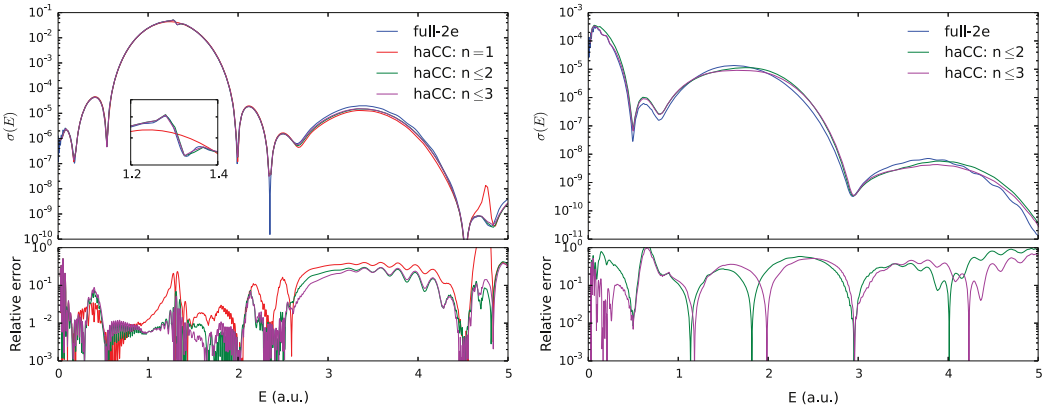

Figure 1. Photoelectron spectra from helium with three-cycle, 21 nm laser pulse with a peak intensity of 10^{15} W cm^{-2}. Left figure: ground state channel (1s) , Right figure: a first excited state channel ($2p_z$). The upper panels show spectra obtained with a full-2e and haCC calculations with different number of ionic states included as indicated in the legend. Here, n is the principal quantum number. The lower panels show relative errors of haCC calculations with respect to full-2e calculations. The inset shows the 2s2p resonance (see main text).

earlier works, for example in [26]. We examine below the validity of treating helium as an effective single electron system, by comparing haCC calculations with full dimensional calculations at different wavelengths.

Figure 1 shows photoelectron spectra from helium with a 21 nm ($\omega = 2.174$ a.u.), three cycle laser pulse with a peak intensity of 10^{15} W cm^{-2}. The one and two photon ionization peaks of 1s and $2p_z$ channel spectra are shown. The relative errors of haCC calculations are computed with respect to the full dimensional calculation. The single photon peak of the 1s channel is computed to a few percent accuracy, except for a feature around 1.3 a.u., with a single ionic state. The resonant feature can be identified with the 2s2p doubly excited state [27], which is reproduced to few percent accuracy with the addition of 2nd shell ionic states. While the position of the resonance is reproduced accurately in the calculations presented here, the propagation time was well below the life-time of this resonance which is reflected in the width of the feature that is well above the natural line width.

The two photon peak of the 1s channel and the $2p_z$ channel spectra (figure 1) need more than a single ionic state and they could be computed only up to 15% accuracy even after inclusion of 9 ionic states ($n \leqslant 3$).

A broadband (few cycle) XUV pulse tends to excite the initial state into a band of final states which may include many correlated intermediate states. Here, the intrinsic limitations of any coupled channels approach that is based on ionic bound states only are exposed. Firstly, a correlated intermediate state with a bound character needs large number of ionic states to be correctly represented. Secondly, the ionic bound states based on Gaussian basis sets do not have the exact asymptotic behavior. This can lead to an inaccuracy in length gauge dipole matrix elements. Finally, the absence of ionic continuum states in our approach is another possible source of inaccuracy. Due to these limitations, we do not expect the shake-up channel spectra to be more accurate than 10–15%.

For obtaining long-lived resonance structures by a time-dependent method one must, as a general feature of such methods, propagate for times at least on the scale of the life time of the resonance. The only alternative is to independently solve the stationary resonant scattering problem and decompose the time-dependent solution after the end of the pulse into the corresponding scattering continuum. Solving the scattering problem, however, is a computationally very demanding task by itself. For obtaining the resonances with tSURFF, one can simply propagate until the resonance has decayed completely and all flux has passed through the surface where the flux is collected. At this point it should be remarked that the relevant information about resonances may be generated more efficiently by stationary methods like time-independent complex scaling [27, 28]. As the comparison in figure 1 is with the two-electron code where long propagation times become rather costly, we compare the spectra at time $T = 60$ laser cycles, where the resonances have not emerged yet.

With haCC, due to its very compact representation, we can easily propagated much longer to obtain the resonances to any desired accuracy. Figure 2 shows how the $n \leqslant 3$ resonances emerge with increasing propagation times in the 1s and $2p_z$ channels. For example, at the 2s2p decay width of $\Gamma = 1.37 \times 10^{-3}$, one expects 76.5% of the Auger electrons to have passed through the surface $|\vec{r}| = 45$ at time $T = 400$, which increases to 95.2% at $T = 800$. The ratio of 1.24 between these numbers closely matches the increase of mass in the 2s2p peak by 1.23 in figure 2. The positions of the resonances are accurate on the level of 10^{-3} a.u. in energy [27], showing that the correlated states are well represented by the method. Here we had chosen a box size of 45 a.u. which is sufficient to represent doubly excited states from 2s2p to 2s6p states. Hence, only these states are

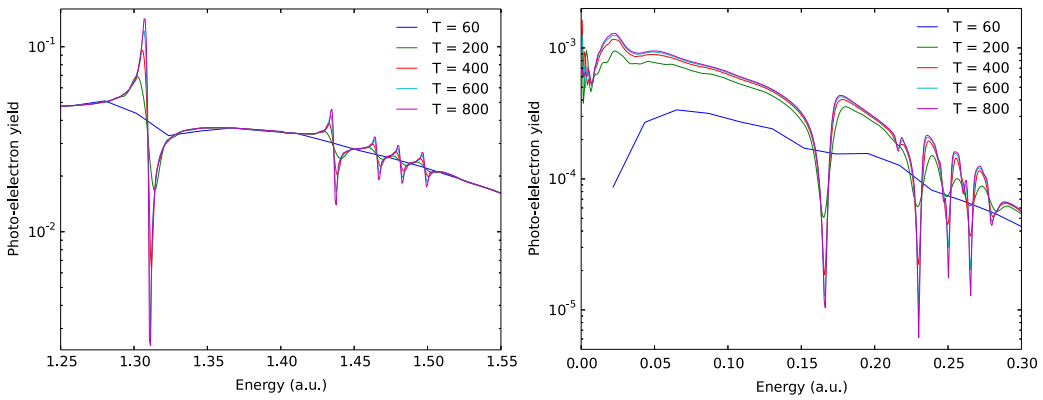

Figure 2. Photoelectron spectra (in selected energy range) from helium for the case $n \leqslant 3$ in figure 1 with different total time propagation. T is the time propagation in the units of laser cycles. Left panel: 1s ionic channel, right panel: $2p_z$ ionic channel. $T = 60$ is from figure 1.

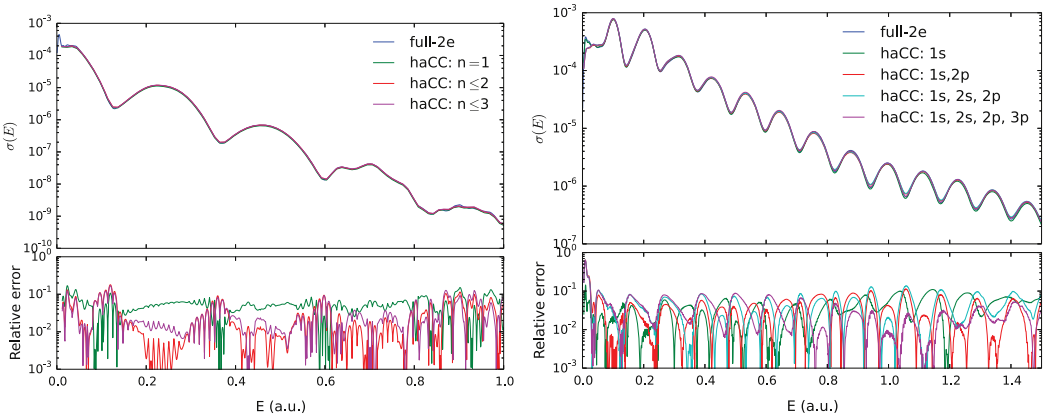

Figure 3. Total photoelectron spectra from helium with Left figure: three-cycle, 200 nm laser pulse with a peak intensity of 10^{14} W cm^{-2}, Right figure: three-cycle, 400 nm laser pulse with a peak intensity of 3×10^{14} W cm^{-2}. The upper panels show spectra obtained with a full-2e and haCC calculations with different number of ionic states included as indicated in the legend. Here, n is the principal quantum number. The lower panels show relative errors of haCC calculations with respect to full-2e calculation.

seen in the spectra. One can obtain the higher excited states by increasing the box size, at the penalty of a larger discretization and somewhat longer propagation times, see discussion in section 2.7. Similar as long lived resonances, threshold behavior of the spectrum near energy zero only emerges with propagation time, figure 2. Further distortions near threshold are due to the effective truncation of the Coulomb tail in the absorbing region. In the present example, these effects produce an artefact at energies $\lesssim$0.02 a.u. in the right panel of figure 2. Accuracies at the lowest energies can be pushed by increasing both, simulation box size and propagation times.

Figure 3 shows total photoelectron spectra from helium at 200 and 400 nm wavelengths. The exact laser parameters are indicated in the figure captions. At 200 nm ($\omega = 0.228$ a.u.), the ionization threshold is four photons. A single ionic state calculation produces spectra that are 10% accurate with respect to a full dimensional calculation. Addition of second and third shell ionic states improves the accuracy of the spectra to few percent level in the important regions of the spectrum. At 400 nm ($\omega = 0.114$ a.u.), the ionization threshold is eight photons. Also here, a single ionic state computation produces spectra that are 10% accurate with respect to a full dimensional calculation. Addition of more ionic states, does not improve the accuracy further. This is possibly due to the missing continuum of the second electron that is needed to fully describe the polarization of the ionic core.

At longer wavelengths, we find that single ionic state computations are sufficient to produce spectra accurate on the level of 10%. This is consistent with the knowledge that at longer wavelengths, it is the ionization

Table 1. Energies of the used single ionic states of beryllium relative to the ground state ion. The COLUMBUS [21] ionic states are computed at MR-CISD level with aug-cc-pvtz basis.

Ionic state	NIST database (eV)	Columbus energies (eV)
$1s^2 2s$	0.0	0.0
$1s^2 2p$	3.9586	3.9767
$1s^2 3s$	10.9393	10.9851
$1s^2 3p$	11.9638	12.1407

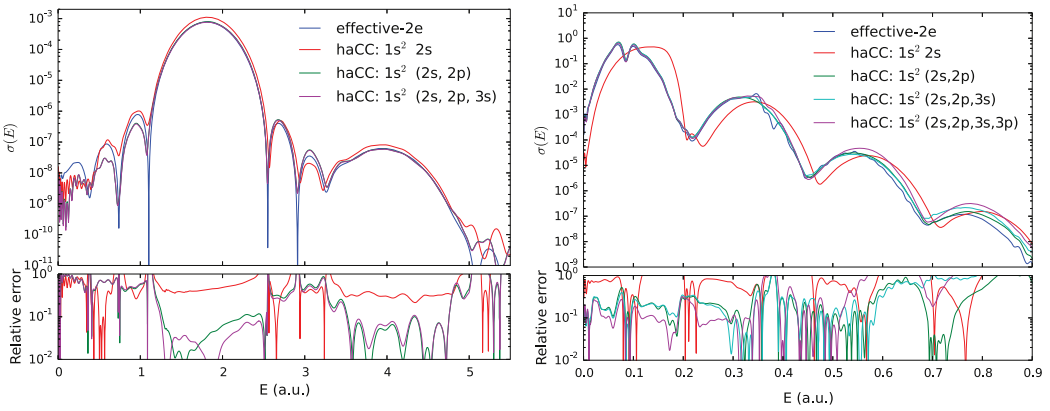

Figure 4. Photoelectron spectra from the beryllium atom. Left figure: ground state channel spectra with three-cycle, 21 nm laser pulse with a peak intensity of 10^{15} W cm^{-2}. Right figure: total spectra with three-cycle, 200 nm laser pulse with a peak intensity of 10^{14} W cm^{-2}. The upper panels show spectra obtained with effective-2e and haCC calculations with different number of ionic states included as indicated in the legend. The lower panels show relative errors of haCC calculations with respect to the effective-2e calculations.

thresholds that play a more important role in determining the ionization yields compared to the exact electronic structure. Our findings show that helium at long wavelengths can be approximated as a single channel system.

4.2. Beryllium

Beryllium is a four electron system that is often treated as a two electron system due to the strong binding of its inner two electrons. The third ionization potential of beryllium is 153.8961 eV [29]. With photon energies below this third ionization potential, it can be safely treated as an effective two electron system. This allows us to have a benchmark for our spectra by adapting the simple Coulomb potential to an effective potential in our two electron code. We use the effective potential given in [6] for our benchmark calculations. We refer to these as 'effective-2e' calculations.

Table 1 lists the energies of the first 8 ionic states of beryllium relative to the ground ionic state. As the ionic excitation energies are much smaller than in Helium one would expect inter-channel couplings to play a greater role.

Figure 4 shows photoelectron spectra from beryllium with 21 and 200 nm wavelength laser pulses. The exact parameters are indicated in the figure caption. The relative errors of spectra from the haCC calculations are computed with respect to the effective-2e calculations.

At 21 nm, the one and two photon ionization peaks of ground state channel spectra are shown. Here, the single photon ionization process itself needs more than the ground ionic state to produce accurate photoelectron spectra. Adding more ionic states improves the accuracy to a few percent level. We find that the close energetic spacing of beryllium ionic states leads to a greater possibility of inter-channel coupling, which requires more than the ground ionic state to be well represented.

Also, at 200 nm we need more than the ground ionic state to compute realistic spectra. With $1s^2 2s$, $1s^2 2p$ ionic states included, the spectra produced have 20% accuracy with respect to the benchmark calculation. With the addition of $1s^2 3s$ and $1s^2 3p$ states, a structure similar to the one predicted by the benchmark calculation develops around 10 eV. This structure may be identified with the lowest resonance $1s^2 2p3s$ at 10.71 eV [6]. The coupled channels calculations with the number of ionic states considered here, however do not reproduce the structure on the second peak exactly. This points to a feature of a coupled channels basis that the correct representation of a strongly correlated state that has bound character requires a large number of ionic states. As

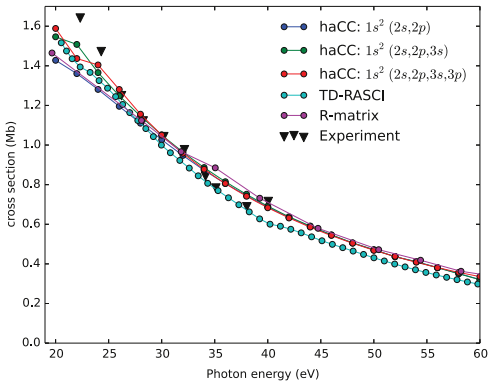

Figure 5. Single photoionization cross-sections for beryllium in the photon range of 20–60 eV. Presented are results from haCC calculations with 4, 5, 8 ionic states. The figure shows a comparison with earlier calculations using TD-RASCI method [11], *R*-matrix method [31] and with experimental results from [32].

an alternative strategy, one can explicitly include the correlated state of importance into the basis, if it can be pre-computed, on the same footing as the correlated ground state.

It has been shown through examples in section 4.1 that helium can be modeled as single channel system at longer wavelengths. Lithium, the smallest alkali metal, also has been successfully modeled as a single electron system in an effective potential, for example in [30]. We find that beryllium needs at least two ionic states, $1s^2 2s$ and $1s^2 2p$, for a realistic modeling. It serves as a first simple example where single electron models break down and multiple channels need to be considered.

In figure 5, we present the single photon ionization cross-sections as a function of photon energy from our haCC method and compare them with the cross-sections calculated with TD-RASCI method [11] and *R*-matrix method [31] and with experimental results from [32]. The cross-sections in our time dependent approach are computed using the equation (51) given in [18] with which the N photon ionization cross-section, $\sigma^{(N)}$ in units $\mathrm{cm}^{2N}/\mathrm{s}^{N-1}$ can be computed as:

$$\sigma^{(N)} = (8\pi\alpha)^N \left(\frac{3.5 \times 10^{16}}{I}\right)^N \omega^N \Gamma a_0^{2N} t_0^{N-1}, \tag{42}$$

where I is the intensity in W cm^{-2}, ω is the laser frequency in a.u., α is the fine structure constant and a_0, t_0 are atomic units of length and time respectively. Γ is the total ionization rate which is computed in a time dependent approach by monitoring the rate at which the norm of the wavefunction in a certain inner region drops. As we are computing the rate, the exact size of the inner region does not play a role. The norm drop reaches a steady state irrespective of the inner region size. We used for our computations presented here a 40-cycle continuous wave laser pulse with a three cycle $\cos^2$ ramp up and ramp down and with an intensity of 10^{12} W cm^{-2}. We checked convergence with respect to the pulse duration and the inner region size, and the computations are converged well below the differences seen by addition of ionic states in the basis.

All the theoretical methods agree with each other qualitatively, though there are differences on the level of 5–10% quantitatively. The experimental results from [32] have error bars on the level $\lesssim$10% (0.1 Mb) which are not shown here. All the theoretical results lie in this range except at low energies. In the higher photon energy range, 30–60 eV, the haCC results and the *R*-matrix results are in good agreement compared to the TD-RASCI. In the haCC calculations, including more than 4 ionic states does not change the cross-sections. In the photon energy range 20–30 eV, the haCC computations with 5 and 8 ionic states are in good agreement with TD-RASCI results compared to the *R*-matrix results. In this energy range, the cross-sections from haCC calculations show a dependence on the number of ionic states included. This modulation may be attributed to the presence of auto-ionizing states in this region. Table 3 in [6] presents a list of resonances that appear in beryllium electronic structure. The first ionization potential is 9.3 eV. With photon energies around 20 eV, the resulting photoelectron reaches continuum region where a number of resonances are present. As correlated resonances need many ionic states to be well represented in a coupled channels basis, this may explain the dependence of the cross-section on the number of ionic states in 20–30 eV photon range.

4.3. Hydrogen molecule

The hydrogen molecule in linearly polarized laser fields parallel to the molecular axis, with fixed nuclei has the same symmetry as helium in linearly polarized laser fields. The off-centered nuclear potential, however,

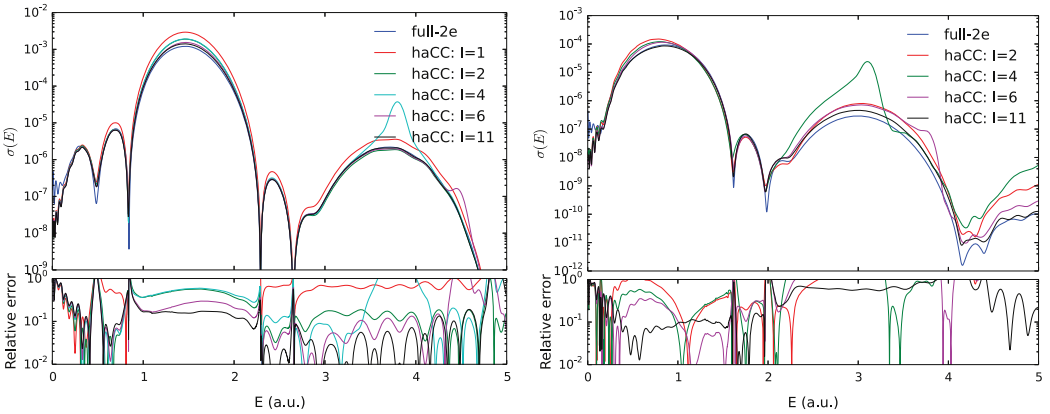

Figure 6. Photoelectron spectra from H_2 with a three-cycle 21 nm laser pulse with a peak intensity of 10^{15} W cm^{-2}. Left figure: ground state channel ($1\sigma_g$) Right figure: first excited state channel ($1\sigma_u$). The upper panels show spectra obtained with full-2e and haCC calculations with different number of ionic states (I) included (as indicated in the legend). The lower panels show relative errors of haCC calculations with respect to the full-2e calculation. With $I = 4, 6$, there are visible artefacts on the two photon peaks around 3 a.u. which are explained in the text.

increases the angular momenta requirement when treated with a single center expansion. While the number of basis functions can be reduced through a choice of a more natural coordinate system like prolate spheroidal coordinates for diatomics [33], the challenge of computing two electron integrals remains. In the case of hydrogen molecule at equilibrium internuclear distance ($R_0 = 1.4$ a.u.), a calculation with single center expansion easily converges, as the proton charges do not significantly distort the spherical symmetry of the electron cloud. As a benchmark for spectra, we use results from a full dimensional calculation, that expands the wavefunction in a single center basis.

Figure 6 shows photoelectron spectra from H_2 at 21 nm wavelength. The exact laser parameters are given in the figure caption. The ground state ($1\sigma_g$) and first excited state ($1\sigma_u$) channel spectra are shown. We find that, at this wavelength, a single ionic state is not sufficient to produce accurate photoelectron spectra. With the addition of more ionic states, there is a systematic improvement in the accuracy of the calculations. With 11 lowest σ and π ionic states included, we obtain an accuracy of about 10% for the $1\sigma_g$ channel. The single photon ionization to the shake-up channel $1\sigma_u$ is also computed to a few percent accuracy with 11 ionic states. We find that the single ionization continuum of H_2 is more complex than helium and it needs more than a single ionic state.

With 4 and 6 ionic states, we find artefacts on the two photon peaks. This is a result of a part of the COLUMBUS neutral ground state $|\mathcal{G}\rangle$ appearing in the eigenvalue spectrum of the Hamiltonian as a spurious doubly excited state $|s\rangle$. Let Π_C be the projector onto the subspace spanned by the coupled-channels basis $\mathcal{A}[|i\rangle|I\rangle$. Then parts of the correlation contained in $|\mathcal{G}\rangle$ cannot be presented in that basis such that a non-zero correlated state

$$|s\rangle = (1 - \Pi_C)|\mathcal{G}\rangle \neq 0 \tag{43}$$

appears at elevated energies. This spurious correlated state moves to higher energy with addition of ionic states. A straight forward solution to this problem is to compute this state and project it out from the basis. But this would require locating the spurious state in the eigenvalue spectrum, which is very demanding for large Hamiltonians. Fortunately, by their dependence on the number of ionic states, artefacts of this kind are easily detected and can be moved out of the region of interest by using sufficiently many ionic states. Such artefacts are a natural consequence of any ansatz of the kind (5) and need to be monitored.

Figure 7 shows total photoelectron spectra at 200 and 400 nm wavelengths. At 200 nm, spectra are accurate up to 10% with 2 ionic states. Addition of more ionic states helps reproduce additional resonant features in the spectrum. Also at 400 nm, 2 ionic states are sufficient to compute spectra that are accurate on 10% level, except for the resonant features. Inclusion of up to 6 ionic states reproduces the feature around 0.62 a.u. in the 400 nm spectrum, which may be attributed to second or third $^1\Sigma_u^+$ doubly excited state [34]. We find that with H_2 at longer wavelengths, ground ionic state is sufficient to compute realistic spectra and only for resonant features a large number ionic states is required.

Figure 8 shows total ionization yield as a function of photon energy in the range 0.17–0.5 a.u. Results from haCC are compared with data available from other theoretical methods—time-dependent CI method from [35] and FNA-TDSE (fixed nuclei approximation) method from [7]. In addition, several points from our tSURFF-

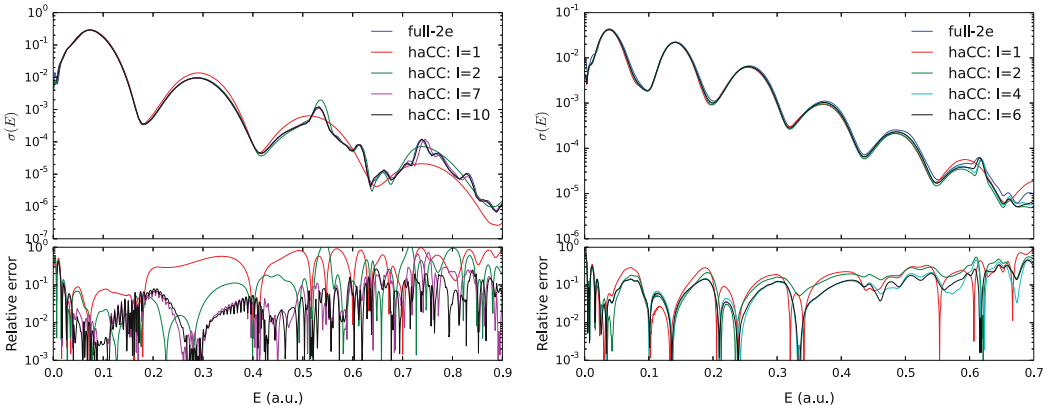

Figure 7. Total photoelectron spectra from H_2 with—left figure: three-cycle 200 nm laser pulse with a peak intensity of 10^{14} W cm^{-2}. Right figure: three-cycle 400 nm laser pulse with a peak intensity of 10^{14} W cm^{-2}. The upper panels show spectra obtained with full-2e and haCC calculations with different number of ionic states (I) included as indicated in the legend. The lower panels show relative errors of haCC calculations with respect to the full-2e calculation.

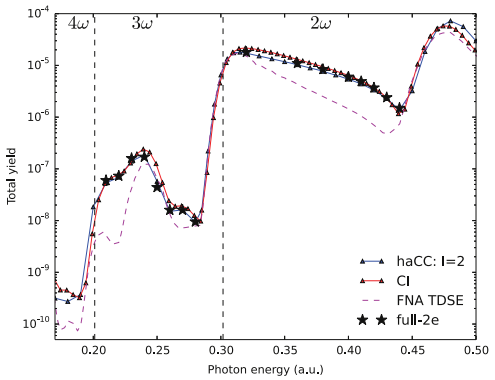

Figure 8. Ionization yield from H_2 at equilibrium internuclear distance ($R_0 = 1.4$ a.u.) as a function of photon energy. Laser parameters: 10^{12} W cm^{-2} peak intensity, cos^2 envelope pulses and 10 fs pulse duration (In equation (40) $2cT = 10$ fs). A comparison of haCC calculations with 2 ionic states with CI results from [35] and FNA-TDSE results from [7] and full-2e results. The dashed vertical lines separate different multi-photon ionization regimes.

based full-2e method are included. The haCC calculations shown were performed using two ionic states, convergence was verified by performing four-state calculations at selected points. The vertical lines in the figure separate different multi-photon ionization regimes. The haCC, CI and full-2e are in fair agreement, while FNA-TDSE reproduces the threshold behavior, but severely, by up to an order of magnitude, deviates from the other calculations. The most conspicuous discrepancies between haCC and CI appear in the range $0.3 \sim 0.4$ a.u. where CI exceeds haCC by about 20%. The discrepancies may be a result of the intrinsic limitations or the convergence of either calculation. For example, there are minor discrepancies in the ionization potential: the accurate value at H_2 equilibrium inter-nuclear distance ($R_0 = 1.4$ a.u.) is 0.6045 a.u.(table 1 in [36]),the ionization potential in [35] is 0.590 36 a.u., whereas in our calculations we obtain 0.6034 a.u. Also note that the results in [35] were shifted by 0.0092 a.u. in energy to match the resonance at 0.46 a.u. Although these differences are miniscule for energies they may indicate for somewhat larger deviations in the wave functions and the values of ionization potentials give a measure for the accuracy of the computations. Our full-2e computations that, in principle, could help to resolve the discrepancy are expensive and have not been pushed to an accuracy level which would allow to decide between the two results. However, we believe that the present level of agreement between haCC and CI is quite satisfactory and supports the validity of both approaches.

5. Conclusions

The hybrid anti-symmetrized coupled channels method introduced here opens the route to the reliable *ab initio* calculation of fully differential single photo-emission spectra from atoms and small molecules for a broad range of photon energies. It unites advanced techniques for the solution of the TDSE for one- and two-electron systems in strong fields with state of the art quantum chemistry methods for the accurate description of electronic structure and field-induced bound state dynamics. For the specific implementation we have relied on a finite element description of the strong field dynamics and Gaussian-based CI package of COLUMBUS.

Key ingredients for the successful implementation are good performance of tSURFF for the computation of spectra from comparatively small spatial domains on the one hand and access to the well established technology of quantum chemistry on the other hand. We could obtain the quantum chemical structure in the form of the complete expansion into determinants from COLUMBUS. In future implementations, it may be sufficient to output from a given package the generalized one, two, and three-electron density matrices together with generalized Dyson orbitals, both defined in the present paper. It turned out to be instrumental for accurate results that haCC allows for the inclusion of neutral states in a natural fashion and at very low computational cost.

Several new techniques were introduced and implemented for the establishment of the method. Most notably, the mixed gauge approach [22] turned out to be crucial for being able to take advantage of the field-free electronic structure in presence of a strong field without abandoning the superior numerical properties of a velocity-gauge like calculation. The finite element method used for single-electron strong-field dynamics is convenient, but certainly not the only possible choice. Similar results should be achievable with higher order B-spline methods or any other discretization suitable for solutions of the single electron strong field Schrödinger equation. Low-rank updates are used in several places for the efficient computation of the inverses of the large overlap matrix and to control the linear dependency problems arising from anti-symmetrizing the essentially complete finite elements basis against the Hartree–Fock orbitals.

We have made an effort to explore the potential range of applicability of the method by performing computations in a wide range of parameters on a few representative systems, where results can be checked against essentially complete methods. Spectra for the He atom were independently obtained from fully correlated two-electron calculations. We could demonstrate that haCC gives spectra on the accuracy level 10% with very low effort. An interesting observation is that in the long wavelength regime indeed a single ionization channel produces correct results, justifying *ex post* wide spread model approaches of the strong field community. As a note of caution, we recall that this is only possible as the *fully correlated initial state* is routinely included in the haCC scheme. At short wavelength, the ionic excited state dynamics plays a larger role and reliable results require inclusion of up to 9 ionic channels. With this we could correctly resolve also the peak due to He's doubly excited state.

The second atomic system, Be, was chosen to expose the role of electronic dynamics in the ionic states. While the 1s core electrons are energetically well-separated and no effect of their dynamics was discernable in a comparison with a frozen core model, the narrow spaced ionic states preclude single channel models. Depending on the observable and on desired accuracies, a minimum of two ionic channels had to be used.

For the comparison of H_2 photoionization and photoelectron spectra, we could refer to literature and supplemented the data with full two-electron calculations. At 400 nm, H_2 can be treated as a single channel system. At intermediate wavelengths, we find the need for at least two ionic channels, and we could obtain a fair agreement with comparison data. Here one has to take into consideration that all alternative methods operate near the limits of their applicability.

With this set of results we demonstrated the correctness of the method and its essential features. In our calculations, also the fundamental limitations of the approach were exposed. Clearly, the field-induced dynamics of the ionic part must be describable by a few states with bound character. haCC shares this limitation with any expansion that is limited to a few ionic states. Note that the problem is partly mitigated by the possibility to include fully correlated ground as well as singly- and doubly-excited states with bound-state character that are known to appear in the dynamics.

The method in its present implementation can be applied to many electron atoms [37] and small molecules such as N_2 and CO_2, which will be reported in a forthcoming publication.The ionic states in these molecules are closely spaced as in beryllium and hence they would also need several ionic states in the basis for convergence. We have no reliable heuristics to *a priori* estimate the number of states needed for a given accuracy. From the present experience, we expect that at long wavelengths, for example at 800 nm, inclusion of ionic states in the range of 5–6 eV below the first ionization threshold may be sufficient for convergence. This translates to about 5–6 ionic states in the basis for these systems which is a feasible problem.

At the moment, the computation of the two-electron integrals poses a mild technical limitation for such calculations, and an improvement of the presently rather straight-forward algorithm is needed for going to

larger systems.Treating molecular systems with lower symmetry leads to a further fill in of the Hamiltonian matrix due to the large number of allowed transitions. Such calculations appear quite feasible as well, however at comparatively higher resource consumption than the few hours on a eight-core machine needed for the majority of the results presented here. Another limitation arises when the molecule becomes too large for computing even strong field single-electron dynamics over its complete extension. At present, tSURFF allows us to limit computation boxes to the scale of ~ 40 a.u. Also, for the single electron part, we use at present single-center expansions, which perform notoriously poorly if scattering centers are distributed over more than a few atomic units. This limitation may well be overcome by a more versatile single-electron discretization, though at significant implementation effort.

Other potential extensions are to double-emission. The tSURFF method was formulated for this situation. Combining such already sizable calculations with a dication described by quantum chemistry in the same spirit as here may be feasible. The formula presented can be readily extended to include that case. However, the scaling is poor such that one may only hope for the simple one- or two-channel situation to be feasible in practice. A cut-down version of such an approach can be used to include non-bound dynamics by describing a second electron's dynamics in a more flexible basis, however, without admitting its emission.

These lines of development will be pursued in forthcoming work.

Acknowledgments

The authors thank the COLUMBUS developers—H Lischka, University of Vienna; T Müller, F Jülich; F Plasser, University of Heidelberg and J Pittner, J Heyrovský Institute for their support with constructing the quantum chemistry interface. Discussions with A Saenz and J Förster on H_2 were very helpful. VPM is a fellow of the EU Marie Curie ITN 'CORINF' and the International Max Planck Research School—Advanced Photon Science. A Z acknowledges support from the DFG through excellence cluster 'Munich Center for Advanced Photonics (MAP)' and from the Austrian Science Foundation project ViCoM (F41).

Appendix. Finite element basis

Let $\{r_0, r_1, \ldots, r_n\}$ be points that define n intervals on the radial axis. In a finite element approach, the basis functions $f_i^n(r)$ are chosen such that

$$f_i^n(r)\begin{cases}\neq 0 & \text{if } r \in [r_{n-1}, r_n],\\ = 0 & \text{otherwise.}\end{cases} \tag{A.1}$$

The individual basis functions can be chosen from any complete set, for example, in our case we use scaled Legendre polynomials of typical orders 10–14. Here, we write the finite element index and the function index separately to emphasize that we have two convergence parameters: the order and the number of finite elements. The calculations converge quickly with increasing order compared to with increasing number of elements [38]. The basis functions should also be tailored to satisfy the continuity conditions. This may be accomplished through a transformation on each interval such that the functions satisfy the following conditions:

$$\begin{aligned} f_0^n(r_{n-1}) &= 1; \quad f_0^n(r_n) = 0\\ f_1^n(r_{n-1}) &= 0; \quad f_1^n(r_n) = 1\\ f_{i\neq 0,1}^n(r_{n-1}) &= 0; \quad f_{i\neq 0,1}^n(r_n) = 0, \end{aligned} \tag{A.2}$$

Even though we are solving a second order differential equation, it is sufficient to impose just the continuity condition to solve the differential equation. It can be shown through a simple computation, for example as shown in [38], that the matrix elements corresponding to the Laplacian operator can be computed even if the functions are not two times differentiable at the finite element boundaries. This is because the δ-like terms arising due the second derivative are integrated over with continuous functions. The matrices corresponding to various operators in a finite element basis have a banded structure, that can be used to perform various linear algebra operations efficiently.

In a three-dimensional situation with spherical symmetry, these radial finite element functions can be multiplied by a complete set of angular basis functions such as the spherical harmonics to construct a three dimensional basis of the form $f_i^n(r)\,Y_{lm}(\theta, \phi)$.

References

[1] Meckel M *et al* 2008 Laser-induced electron tunneling and diffraction *Science* **320** 1478–82
[2] Kienberger R *et al* 2004 Atomic transient recorder *Nature* **427** 817–21

[3] Pabst S and Santra R 2013 Strong-field many-body physics and the giant enhancement in the high-harmonic spectrum of xenon *Phys. Rev. Lett.* **111** 233005
[4] Spanner M and Patchkovskii S 2009 One-electron ionization of multielectron systems in strong nonresonant laser fields *Phys. Rev.* A **80** 063411
[5] Jose J, Lucchese R R and Rescigno T N 2014 Interchannel coupling effects in the valence photoionization of SF_6 *J. Chem. Phys.* **140** 204305
[6] Djiokap J M N and Starace A F 2013 Resonant enhancement of the harmonic-generation spectrum of beryllium *Phys. Rev.* A **88** 053412
[7] Palacios A, Bachau H and Martín F 2006 Enhancement and control of H_2 dissociative ionization by femtosecond VUV laser pulses *Phys. Rev. Lett.* **96** 143001
[8] Timmers H, Li Z, Shivaram N, Santra R, Vendrell O and Sandhu A 2014 Coherent electron hole dynamics near a conical intersection *Phys. Rev. Lett.* **113** 113003
[9] Greenman L, Ho P J, Pabst S, Kamarchik E, Mazziotti D A and Santra R 2010 Implementation of the time-dependent configuration-interaction singles method for atomic strong-field processes *Phys. Rev.* A **82** 023406
[10] Caillat J, Zanghellini J, Kitzler M, Koch O, Kreuzer W and Scrinzi A 2005 Correlated multielectron systems in strong laser fields: a multiconfiguration time-dependent Hartree–Fock approach *Phys. Rev.* A **71** 012712
[11] Hochstuhl D and Bonitz M 2012 Time-dependent restricted-active-space configuration-interaction method for the photoionization of many-electron atoms *Phys. Rev.* A **86** 053424
[12] Miyagi H and Madsen L B 2013 Time-dependent restricted-active-space self-consistent-field theory for laser-driven many-electron dynamics *Phys. Rev.* A **87** 062511
[13] Sato T and Ishikawa K L 2013 Time-dependent complete-active-space self-consistent-field method for multielectron dynamics in intense laser fields *Phys. Rev.* A **88** 023402
[14] Miyagi H and Madsen L B 2014 Time-dependent restricted-active-space self-consistent-field theory for laser-driven many-electron dynamics: II. Extended formulation and numerical analysis *Phys. Rev.* A **89** 063416
[15] Bauch S, Sørensen L K and Madsen L B 2014 Time-dependent generalized-active-space configuration-interaction approach to photoionization dynamics of atoms and molecules *Phys. Rev.* A **90** 062508
[16] Haxton D J and McCurdy C W 2015 Two methods for restricted configuration spaces within the multiconfiguration time-dependent Hartree–Fock method *Phys. Rev.* A **91** 012509
[17] Sato T and Ishikawa K L 2015 Time-dependent multiconfiguration self-consistent-field method based on the occupation-restricted multiple-active-space model for multielectron dynamics in intense laser fields *Phys. Rev.* A **91** 023417
[18] Lysaght M A, van der Hart H W and Burke P G 2009 Time-dependent *r*-matrix theory for ultrafast atomic processes *Phys. Rev.* A **79** 053411
[19] Tao L and Scrinzi A 2012 Photo-electron momentum spectra from minimal volumes: the time-dependent surface flux method *New J. Phys.* **14** 013021
[20] Scrinzi A 2012 t-surff: fully differential two-electron photo-emission spectra *New J. Phys.* **14** 085008
[21] Lischka H, Müller T, Szalay P G, Shavitt I, Pitzer R M and Shepard R 2011 Columbus—a program system for advanced multireference theory calculations *WIREs Comput. Mol. Sci.* **1** 191–9
[22] Majety V P, Zielinski A and Scrinzi A 2014 Mixed gauge in strong laser-matter interaction *J. Phys. B: At. Mol. Opt. Phys.* **48** 025601
[23] Scrinzi A 2010 Infinite-range exterior complex scaling as a perfect absorber in time-dependent problems *Phys. Rev.* A **81** 053845
[24] Zielinski A, Majety V P and Scrinzi A 2015 A general solver for the time-dependent schorödinger equation of one and two particle systems, in preparation
[25] Woodbury M 1950 *Inverting Modified Matrices* (*Memorandum Rept., 42, Statistical Research Group*) (Princeton, NJ: Princeton University Press)
[26] Ivanov I A and Kheifets A S 2014 Strong-field ionization of he by elliptically polarized light in attoclock configuration *Phys. Rev.* A **89** 021402
[27] Kaprálová-Žánská P R, Šmydke J and Civiš S 2013 Excitation of helium Rydberg states and doubly excited resonances in strong extreme ultraviolet fields: full-dimensional quantum dynamics using exponentially tempered gaussian basis sets *J. Chem. Phys.* **139** 104314
[28] Scrinzi A and Piraux B 1998 Two-electron atoms in short intense laser pulses *Phys. Rev.* A **58** 1310–21
[29] Drake G W 1988 Theoretical energies for the $n = 1$ and 2 states of the helium isoelectronic sequence up to $z = 100$ *Can. J. Phys.* **66** 586–611
[30] Morishita T and Lin C D 2013 Photoelectron spectra and high Rydberg states of lithium generated by intense lasers in the over-the-barrier ionization regime *Phys. Rev.* A **87** 063405
[31] Berrington K, Quigley L and Zhang H L 1997 The calculation of high-energy photoionization cross sections for the Be isoelectronic sequence *J. Phys. B: At. Mol. Opt. Phys.* **30** 5409
[32] Wehlitz R, Lukić D and Bluett J B 2005 Single and double photoionization of beryllium below 40 eV *Phys. Rev.* A **71** 012707
[33] Vanne Y V and Saenz A 2004 Numerical treatment of diatomic two-electron molecules using a b -spline based ci method *J. Phys. B: At. Mol. Opt. Phys.* **37** 4101
[34] Sánchez I and Martín F 1997 The doubly excited states of the H_2 molecule *J. Chem. Phys.* **106** 7720–30
[35] Förster J, Vanne Y V and Saenz A 2014 Ionization behavior of molecular hydrogen in intense laser fields: Influence of molecular vibration and alignment *Phys. Rev.* A **90** 053424
[36] Lühr A, Vanne Y V and Saenz A 2008 Parameter-free one-center model potential for an effective one-electron description of molecular hydrogen *Phys. Rev.* A **78** 042510
[37] Majety V P and Scrinzi A 2015 Photo-ionization of noble gases: a demonstration of hybrid coupled channels approach *Photonics* **2** 93–103
[38] Scrinzi A and Elander N 1993 A finite element implementation of exterior complex scaling for the accurate determination of resonance energies *J. Chem. Phys.* **98** 3866–75

IOP Publishing Journal of Physics B: Atomic, Molecular and Optical Physics
J. Phys. B: At. Mol. Opt. Phys. **48** (2015) 025601 (9pp) doi:10.1088/0953-4075/48/2/025601

Mixed gauge in strong laser-matter interaction

Vinay Pramod Majety, Alejandro Zielinski and Armin Scrinzi

Physics Department, Ludwig Maximilians Universität, D-80333 Munich, Germany

E-mail: armin.scrinzi@lmu.de

Received 28 August 2014, revised 14 October 2014
Accepted for publication 10 November 2014
Published 24 December 2014

Abstract

We show that the description of laser–matter interaction in length gauge at short distances and in velocity gauge at longer distances allows for compact physical modeling in terms of field free states, rapidly convergent numerical approximation, and efficient absorption of outgoing flux. The mathematical and numerical framework for using mixed gauge in practice is introduced. We calculate photoelectron spectra generated by a laser field at wavelengths of 400 $\sim$ 800 nm from single-electron systems and from the helium atom and hydrogen molecule. We assess the accuracy of coupled channels calculations by comparison to full two-electron solutions of the time-dependent Schrödinger equation and find substantial advantages of mixed over velocity and length gauges.

Keywords: laser-matter interaction, gauge, TDSE

(Some figures may appear in colour only in the online journal)

1. Introduction

The choice of gauge in the interaction of strong, long wavelength fields with atoms and molecules affects the physical modeling [1], perturbative expansions as the *S*-matrix series [2, 3], as well as the efficiency of numerical solutions [4]. For systems where field quantization can be neglected and the field appears only as a time- and space-dependent external parameter, the wavefunctions in all gauges are unitarily related by time- and space-dependent multiplicative phases. An extensive discussion of gauge transformations in the context of strong field phenomena can be found in [5]. When approximations are made, the unitary equivalence of the wavefunctions and the corresponding time-dependent Schrödinger equation (TDSE) can easily be lost. An important example is the strong field approximation (SFA), where the system is assumed to either remain in the field-free initial state or move exclusively under the influence of the laser field: the function representing the field-free initial state depends on gauge. A similar situation arises, when a series expansion is truncated to a finite number of terms, as in an *S*-matrix expansion: the physical meaning of any finite number of terms is different in different gauges. Also the discretization errors in a numerical calculation are gauge dependent. In particular, multiplication by a space-dependent phase changes the smoothness of the solution. As a result, numerical accuracy and convergence depend on gauge.

Mathematical and numerical aspects of using general gauges were addressed in [6–8] in the context of Floquet theory and the time dependent Schrödinger equation, where various options for mixing different gauges were discussed. In [6, 7], mixing length and velocity gauge in the R-matrix Floquet method was achieved by calculating the R-matrix in length gauge and then transforming it to the velocity gauge to connect to the numerical velocity gauge calculation in the outer region. In [8], it was pointed out that alternatively the transition between regions can be taken to be differentiably smooth, which also allows application to the TDSE.

Here we will show that physical modeling on the one hand and efficient numerical solution on the other hand impose conflicting requirements on the choice between the standard length and velocity gauges. We introduce the mathematical and numerical techniques for resolving this conflict by using general gauges. We restrict our discussion to gauge transformations in the strict sense, i.e. local phase multiplications, which does not include the acceleration 'gauge', as it involves a time-dependent coordinate transformation. Numerical performance of the various gauges is compared on a one-dimensional (1D) model system. We show that, also with discontinuous transition between gauges,

 © 2015 IOP Publishing Ltd Printed in the UK

there is no need for the explicit inclusion of operators containing δ-function-like singularities. We demonstrate validity and accuracy of calculations that mix length and velocity gauges in three dimensions by comparing to accurate velocity gauge results for the hydrogen atom at 800 nm wavelength. Finally, we combine local length gauge with asymptotic velocity gauge to compute photoelectron spectra of He and H_2 at a laser wavelength of 400 nm. Efficiency and accuracy of the approach are shown by comparing to complete numerical solutions of the two-electron (2e) problem. We find that mixed gauge allows low-dimensional approximations, while in velocity gauge we achieve convergence only when we allow essentially complete 2e dynamics. We will conclude that few-body dynamics in the realm of bound states is more efficiently represented in length gauge, while the long-range representation of the solution prefers the velocity gauge.

2. Length, velocity, and general gauges

In the interaction of small systems of sizes $\lesssim$0.1 nm with light at wavelengths down to the extreme ultraviolet $\lambda \gtrsim 10$ nm one employs the dipole approximation, i.e. one neglects the variation of the field across the extension of the system $\vec{\mathcal{E}}(\vec{r}, t) \approx \vec{\mathcal{E}}(t)$. In length gauge, the interaction of a charge q with the dipole field is

$$I_L(t) = q\vec{\mathcal{E}}(t) \cdot \vec{r}, \tag{1}$$

while in velocity gauge it is

$$I_V(t) = -\vec{A}(t) \cdot \vec{p} + \frac{1}{2}\left|\vec{A}(t)\right|^2,$$
$$\vec{A}(t) := \int_{-\infty}^{t} q\vec{\mathcal{E}}(\tau)\mathrm{d}\tau. \tag{2}$$

Here and below we use atomic units with $\hbar = 1$, electron mass $m_e = 1$, and electron charge $e = -1$, unless indicated otherwise. In these two gauges the dependence of the dipole interaction operators on $\vec{r}$ is particularly simple and wavefunctions are unitarily related by

$$\Psi_V(\vec{r}, t) = \mathrm{e}^{\mathrm{i}\vec{A}(t)\cdot\vec{r}}\Psi_L(\vec{r}, t). \tag{3}$$

The transformation from length to velocity gauge is a special case of the general gauge transformation, namely multiplication by a space- and time-dependent phase

$$\Psi_g = U_g\Psi, \quad U_g := \mathrm{e}^{\mathrm{i}g(\vec{r},t)}. \tag{4}$$

As U_g is unitary, it leaves the system's dynamics unaffected, if operators and the time-derivative are transformed as

$$O \to O_g = U_g O U_g^*,$$
$$\frac{\mathrm{d}}{\mathrm{d}t} \to \frac{\mathrm{d}}{\mathrm{d}t} + U_g\dot{U}_g^* = \frac{\mathrm{d}}{\mathrm{d}t} - \mathrm{i}\dot{g}. \tag{5}$$

The above relations are valid for general $g(\vec{r}, t)$ that are differentiable w.r.t. t. If g is twice differentiable in space, the gauge transforms of momentum operator and Laplacian are

$$\vec{p} = -\mathrm{i}\vec{\nabla} \to \vec{p}_g = -\mathrm{i}\vec{\nabla} - \vec{B},$$
$$\Delta \to \Delta_g = \left[-\mathrm{i}\vec{\nabla} - \vec{B}\right]^2, \quad \vec{B} := \vec{\nabla}g. \tag{6}$$

We see, in particular, that a gauge transform introduces a time- and space-dependent momentum boost $\vec{B}(\vec{r}, t)$.

A standard TDSE transforms as

$$\mathrm{i}\tfrac{\mathrm{d}}{\mathrm{d}t}\Psi = \left[\frac{\vec{p}^2}{2} + V + q\vec{\mathcal{E}}(t) \cdot \vec{r}\right]\Psi$$
$$\to \mathrm{i}\tfrac{\mathrm{d}}{\mathrm{d}t}\Psi_g = \left[\frac{\left(\vec{p} - \vec{B}\right) \cdot \left(\vec{p} - \vec{B}\right)}{2} + V + q\vec{\mathcal{E}}(t) \cdot \vec{r} - \dot{g}\right]\Psi_g. \tag{7}$$

By explicitly writing the dot-product in the kinetic energy we emphasize that $\vec{p}$ does not commute with space-dependent $\vec{B}(\vec{r}, t)$ and space derivatives of $\vec{B}$ appear in the Hamiltonian. The velocity gauge interaction, equation (2), requires spatially uniform $\vec{B}(\vec{r}, t) \equiv \vec{A}(t)$. More generally, any time-dependence of the potential energy $V(\vec{r}, t)$ can be transformed into a time- and space-dependent momentum by defining

$$g_V(\vec{r}, t) = \int^t V(\vec{r}, t')\mathrm{d}t'. \tag{8}$$

The local phase multiplication need not be continuously differentiable or even continuous in space. One only must make sure that the gauge transformed differential operators $\vec{\nabla}_g$ are defined on functions χ from a suitable domain $\mathcal{D}(\vec{\nabla}_g)$. With discontinuous g, formally, δ-function-like singularities appear in equation (7). $\mathcal{D}(\vec{\nabla}_g)$ must be adjusted to compensate for those terms. The very simple, mathematically correct solution is to choose $\mathcal{D}(\vec{\nabla}_g) = U_g\mathcal{D}(\vec{\nabla})$, i.e. functions of the form

$$\chi(\vec{r}, t) = U_g(\vec{r}, t)\varphi(\vec{r}), \tag{9}$$

where the $\varphi \in \mathcal{D}(\vec{\nabla})$ are differentiable.

2.1. Gauge in the SFA

When we describe a physical process in terms of a few quantum mechanical states it is implied that the system does not essentially evolve beyond those states. The SFA is a simple model of this kind, which plays a prominent role in strong field physics. One assumes that an electron either resides in its initial state or, after ionization, moves as a free particle in a field whose effect largely exceeds the atomic binding forces.

The SFA must be reformulated appropriately depending on the gauge one chooses. Let $\Phi_0(\vec{r})$ be the initial state in absence of the field. The physical picture above implies that the velocity distribution of the initial state remains essentially unchanged also in presence of the field. However, using the same function Φ_0 for all gauges, effectively leads to a set of different models with different, time-dependent velocity

distributions for different gauges. In length gauge the operator $-\frac{\mathrm{i}}{m_e}\vec{\nabla}$ has the meaning of velocity of the electron and the velocity distribution is independent of the field:

$$n_L(\vec{p}, t) \equiv n_0(\vec{p}) = \left|\tilde{\Phi}_0(\vec{p})\right|^2. \tag{10}$$

In contrast, in velocity gauge, the velocity distribution varies with time as

$$n_V(\vec{p}, t) = \frac{1}{m_e}\left|\tilde{\Phi}_0\left[\vec{p} + \vec{A}(t)\right]\right|^2. \tag{11}$$

The difference becomes noticeable when the variation of $\vec{A}(t)$ is not negligible compared to the width of the momentum distribution. This is typically the case in strong field phenomena. Findings that SFA in length gauge better approximates the exact solution in cases where the picture remains suitable at all [9, 10] are consistent with this reasoning.

2.2. Single active electron (SAE) approximation

The gauge-dependent meaning of eigenstates has important consequences for the numerical approximation of few-electron systems. The functions corresponding to few-electron bound states have their intended physical meaning only in length gauge. In velocity gauge, the same functions correspond to time-varying velocity distributions. The problem affects the SAE approximation, where one lets one 'active' electron freely react to the laser field, but freezes all other electrons in their field-free states. Below we will demonstrate that this ansatz generates artefacts in velocity gauge.

As the simplest possible example, we demonstrate that even two non-interacting electrons show gauge-dependent artefacts if modeled in a restricted basis. Let us consider the 2e Hamiltonian $H(x, y) = h(x) + h(y)$. The ansatz for the solution $\Phi(x, y, t) = \varphi(x, t)\chi(y, t) - \chi(x, t)\varphi(y, t)$ is exact, if the functions φ and χ are unrestricted. Matrix elements of the Hamiltonian are

$$\begin{aligned}\langle\Phi\,|H|\,\Phi\rangle = {} & \langle\varphi\,|h|\,\varphi\rangle\langle\chi|\chi\rangle + \langle\varphi|\varphi\rangle\langle\chi|h|\chi\rangle \\ & -\langle\varphi\,|h|\,\chi\rangle\langle\chi|\varphi\rangle - \langle\varphi|\chi\rangle\langle\chi|h|\varphi\rangle.\end{aligned} \tag{12}$$

In an exact calculation, the exchange terms in the second line vanish, if $\langle\varphi|\chi\rangle = 0$ initially, as the unitary time evolution maintains orthogonality. However, if we restrict the time evolution of one of the functions, say φ, orthogonality is violated and unphysical exchange terms appear in the Hamiltonian matrix as the system evolves. Their size depends on the extent to which orthogonality is lost. If e.g. φ remains very close to its field-free state (e.g. if it is closely bound), then in length gauge the time evolution is well approximated as $\varphi(t) \approx \varphi(0)$. However, depending on the size of $\vec{A}(t)$, in velocity gauge this does not hold and the exchange terms become sizable.

If one attempts to suppress the artefacts due to lack of orthogonality by enforcing orthogonality of $|\chi\rangle$ to the static $|\varphi\rangle$, corresponding errors appear directly in $|\chi\rangle$, rather than being mediated by the artefacts in the matrix elements.

With interacting electrons, the direct term (Hartree potential) of electron–electron interactions is unaffected, as it only depends on the gauge-invariant electron density. In the exchange terms, however, the frozen orbitals with their length gauge meaning are inconsistently combined with the velocity gauge functions of the active electron.

The same gauge dependence appears also when the non-active electrons are not frozen in their initial states, but restricted in their freedom to evolve. We will demonstrate the superiority of length gauge for He and H_2 with limited freedom for the non-active electron in section 3.3.

2.3. Gauge in numerical solutions

While length gauge lends itself to intuitive interpretation and modeling, velocity gauge performs better in numerical calculations [4]. Fewer discretization coefficients can be used and the stiffness of the equations is reduced. This is due to the dynamics of free electrons in the field. From equation (7) one sees that for a free electron ($V_0 = 0$) the velocity gauge canonical momentum $\vec{p} = -\mathrm{i}\vec{\nabla}$ is conserved. In contrast, in length gauge, momenta are boosted by $\vec{A}(t)$, reflecting the actual acceleration of the electron in the field. As large momenta correspond to short range modulations of the solution, length gauge requires finer spatial resolution than velocity gauge. This modulation affects numerical efficiency, when the variation of $\vec{A}(t)$ is comparable or exceeds the momenta occurring in the field-free system. We will illustrate this below with one- and three-dimensional examples.

A second important reason for velocity gauge in numerical simulations is the use of infinite range exterior complex scaling (irECS) [11] for absorption at the box boundaries. This method is highly efficient and free of artefacts, but it cannot be applied for systems with length gauge asymptotics, as clearly observed in simulations [12]. An intuitive explanation of this fact can be found in [13] and the wider mathematical background is laid out in [14].

2.4. Mixed gauge

The conflicting requirements on gauge can be resolved by observing that bound states are, by definition, confined to moderate distances, whereas the effect of phase modulation is important for free electrons, usually far from the bound states. Using length gauge within the reach of bound states and velocity gauge otherwise largely unites the advantages of both gauges: locally, the system can be modeled intuitively, while at the same time maintaining efficient numerical spatial discretization and asymptotics suitable for absorption by irECS.

3. Implementations and examples

3.1. TDSE in 1D

We use a basic model for discussing the various options for implementing mixed gauges. We solve the TDSE with the

length gauge Hamiltonian

$$H_L(t) = -\frac{1}{2}\partial_x^2 - \frac{1}{\sqrt{x^2+2}} - x\mathcal{E}(t). \tag{13}$$

In absence of the field, the ground state energy is exactly −0.5.

Spatial discretization is by a high order finite element basis, which is described in detail in [12]. Apart from being numerically robust, the basis is flexible, which allows, in particular, easy implementation of the discontinuity equation (9).

In general, basis functions $|j\rangle$ used for spatially discretizing the TDSE do not need to be twice differentiable. Rather, it is sufficient that they are differentiable once, and, implied by this, go to zero at the end of the computational domain. However, they can have discontinuous first derivatives. On such functions, the second derivative produces δ-function like singularities at the points where the derivative is discontinuous. However, integrals over the singularities are well defined. A brief calculation shows that the symmetric matrix elements obtained by formal partial integration

$$\left\langle k \left| -\partial_x^2 \right| j \right\rangle := \left\langle \partial_x k \middle| \partial_x j \right\rangle \tag{14}$$

exactly take these δ-singularities into account (see, e.g., [15]). This relaxed condition on the differentiability is explicitly used with finite element bases, where usually first derivatives are discontinuous at the boundaries between elements. A detailed description of how the $|j\rangle$ are constructed is given in the technical appendix of [12].

The ansatz

$$|\Psi(t)\rangle \approx \sum_{j=1}^{N} |j\rangle c_j(t) \tag{15}$$

leads to the system of ordinary differential equations for the expansion coefficients $\vec{c}$, $(\vec{c})_j = c_j$

$$\mathrm{i}\frac{\mathrm{d}}{\mathrm{d}t}\hat{S}\vec{c}(t) = \hat{H}(t)\vec{c}(t) \tag{16}$$

with the matrices

$$\widehat{H}_{kj}(t) = \langle k | H(t) | j \rangle, \quad \widehat{S}_{kj} = \langle k | j \rangle. \tag{17}$$

For time-integration, we use the classical 4th order explicit Runge–Kutta solver. As an explicit method it is easy to apply, but it is also susceptible to the stiffness of the system of equations (16). This is a realistic setting, as in many practical implementations explicit time-integrators are used. For the present purpose, it clearly exposes the numerical properties of the different gauges. In the 1D case we use a simulation box large enough such that reflections at the boundary remain well below the desired error level.

3.1.1. Three forms of mixed gauge (1D). Matrix elements of the kinetic energy are always computed in the explicitly hermitian form

$$\left\langle k \left| \left[-\mathrm{i}\partial_x - B\right]^2 \right| j \right\rangle \left\langle \partial_x k \middle| \partial_x j \right\rangle - \mathrm{i}\left\langle \partial_x k \middle| Bj \right\rangle + \mathrm{i}\left\langle Bk \middle| \partial_x j \right\rangle + \left\langle k \left| B^2 \right| j \right\rangle, \tag{18}$$

which also avoids the calculation of spatial derivatives of $B(x, t)$. Also, for non-differentiable B, no δ-function-like singularities appear.

Differentiable functions $B(x, t)$ are associated with a smooth gauge transform U_S. The smoothly gauge-transformed Laplacian is defined on the same functions as the standard Laplacian $\mathcal{D}(\Delta_S) = \mathcal{D}(\Delta)$ and no adjustments need to be made for the basis functions. To avoid loss of numerical approximation order, one must make sure that $B(x, t)$ is smooth to the same derivative order as the numerical approximation.

With an abrupt change of gauge

$$U_A = \begin{cases} 1 & \text{for } |x| < R_g \\ \mathrm{e}^{\mathrm{i}A(t)x} & \text{for } |x| > R_g \end{cases} \tag{19}$$

the Hamiltonian is

$$H_A(t) = \begin{cases} H_L(t) & \text{for } |x| < R_g \\ H_V(t) & \text{for } |x| > R_g, \end{cases} \tag{20}$$

where we denote the standard velocity gauge Hamiltonian as $H_V(t)$. There appear time-dependent discontinuities at the 'gauge radius' R_g

$$\Psi_A\left(\pm R_g + \epsilon\right) = \mathrm{e}^{\mathrm{i}A(t)R_g}\Psi_A\left(\pm R_g - \epsilon\right). \tag{21}$$

One can avoid discontinuities at R_g by defining a continuous gauge transform

$$U_C = \begin{cases} 1 & \text{for } |x| < R_g \\ \mathrm{e}^{\mathrm{i}A(t)\left(x \mp R_g\right)} & \text{for } x \gtrless \pm R_g \end{cases} \tag{22}$$

with the Hamiltonian

$$H_C(t) = \begin{cases} H_L(t) & \text{for } |x| < R_g, \\ H_V(t) \pm q\mathcal{E}(t)R_g & \text{for } x \gtrless \pm R_g. \end{cases} \tag{23}$$

Note that U_C is continuous, but not differentiable at R_g, which leads to discontinuous first derivatives in the solution.

3.1.2. Smooth versus non-differentiable switching. While mathematically all gauges are completely equivalent, the various gauges have each their own specific numerics. If smooth switching is chosen, clearly, the particular form of the transition and the corresponding modulations of the wavefunction do not bear any physical meaning. Still, the transition from one region to the other must be accurately modeled to correctly connect the length to the velocity gauge part of the solution. In the transition region one needs to densely sample the solution, which increases the number of expansion coefficients. In many cases, this will also increase the stiffness of the time propagation equations and further raise the penalty for a smooth transition.

In contrast, when g or any of its derivatives is discontinuous, the discretization in the vicinity of the discontinuity must be adjusted appropriately. Because of the lack of differentiability, any higher order finite difference scheme or approximations by analytic basis functions will fail to improve the approximation or may even lead to artefacts. The general solution for this problem is to explicitly build the known non-analytic behavior of the solution into the discretization. With the finite element basis set used here, this is particularly simple, as well-defined discontinuities can be imposed easily.

3.1.3. Continuous versus abrupt switching. The U_A and U_C formulations are nearly equivalent in their numerical behavior, as

$$U_C = U_0 U_A,$$
$$U_0 = \begin{cases} 1 & \text{for } |x| < R_g, \\ e^{\mp iA(t)R_g} & \text{for } x \gtrless \pm R_g. \end{cases} \quad (24)$$

The respective solutions differ only by the phases $e^{\mp iA(t)R_g}$:

$$\Psi_C = U_0 \Psi_A. \quad (25)$$

Depending on R_0, the time-dependence of this phase is slow compared to phase-oscillations caused by high energy content of the solution and does not change stiffness for numerical integration.

However, equation (21) shows that abrupt switching implies a time-dependent discontinuity of the solution Ψ_A. Again, this must be accurately numerically represented. One way of implementing this is to use, in the region containing R_g, basis functions with a time-dependent discontinuity. Technically, this is feasible in a finite element basis, but it invariably leads to time-dependent overlap matrices $\widehat{S}(t)$, see equation (16). With continuous switching, the solution remains continuous and a standard finite element basis can be used. The fact that the derivatives will be discontinuous is admitted in a finite element basis, where there are no constraints on the derivative across element boundaries. One only needs to make sure that R_g falls onto an element boundary. The same applies to B-splines, if one of the collocation points is made to coincide with R_g. For general analytic basis sets, also with continuous switching the time-dependence needs to be built into the basis. We have not investigated, whether this can be achieved in a computationally efficient way.

3.1.4. Numerical comparison of the gauges. We compare electron densities $n(x)$ at the end of the laser pulse. The size of the spatial discretization and the number of time-steps are adjusted to reach the same local error $\epsilon(x)$ in all gauges relative to a fully converged density $n_0(x)$. For suppressing spurious spikes at near-zeros of the density, we include some averaging into the definition of the error:

$$\epsilon(x) = 2\Delta x \left| n_0(x) - n(x) \right| \Big/ \int_{-\Delta x}^{\Delta x} \mathrm{d}x' n_0(x') \quad (26)$$

with $\Delta x = 1$.

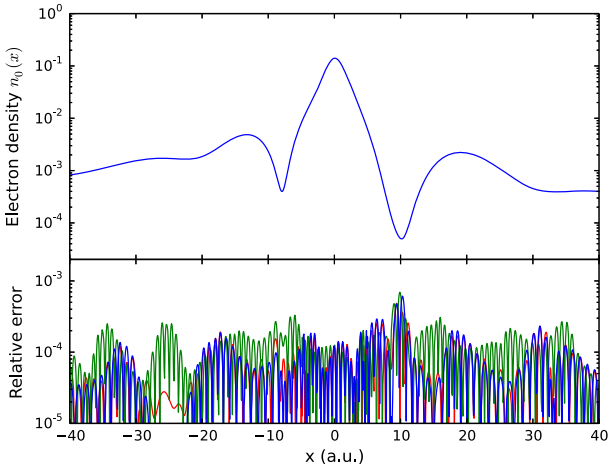

Figure 1. Electron density of the one-dimensional model system at the end of a single-cycle pulse (see text for exact pulse definition). Upper panel: fully converged velocity gauge calculation with simulation box size [−1000, 1000], finite element order 20, $N \approx 5500$ discretization coefficients, $T = 12 \times 10^4$ time steps. Lower panel: relative errors, equation (27), in various gauges. Velocity gauge, $N \approx 3000$, $T = 7.1 \times 10^4$ (red line), length gauge, $N \approx 4000$,$T = 8.8 \times 10^4$ (green), mixed gauge, $R_g = 5$, $N \approx 3000$, $T = 7.1 \times 10^4$ (blue). Errors of velocity and mixed gauge nearly coincide.

We use a single cycle 800 nm pulse with $\cos^2$-shape and peak intensity 2×10^{14} W cm^{-2}, which leads to about 25% ionization of this 1D system. The x-axis is confined to [−1000, 1000] with Dirichlet boundary conditions, discretized by finite elements of polynomial order 20. Figure 1 shows results in the different gauges. Velocity gauge requires $N \approx 3000$ linear coefficients (150 elements) and about $T \approx 71\,000$ time steps for accuracy $\epsilon(x) \lesssim 10^{-4}$. Length gauge has the largest discretization with $N \approx 4000$ and $T \approx 88\,000$, amounting to an overall increase in computation time of almost a factor 2. The larger number of time-steps arises because the explicit propagation scheme is sensitive to the stiffness of the equations, which can grow $\propto N^2$. The actual increase of time steps does not exactly reflect this behavior, as a finer discretization is used in the inner region to obtain comparably accurate initial states in all calculations. Stiffness from this part of the discretization is always present in the calculations. For the mixed gauge, we use continuous switching, equation (23), with $R_g = 5$. With this small length gauge section, the same discretization as in the velocity gauge can be used with $N \approx 3000$ and $T \approx 71\,000$.

We also investigated the effect of a smooth transition between the gauges over an interval of size S, using

$$g(x,t)=\begin{cases}0 & \text{for } |x| < R_g\\ xs(x)A(t) & \text{for } |x| \in \left[R_g, R_g+S\right]\\ xA(t) & \text{for } |x| > R_g+S,\end{cases} \quad (27)$$

where $s(x)$ is a 3rd order polynomial smoothly connecting the length with the velocity gauge region.

For a smoothing interval $S = 5$, we need a rather dense discretization by 18th order polynomials on the small interval to maintain the spatial discretization error of $\approx 10^{-4}$. While this leads only to a minor increase in the total number of discretization coefficients, it significantly increases the stiffness of the equations requiring $T = 1.4 \times 10^5$ time steps. With smoothing $S = 10$, stiffness is reduced and $T \approx 10^5$, which still exceeds by 50% the number of time steps with continuous, but non-differentiable transition.

The dependence on S is not surprising: the correction terms to the kinetic energy involve derivatives of $s(x)$, which grow inversely proportional to the size of the transition region, leading to large matrix elements. Thinking in terms of the solution, we need to follow a rather strong change in temporal and spatial behavior of the solution, which necessitates the dense grid. With the sudden transition, this change is reduced to a single discontinuity, whose behavior we know analytically. It can either be built explictly into the solution, when using the discontinuous Hamiltonian $H_A(t)$, equation (20), or be left to be adjusted numerically with the continuous Hamiltonian $H_C(t)$, equation (23). We conclude that, wherever technically possible, a sudden transition is to be preferred.

3.2. Mixed gauge for the hydrogen atom

The length gauge Hamiltonian for the hydrogen atom in a laser field is

$$H_L(t) = -\frac{1}{2}\Delta - \frac{1}{r} - \vec{\mathcal{E}}(t)\cdot\vec{r}. \quad (28)$$

The velocity gauge Hamiltonian is

$$H_V(t) = \frac{1}{2}\left[-\mathrm{i}\vec{\nabla} - \vec{A}(t)\right]^2 - \frac{1}{r}. \quad (29)$$

Equation (29) results when applying the gauge transform with $g(\vec{r},t) = \vec{A}(t)\cdot\vec{r}$, as indicated in equation (3). Often, in practice the $\vec{A}(t)^2$ term in this expression is omitted. This amounts to yet another, in this case space-independent gauge transformation with $g(\vec{r},t) = \int^t \mathrm{d}\tau \vec{A}(\tau)^2$. Both differ only by a global, time-dependent phase. Physically, this amounts to a time-dependent energy offset. As a global phase, it has hardly any influence on the numerical behavior of the solution.

In three dimensions, problem size grows rapidly and truncation of the simulation volume is advisable. As the error free absorbing boundary method irECS [12] is incompatible with length gauge calculations, in this section we only compare velocity to mixed gauge calculations. Following the findings of the 1D calculations, we use continuous gauge switching for its numerical efficiency and moderate programming effort. In three dimensions, it can be defined as

$$U_C = \begin{cases}1 & \text{for } r < R_g,\\ \exp\left[\mathrm{i}\vec{A}(t)\cdot\hat{r}\left(r-R_g\right)\right] & \text{for } r > R_g,\end{cases} \quad (30)$$

denoting $\hat{r} := \vec{r}/r$. The corresponding Hamiltonian is

$$H_C(t) = \begin{cases}H_L(t) & \text{for } r < R_g,\\ \left[-\mathrm{i}\vec{\nabla} - \vec{B}(\vec{r},t)\right]^2 - \frac{1}{r} - \vec{\mathcal{E}}(t)\cdot\hat{r}R_g & \text{for } r > R_g.\end{cases} \quad (31)$$

The gradient of the angle-dependent phase introduces an extra quadrupole type coupling:

$$\vec{B}(\vec{r},t) = \vec{\nabla}\left[\vec{A}(t)\cdot\hat{r}\left(r-R_g\right)\right] = \vec{A}(t)\left[1-\frac{R_g}{r}\right] + \frac{1}{2}\left[\vec{A}(t)\cdot\hat{r}\right]\frac{\hat{r}R_g}{r}. \quad (32)$$

$H_C(t)$ asymptotically coincides with standard velocity gauge as $|\vec{r}|$ tends to ∞. In an expansion into spherical harmonics, the quadrupole terms introduce additional non-zeros into the Hamiltonian matrix, which increase the operations count for applying the Hamiltonian by ~60%.

3.2.1. Comparisons. For the numerical solution we use polar coordinates with a finite element basis on the radial coordinate and spherical harmonics for the angular dependence. Specifics about this three-dimensional basis can be found in [11]. We want to emphasize that this basis is strictly numerical and does not make any reference to bound or continuum states. Rydberg states, which may become populated in the processes, may require large box sizes but are otherwise properly represented in either gauge.

We assume linear polarization and fix the magnetic quantum number at $m \equiv 0$. We use a $\cos^2$-shaped pulse with three optical cycles FWHM at central wavelength $\lambda = 800$ nm and peak intensity 2×10^{14} W cm^{-2}, which leads to about 16% ionization.

We compare the errors of the different gauges in the angle-integrated electron density $n(r)$ at the end of the pulse and in the photoelectron spectra. The spectra are computed by the tSURFF method described in [11, 16]. Errors are again defined relative to a fully converged velocity gauge calculation.

On the radial coordinate we use five finite elements of order 16 up to radius $R_0 = 25$ in all gauges. Beyond that, the solution is absorbed by irECS. The stronger phase oscillations of the length gauge solution require more angular momenta compared to velocity gauge [4].

Figure 2 shows the relative errors in $n(r)$ of a velocity gauge calculation with $L_{\max} = 21$ angular momenta and mixed gauge calculations at two different gauge radii $R_g = 5$, $L_{\max} = 30$, and $R_g = 20$, $L_{\max} = 35$. As expected, the mixed gauge calculation needs higher $L_{\max}$ as R_g increases for achieving comparable accuracies.

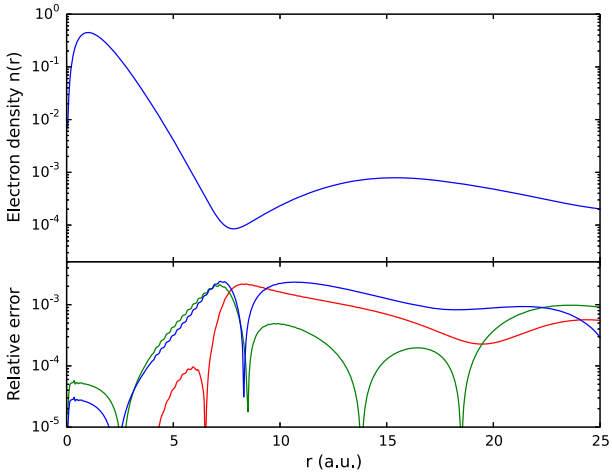

Figure 2. Velocity versus mixed gauge for the hydrogen atom in three dimensions. Upper panel: electron-density up to the absorption radius $R_0 = 25$, fully converged calculation. Lower panel: relative errors, equation (26), compared to the fully converged calculation. Red: velocity gauge $L_{\max} = 21$, green: mixed gauge, $R_g = 5$, $L_{\max} = 30$, blue: mixed gauge at $R_g = 20$, $L_{\max} = 35$. Radial discretization by $N = 80$ functions.

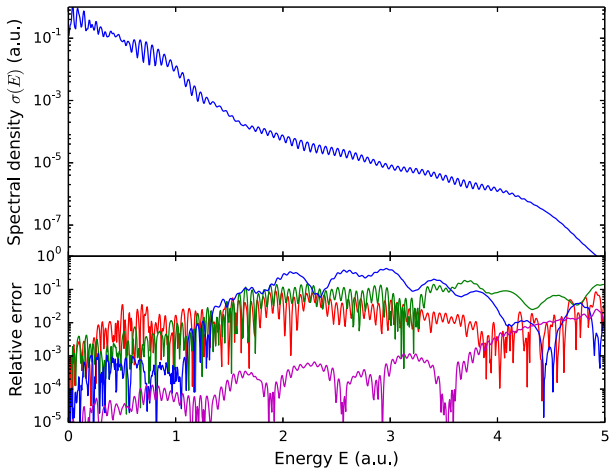

Figure 3. Photoelectron spectrum of the hydrogen atom. Upper panel: highly accurate reference spectrum, obtained in velocity gauge. For pulse parameters see text. Lower panel: comparison of the reference spectrum with spectra obtained in different gauges. The number of angular momenta was adjusted to obtain comparable errors. Red: velocity gauge $L_{\max} = 21$, green: mixed gauge, $R_g = 5$, $L_{\max} = 30$, blue: mixed gauge at $R_g = 20$, $L_{\max} = 40$. Radial discretization as in figure 2. The magenta line gives the error of a more accurate mixed gauge calculation with $R_g = 20$, $L_{\max} = 60$.

The same general error behavior of the different gauges is also found in the photoelectron spectra, figure 3. Here, the $R_g = 20$ requires even more angular momenta $L_{\max} = 40$. This may be due to the particular sensitivity of photoelectron spectra to the wavefunction at the radius where the surface flux is picked up and integrated, in the present case at $r = 25$. To emphasize that with larger effort photo-electron spectra can be computed to very high precision also in mixed gauge, we include a mixed gauge computation with $L_{\max} = 60$ in figure 3.

3.3. Helium atom and H_2 molecule

The length gauge Hamiltonian for a 2e problem interacting with a dipole laser field is

$$H_L(t) = \sum_{k=1,2}\left[-\frac{1}{2}\Delta_k - \frac{1}{\left|\vec{r}_k - \vec{R}/2\right|} - \frac{1}{\left|\vec{r}_k + \vec{R}/2\right|} - \vec{\mathcal{E}}(t)\cdot\vec{r}_k\right] + \frac{1}{\left|\vec{r}_1 - \vec{r}_2\right|}. \quad (33)$$

This includes the H_2 molecule with the nuclei fixed at equilibrium distance $\vec{R} = (0, 0, 1.4)$ and the helium atom $|\vec{R}| = 0$. We assume linear polarization in z-direction.

We compare total photoelectron spectra. As a reference, we solved the 2e TDSE fully numerically in velocity gauge using a single-center expansion. Details of this calculation will be reported elsewhere [17]. Photoelectron spectra for the various ionic channels were computed using the 2e form of tSURFF (see [16]). As 2e calculations are very challenging at long wavelength, we use a 3-cycle pulse at somewhat shorter wavelength of $\lambda = 400$ nm and an intensity of only 1×10^{14} W cm^{-2}. To facilitate the extraction of photoelectron momenta, all potentials were smoothly turned off beyond distances $|\vec{r}_i| > 25$ au, as described in [16].

The 2e calculation is compared with a coupled channels computation using the expansion

$$\left|\Psi(t)\right\rangle = |0\rangle c_0(t) + \sum_{I,j}\mathcal{A}[|I\rangle|j\rangle]c_{Ij}(t), \quad (34)$$

which includes the field-free neutral ground state $|0\rangle$ and the ionic states $|I\rangle$ multiplied by the same single-electron basis functions $|j\rangle$ as for the hydrogen atom. Anti-symmetrization is indicated by $\mathcal{A}[\ldots]$. The neutral ground state $|0\rangle$ as well as the ionic states $|I\rangle$ were obtained from the COLUMBUS quantum chemistry package [18]. Calculations were performed in velocity and mixed gauge (continuous switching), as described for the hydrogen atom. Details of the coupled channels method will be reported elsewhere [19]. A similar method was published recently, where no anti-symmetrization $\mathcal{A}$ was imposed during time propagation [20]. It remains to be investigated whether in that case gauge questions play the same prominent role as in our fully anti-symmetrized approach.

By the arguments above, in the coupled channels basis we expect the mixed-gauge calculation to converge better than the velocity gauge calculation: the COLUMBUS wavefunctions $|0\rangle$ and $|I\rangle$ have their intended physical meaning only in length gauge. Figures 4 and 5 confirm this expectation.

For helium, figure 4, the velocity gauge 2e calculation agrees well with the mixed gauge coupled channels calculation using the neutral and only the 1s ionic state. With the five

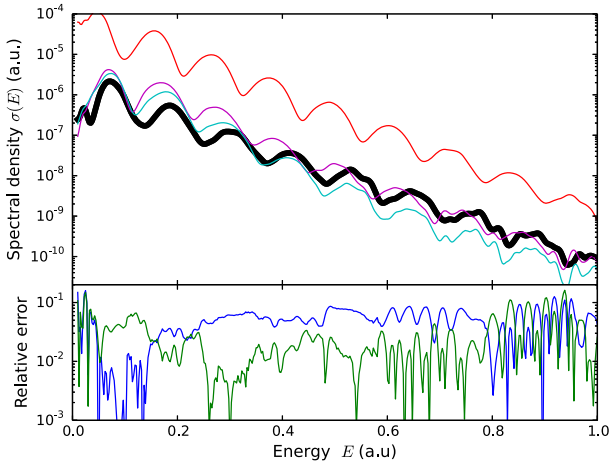

Figure 4. Photoelectron spectrum of helium at 400 nm. Upper panel, thick black line: full 2e calculation in velocity gauge. Upper panel, thin lines: coupled channels, equation (34), in velocity gauge. Red: include $n = 1$ ionic state, magenta: $n \leqslant 2$ ionic states, cyan: $n \leqslant 3$ s and p ionic states. The mixed gauge coupled channels calculations nearly coincide with the 2e calculation and fall into the thick black line. Lower panel: relative difference between mixed gauge coupled channels calculation and the 2e calculation. Blue line: include only ionic ground $n = 1$ state, green line: include all $n \leqslant 2$ states. Agreement between the 2e velocity gauge calculation and mixed gauge coupled-channels type calculation is within the estimated accuracy of the 2e calculation.

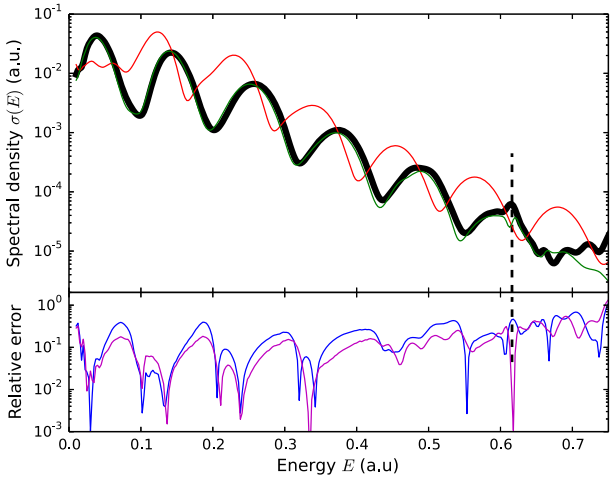

Figure 5. Photoelectron spectrum of H_2 at 400 nm. Upper panel, thick line: full 2e calculation in velocity gauge. Thin lines: velocity gauge coupled channels calculation, equation (34). Thin red line: include lowest σ_g ionic state, thin green line: include the six lowest σ and π ionic states. Lower panel: relative difference between mixed gauge coupled channels calculation and the 2e calculation. Blue line: include only σ_g ionic ground state, magenta line: include the six lowest σ and π ionic states. The dashed line marks the position of the resonance discussed in the text.

ionic states with principal quantum numbers $n \leqslant 2$ the error is ~2% for a large part of the spectrum up to 1 au. In contrast, the single-ion velocity gauge calculation is far off. It does somewhat approach the 2e result when the number of ionic states is increased to include the states up to $n = 3$. In velocity gauge, convergence could not be achieved for two reasons. One reason is a technical limitation of the coupled channels code, which uses Gaussian basis functions that do not properly represent the higher ionic states. The second reason is more fundamental: in velocity gauge the ionic core transiently contains significant continuum contributions, which are not included in our ionic basis by construction.

The error pattern is similar in H_2, but the accuracy of all calculations is poorer, figure 5: 2e and coupled channel mixed gauge calculations qualitatively agree already when only the σ_g ionic ground state is included. With the lowest six ionic π and σ states the two spectra differ by $\lesssim$20%. Remarkably, the height of a small resonant peak at ~0.62 au is faithfully reproduced in mixed gauge with six ionic states. The resonance can be tentatively assigned to the near degenerate second and third $^1\Sigma_u^+$ doubly excited states of H_2 at the internuclear equilibrium distance of 1.4 au (see [21]). As a note of caution, the single center expansion used in the 2e code converges only slowly for H_2 and cannot be taken as an absolute reference. The coupled channels velocity gauge calculation is off by almost an order of magnitude when only a single ionic state is included. With six ionic states it compares to the full 2e on a similar level as the mixed gauge. However, in velocity gauge the resonance is not reproduced correctly.

For both systems, analogous results were found at shorter wavelengths down to $\lambda = 200$ nm. At even shorter wavelength and realistic laser intensities, gauge questions are less important as the magnitude of $|\vec{A}(t)| \propto \lambda$.

4. Conclusions

In summary, we have shown that a transition between gauges within the same calculation bears substantial advantages and requires only moderate implementation effort. For low-dimensional problems, the advantage can be technical, such as reducing the size of the spatial discretization and the equations' stiffness. We have shown that with a suitably chosen basis a sudden, non-differentiable transition from length to velocity gauge is preferable over a differentiably smooth transition in terms of both, simplicity of implementation and numerical efficiency.

Mixed gauge opens the route to a highly efficient coupled channels type description of laser–matter interaction. As the meaning of the individual channel functions is gauge-dependent, a finite set of channels leads to gauge-dependent results. We argued that only in length gauge the field free ionic eigenfunctions retain their intended physical meaning in presence of a strong pulse. In contrast, in velocity gauge the same functions represent a momentum-boosted system with unphysical dynamics. Therefore typical physical models suggest the use of length gauge. This was clearly demonstrated by mixed gauge calculations of two electron sytems. When the length gauge region was chosen to cover the ionic channel functions, the calculations converged with very few channels. Most dramatically, the single-ionization spectrum of helium was calculated to $\lesssim$10% error using only the ionic

ground state channel. In contrast, in velocity gauge the single channel result is by nearly two orders of magnitude off and convergence could not be achieved with up to nine channels. In pure length gauge a computation is out of reach because of the required discretization size.

Convergence with only the field-free neutral and very few ionic states can justify *a posteriori* wide-spread modeling of laser–atom interactions in terms of such states. It also supports the view that length gauge is the natural choice for this type of models. The convergence behavior of mixed gauge calculations—possibly contrasted with pure velocity gauge calculations—may help to judge the validity of these important models in more complex few-electron systems.

Acknowledgments

VPM is a fellow of the EU Marie Curie ITN 'CORINF', AZ acknowledges support by the DFG through the excellence cluster 'Munich Center for Advanced Photonics (MAP)', and by the Austrian Science Foundation project ViCoM (F41). AS gratefully acknowledges partial support by the National Science Foundation under Grant No. NSF PHY11–25915.

References

[1] Bauer D, Milosevic D B and Becker W 2005 *Phys. Rev.* A **72** 23415
[2] Faisal F H M 2007 *Phys. Rev.* A **75** 063412
[3] Vanne Y V and Saenz A 2009 *Phys. Rev.* A **79** 023421
[4] Cormier E and Lambropoulos P 1996 *J. Phys. B: At. Mol. Opt. Phys.* **29** 1667
[5] Bandrauk A D, Fillion-Gourdeau F and Lorin E 2013 *J. Phys. B: At. Mol. Opt. Phys.* **46** 153001
[6] Burke P G, Francken P and Joachain C J 1991 *J. Phys. B: At. Mol. Opt. Phys.* **24** 761
[7] Dörr M, Terao-Dunseath M, Purvis J, Noble C J, Burke P G and Joachain C J 1992 *J. Phys. B: At. Mol. Opt. Phys.* **25** 2809
[8] Robicheaux F, Chen C T, Gavras P and Pindzola M S 1995 *J. Phys. B: At. Mol. Opt. Phys.* **28** 3047
[9] Awasthi M, Vanne Y V, Saenz A, Castro A and Decleva P 2008 *Phys. Rev.* A **77** 063403
[10] Busuladžić M and Milošević D B 2010 *Phys. Rev.* A **82** 015401
[11] Tao L and Scrinzi A 2012 *New J. Phys.* **14** 013021
[12] Scrinzi A 2010 *Phys. Rev.* A **81** 053845
[13] McCurdy C, Baertschy M and Rescigno T 2004 *J. Phys. B: At. Mol. Opt. Phys.* **37** R137
[14] Reed M and Simon B 1982 *Methods of Modern Mathematical Physics* vol 4 (New York: Academic) p 183
[15] Scrinzi A and Elander N 1993 *J. Chem. Phys.* **98** 3866
[16] Scrinzi A 2012 *New J. Phys.* **14** 085008
[17] Zielinski A, Majety V P and Scrinzi A 2014 A general solver for the time-dependent schrödinger equation of one and two particle systems (in preparation)
[18] Lischka H, Mueller T, Szalay P G, Shavitt I, Pitzer R M and Shepard R 2011 *Wiley Interdiscip. Rev. Comput. Mol. Sci.* **1** 191
[19] Majety V P, Zielinski A and Scrinzi A 2014 Photoionization of few electron systems with a hybrid Coupled Channels approach arXiv:1412.3666
[20] Spanner M and Patchkovskii S 2009 *Phys. Rev.* A **80** 063411
[21] Sanchez I and Martin F 1997 *J. Chem. Phys.* **106** 7720

Photonics **2015**, *2*, 93-103; doi:10.3390/photonics2010093

OPEN ACCESS

photonics

ISSN 2304-6732

www.mdpi.com/journal/photonics

Article

Photo-Ionization of Noble Gases: A Demonstration of Hybrid Coupled Channels Approach

Vinay Pramod Majety * and Armin Scrinzi

Physics Department, Ludwig Maximilians Universität, D-80333 Munich, Germany;
E-Mail: armin.scrinzi@lmu.de

* Author to whom correspondence should be addressed;
E-Mail: Vinay.Majety@physik.uni-muenchen.de; Tel.: +49-089-2180-4150.

Received: 15 December 2014 / Accepted: 14 January 2015 / Published: 16 January 2015

Abstract: We present here an application of the recently developed hybrid coupled channels approach to study photo-ionization of noble gas atoms: Neon and Argon. We first compute multi-photon ionization rates and cross-sections for these inert gas atoms with our approach and compare them with reliable data available from R-matrix Floquet theory. The good agreement between coupled channels and R-matrix Floquet theory show that our method treats multi-electron systems on par with the well established R-matrix theory. We then apply the time dependent surface flux (tSURFF) method with our approach to compute total and angle resolved photo-electron spectra from Argon with linearly and circularly polarized 12 nm wavelength laser fields, a typical wavelength available from Free Electron Lasers (FELs).

Keywords: photo-ionization; coupled channels approach

1. Introduction

Photo-ionization has been a useful tool in understanding electronic structure of materials for several decades. The availability of highly tunable, high photon flux sources like FELs and synchrotron has deepened our dependence on photo-ionization experiments by providing very accurate structural information [1]. Noble gas atoms are chemically inert due to their closed shell electronic configuration. This makes them attractive systems for experimental studies. In the field of strong field physics, they have been extensively used to study ionization properties and core-hole dynamics, and they were used in

proof of principle experiments to demonstrate time resolved electron spectroscopy. Krypton atoms were used in [2] to demonstrate that attosecond transient absorption spectroscopy can be used to observe real time motion of valence electrons. The presence of cooper minimum in high harmonic spectra from Argon is considered as a proof that high harmonic generation carries the electronic structural information in it and has attracted many photo-ionization studies, for example [3,4]. Inert gas atoms like helium and neon have also been widely used to investigate double ionization [1], a process that can be used to understand electron correlation in photo-emission. Using attosecond streaking, time delays in photo-emission from Neon were measured in [5]. It was experimentally found that the 2s and 2p electrons are emitted with a relative time delay of 20 as. This remains an unexplained result to date. The closest theoretical estimate so far has been from the R-matrix theory that predicts around 10 as [6] for the time delay. The difficulty in producing accurate theoretical estimates stems from the difficulties in numerical treatment of many body problem.

In the theoretical domain, the major road block in understanding these photo-ionization processes is the multi-dimensionality of the wavefunction which leads to a very unfavorable scaling of numerical solvers for the time dependent Schrödinger equation (TDSE). In the weak field regime, it may be possible to use perturbation theory to compute the ionization properties. In [7], multi-photon perturbation theory was used to compute two, three and four photon ionization cross-sections of helium. However, in [8] it has been shown that even in the "perturbative" regime, resonances in helium can lead to non-perturbative effects in photo-ionization, pointing to the limits of applicability of multi-photon perturbation theory. Multi-photon perturbation theory is also limited in its application to multi-electron systems as computing the multi-electron scattering states and the whole set of intermediate states involved in a multi-photon ionization process can be an impractical task. Therefore, one resorts to numerical solutions of the TDSE even in the perturbative regime.

As a full dimensional numerical solution for multi-electron TDSE is not feasible, several methods have been developed in the past decade that only use a part of the Hilbert space that is seemingly important for the ionization process. Some of them include multi-configuration time dependent hartree-fock method [9], time dependent Configuration Interaction method [10], time dependent restricted-active-space configuration-interaction method [11], time dependent R-matrix method [12] and coupled channels method [13]. However, in terms of multi-photon ionization of atoms, R-matrix theory is the main source of available theoretical data. There have been many studies on multi-photon ionization of noble gas atoms performed using R-matrix theory, for example [12,14,15].

We recently developed a hybrid coupled channels method [16] to study photo-ionization of multi-electron systems. The method combines multi-electron bound states from quantum chemistry and one-electron numerical basis sets to construct N-electron wavefunctions that are used as basis functions to solve the TDSE. This method in conjunction with the time dependent surface flux method [17,18] can compute accurate single photo-electron spectra. We present here an application of our method to study photo-ionization from noble gas atoms-Neon and Argon. We compute multi-photon ionization rates and cross-sections and compare them with reliable data available from the R-matrix Floquet approach. We find that our results are in good agreement with the R-matrix Floquet (RMF) calculations. This shows that our method treats ionization of multi-electron systems on par with the well established R-matrix theory. We then compute photo-electron spectra from Argon with linearly and circularly polarized

12 nm wavelength laser fields. The results presented here are the first steps to computing photo-electron spectra at long wavelengths that are currently inaccessible from any theoretical approach that considers multi-electron effects.

2. Hybrid Coupled Channels Method

We solve the N-electron TDSE:

$$i\frac{\partial\Psi}{\partial t} = \hat{H}\Psi \tag{1}$$

in dipole approximation using a hybrid anti-symmetrized coupled channels (haCC) basis composed of multi-electron states from quantum chemistry and a numerical one-electron basis. We refer the reader to [16] for an elaborate description of the approach and present here the salient features of the method. We discretize the N-electron wavefunction as:

$$|\Psi(t)\rangle \approx \sum_{\mathcal{I}} |\mathcal{I}\rangle C_{\mathcal{I}}(t) + |\mathcal{G}\rangle C_{\mathcal{G}}(t) \tag{2}$$

where

$$|\mathcal{I}\rangle = \mathcal{A}[|i\rangle|I\rangle] \tag{3}$$

Here, $\mathcal{A}$ indicates anti-symmetrization, $C_{\mathcal{G}}$ and $C_{\mathcal{I}}$ are the time dependent coefficients, $|i\rangle$ represents a numerical one-electron basis and $|I\rangle$ are (N-1) electron wavefunctions which are chosen to be the eigen states of the single ionic hamiltonian obtained from the Multi-Reference Configuration Interaction Singles Doubles (MR-CISD) [19] level of quantum chemistry. $|\mathcal{G}\rangle$ is chosen as the ground state of the N-electron system, also obtained from MR-CISD level of quantum chemistry. As correlated states need many ionic states to be correctly represented, we include the ground state explicitly in the basis for the sake of efficiency. We use COLUMBUS [19] quantum chemistry code to compute these states. The basis is suitable to study single ionization problems, and it can represent an active electron in a polarizable core. By active electron we mean, the basis set representing this electron is flexible enough to represent bound as well as continuum states. The active electron is represented using a high order finite element basis, $|f_i(r)\rangle$, for the radial coordinate and spherical harmonics, $Y_{l_i m_i}$, for the angular coordinates.

$$|i(\vec{r})\rangle = |f_i(r)\rangle|Y_{l_i m_i}(\Omega)\rangle \tag{4}$$

Using basis Equation (2) with TDSE Equation (1) leads to a set of coupled ordinary differential equations for the time dependent coefficients:

$$i\left[\langle\mathcal{G}|\mathcal{G}\rangle\frac{dC_{\mathcal{G}}}{dt} + \langle\mathcal{G}|\mathcal{I}\rangle\frac{dC_{\mathcal{I}}}{dt}\right] = \langle\mathcal{G}|\hat{H}|\mathcal{G}\rangle C_{\mathcal{G}} + \langle\mathcal{G}|\hat{H}|\mathcal{I}\rangle C_{\mathcal{I}} \tag{5}$$

$$i\left[\langle\mathcal{I}|\mathcal{G}\rangle\frac{dC_{\mathcal{G}}}{dt} + \langle\mathcal{I}|\mathcal{I}\rangle\frac{dC_{\mathcal{I}}}{dt}\right] = \langle\mathcal{I}|\hat{H}|\mathcal{G}\rangle C_{\mathcal{G}} + \langle\mathcal{I}|\hat{H}|\mathcal{I}\rangle C_{\mathcal{I}}. \tag{6}$$

We solve them with an explicit fourth order Runge-Kutta solver with an automatic step size controller. A mixed gauge representation of the dipole operator is used for the reasons discussed in [20]. To absorb the wavefunction at the box boundaries we use infinite range Exterior Complex scaling (irECS) [21]. Finally, we employ the time dependent surface flux (tSURFF) method [17,18] to compute photo-electron spectra.

One of the main advantages of a coupled channels ansatz is that the time propagation scales quadratically with the number of ionic channels included and is independent of the number of electrons. In our haCC scheme, the ionic states are directly read from the output of a quantum chemistry calculation. This gives us the flexibility to treat ionic states at different levels of quantum chemistry. Any coupled channels scheme based only on ionic bound state channels also suffers from several limitations. The description of polarization of the ionic core is incomplete without the ionic continuum. The quantum chemistry ionic states based on gaussian orbitals will not have the exact asymptotic behavior. These limitations can lead to certain inaccuracies in our calculations. However, the high dimensionality of the multi-electron wavefunction limits us to go beyond these kind of approximations and all multi-electron TDSE solvers suffer from these kind of limitations.

3. Results

3.1. One- and Two-Photon Cross-Sections of Neon

In this section, we compute the one- and the two-photon ionization cross-sections of Neon and compare them with the results from experiments and the R-matrix theory. We use in our Neon basis four ionic states-the three fold degenerate $1s^2 2s^2 2p^5$ state and the $1s^2 2s 2p^6$ state. This implies that we have four possible ionization channels:

$$\begin{aligned} 1s^2 2s^2 2p^6 &\rightarrow 1s^2 2s^2 2p^5 + e^- \\ &\rightarrow 1s^2 2s 2p^6 + e^- \end{aligned} \tag{7}$$

The configurations used to represent the states are only symbolic and as we compute them using Configuration Interaction theory [19], each multi-electron state is composed of several configurations. In our time dependent approach we compute cross-sections using Equation (51) in [12]:

$$\sigma^{(n)} = (8\pi\alpha)^n \left(\frac{3.5 \times 10^{16}}{I}\right)^n \omega^n \Gamma a_0^{2n} t_0^{n-1} \tag{8}$$

where $\sigma^{(n)}$ is the n photon ionization cross-section in units cm^{2n}/s^{n-1}, I is the intensity in W/cm^2, ω is the laser frequency in a.u, α is the fine structure constant and a_0, t_0 are atomic units of length and time respectively in cms. Γ is the total ionization rate in a.u. which is computed in a time dependent approach by monitoring the rate at which the norm of the wavefunction in a certain inner region drops. We use for our computations a 150-cycle continuous wave laser pulse with a 3-cycle $\cos^2$ ramp up and ramp down and with an intensity of $10^{12} W/cm^2$. Calculations were performed with a simulation volume radius of up to 100 a.u. and an angular momentum expansion of upto $L_{max} = 6$ for the active electron basis.

Figure 1 shows one-photon ionization cross-sections from Neon in the photon energy range 50–125 eV with haCC and from experimental results published in [22]. We find a very good agreement between the experimental results and our calculations.

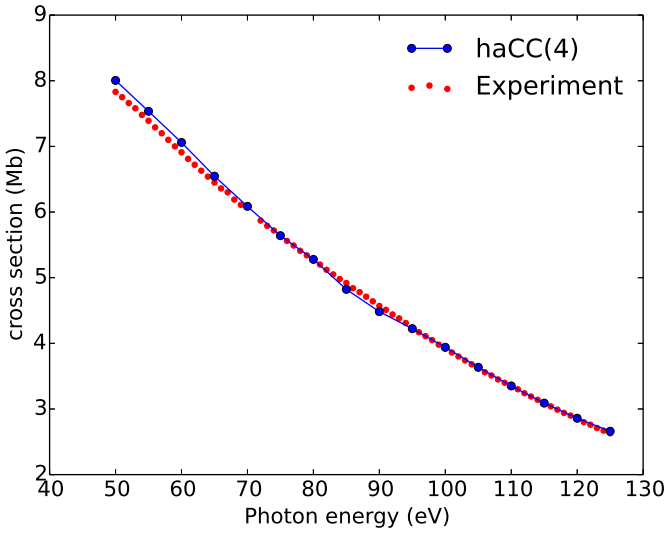

Figure 1. One-photon ionization cross-sections of Neon as a function of photon energy from haCC and from experiments [22]. haCC(4): Ionic basis consists of both $1s^2 2s^2 2p^5$ states and $1s^2 2s 2p^6$ state.

Figure 2 shows two-photon cross-sections from Neon with haCC, RMF and time dependent R-matrix (TDRM) methods. haCC(3) indicates computations with only the $1s^2 2s^2 2p^5$ ionic states and haCC(4) indicates computations including both the $1s^2 2s^2 2p^5$ states and the $1s^2 2s 2p^6$ state. Firstly, we find that haCC(3) and haCC(4) calculations give identical results. This is consistent with the knowledge that the $1s^2 2s 2p^6$ ionization channel is strongly closed [14]. Hence, there is no influence of this state on the two-photon cross-sections.

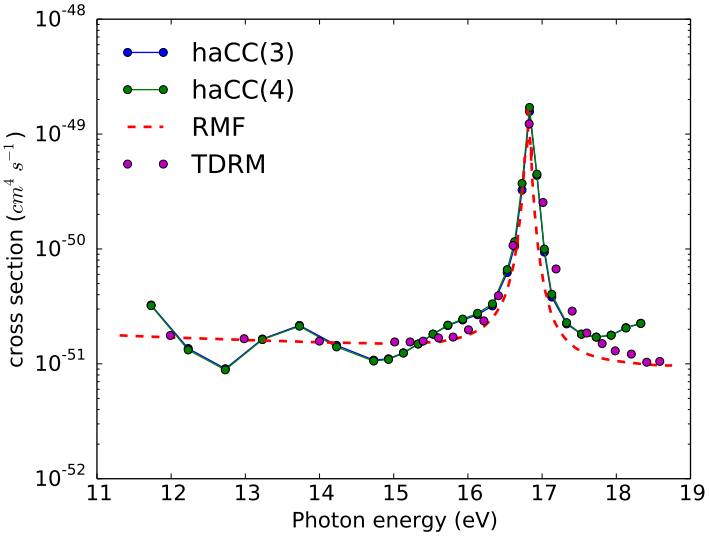

Figure 2. Two photon ionization cross-sections of Neon as a function of photon energy. The RMF and the TDRM results are from [12]. haCC(3): Ionic basis consists of only $1s^2 2s^2 2p^5$ states. haCC(4): Ionic basis consists of both $1s^2 2s^2 2p^5$ states and $1s^2 2s 2p^6$ state. The results from haCC(3) and haCC(4) are superposed.

The R-matrix calculations [12] and haCC calculations have an overall good agreement. The resonance structure at 16.83 eV photon energy corresponds to the $1s^2 2s^2 2p^5 3s$ state [12]. The peak heights of the resonant structure in all the computations agree very well. The peak is broader in the haCC and TDRM results compared to the RMF results. A contribution to this width is from the finite bandwidth of the laser pulse. In principle, the RMF results are exactly comparable to a result from a time dependent method only in the continuous wave limit. There is also an additional oscillation in the haCC cross-sections which is not present in the R-matrix results. This oscillation is stable with respect to the variation of the active electron discretization parameters. By construction haCC does not include any double continuum, which, if in turn included in R-matrix, could be one possible source of the differences. Other possible sources may be in the description of the atomic structure. The TDRM calculations in [12] were performed with a 20 a.u. inner region, $L_{max} = 5$ angular momentum expansion and 60 continuum functions per each angular momentum of the continuum electron. In general, a numerical discretization of the continuum as used in haCC yields more accurate results compared to the spectral descritization of the continuum used in [12]. A more exact definition of the discretization used for the calculations in [12] would be needed for an analysis of these differences. Apart from these minor differences, it should be emphasized that this agreement is achieved without any adjustment of parameters, which provides for a quantitative confirmation of all the results.

3.2. Five-Photon Ionization Rates from Argon

In this section, we compute the five-photon ionization rates from Argon and compare them with RMF calculations at laser intensity $10^{13} W/cm^2$. We use in our Argon basis four ionic states-the three fold degenerate $[Ne]3s^2 3p^5$ state and the $[Ne]3s3p^6$ state. This implies we have four possible ionization channels:

$$\begin{aligned} [Ne]\, 3s^2 3p^6 &\rightarrow [Ne]3s^2 3p^5 + e^- \\ &\rightarrow [Ne]3s3p^6 + e^- \end{aligned} \tag{9}$$

Again here, the configurations used to represent the states are only symbolic and in practice we use configuration interaction theory to treat them.

Figure 3 shows the five-photon ionization rates from haCC computations and RMF theory [14]. We use a simulation volume radius of 40 a.u. and an angular momentum expansion up to $L_{max} = 9$ for the active electron basis. The ionization rates are computed by monitoring the rate at which the norm of the wavefunction in the simulation box drops. We use continuous wave laser pulses with ramp up and ramp down for our calculations. Hence, the rate at which the norm of the wavefunction drops reaches a steady state for any given simulation box size. We find that our haCC computations are in very good agreement with the RMF results. Both the approaches produce the two resonances $3p^5 4p\ ^1S$ at 364 nm and $3p^5 4p\ ^1D$ at 370 nm. The resonant structures are broader with the haCC method due to the finite bandwidth of the laser pulse.

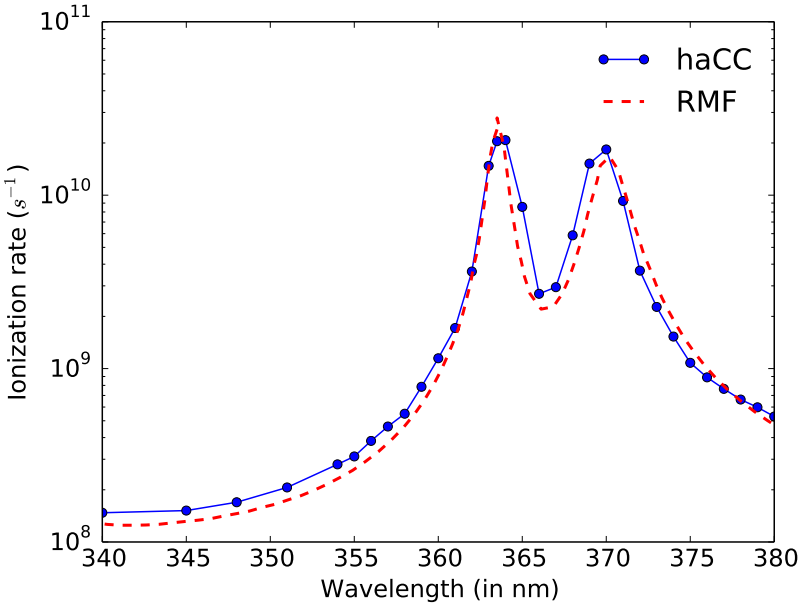

Figure 3. Five-photon ionization rates as a function of wavelength. The peak intensity of the laser fields used is $10^{13} W/cm^2$. The RMF results are from [14].

3.3. Photo-Electron Spectra from Argon with 12 nm Wavelength Laser Fields

As photo-electron spectra is a typical quantity measured in photo-ionization experiments such as with FELs, we present as a demonstration, photo-electron spectra from Argon at a typical wavelength produced at FELs, 12 nm ($\hbar\omega \approx 105$ eV). This wavelength has been of experimental interest and also attracted theoretical attention recently [23].

Figure 4 shows total photo-electron spectra from Argon with linearly and circularly polarized 12 nm wavelength laser pulses. The exact pulse parameters are in the figure caption. The pulse shape used is

$$A_{z/x}(t) = A_{0z/x} \cos^2(\frac{\pi t}{2cT})\ \sin(\frac{2\pi t}{T} + \beta) \tag{10}$$

where $A_{0z/x}$ is the peak vector potential of the z component or the x component, T is the single cycle duration, c is the number of laser cycles and β is the carrier envelope phase. Here, the xz plane is the polarization plane for the circularly polarized laser pulses.

Figure 4 shows the one- and two-photon ionization peaks. The two peak structure in the spectrum is a result of ionization to two different channels. Single photon ionization to $[Ne]3s^2 3p^5$ is the dominant ionization process with these pulse parameters. Single photon ionization is a linear process and ionization with circular polarization can be understood as a simple sum of ionization from two perpendicular linear polarized laser fields. The single photon peaks with circular polarization are twice as large as the single photon peaks with linear polarization, supporting this fact.

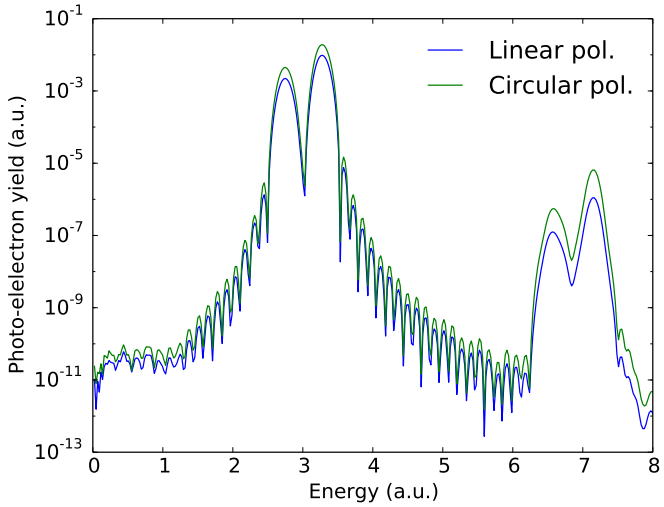

Figure 4. Total photo-electron spectra from Argon with linearly and circulary polarized 15 cycle, 12 nm wavelength, $\cos^2$ envelope laser pulses with a peak intensity of $9 \times 10^{13} W/cm^2$. The figure shows the one- and two-photon ionization peaks.

Figure 5 shows the partial wave decomposition and angle resolved spectra corresponding to the single photon ionization peaks with linear polarization. The partial wave decomposition shows the typical dipole selection rules. The spectra corresponding to the $[Ne]3s3p^6$ ionization channel, which is the inner structure in the angle resolved spectra, has a node in the plane perpendicular to the laser polarization. In order to ionize into this channel, the s electron is ionized to a $l = 1$ continuum, resulting in the node. The outer structure, corresponding to ionization to $[Ne]3s^23p^5$ channels, is a superposition of s and d waves.

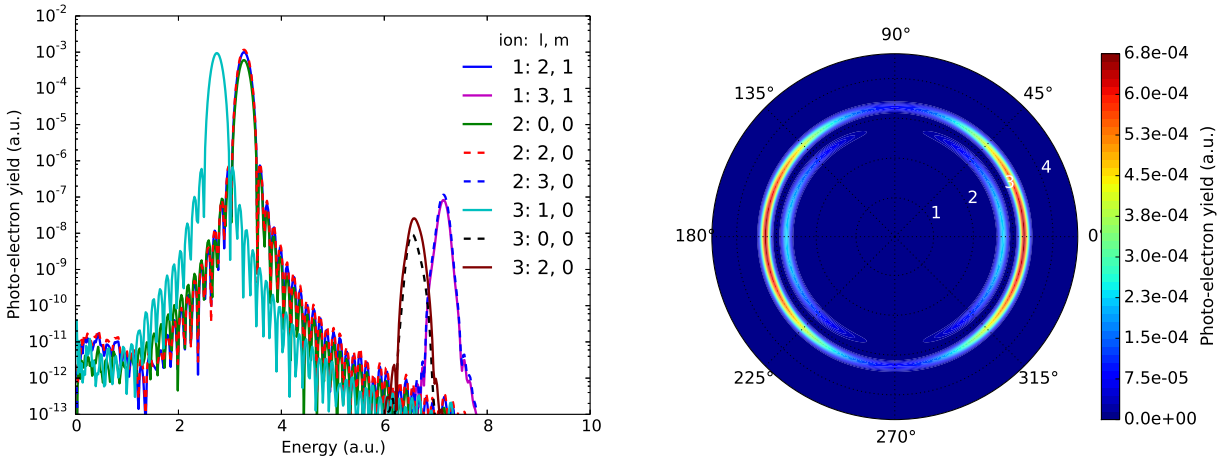

Figure 5. Resolving photo-electron spectra from Argon with linearly polarized 12 nm wavelength laser fields. Left figure: dominant partial waves in the ionic channels 1: $[Ne]3s^23p_x^23p_y3p_z^2$, 2: $[Ne]3s^23p_x^23p_y^23p_z$, 3: $[Ne]3s3p^6$. The channel 2 is dominated by the s-d superposition. Right figure: Angle resolved spectra corresponding to the one-photon ionization double peak in Figure 4. The angle is defined with respect to the laser polarization direction.

With circular polarization, the photo-emission is nearly uniform in all the directions in the plane of laser polarization and its a sum of dipole emissions into all the directions.

4. Conclusions

The hybrid coupled channels technique has been shown to be a promising tool in studying single ionization dynamics of multi-electron systems in [16]. The applications of this method presented here strengthens this observation. The applications considered here are computation of multi-photon cross-sections, ionization rates and fully differential photo-electron spectra of inert gas atoms. We computed one- and two-photon cross-sections from Neon and five-photon ionization rates from Argon. The good agreement between the haCC results and RMF results shows that haCC can treat multi-electron systems on par with the well established multi-electron theories. However, the haCC approach promises to reach a step ahead of the other multi-electron theories in terms of flexibility that it possesses due to a direct interface to state of the art quantum chemistry and its compatibility with the efficient tSURFF spectra method. haCC can be used to compute photo-electron spectra from multi-electron systems at long wavelengths which has not been accessible from any multi-electron methods so far. As a first step in this direction, we presented total and angle resolved photo-electron spectra from Argon at an XUV wavelength.

Acknowledgments

V.P.M. is a fellow of the EU Marie Curie ITN "CORINF" and the International Max Planck Research School-Advanced Photon Science. The authors are grateful to the COLUMBUS developers-Hans Lischka, University of Vienna; Thomas Müller, Forschungszentrum Jülich; Felix Plasser, University of Heidelberg and Jiri Pittner, J. Heyrovský Institute for their support with constructing the quantum chemistry interface. The authors also thank Alejandro Zielinski for useful discussions and for his implementation of tSURFF.

Author Contributions

VPM undertook this project under the supervision of AS.

Conflicts of Interest

The authors declare no conflict of interest.

References

1. Feldhaus, J.; Krikunova, M.; Meyer, M.; Möller, T.; Moshammer, R.; Rudenko, A.; Tschentscher, T.; Ullrich, J. AMO science at the FLASH and European XFEL free-electron laser facilities. *J. Phys. B Atomic Mol. Opt. Phys.* **2013**, *46*, 164002.
2. Goulielmakis, E.; Loh, Z.H.; Wirth, A.; Santra, R.; Rohringer, N.; Yakovlev, V.S.; Zherebtsov, S.; Pfeifer, T.; Azzeer, A.M.; Kling, M.F.; *et al*. Real-time observation of valence electron motion. *Nature* **2010**, *466*, 739–743.

3. Wörner, H.; Niikura, H.; Bertrand, J.; Corkum, P.; Villeneuve, D. Observation of Electronic Structure Minima in High-Harmonic Generation. *Phys. Rev. Lett.* **2009**, *102*, 103901.
4. Bhardwaj, S.; Son, S.K.; Hong, K.H.; Lai, C.J.; Kärtner, F.; Santra, R. Recombination-amplitude calculations of noble gases, in both length and acceleration forms, beyond the strong-field approximation. *Phys. Rev. A* **2013**, *88*, 053405.
5. Schultze, M.; Fieß, M.; Karpowicz, N.; Gagnon, J.; Korbman, M.; Hofstetter, M.; Neppl, S.; Cavalieri, A.L.; Komninos, Y.; Mercouris, T.; *et al*. Delay in Photoemission. *Science* **2010**, *328*, 1658–1662.
6. Moore, L.; Lysaght, M.; Parker, J.; van der Hart, H.; Taylor, K. Time delay between photoemission from the $2p$ and $2s$ subshells of neon. *Phys. Rev. A* **2011**, *84*, 061404.
7. Saenz, A.; Lambropoulos, P. Theoretical two-, three- and four-photon ionization cross sections of helium in the XUV range. *J. Phys. B Atomic Mol. Opt. Phys.* **1999**, *32*, 5629.
8. Van der Hart, H.W.; Bingham, P. Two- and three-photon ionization of He between 10^{13} and 10^{14} W/cm^2. *J. Phys. B Atomic Mol. Opt. Phys.* **2005**, *38*, 207.
9. Caillat, J.; Zanghellini, J.; Kitzler, M.; Koch, O.; Kreuzer, W.; Scrinzi, A. Correlated multielectron systems in strong laser fields: A multiconfiguration time-dependent Hartree-Fock approach. *Phys. Rev. A* **2005**, *71*, 012712.
10. Greenman, L.; Ho, P.J.; Pabst, S.; Kamarchik, E.; Mazziotti, D.A.; Santra, R. Implementation of the time-dependent configuration-interaction singles method for atomic strong-field processes. *Phys. Rev. A* **2010**, *82*, 023406.
11. Hochstuhl, D.; Bonitz, M. Time-dependent restricted-active-space configuration-interaction method for the photoionization of many-electron atoms. *Phys. Rev. A* **2012**, *86*, 053424.
12. Lysaght, M.A.; van der Hart, H.W.; Burke, P.G. Time-dependent R-matrix theory for ultrafast atomic processes. *Phys. Rev. A* **2009**, *79*, 053411.
13. Spanner, M.; Patchkovskii, S. One-electron ionization of multielectron systems in strong nonresonant laser fields. *Phys. Rev. A* **2009**, *80*, 063411.
14. Van der Hart, H.W. Ionization rates for He, Ne, and Ar subjected to laser light with wavelengths between 248.6 and 390 nm. *Phys. Rev. A* **2006**, *73*, 023417.
15. Van der Hart, H.W.; Lysaght, M.A.; Burke, P.G. Time-dependent multielectron dynamics of Ar in intense short laser pulses. *Phys. Rev. A* **2007**, *76*, 043405.
16. Majety, V.P.; Zielinski, A.; Scrinzi, A. Photoionization of few electron systems with a hybrid Coupled Channels approach. 2014, *arXiv:1412.3666*.
17. Tao, L.; Scrinzi, A. Photo-electron momentum spectra from minimal volumes: The time-dependent surface flux method. *New J. Phys.* **2012**, *14*, 013021.
18. Scrinzi, A. t -SURFF: Fully differential two-electron photo-emission spectra. *New J. Phys.* **2012**, *14*, 085008.
19. Lischka, H.; Müller, T.; Szalay, P.G.; Shavitt, I.; Pitzer, R.M.; Shepard, R. Columbus—A program system for advanced multireference theory calculations. *WIREs Comput. Mol. Sci.* **2011**, *1*, 191–199.
20. Majety, V.P.; Zielinski, A.; Scrinzi, A. Mixed gauge in strong laser-matter interaction. *J. Phys. B Atomic Mol. Opt. Phys.* **2015**, *48*, 025601.

21. Scrinzi, A. Infinite-range exterior complex scaling as a perfect absorber in time-dependent problems. *Phys. Rev. A* **2010**, *81*, 053845.
22. Samson, J.; Stolte, W. Precision measurements of the total photoionization cross-sections of He, Ne, Ar, Kr, and Xe. *J. Electron Spectrosc. Relat. Phenom.* **2002**, *123*, 265–276.
23. Karamatskou, A.; Pabst, S.; Chen, Y.J.; Santra, R. Calculation of photoelectron spectra within the time-dependent configuration-interaction singles scheme. *Phys. Rev. A* **2014**, *89*, 033415.

© 2015 by the authors; licensee MDPI, Basel, Switzerland. This article is an open access article distributed under the terms and conditions of the Creative Commons Attribution license (http://creativecommons.org/licenses/by/4.0/).

Static field ionization rates for multi-electron atoms and small molecules

Vinay Pramod Majety‡ and Armin Scrinzi§

Physics Department, Ludwig Maximilians Universität, D-80333 Munich, Germany.

Abstract. We present an application of the hybrid anti-symmetrized coupled channels approach to compute static field ionization rates for multi-electron atoms (He, Ne, Ar) and small molecules (H_2, N_2, CO). While inert atoms behave as effective single electron systems, molecules exhibit multi-electron effects in the form of core polarization. It is shown that at moderate field strengths, these effects can be modeled to about 10% accuracy using a few (5∼6) channel ansatz. In the case of the CO molecule, description of core polarization is essential for the correct prediction of the maximum ionization direction and our converged results are in good agreement with the experimental measurements.

Keywords: static field ionization, coupled channels approach, exterior complex scaling and polarization

‡ vinay.majety@physik.uni-muenchen.de
§ armin.scrinzi@lmu.de

1. Introduction

When an atom or a molecule interacts with a low frequency laser field whose field strength is comparable to the Coulomb potential, the atom or the molecule ionizes by tunneling through the potential barrier formed by the superposition of the Coulomb potential and the external field. If the field is strong enough to suppress the net potential barrier below the ground state of the system, one speaks of above barrier ionization (ABI). Several experiments like high harmonic spectroscopy (HHS) of molecules [1] and laser induced electron diffraction (LIED) [2] are based on these strong field ionization processes. The interpretation of the experiments is typically based on the Lewenstein model [3] or the quantitative re-scattering model (QRS) [4] which depend on the accurate understanding of the three independent steps: ionization, propagation of the continuum wavepacket, and re-scattering of this wavepacket by the ion.

In the low frequency limit, a quasistatic approximation of ionization is known to work well, which implies that the ground state depletion in the three-step like models can be modeled using static field ionization rates. This has resulted in the popularity of analytical formulae that give ionization rates obtained using various semi-classical approximations like the WKB approximation and the saddle point approximation. Some of the widely used analytical formulae are the Ammosov-Delone-Krainov (ADK) formula [5, 6, 7], its modification for molecules: the MO-ADK [8] formula and their empirical corrections, e.g. [9]. These formulae are also based on the effective single electron approximation.

While the ADK type formulae are easy to use they suffer from several shortcomings: at the level of single electron theory, they do not properly account for the transition region where the Coulomb and the external field compete in their influence on the dynamics. From comparison with numerical studies [10, 11] it has long been known that ADK overestimates rates even in the Helium atom which can be treated as a single electron system. In such situations one can resort to exact solutions of single-electron models to obtain correct rates [12, 13]. One also finds examples in literature where a theoretical treatment beyond single electron approximation is needed to study static field ionization. Neglect of exchange effects is responsible for the failure of MO-ADK and other single electron models in describing the angle dependent ionization of the CO_2 molecule [14, 15]. Multi-electron effects may be responsible for the failure of ADK in describing ionization of correlated transition metal atoms [16]. In spite of these known failures, the current interpretations of HHS and LIED experiments rely on ionization rates from single electron models due to the lack of more accurate data.

A full dimensional numerical treatment of the Schrödinger equation is only feasible for one- and two-electron systems [17, 10, 11, 18]. Hence, development of simpler techniques that include all the necessary ingredients to describe strong field ionization, based on the findings in one- and two-electron systems is necessary. This is a topic of ongoing research with some of the most recent contributions being from single electron models based on effective core potentials [19, 12, 13] and from the weak field asymptotic theory (WFAT) [20]. In [10], a comparison was made between the full dimensional calculations and some of the widely used models like the frozen core and Hartree-Fock models. It was found that, in the case of the helium atom, correlation plays a role only through the initial state and a practical way to compute accurate ionization rates for multi-electron systems could be to use a frozen core ansatz with

the addition of the fully correlated ground state wavefunction.

In the spirit of these findings, we pursue here a numerical approach based on our recently developed hybrid anti-symmetrized coupled channels basis (`haCC`) [21] with the exterior complex scaling method. In this approach, the wavefunction is discretized using a multi-electron basis that consists of several single ionic states fully anti-symmetrized with a numerical one-electron basis. In addition, the fully correlated neutral ground state is included. The basis allows for complete description of exchange interaction, inter-channel coupling, it contains initial state correlation and describes ionic core polarization in terms of the ionic bound states. Unlike simpler empirical models, the `haCC` scheme allows for systematic convergence studies in terms of the ionic channels included in the basis.

Within this framework we can separate effects of exchange from proper multi-electron effects: the single channel limit corresponds to a single active electron approximation where exchange with the ionic core is fully taken into account. The signature of proper multi-electron effects is that the ionization rates change as more ionic channels are included in the calculation.

We present rates for a few typical model systems in strong field physics: the inert gas atoms He, Ne, Ar and the molecules H_2, N_2 and CO. The benchmarking studies for two electron systems performed by comparing the `haCC` results with full dimensional calculations show that the `haCC` method can produce rates accurate on the level of 5-10%. Inert gas atoms behave as effective single electron systems while N_2 and CO molecules exhibit multi-electron effects in the form of core polarization. This is due to the closer spacing of the ionic bound states and is seen through the need for several ionic bound states in the basis for convergence. The reassuring finding however is that these polarization effects at moderate intensities can be modeled using a few (5∼6) channel ansatz.

For the CO molecule one expects ionization to be stronger towards the electronegative side, i.e. to the side of the C atom. However, some controversy about this fact arose among different calculations [22, 23, 24, 25]. The sign of the linear Stark shift for the CO molecule depends on the field orientation with respect to the molecule. The interplay between the electron density distribution in the highest occupied molecular orbital and the changes in the effective ionization potentials due to Stark shifts must be captured correctly [24]. We will show that core polarization is essential for accurate Stark shifts and for a correct prediction of the direction of maximal ionization. Our converged results are consistent with the measurements [22, 23].

The article is organized as follows. The computational scheme is outlined in section 2. In sections 3,4 and 5, benchmarking studies for two electron systems, rates for inert gas atoms and molecules are presented, respectively. We also compare our rates with the ADK theory and discuss the applicability of ADK. Finally, an appendix with angle dependent ionization rates for the molecules N_2 and CO is provided.

2. Computational method

In this section, we describe briefly the multi-electron basis that we use for solving the Schrödinger equation and the exterior complex scaling method for computing the

ionization rates. The multi-electron wavefunction is discretized as:

$$|\Psi(\vec{r}_1,\cdots,\vec{r}_N)\rangle = \sum_{i,I} \mathcal{A}[\ |I(\vec{r}_1,\cdots,\vec{r}_{N-1})\rangle\ |i(\vec{r}_N)\rangle\ ]\ C_{i,I} + |\mathcal{G}(\vec{r}_1,\cdots,\vec{r}_N)\rangle\ C_{\mathcal{G}}. \quad (1)$$

Here, $C_{i,I}$,$C_{\mathcal{G}}$ are the linear expansion coefficients; $\mathcal{A}$ indicates anti-symmetrization; $|i\rangle$ is a single electron numerical basis; and $|I\rangle$, $|\mathcal{G}\rangle$ are Configuration Interaction (CI) ionic and neutral wavefunctions, respectively. The CI functions are based on atom centered Gaussian basis functions obtained from the COLUMBUS quantum chemistry code [26]. The single electron basis is composed of finite element radial basis functions and single center real spherical harmonics for the angular coordinates. A detailed description of the basis can be found in [21]. The large angular momenta expansions that occur when treating molecules is mitigated in this basis, through the inclusion of the ground state neutral, $|\mathcal{G}\rangle$, in which all the electrons are described using atom-centered basis functions. A basis set of this type can help to examine the influence of several multi-electron effects like inter-channel coupling, ionic core polarization and exchange interaction in static field ionization. The labeling of the basis is done as follows: a basis named `haCC`(n) indicates that the ionic basis consists of the lowest n ionic states. Degenerate states are counted separately and the ground state neutral is always included.

It was realized in [27] that describing the asymptotic behavior of the ionizing orbital accurately is essential to obtain reliable rates. In our context, treating the ionizing electron with a finite element basis allows us to describe the asymptotic behavior accurately.

An efficient way to find the decay rates of eigenstates of a Hamiltonian is to transform it into a non-hermitian Hamiltonian via complex scaling. In complex scaling, real coordinates are transformed into complex coordinates through the transformation

$$r_\theta = \begin{cases} r & \text{for } r \le R_0 \\ e^{i\theta}(r - R_0) + R_0. & \text{for } r > R_0, \end{cases} \quad (2)$$

with the complex scaling radius R_0 and the complex scaling angle θ.

The electronic Hamiltonian for a multi-electron system with fixed nuclei is given by

$$H = \sum_{n=1}^{N} \left[T_n + V_n + \vec{r}_n \cdot \vec{E} \right] + v_{e-e} \quad (3)$$

where T_n is the single particle kinetic energy operator, V_n is the nuclear potential on the n^{th} coordinate, v_{e-e} is the electron-electron repulsion term, and $\vec{E}$ is the static electric field vector. The exact form of matrix elements with the haCC discretization is detailed in Ref [21].

Here, we are only interested in single ionization rates. Therefore we choose the complex scaling radius R_0 large enough such that all the molecular orbitals that compose the CI functions used in the haCC basis are negligible beyond R_0. Consequently, in this region the exchange terms are negligible. In addition, we smoothly turn off nuclear and the Hartree potentials over an interval of length a immediately before R_0. The dependence of our results on these parameters is routinely verified. The typical values used in the present work range from 25-40 a.u for R_0 and 5-10 a.u for a.

With these approximations complex scaling of the Hamiltonian reduces to N single-electron problems. We partition configuration space into the unscaled region $|\vec{r}_m| \leq R_0, m = 1, \ldots N$ and the singly scaled regions $S_n : |\vec{r}_n| > R_0, |\vec{r}_m| \leq R_0, m \neq n$. The remaining multiply scaled regions are excluded from our present ansatz functions. In the inner region, the Hamiltonian remains unchanged. As we neglect all interactions for $\vec{r}_n > R_0$, the complex scaled Hamiltonian in S_n takes the simple form

$$H_n = H_{ion}^{(\check{n})} + e^{-2i\theta} T_n + \left[R_0 + e^{i\theta}(r_n - R_0)\right] \hat{r}_n \cdot \vec{E} \tag{4}$$

where $H_{ion}^{(\check{n})}$ indicates the Hamiltonian of the ionic system obtained by removal of the n^{th} electron. Further details on the implementation can be found in [28].

With such a transformation, the eigenvalues corresponding to the field-free ground state in presence of a static electric field are of the form $E_f = r_f - i\hbar\frac{\Gamma_f}{2}$, where Γ_f is the ionization rate. We refer the readers to earlier articles [29, 30] and the references therein for more details on the complex scaling method and its deeper mathematical background. In order to compute the required eigenvalues E_f, we first compute the ground state of the field-free Hamiltonian and then adiabatically follow the root with respect to the field strength using the Arnoldi solver of the arpack code [31].

Limitations

At moderate field strengths the complex scaled eigenstate retains a quasi-bound character and its complex eigen energy remains well isolated except for occasional avoided crossings. In this regime one can easily trace the solution as the field strength is increased. At very high field strength, especially in the above barrier regime, the state looses this quasi-bound character and root tracing becomes increasingly difficult or may even fail. Such field strengths are rarely of practical interest as the system ionizes instantaneously.

In its present form, `haCC` has an intrinsic limitation at very high field strengths where the ionic core is strongly polarized. While polarization of the active electron orbital is fully described by the finite element basis, core ionic polarization is restricted to ionic bound states only. Even if, hypothetically, all ionic bound states were included, all continuum contributions to polarization are still missing. The relative importance of continuum compared to bound state contributions depends on the system's electronic structure.

While the hybrid nature of the basis helps in keeping the basis compact, the problem with the lower symmetry of a molecule persists. A lower symmetry group implies matrices with larger number of non-zero elements and this increases the computational cost, despite having the same number of basis functions.

The current implementation of the method can handle linear molecules. The calculations presented here were done on standard 8 core machines with computation times ranging from a few hours to about 2 days. Extensions to non-linear molecules would need implementation of a larger scale parallelization and will be a topic of future study.

3. Benchmarking for two-electron systems

Two electron systems are the largest systems where a full dimensional numerical treatment of the Schrödinger equation is possible and hence these are the typical

benchmark systems for new methods.

Table 1 presents a comparison of the ionization rates of Helium from the haCC method with the full dimensional calculations presented in references [17, 11, 32]. Results from haCC(1) and haCC(5) schemes are presented. haCC(1) scheme refers to the basis with only the 1s ionic channel and haCC(5) refers to the basis with the first and the second shell ionic channels. Inclusion of second shell ionic channels in general improves the results. For field strengths, F < 0.1 a.u, we obtain agreement with literature values on the level of 10%. Above 0.1 a.u, the agreement improves and the largest difference is on the level of 5%. Notably, above 0.1 a.u field strength, the haCC(5) rates differ from rates in Ref [17] by less than 1%. The ADK theory overestimates the rates in general.

F (a.u)	haCC(1)	haCC(5)	Ref [11]	Ref [17]	Ref [32]	ADK theory
0.06	$< 10^{-10}$	$< 10^{-10}$	7.8936×10^{-11}			1.23×10^{-10}
0.07	3.673×10^{-9}	3.755×10^{-9}	3.6360×10^{-9}		3.6×10^{-9}	5.42×10^{-9}
0.08	5.967×10^{-8}	6.097×10^{-8}	6.2093×10^{-8}	4.63×10^{-8}	5.57×10^{-8}	9.15×10^{-8}
0.09	5.131×10^{-7}	5.243×10^{-7}	5.3387×10^{-7}	5.09×10^{-7}	5.23×10^{-7}	8.20×10^{-7}
0.10	2.824×10^{-6}	2.888×10^{-6}	2.9391×10^{-6}	2.88×10^{-6}	2.92×10^{-6}	4.71×10^{-6}
0.11	1.128×10^{-5}	1.156×10^{-5}	1.1755×10^{-5}	1.15×10^{-5}	1.17×10^{-5}	1.96×10^{-5}
0.12	3.533×10^{-5}	3.613×10^{-5}	3.6829×10^{-5}	3.62×10^{-5}	3.66×10^{-5}	6.42×10^{-5}
0.13	9.193×10^{-5}	9.436×10^{-5}	9.5748×10^{-5}	9.43×10^{-5}	9.50×10^{-5}	1.74×10^{-4}
0.14	2.051×10^{-4}	2.106×10^{-4}	2.1495×10^{-4}	2.12×10^{-4}	2.13×10^{-4}	4.09×10^{-4}
0.15	4.115×10^{-4}	4.209×10^{-4}	4.2913×10^{-4}	4.23×10^{-4}	4.25×10^{-4}	8.56×10^{-4}
0.16	7.507×10^{-4}	7.695×10^{-4}	7.7875×10^{-4}	7.68×10^{-4}	7.70×10^{-4}	1.63×10^{-3}
0.18	1.966×10^{-3}	2.035×10^{-3}	2.0578×10^{-3}	2.03×10^{-3}	2.03×10^{-3}	4.73×10^{-3}
0.20	4.144×10^{-3}	4.308×10^{-3}	4.3347×10^{-3}	4.31×10^{-3}	4.30×10^{-3}	1.07×10^{-2}

Table 1. Static field ionization rates (a.u) at fields, F (a.u), for Helium atom with haCC(1) and haCC(5) schemes compared to literature values and the ADK theory.

F (a.u)	haCC(1)	haCC(2)	haCC(4)	haCC(5)	Ref [18]
0.06	3.22×10^{-5}	3.34×10^{-5}	3.34×10^{-5}	3.36×10^{-5}	3.36×10^{-5}
0.08	7.59×10^{-4}	8.02×10^{-4}	8.03×10^{-4}	8.04×10^{-4}	8.29×10^{-4}
0.10	4.31×10^{-3}	4.59×10^{-3}	4.59×10^{-3}	4.60×10^{-3}	4.71×10^{-3}
0.12	1.24×10^{-2}	1.33×10^{-2}	1.33×10^{-2}	1.33×10^{-2}	1.29×10^{-2}

Table 2. Static field ionization rates (a.u) at fields, F (a.u), for Hydrogen molecule from haCC(1) to haCC(5) schemes compared to literature for the case where the field is parallel to the molecular axis.

Tables 2 and 3 present a comparison of rates for the hydrogen molecule at the equilibrium inter-nuclear distance, 1.4 a.u, from the haCC method with data available from full dimensional calculations.

Full dimensional benchmark data is only available in literature for the case where the field is parallel to the molecular axis [18]. In this case, the single ionic state calculations, haCC(1), yield rates that differ from the benchmark calculations by about 10%. The inclusion of excited ionic states, that have dipole coupling with the $1\sigma_g$ ionic state, allow for ionic core polarization and improve the rates systematically. The rates

F (a.u)	haCC(1)	haCC(2)	haCC(4)	haCC(5)
0.06	2.45×10^{-5}	2.45×10^{-5}	2.52×10^{-5}	2.55×10^{-5}
0.08	6.02×10^{-4}	6.02×10^{-4}	6.22×10^{-4}	6.25×10^{-4}
0.10	3.54×10^{-3}	3.54×10^{-3}	3.67×10^{-3}	3.68×10^{-3}
0.12	1.044×10^{-2}	1.045×10^{-2}	1.09×10^{-2}	1.10×10^{-2}

Table 3. Static field ionization rates (a.u) at fields, F (a.u), for Hydrogen molecule from haCC(1) to haCC(5) schemes for the case where the field is perpendicular to the molecular axis.

from the haCC(5) scheme are accurate below 4% with respect to the full dimensional calculations.

For the case where the field is perpendicular to the molecular axis, the rates converge systematically to less than a few percent within the haCC schemes.

The two electron systems considered here have small polarizabilities and hence single ionic channel computations, with the inclusion of the fully correlated ground state, already provide a good estimate for ionization rates. However, inclusion of a few excited ionic channels does improve the rates systematically to a few percent accuracy demonstrating consistency of the method. In all these cases (Tables 1,2 and 3) the inclusion of the excited ionic channels increased the rates. The inclusion of excited states has two effects: to improve the accuracy of the Stark shifted energies and to improve the quality of the ionizing wavefunction. For He and H_2, the Stark shifts lead to an increase in the effective ionization potential which would reduce ionization rates. On the other hand, improvement of the asymptotic behavior of the wavefunction can be critical for tunneling and lead to an increase or a decrease of the rates depending on the specific case. Here, the effect of the Stark shifts turned out to be secondary and the improvement of the wavefunction has led to an increase in the rate in the correct direction towards the benchmark calculations.

These results demonstrate that the haCC method can be used to achieve accuracies on the level of 5-10% at moderate field strengths and where few channels are sufficient to describe the ionization process, as is the case of He and H_2.

4. Inert gas atoms: Ne, Ar

Inert gases have been widely used in strong field experiments and they are known to behave as effective single electron systems [9] due to the deep binding potentials for their excited ionic channels. In reference [33], we had shown that the haCC method delivers multi-photon ionization cross-sections and rates for inert gas atoms that are accurate and on par with other established atomic methods like the R-matrix method. Here, we present static field ionization rates for these atoms.

In figure 1, we compare the rates for Neon and Argon from the haCC approach with several complete single electron calculations [12, 13], the ADK and an empirically corrected ADK theory [9], that we refer to as E-ADK. The haCC rates were computed with two different basis schemes. The haCC(3) scheme includes the three fold degenerate ionic ground state channels of the respective atom, and the haCC(4) scheme includes the first excited ionic state channel in addition. The results from the two schemes differ by less than 2% and are indistinguishable in a plot. The comparison with the standard ADK theory shows that it over-estimates the rates in general, which is consistent with the observations in two electron systems. The

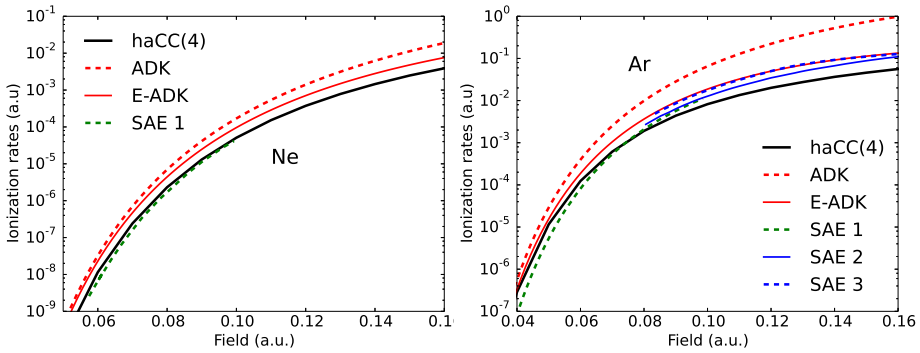

Figure 1. Static field ionization rates of Neon (left) and Argon (right) computed by different methods: `haCC`(4) (black solid lines), ADK (red dashed lines), E-ADK [9] (red solid), single electron model calculations from Ref. [12] up to field $0.1\,a.u.$ (SAE 1, green dashed) and [13] at fields $\gtrsim 0.08\,a.u.$ (SAE 2, blue solid and SAE 3, blue dashed). E-ADK and SAE 3 overlap within the resolution of the graph. All single electron values include multiplication by a factor 2 for the double occupancy of the ionizing orbital. SAE data were digitized from the respective figures of Refs.[12, 13]. SAE 1 data at fields $> 0.1\,a.u.$ could not be digitized because of insufficient resolution in the original graph.

E-ADK formula proposed in [9], which multiplies the ADK formula by a factor of the form $\exp(-cF/I_p)$, for the ionization potential I_p improves the rates at higher field strengths but still over-estimates by at least a factor 2. The full single electron calculations labeled SAE 1 [12], SAE 2 and SAE 3 [13] employ different effective potentials. The comparison among them shows that the rates are slightly sensitive to the choice of the effective potential. Agreement of haCC is better with the SAE calculations than with ADK. This indicates that inert gas atoms Ne and Ar can be treated as single electron systems. The remaining differences between haCC and SAE may be attributed to details of the effective single-electron potentials as well as to minor impact of exchange and proper multi-electron effects included in `haCC` .

5. Molecules

Molecules are known to show multi-electron effects in strong field ionization based studies [1, 24, 34]. The ionic states in molecular systems are closely spaced compared to inert gas atoms and this leads to a greater influence of inter-channel coupling and polarization. In the following sub-sections, we present orientation dependent rates for two important molecules in strong field physics: N_2 and CO. We demonstrate the importance of polarization in these molecules, which is seen through the need for several ionic excited state channels in the basis for convergence.

5.1. N_2 molecule

For the N_2 calculations, we use `haCC`(1) to `haCC`(7) bases schemes. Table 4 lists the energies of the ionic states used for constructing the `haCC` basis relative to the neutral ground state, $|\mathcal{G}\rangle$, at equilibrium geometry. The ionic and the neutral states were computed using the multi-reference CI singles level of the quantum chemical theory. A comparison with experimental data is also given. The first ionization potential, that

is crucial for total ionization rates varies on the level of 10^{-3} a.u within different `haCC` schemes and the experimental value. According to the MO-ADK theory, in the field strength range of 0.04-0.15 a.u such a difference in ionization potential changes the rates by 5-1%. As the absence of the ionic continuum that is needed for the complete description of polarization does not allow for rates of very high accuracy ($\leq 5\%$), we limit our accuracy requirement to $\lesssim 10\%$, and hence the small discrepancies caused due to the differences in the ionization potential are acceptable.

State	m-aug-cc-pvtz	m-aug-cc-pvqz	Svensson *et al.* [35]
$X^2\Sigma_g^+$	15.5	15.60	15.58
$A^2\Pi_u$	17.18	-	17.0
$B^2\Sigma_u^+$	18.93	-	18.8
$C^2\Sigma_u^+$	26.0	-	25.0
$D^2\Pi_g$	25.45	-	24.5

Table 4. Vertical energies (in eV) of ionic states used here, with respect to the neutral. The primitive Gaussian basis sets used are minimally augmented correlation consistent triple and quadruple zeta basis sets labeled as m-aug-cc-pvtz and m-aug-cc-pvqz respectively.

As N_2 is the first molecule in our examples that does not have benchmark data from alternate more accurate models, we present a systematic convergence study.

Figure 2 presents a convergence study for the rates with respect to the single electron basis parameters - scaling radius (R_0) , angular momenta, l_{max} (which is also equal to m_{max} here) and the primitive Gaussian basis within the `haCC`(1) scheme. The reference computation has the following parameters: $R_0 = 25$ a.u, $l_{max} = 9$ which leads to an angular momentum expansion of 100 functions and a minimally augmented correlation consistent triple zeta Gaussian basis (m-aug-cc-pvtz). Increasing the scaling radius or the angular momenta shows that the rates are converged to $\leq 2\%$ with respect to these parameters. Changing the gaussian basis to a quadruple zeta basis however changes the rates by about 10% at low field strengths (F < 0.5 a.u), but only by less than 5% at higher field strengths. Again, since we are only looking for rates accurate on the level of 10 % due to the before mentioned limitations of the method, we simply use the reference single electron parameters, to study the dependence of rates on the number of ionic channels.

In figure 3, the dependence of rates on the number of ionic channels in the `haCC` basis is presented for parallel orientation of the molecule and the field. The figure shows ionization rates and the shift of the ground state energy in presence of the field with respect to the field-free energy. The influence of ionic excited channels is to reduce the ionization rates. The presence of excited ionic states improves the description of the core electron polarizability and this leads to larger Stark shifts in the neutral energy. The ionic states are however less affected. The effective increase of the first ionization potential reduces the ionization rates. Tunnel ionization depends exponentially on the ionization potential. As a result, the stronger bound excited ionic channels become increasingly irrelevant. Addition of only the $A^2\Pi_u$ and $B^2\Sigma_u^+$ channels leads to relevant changes in the rates and energy shifts.

A comparison of rates from MO-ADK is also provided in figure 3. As in the case of atoms, the ADK theory over-estimates the rates at high field strengths. Also, since MO-ADK is a single electron theory, it cannot describe the multi-electron effects included in the `haCC` approach.

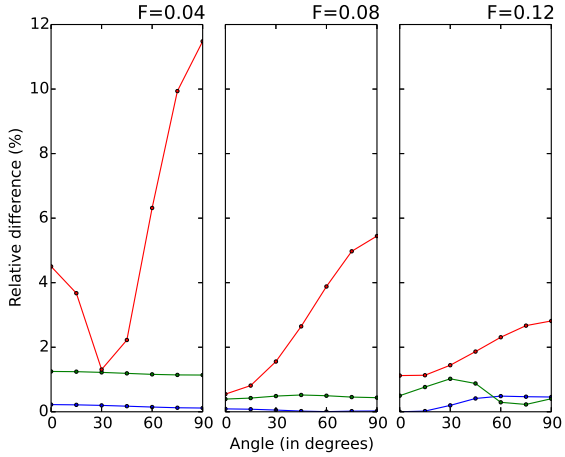

Figure 2. Convergence of angle dependent ionization rates of N_2 with respect to one-electron basis at selected field strengths within haCC(1) scheme. Reference computation: Gaussian basis- m-aug-cc-pvtz, $l_{max} = 9$, $R_0 = 25$ a.u.; Blue: Gaussian basis- m-aug-cc-pvtz, $l_{max} = 12$, $R_0 = 25$ a.u.; Green: Gaussian basis- m-aug-cc-pvtz, $l_{max} = 9$, $R_0 = 35$ a.u.; Red, Gaussian basis- m-aug-cc-pvqz, $l_{max} = 9$, $R_0 = 25$ a.u. The relative differences in percentage are computed as $\frac{\Gamma(F)-\Gamma_{ref}(F)}{\Gamma_{ref}(F)} \times 100$.

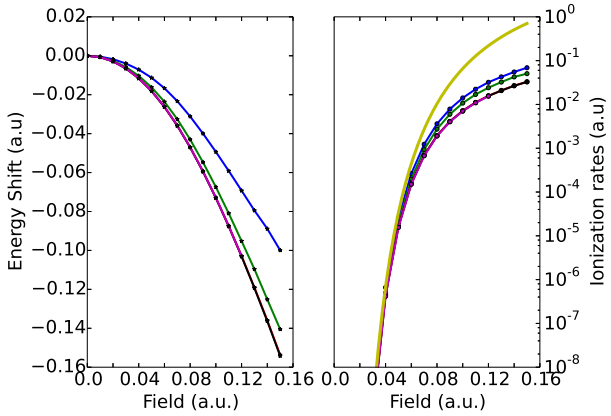

Figure 3. Ionization rates and the neutral energy shifts as a function of field strength (F in a.u) for N_2 molecule. The energy shift is defined as $E_{neut}(F) - E_{neut}(0)$. Color codes - Blue: haCC(1). Green: haCC(3). Red: haCC(4). Black: haCC(5). Magenta: haCC(7) The results from haCC(4), haCC(5) and haCC(7) nearly overlap. The yellow curve in the right panel gives ionization rates from the MO-ADK theory.

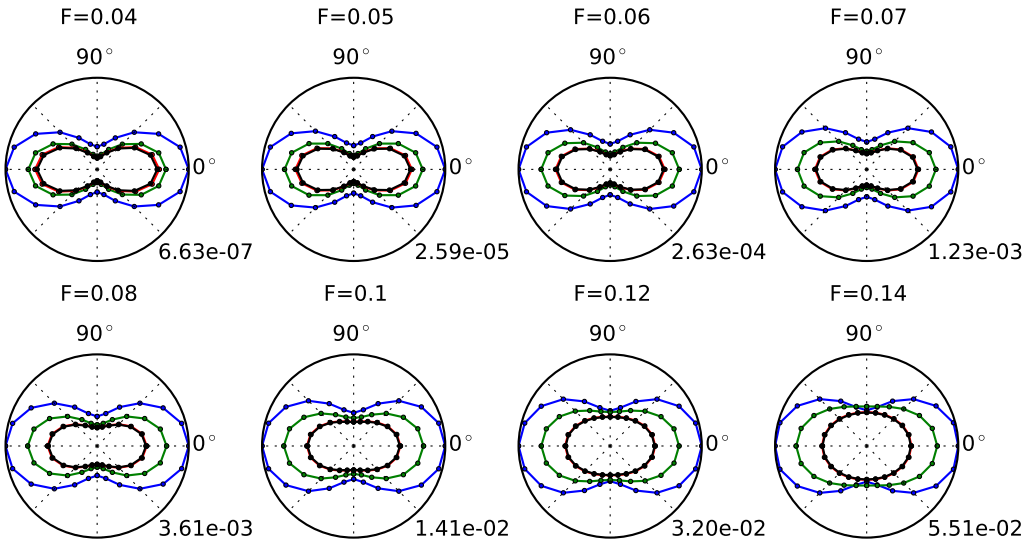

Figure 4. Angle dependent ionization rates of N_2 with different number of ionic channels included at various field strengths (F) in atomic units. The angle is defined with respect to the molecular axis. Blue: haCC(1). Green: haCC(3). Red: haCC(4). Black: haCC(5).

Finally, figure 4 presents angle dependent ionization rates obtained from haCC(1) to haCC(5) schemes at selected field strengths. The influence of adding the $D^2\Pi_g$ channel was also verified at selected points and it changes the rates by less than 2% with respect to the haCC(5) scheme. We find that the dependence of rates on the number of ionic channels at all orientations follows a similar pattern as for parallel orientation.

At low field strengths, the qualitative emission profile obtained from different haCC schemes is the same. At high field strengths, the qualitative behavior also changes: possibly due to contributions from ionization of inner lying orbitals. When ionization from inner orbitals that have different spatial profiles becomes significant, the overall ionization profile changes. This fact can only be established by calculating partial ionization rates corresponding to each channel. Such a channel analysis is not trivial in the current setup due to non-orthogonality and will be a topic of future time dependent studies, where an asymptotic channels analysis is possible.

A table of the angle dependent rates from the haCC(5) scheme is given in the appendix.

5.2. CO molecule

We use haCC(1) to haCC(7) schemes for our CO calculations. Table 5 lists the vertical binding energies of various ionic states used for our haCC calculations and compare them with literature values. Again here, the first ionization potential from different haCC schemes vary on the level of 10^{-3} a.u. Following the same lines of reasoning as for N_2, these discrepancies are acceptable.

Figure 5 shows angle dependent ionization rates from different haCC schemes. The angle is defined as 0° when the field points from the O atom to the C atom. The

State	m-aug-cc-pvtz	Baltzer *et al.* [36]	Svensson *et al.* [35]
$X^2\Sigma^+$	13.97	14.0	14.01
$A^2\Pi$	17.35	17.0	17.0
$B^2\Sigma^+$	19.9	19.8	19.7
$D^2\Pi_u$	24.79	-	22.7
$3^2\Sigma^+$	25.25	24.2	23.7

Table 5. Vertical energies (in eV) of ionic states used here, with respect to the neutral. The primitive basis sets used are minimally augmented correlation consistent triple zeta basis. A comparison with earlier works is given.

single electron parameters used are converged to below 10 %. We find that the first four bound states are sufficient for convergence within the `haCC` scheme. The addition of excited ionic states reduces the ionization rates in general due to an improved description of molecular polarizability. The influence of adding the $3^2\Sigma^+$ channel was also studied at selected points and it changes the rates by less than 2% with respect to the `haCC`(6) scheme. A table of static field ionization rates from `haCC`(6) scheme is given in the appendix.

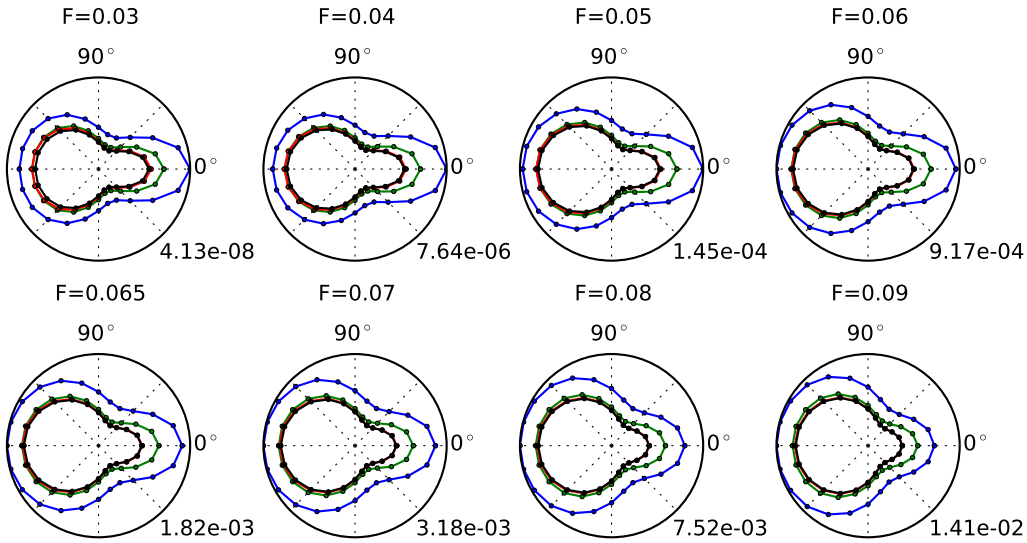

Figure 5. Angle dependent ionization rates of CO with different number of ionic channels included at various field strengths (F) in atomic units. The angle is defined with respect to the molecular axis. Blue: `haCC`(1). Green: `haCC`(3). Red: `haCC`(4). Black: `haCC`(6). The angle is 0° when the field points from O atom to C atom.

A plot giving the asymmetry parameter for ionization rates defined as $(\Gamma_{0^\circ} - \Gamma_{180^\circ})/(\Gamma_{0^\circ} + \Gamma_{180^\circ})$, where Γ_θ is the rate at angle θ, is shown in figure 6. The asymmetry parameter has a near linear dependence on the intensity. At all the field strengths considered, maximum emission occurs when the field point from C to O which means the preferred emission end is toward the C atom. This is consistent with the experimental findings [22, 23].

The results from `haCC`(1) however show that there is a transition at around

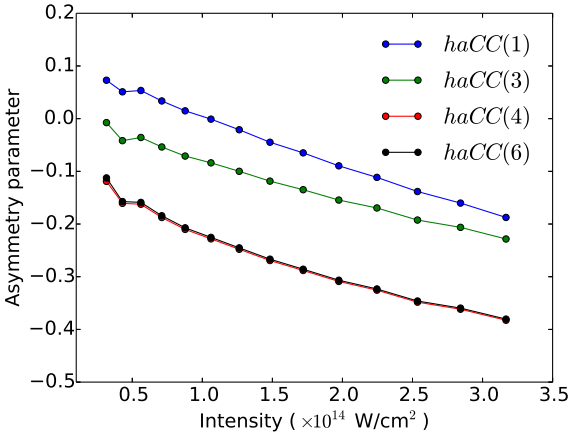

Figure 6. Asymmetry parameter as a function of intensity ($I \propto F^2$) for CO obtained with different `haCC` schemes. Role of polarization in CO: the `haCC`(1) scheme even predicts an incorrect maximum emission direction below an intensity of $10^{14} W/cm^2$.

$1.0 \times 10^{14} W/cm^2$ intensity where the maximum emission direction swaps, but the converged `haCC`(6) results show that the preferred direction of emission is always the C end in the considered range of field strengths. This shows that accurate description of the strong field ionization of CO needs to include the response of inner electrons, introduced here through a multi-channel approach. This re-emphasizes the earlier finding from a time dependent Hartree-Fock approach [24] which revealed the importance of polarization in strong field ionization of CO. The current approach provides an alternate perspective. The qualitative failure of the single channel ansatz which is equivalent to a single electron model shows that simple single electron pictures can lead to artifacts in the case of CO and indicates the reason for different predictions from different simple models [25].

The rates computed so far can be used to compute ionization yields for a given time varying field under quasistatic approximation as:

$$Y = 1 - \exp\left(-\int dt\, \Gamma(F(t))\right) \tag{5}$$

where Y is the yield and $F(t)$ is the time varying field. Using $\cos^2$ envelope pulses, we compute the asymmetry parameter for yields defined as $((Y_0 - Y_{180})/(Y_0 - Y_{180}))$ at the experimental parameters in [22]. We obtain a value of -0.25±0.02 for the asymmetry parameter from our `haCC`(6) method which is in close agreement with the experimentally obtained value of -0.30 [22]. The 0.02 uncertainty corresponds to the 10 fs uncertainty in the pulse duration in the experiment.

5.3. Implications for other molecules

Apart from the accurate static field ionization rates, the key result from the above sub-sections is that the polarization in the prototype systems N_2 and CO can be described using a few channel ansatz. We find that only those channels whose

ionization potentials lie in the range $[I_p, I_p + 5eV]$ have a relevant impact on the tunnel ionization. Here, I_p indicates the first ionization potential.

Several small molecules of experimental interest like CO_2 [37], NO [38], hydrocarbons [39] - C_2H_2 and C_2H_4 exhibit similar ionic spectrum, that is, they too have about 5∼6 ionic channels in the range $[I_p, I_p + 5eV]$. Using the empirical evidence from the systems studied here, it is possible to conclude that a similar few channel ansatz can be used to accurately model static field ionization of other small molecules. As an extension, it should be also possible to study strong field ionization in time varying fields with similar number of ionic channels.

These conclusions, however, cannot be trivially extended to large molecules where additional parameters become important: for example, the complex spatial dependence of the potential and localization of electronic states on a few atomic sites placing the wavefunction far-away or in the vicinity of the tunnel barrier, thereby suppressing or enhancing tunneling probability.

6. Conclusions

We presented here static field ionization rates for experimentally relevant multi-electron systems computed for the first time using a multi-channel approach and demonstrated the capabilities of our recently developed hybrid anti-symmetrized coupled channels approach. The main advantage of the current method is the possibility to perform a systematic convergence study in terms of ionic bound state channels.

The benchmarking results for two electron systems showed that the `haCC` scheme is capable of providing rates accurate on the level of 5-10%. Typical molecular systems have closely spaced ionic states and this leads to a greater ionic polarizability. Hence strong field ionization of these systems cannot be described by simple single electron or single channel approaches. This is demonstrated through the examples of N_2 and CO molecules where several excited ionic channels were required for convergence of ionization rates. The results for CO molecule are also consistent with the experimental measurements, a system for which several single electron approaches even qualitatively fail. ADK theory is known to over-estimate rates at high field strengths. We re-confirmed this fact by comparing the ADK results with our numerical results. Finally, we also provide in the appendix, tables of angle dependent ionization rates for N_2 and CO molecules that can be used for future benchmarking studies or experimental analysis of strong field ionization based experiments.

The `haCC` method, in its current implementation is capable of handling linear molecules beyond diatomics. Extensions to non-linear molecules would need implementation of a larger scale parallelization which will be a topic of future work. Benchmarking future simpler models/schemes against `haCC` for small molecules would help in finding suitable approximations to treat even larger systems that are not accessible to the current method.

Acknowledgements

The authors acknowledge financial support from the EU Marie Curie ITN CORINF, the German excellence initiative - Munich Advanced Photonics and by the Austrian Research Fund (ViCoM, F41).

References

[1] Smirnova O, Mairesse Y, Patchkovskii S, Dudovich N, Villeneuve D, Corkum P and Ivanov M Y 2009 *Nature* **460** 972–977 ISSN 0028-0836 URL http://dx.doi.org/10.1038/nature08253

[2] Xu J, Blaga C I, Zhang K, Lai Y H, Lin C D, Miller T A, Agostini P and DiMauro L F 2014 *Nat Commun* **5** – URL http://dx.doi.org/10.1038/ncomms5635

[3] Lewenstein M, Balcou P, Ivanov M Y, L'Huillier A and Corkum P B 1994 *Phys. Rev. A* **49**(3) 2117–2132 URL http://link.aps.org/doi/10.1103/PhysRevA.49.2117

[4] Le A T, Lucchese R R, Tonzani S, Morishita T and Lin C D 2009 *Phys. Rev. A* **80**(1) 013401 URL http://link.aps.org/doi/10.1103/PhysRevA.80.013401

[5] Smirnov B M and Chibisov M I 1966 *Sov. Phys. JETP* **22** 585

[6] Perelomov A M, Popov V S and Terentev M V 1966 *Sov. Phys. JETP* **23** 924

[7] Ammosov M, Delone N and Krainov V 1986 *Sov. Phys. JETP* 1191

[8] Tong X M, Zhao Z X and Lin C D 2002 *Phys. Rev. A* **66**(3) 033402 URL http://link.aps.org/doi/10.1103/PhysRevA.66.033402

[9] Tong X M and Lin C D 2005 *Journal of Physics B: Atomic, Molecular and Optical Physics* **38** 2593 URL http://stacks.iop.org/0953-4075/38/i=15/a=001

[10] Scrinzi A 2000 *Phys. Rev. A* **61**(4) 041402 URL http://link.aps.org/doi/10.1103/PhysRevA.61.041402

[11] Parker J S, Armstrong G S J, Boca M and Taylor K T 2009 *Journal of Physics B: Atomic, Molecular and Optical Physics* **42** 134011 URL http://stacks.iop.org/0953-4075/42/i=13/a=134011

[12] Batishchev P A, Tolstikhin O I and Morishita T 2010 *Phys. Rev. A* **82**(2) 023416 URL http://link.aps.org/doi/10.1103/PhysRevA.82.023416

[13] Fabrikant I I and Zhao L B 2015 *Phys. Rev. A* **91**(5) 053412 URL http://link.aps.org/doi/10.1103/PhysRevA.91.053412

[14] Pavičić D, Lee K F, Rayner D M, Corkum P B and Villeneuve D M 2007 *Phys. Rev. Lett.* **98**(24) 243001 URL http://link.aps.org/doi/10.1103/PhysRevLett.98.243001

[15] Majety V P and Scrinzi A 2015 *Phys. Rev. Lett.* **115**(10) 103002 URL http://link.aps.org/doi/10.1103/PhysRevLett.115.103002

[16] Smits M, de Lange C A, Stolow A and Rayner D M 2004 *Phys. Rev. Lett.* **93**(21) 213003 URL http://link.aps.org/doi/10.1103/PhysRevLett.93.213003

[17] Scrinzi A, Geissler M and Brabec T 1999 *Phys. Rev. Lett.* **83**(4) 706–709 URL http://link.aps.org/doi/10.1103/PhysRevLett.83.706

[18] Saenz A 2000 *Phys. Rev. A* **61**(5) 051402 URL http://link.aps.org/doi/10.1103/PhysRevA.61.051402

[19] Milošević M Z and Simonović N S 2015 *Phys. Rev. A* **91**(2) 023424 URL http://link.aps.org/doi/10.1103/PhysRevA.91.023424

[20] Tolstikhin O I, Madsen L B and Morishita T 2014 *Phys. Rev. A* **89**(1) 013421 URL http://link.aps.org/doi/10.1103/PhysRevA.89.013421

[21] Majety V P, Zielinski A and Scrinzi A 2015 *New Journal of Physics* **17** 063002– ISSN 1367-2630 URL http://stacks.iop.org/1367-2630/17/i=6/a=063002

[22] Li H, Ray D, De S, Znakovskaya I, Cao W, Laurent G, Wang Z, Kling M F, Le A T and Cocke C L 2011 *Phys. Rev. A* **84**(4) 043429 URL http://link.aps.org/doi/10.1103/PhysRevA.84.043429

[23] Wu J, Schmidt L P H, Kunitski M, Meckel M, Voss S, Sann H, Kim H, Jahnke T, Czasch A and Dörner R 2012 *Phys. Rev. Lett.* **108**(18) 183001 URL http://link.aps.org/doi/10.1103/PhysRevLett.108.183001

[24] Zhang B, Yuan J and Zhao Z 2013 *Phys. Rev. Lett.* **111**(16) 163001 URL http://link.aps.org/doi/10.1103/PhysRevLett.111.163001

[25] Śpiewanowski M D and Madsen L B 2015 *Phys. Rev. A* **91**(4) 043406 URL http://link.aps.org/doi/10.1103/PhysRevA.91.043406

[26] Lischka H, Müller T, Szalay P G, Shavitt I, Pitzer R M and Shepard R 2011 *WIREs Comput Mol Sci* **1** 191–199 ISSN 1759-0884 URL http://dx.doi.org/10.1002/wcms.25

[27] Zhao S F, Jin C, Le A T, Jiang T F and Lin C D 2009 *Phys. Rev. A* **80**(5) 051402 URL http://link.aps.org/doi/10.1103/PhysRevA.80.051402

[28] Scrinzi A 2010 *Phys. Rev. A* **81**(5) 053845 URL http://link.aps.org/doi/10.1103/PhysRevA.81.053845

[29] Simon B 1979 *Phys. Lett. A* **71** 211–214

[30] Reinhardt W P 1982 *Annual Review of Physical Chemistry* **33** 223–255 (*Preprint* http://dx.doi.org/10.1146/annurev.pc.33.100182.001255) URL http://dx.doi.org/10.1146/

annurev.pc.33.100182.001255

[31] Lehoucq R, Sorensen D and Yang C 1998 *ARPACK Users' Guide* (Society for Industrial and Applied Mathematics) URL http://dx.doi.org/10.1137/1.9780898719628

[32] Themelis S I, Mercouris T and Nicolaides C A 1999 *Phys. Rev. A* **61**(2) 024101 URL http://link.aps.org/doi/10.1103/PhysRevA.61.024101

[33] Majety V P and Scrinzi A 2015 *Photonics* **2** 93–103 ISSN 2304-6732 URL http://www.mdpi.com/2304-6732/2/1/93

[34] Ferr A, Boguslavskiy A E, Dagan M, Blanchet V, Bruner B D, Burgy F, Camper A, Descamps D, Fabre B, Fedorov N, Gaudin J, Geoffroy G, Mikosch J, Patchkovskii S, Petit S, Ruchon T, Soifer H, Staedter D, Wilkinson I, Stolow A, Dudovich N and Mairesse Y 2015 *Nat Commun* **6** – URL http://dx.doi.org/10.1038/ncomms6952

[35] Svensson S, Carlsson-Gthe M, Karlsson L, Nilsson A, Mrtensson N and Gelius U 1991 *Physica Scripta* **44** 184– ISSN 1402-4896 URL http://stacks.iop.org/1402-4896/44/i=2/a=012

[36] Baltzer P, Lundqvist M, Wannberg B, Karlsson L, Larsson M, Hayes M A, West J B, Siggel M R F, Parr A C and Dehmer J L 1994 *Journal of Physics B: Atomic, Molecular and Optical Physics* **27** 4915– ISSN 0953-4075 URL http://stacks.iop.org/0953-4075/27/i=20/a=011

[37] Ehara M and Nakatsuji H 1999 *Spectrochimica Acta Part A: Molecular and Biomolecular Spectroscopy* **55** 487–493 ISSN 1386-1425 URL http://www.sciencedirect.com/science/article/pii/S1386142598002571

[38] Albritton D L, Schmeltekopf A L and Zare R N 1979 *The Journal of Chemical Physics* **71** 3271–3279 URL http://scitation.aip.org/content/aip/journal/jcp/71/8/10.1063/1.438757

[39] Bieri G and sbrink L 1980 *Journal of Electron Spectroscopy and Related Phenomena* **20** 149–167 ISSN 0368-2048 URL http://www.sciencedirect.com/science/article/pii/0368204880850134

Appendix A. Tables of static field ionization rates for N_2 and CO.

Field Strength (a.u)	Angle between the molecular axis and the field vector						
	0°	15°	30°	45°	60°	75°	90°
0.02	$< 10^{-12}$	$< 10^{-12}$	$< 10^{-12}$	$< 10^{-12}$	$< 10^{-12}$	$< 10^{-12}$	$< 10^{-12}$
0.03	7.80×10^{-10}	7.13×10^{-10}	5.51×10^{-10}	3.71×10^{-10}	2.34×10^{-10}	1.57×10^{-10}	1.34×10^{-10}
0.04	4.35×10^{-7}	3.99×10^{-7}	3.11×10^{-7}	2.13×10^{-7}	1.38×10^{-7}	9.52×10^{-8}	8.20×10^{-8}
0.05	1.61×10^{-5}	1.48×10^{-5}	1.17×10^{-5}	8.17×10^{-6}	5.46×10^{-6}	3.92×10^{-6}	3.44×10^{-6}
0.06	1.54×10^{-4}	1.42×10^{-4}	1.14×10^{-4}	8.24×10^{-5}	5.76×10^{-5}	4.34×10^{-5}	3.89×10^{-5}
0.07	6.84×10^{-4}	6.37×10^{-4}	5.23×10^{-4}	3.93×10^{-4}	2.89×10^{-4}	2.29×10^{-4}	2.10×10^{-4}
0.08	1.92×10^{-3}	1.81×10^{-3}	1.52×10^{-3}	1.19×10^{-3}	9.25×10^{-4}	7.69×10^{-4}	7.19×10^{-4}
0.09	4.06×10^{-3}	3.84×10^{-3}	3.31×10^{-3}	2.69×10^{-3}	2.20×10^{-3}	1.90×10^{-3}	1.81×10^{-3}
0.1	7.10×10^{-3}	6.77×10^{-3}	5.97×10^{-3}	5.04×10^{-3}	4.29×10^{-3}	3.83×10^{-3}	3.68×10^{-3}
0.11	1.10×10^{-2}	1.06×10^{-2}	9.49×10^{-3}	8.27×10^{-3}	7.27×10^{-3}	6.65×10^{-3}	6.44×10^{-3}
0.12	1.56×10^{-2}	1.51×10^{-2}	1.38×10^{-2}	1.24×10^{-2}	1.12×10^{-2}	1.04×10^{-2}	1.01×10^{-2}
0.13	2.07×10^{-2}	2.01×10^{-2}	1.88×10^{-2}	1.72×10^{-2}	1.60×10^{-2}	1.52×10^{-2}	1.49×10^{-2}
0.14	2.66×10^{-2}	2.60×10^{-2}	2.46×10^{-2}	2.29×10^{-2}	2.15×10^{-2}	2.05×10^{-2}	2.01×10^{-2}

Table A1. Angle dependent static field ionization rates for N_2 at equilibrium inter-nuclear distance with `haCC`(5) scheme.

Field Strength	Angle between the molecular axis and the field vector						
(a.u)	0°	15°	30°	45°	60°	75°	90°
0.020	$< 10^{-12}$	$< 10^{-12}$	$< 10^{-12}$	$< 10^{-12}$	$< 10^{-12}$	$< 10^{-12}$	$< 10^{-12}$
0.025	3.16×10^{-10}	2.81×10^{-10}	2.05×10^{-10}	1.38×10^{-10}	1.00×10^{-10}	8.71×10^{-11}	8.88×10^{-11}
0.030	2.28×10^{-8}	2.06×10^{-8}	1.57×10^{-8}	1.14×10^{-8}	9.39×10^{-9}	9.74×10^{-9}	1.21×10^{-8}
0.035	4.63×10^{-7}	4.19×10^{-7}	3.21×10^{-7}	2.33×10^{-7}	1.91×10^{-7}	1.98×10^{-7}	2.44×10^{-7}
0.040	4.14×10^{-6}	3.75×10^{-6}	2.91×10^{-6}	2.15×10^{-6}	1.79×10^{-6}	1.88×10^{-6}	2.32×10^{-6}
0.045	2.15×10^{-5}	1.96×10^{-5}	1.53×10^{-5}	1.14×10^{-5}	9.59×10^{-6}	1.02×10^{-5}	1.28×10^{-5}
0.050	7.67×10^{-5}	7.00×10^{-5}	5.49×10^{-5}	4.14×10^{-5}	3.55×10^{-5}	3.82×10^{-5}	4.81×10^{-5}
0.055	2.07×10^{-4}	1.89×10^{-4}	1.50×10^{-4}	1.14×10^{-4}	1.00×10^{-4}	1.09×10^{-4}	1.38×10^{-4}
0.060	4.55×10^{-4}	4.18×10^{-4}	3.34×10^{-4}	2.59×10^{-4}	2.30×10^{-4}	2.55×10^{-4}	3.24×10^{-4}
0.065	8.57×10^{-4}	7.90×10^{-4}	6.37×10^{-4}	5.03×10^{-4}	4.56×10^{-4}	5.12×10^{-4}	6.53×10^{-4}
0.070	1.43×10^{-3}	1.32×10^{-3}	1.08×10^{-3}	8.64×10^{-4}	8.01×10^{-4}	9.14×10^{-4}	1.17×10^{-3}
0.075	2.17×10^{-3}	2.01×10^{-3}	1.66×10^{-3}	1.36×10^{-3}	1.29×10^{-3}	1.49×10^{-3}	1.90×10^{-3}
0.080	3.08×10^{-3}	2.87×10^{-3}	2.39×10^{-3}	1.99×10^{-3}	1.93×10^{-3}	2.26×10^{-3}	2.89×10^{-3}
0.085	4.09×10^{-3}	3.83×10^{-3}	3.24×10^{-3}	2.77×10^{-3}	2.74×10^{-3}	3.22×10^{-3}	4.13×10^{-3}
0.090	5.26×10^{-3}	4.94×10^{-3}	4.25×10^{-3}	3.67×10^{-3}	3.70×10^{-3}	4.42×10^{-3}	5.64×10^{-3}
	105°	120°	135°	150°	165°	180°	
0.020	$< 10^{-12}$	$< 10^{-12}$	$< 10^{-12}$	$< 10^{-12}$	$< 10^{-12}$	$< 10^{-12}$	
0.025	9.71×10^{-11}	1.06×10^{-10}	1.13×10^{-10}	1.17×10^{-10}	1.19×10^{-10}	1.19×10^{-10}	
0.030	1.59×10^{-8}	2.03×10^{-8}	2.41×10^{-8}	2.68×10^{-8}	2.82×10^{-8}	2.86×10^{-8}	
0.035	3.20×10^{-7}	4.10×10^{-7}	4.99×10^{-7}	5.72×10^{-7}	6.20×10^{-7}	6.37×10^{-7}	
0.040	3.02×10^{-6}	3.81×10^{-6}	4.57×10^{-6}	5.18×10^{-6}	5.57×10^{-6}	5.70×10^{-6}	
0.045	1.67×10^{-5}	2.11×10^{-5}	2.53×10^{-5}	2.86×10^{-5}	3.06×10^{-5}	3.13×10^{-5}	
0.050	6.26×10^{-5}	7.89×10^{-5}	9.42×10^{-5}	1.06×10^{-4}	1.14×10^{-4}	1.17×10^{-4}	
0.055	1.80×10^{-4}	2.25×10^{-4}	2.67×10^{-4}	3.00×10^{-4}	3.20×10^{-4}	3.27×10^{-4}	
0.060	4.21×10^{-4}	5.26×10^{-4}	6.19×10^{-4}	6.91×10^{-4}	7.36×10^{-4}	7.51×10^{-4}	
0.065	8.44×10^{-4}	1.05×10^{-3}	1.23×10^{-3}	1.37×10^{-3}	1.45×10^{-3}	1.48×10^{-3}	
0.070	1.50×10^{-3}	1.85×10^{-3}	2.15×10^{-3}	2.38×10^{-3}	2.53×10^{-3}	2.58×10^{-3}	
0.075	2.44×10^{-3}	2.98×10^{-3}	3.44×10^{-3}	3.79×10^{-3}	4.01×10^{-3}	4.09×10^{-3}	
0.080	3.67×10^{-3}	4.46×10^{-3}	5.13×10^{-3}	5.62×10^{-3}	5.92×10^{-3}	6.02×10^{-3}	
0.085	5.23×10^{-3}	6.29×10^{-3}	7.18×10^{-3}	7.87×10^{-3}	8.29×10^{-3}	8.43×10^{-3}	
0.090	7.08×10^{-3}	8.49×10^{-3}	9.65×10^{-3}	1.05×10^{-2}	1.10×10^{-2}	1.12×10^{-2}	

Table A2. Angle dependent static field ionization rates for CO at equilibrium inter-nuclear distance with `haCC`(6) scheme.

Dynamic Exchange in the Strong Field Ionization of Molecules

Vinay Pramod Majety* and Armin Scrinzi†
Physics Department, Ludwig Maximilians Universität, D-80333 Munich, Germany
(Received 15 May 2015; published 1 September 2015)

We show that dynamic exchange is a dominant effect in strong field ionization of molecules. In CO_2 it fixes the peak ionization yield at the experimentally observed angle of 45° between polarization direction and the molecular axis. For O_2 it changes the angle of peak emission and for N_2 the alignment dependence of yields is modified by up to a factor of 2. The effect appears on the Hartree-Fock level as well as in full *ab initio* solutions of the Schrödinger equation.

DOI: 10.1103/PhysRevLett.115.103002 PACS numbers: 33.80.Eh, 31.15.ac, 33.80.Rv

Experimental techniques like molecular orbital tomography [1,2], laser-driven electron diffraction [3,4], and high harmonic imaging [5] are based on the control of ionization by the strong field of a laser. They share the concept that an electron is emitted by a strong laser field and redirected by the same field to its parent system, where it produces a snapshot of the system's time evolution in the angle-resolved electron momentum or harmonic spectra. The analysis of these experiments relies on the idea that the steps of initial electron emission, propagation, and scattering of the returning electron can be considered as largely independent. Adequate understanding of each of these three steps is a prerequisite for proper use of the techniques.

In this Letter we deal with the ionization step. With atoms, there are several models that deliver correct ionization yields at infrared (IR) wavelength. In contrast, for molecules a disquieting discrepancy between theoretical predictions and experiment appeared: two independent experiments at two different intensities [6,7] reported maximal ionization of CO_2 when the molecular axis was aligned at 45° to the polarization direction of a linearly polarized pulse. In contrast, most theoretical calculations found angles in the range 30°–40°.

It is usually assumed that ionization at IR wavelength is a tunneling process and yields can be obtained as the integral over the tunneling rates computed at the instantaneous field strengths. As the field ionization rates drop exponentially with the ionization potential, one expects that the highest occupied molecular orbital (HOMO) in a molecule determines ionization. In particular, the angle dependence of the ionization rate should reflect the electron density distribution of the HOMO. Combining this idea with the Ammosov-Delone-Krainov (ADK) [8] formula for tunneling from effective single-electron systems, the molecular ADK (MO-ADK) approach was formulated [9]. In more complicated molecular systems with energetically closely spaced ionic states this approach may become invalid [5,10]: at the nodal directions of the HOMO, where MO-ADK would show nearly no ionization, the energetically next lower orbital HOMO-1 could contribute. On this level of theory, the discrepancy with experiments [6,7] could not be removed.

A large number of models and computations have been tried to clarify the point. Density functional theory (DFT) calculations indicated that energetically lower molecular orbitals cannot account for the experimental observation [11]. A time-dependent DFT calculation [12] predicts peak yield at 40°. A single electron model with a frozen core potential produced the experimental value of 45° [13]. A coupled channels calculation partially including multielectron effects [14] showed that a single channel picture leads to peak angles ∼30° and it was conjectured that interchannel couplings could explain the experimental observation. A recent time-dependent configuration-interaction (TDCI) calculation using a Gaussian basis expansion [15] in turn reports a peak angle of 50°. Other efforts using the semiclassical WKB approximation [16] and the strong field eikonal Volkov approximation [5] also fail to yield accurate predictions. Recently, it was shown that field distortion of the orbitals plays a role, but the predicted angles of 36° to 39° [17] fall short of the experimental values. In spite of all efforts, the discrepancy remained unresolved.

In the discussion so far, little attention has been paid to exchange symmetry. Ideally, in DFT such effects would be fully included, but in practice this is hardly ever achieved due to limitations of the exchange-correlation potentials. The value of 45° obtained in Ref. [13] using a single electron potential supplemented with a DFT-based exchange correction was attributed to excited state dynamics rather than exchange. The fact that the result is not reproduced by pure DFT using different exchange correlation functionals [11,12] suggests that the agreement may be coincidental. The TDCI of Ref. [15] naturally includes exchange, but in turn the Gaussian expansion is known to have shortcomings in the description of strong-field effects.

In this Letter, we show that dynamic exchange occupies a central place in strong field ionization (SFI). Specifically, in CO_2 exchange forces lead to peak ionization at an alignment of 45°. Effects on the alignment dependence of O_2 and N_2 ionization are sizable but less conspicuous. By

 © 2015 American Physical Society

dynamic exchange we designate effects beyond the antisymmetry of initial and final states. Exchange had been considered for the initial states. In stationary first order perturbative transitions final state antisymmetry can be disregarded for symmetric transition operators. However, omitting antisymmetrization of the virtual states appearing during ionization turns out to constitute, somewhat counterintuitively, an important dynamical restriction. Qualitatively, this will be shown already on the Hartree-Fock level.

We compute SFI rates and solutions of the time-dependent Schrödinger equation (TDSE) by the *ab initio* hybrid antisymmetrized coupled channels (haCC) approach [18]. haCC uses a multielectron wave function in terms of several ionic states $|I\rangle$ that are fully antisymmetrized with a numerical single electron basis, $|i\rangle$. In addition, the neutral ground and excited states $|\mathcal{N}\rangle$ can be included, resulting in the wave function

$$|\Psi_A\rangle = \sum_{i,I} \mathcal{A}[|i\rangle|I\rangle]C_{i,I} + \sum_{\mathcal{N}} |\mathcal{N}\rangle C_{\mathcal{N}}, \qquad (1)$$

which we will refer to as ansatz A in the following. The $C_{i,I}, C_{\mathcal{N}}$ are the respective expansion coefficients and $\mathcal{A}$ indicates antisymmetrization. The $|I\rangle$ and $|\mathcal{N}\rangle$ states were obtained from the COLUMBUS quantum chemistry package [19]. For $|i\rangle$ we use a high-order finite element radial basis combined with single center spherical harmonics. A complete description of the method can be found in Ref. [18]. The ansatz accurately describes the single-electron asymptotic behavior, whose importance is discussed in Ref. [20]. Neutral and ionic states can be included to examine multielectron effects like field-free correlation, interchannel coupling and ionic core polarization.

Tunneling ionization rates are computed using exterior complex scaling [21–23]: the Hamiltonian is analytically continued by transforming the electron coordinates into the complex plane. For radii $r > R_0$ one uses $r_\theta = e^{i\theta}(r - R_0) + R_0$ with the complex scaling angle $\theta > 0$. The resulting Hamiltonian is non-Hermitian with a complex ground state eigenvalue $W = E_0 + E_s - (i/2)\Gamma$, where E_0 is the field-free ground state energy, E_s is its dc-Stark shift and $\Gamma/\hbar$ is the static field ionization rate. Apart from errors due to finite computational approximation, W is independent of $\theta > 0$ and $R_0 \geq 0$.

We treat the CO_2 molecule with nuclear positions fixed at the equilibrium C-O bond length of 116.3 pm. The multielectron states of neutral and ion are computed using COLUMBUS with the minimally augmented cc-pvtz basis at the multireference configuration interaction singles level. We used up to 6 ionic channels which include the doubly degenerate $X^2\Pi_g$, $A^2\Pi_u$, and the singly degenerate $B^2\Sigma_u^+$, $C^2\Sigma_g^+$ states. Single electron functions with up to 84 linear coefficients with finite element orders 12 on a radial box of 30 a.u. and up to 269 spherical harmonics ($L_{\max} = 12, M_{\max} = 12$) were used for the stationary problem. For solutions of the TDSE the number of spherical harmonics was increased up to 324. This numerical basis is complemented by the atom-centered Gaussians that constitute the neutral and ionic functions. For complex scaling, we chose R_0 values well outside the range of neutral and ionic orbitals, such that only the coordinate of the single-electron basis is continued to complex values. Basis and the scaling parameters R_0 and θ were varied to ensure that results are converged to better than 2%. The main approximation is introduced by the limited number of ionic channels. With 6 ionic channels, we obtain a first ionization potential of $I_p = 13.85$ eV (experimental value: 13.78 eV [24]), which decreases by about 0.14 eV with fewer ionic channels.

The central results are shown in Figs. 1, 2, and 6. In Fig. 1, one sees that the static field ionization rates peak at an alignment angle of 45°. Minima appear at 0° and 90° corresponding to the nodal planes of the CO_2 HOMO. These findings agree with experiments [6,7]. Multielectron effects reduce the ionization rates as the number of ionic channels grows: quadratic dc-Stark shifts increase as the basis becomes more flexible. This affects the neutral more strongly than the tightly bound ion and raises the effective ionization potential.

Figure 2 shows the angle of the peak rate as a function of intensity: except for the highest intensities, the angle varies by $\lesssim 2°$, depending on the number of ionic channels included. We cannot confirm any intensity dependence as was predicted in Ref. [16] based on analytic arguments. Dependence on the number of channels is strongest at the higher intensities $I \gtrsim 2.5 \times 10^{14}$ W/cm^2. There, the tunneling picture ceases to be applicable: according to a simple estimate [23] at intensities $I_b \approx I_p^2/4 = 1.5 \times 10^{14}$ W/cm^2 the molecular binding barrier of CO_2 is suppressed to

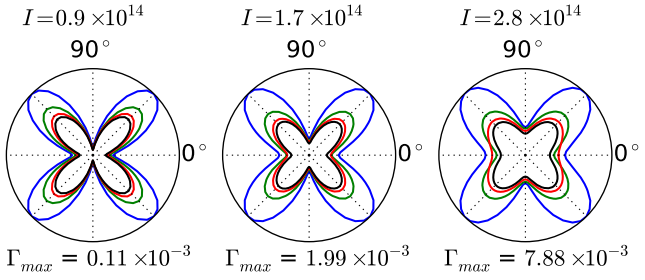

FIG. 1 (color online). Alignment angle dependent CO_2 ionization rates at selected intensities I (in W/cm^2). The convergence with the number of ionic channels indicates the role of multielectron effects. Blue: including only the neutral ground state and ionic $X^2\Pi_g$ ground states, green: as blue with the ionic $A^2\Pi_u$ channel added. Red: as green with $B^2\Sigma_u^+$ channel. Black: as red with $C^2\Sigma_g^+$ channel. Computations were performed for static fields of strengths $F = 0.05$, 0.07, and 0.09 a.u. corresponding to intensities $I = F^2/2$ that label the plots. $\Gamma_{\max}$ indicates maximal decay width in atomic units at the inclosing circle. A total of 6 ionic channels are used in the calculations.

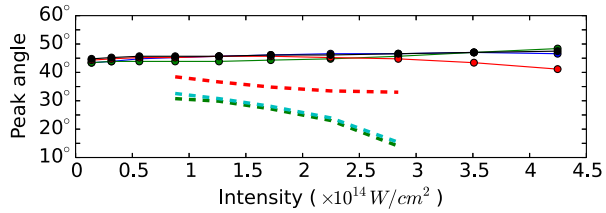

FIG. 2 (color online). Peak ionization angles as a function of intensity. Solid lines: results with the antisymmetrized ansatz A, Eq. (1). Dashed lines: results without antisymmetrization, ansatz B, Eq. (2). Colors correspond to different numbers of neutral states and ionic channels, see Fig. 1 (solid lines) and Fig. 4 (dashed lines).

below the field free ground state energy. In this regime, virtual continuum states for polarization of the ionic core may become important, which is not modeled by the haCC ansatz as used here and therefore no dependable statement about the accuracy of our results can be made.

The alignment dependence of ionization obtained in quasistatic approximation (QSA) by integrating the tunnel ionization rate is confirmed by solutions of the complete TDSE. In Fig. 3, normalized angle dependent yields obtained from TDSE and QSA within the single channel model are compared with experiments performed at near infrared ($\lambda \approx 800$ nm) wavelength. The angle dependence in TDSE is well approximated in QSA, with better agreement for higher intensities, where the QSA is more appropriate [23]. This agreement is gratifying, considering that in the intensity range $3 \times 10^{13} - 1.1 \times 10^{14}$ W/cm^2 with Keldysh parameters $\gamma = 2 \sim 1$, one can hardly expect ionization to be of pure tunneling type. A failure of the tunneling picture is exposed in the *magnitudes* of the yields, where the TDSE results exceed the QSA by a factor 2 at 1.1×10^{14} W/cm^2 and by nearly 2 orders of magnitude at 3×10^{13} W/cm^2. The fact that angle dependence

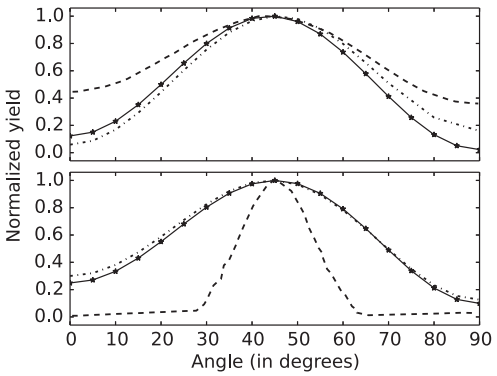

FIG. 3. Normalized angle dependent yields from TDSE (lines), QSA (dash-dotted lines) in the single channel picture, and experiments [6,7] (dashed lines). The laser parameters are 800 nm central wavelength, 40 fs duration with peak intensities of 3×10^{13} W/cm^2 (Upper panel) and 1.1×10^{14} W/cm^2 (lower panel).

largely agrees between time-dependent and quasistatic ($\lambda \to \infty$) results shows that wavelength effects are secondary compared to exchange. The peak angle is consistent with the experiments, but yields found in one of the experiments [6] are more narrowly confined around the maximum angle. It was noted in Ref. [20] that the experimental result may be artificially narrowed due to the deconvolution procedure.

The failure of earlier theory in reproducing the peak angle of 45° is due to the absence or insufficient inclusion of dynamical exchange. This is clearly seen by omitting from the haCC ansatz A the antisymmetrization of the single-electron basis against the multielectron states in an otherwise identical wave function, ansatz B:

$$|\Psi_B\rangle = \sum_{i,I} |i\rangle|I\rangle C_{i,I} + \sum_{\mathcal{N}} |\mathcal{N}\rangle C_{\mathcal{N}}, \qquad (2)$$

In Fig. 4 one sees that with ansatz B one obtains the peak rate at an angle around 30° at low intensities that then dips off as the intensity is increased; see also Fig. 2.

Our results without antisymmetrization for the dynamics are consistent with Ref. [14], where it was proposed that the remaining discrepancy to the experimental value was caused by neglecting coupling between $X^2\Pi_g$ and $A^2\Pi_u$ ionic channels in the calculation. In contrast, in Ref. [13], the angle near 45° was attributed to dynamics of excited neutral states, mostly the first excited neutral state. However, neither excited state dynamics nor coupling of ionic channels, in the absence of dynamical exchange, result in correct angles.

Figure 4 shows that the first excited state of the neutral has hardly any discernable role in determining the emission profile and does not influence the angle of peak emission. Coupling of channels as proposed in Ref. [14] does move the angle closer to experiment, but still does not yield the correct result. The improvement can be understood as, in the limit of a complete set of channels, ansatz A and B are

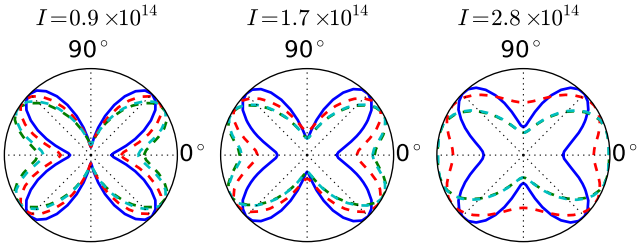

FIG. 4 (color online). The role of exchange in CO_2 ionization: alignment angle dependence of normalized static SFI rates in different single-channel models. Blue: antisymmetrized ansatz A with the neutral ground state and ionic $X^2\Pi_g$ ground state channels. Green: ansatz B with the same states as blue, red: as green, with the addition of the ionic $A^2\Pi_u$ state. Cyan: as green with the addition of the first excited neutral state. The green and cyan lines coincide at the two higher intensities.

equivalent. However, the primary role of the seemingly complicated multi-electron dynamics is to mimic dynamical exchange. In contrast, with dynamical exchange properly considered, a simple essentially single-electron picture of field ionization reemerges.

We demonstrate this by reducing the problem to the simplest possible case. We use the Hartree-Fock neutral state of CO_2 and the ion ground state in Koopman's approximation. Denoting by $\{\phi_1, \ldots, \phi_N\}$ the occupied Hartree-Fock orbitals of the neutral and by $\psi(t)$ the active electron, ansatz A and B are reduced to

$$|\Psi_A\rangle = \det(|\psi(t)\rangle|\phi_2\rangle \ldots |\phi_N\rangle)C_{11} + |\mathcal{N}\rangle C_{\mathcal{N}} \quad (3)$$

$$|\Psi_B\rangle = |\psi(t)\rangle \det(|\phi_2\rangle \ldots |\phi_N\rangle)C_{11} + |\mathcal{N}\rangle C_{\mathcal{N}}, \quad (4)$$

where det indicates the Slater determinant. The effective Hamiltonians governing the time evolution of $\psi(t)$ for the two cases differ only by the exchange term

$$(V_x\psi)(\vec{r}) = \sum_{k=2}^{N} \phi_k(\vec{r}) \int d^3r' \frac{\phi_k(\vec{r}')\psi(\vec{r}')}{|\vec{r} - \vec{r}'|}. \quad (5)$$

In Ref. [20] it was pointed out that the long-range interactions also affect emission. To exclude those, we smoothly truncate the Coulomb tail of the potential at 10 a.u. Figure 5 shows that also here exchange shifts the peak angle by $\sim 7°$.

Apart from the exchange term, ansatz A effectively enforces orthogonality of the active electron orbital against the ionic HF orbitals $\langle\psi|\phi_k\rangle = 0, k \geq 2$. If this were the dominant effect of antisymmetrization, one would expect that in the absence of the constraint (ansatz B) the ground state energy would be lowered. On the other hand, antisymmetrization effectively enlarges the ansatz space: it operates in the N-fold larger space containing all permutations of ψ through the $\phi_2 \ldots \phi_N$, but including explicitly only the dynamically accessible subspace of antisymmetrized linear combinations. Conversely, omitting antisymmetrization amounts to a restriction of the accessible space. By this reasoning, Stark-shift (polarization) should be larger in ansatz A. Indeed, we find the latter in our calculations. We also directly verified that an orthogonality constraint on $\psi(t)$ against the ϕ_k in ansatz B causes only $\lesssim 1\%$ of the overall difference between the results of A and B. This finally establishes that indeed the dynamical effects of exchange play the decisive role in ionization.

Dynamical exchange is most conspicuous in CO_2, but the mechanism as such is universal and must be included for obtaining correct ionization rates from any system. As further examples, we studied the effect on N_2 and O_2, which are standard model systems for strong field physics. Figure 6 shows normalized ionization rates at the respective equilibrium nuclear positions with a single channel in ansatz A and B. In N_2, dynamical exchange leads to a broadening of the ionization profile, where the ratio between the rates at 0° and 90° changes by up to a factor ~ 2. For O_2, dynamic exchange shifts the peak angle by 5° to 45° in agreement with the experimental value [6]. Without exchange, our result agrees with the MO-ADK findings and DFT [6,11]. This small discrepancy had not drawn much attention earlier.

In conclusion, we have established that dynamical exchange takes a central place in the ionization of molecules. The effects on CO_2 are striking, but also for O_2 the peak emission angle is affected and for N_2 results can change by up to a factor 2 merely due to exchange. This indicates that dynamical exchange must be considered in any attempt to understand strong field ionization also of more complex multielectron systems. Depending on the system's structure, effects can range from a minor correction to dramatic qualitative changes. Apart from the ionization yields discussed here, the angular distribution of electron emission at fixed alignment may be affected. A critical assessment of the importance of these distributions for rescattering-based attosecond experiments appears in place. On the other hand, simple antisymmetrization may enhance single-electron and single-channel models that have been applied so far, even without the comparatively heavy numerical apparatus used to establish the fact in the present Letter.

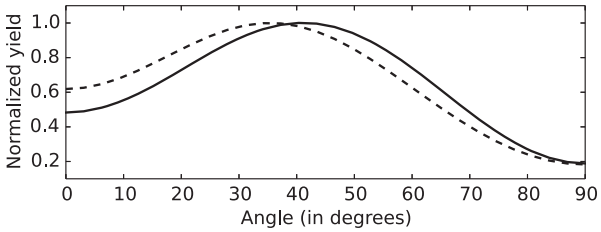

FIG. 5. Rate as a function of alignment, computed with the Hartree-Fock neutral ground state, ionic ground state in Koopman's approximation, and Coulomb potential truncated at 10 a.u. Solid line, with exchange, ansatz A, and dashed line, without dynamical exchange, ansatz B. Field strength = 0.06 a.u.

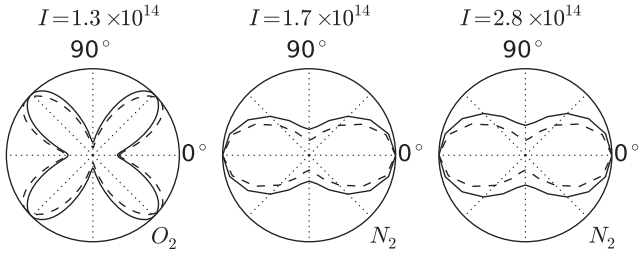

FIG. 6. Normalized ionization rates of O_2 (left panel) and N_2 (center and right) as a function of alignment angle, using only neutral and ionic ground states. Solid: with dynamic exchange, ansatz A, and dashed, without exchange, ansatz B.

The authors acknowledge financial support from the EU Marie Curie ITN CORINF, German excellence cluster-Munich Advanced Photonics, and by the Austrian Research Fund (ViCoM, F41).

*vinay.majety@physik.uni-muenchen.de
†armin.scrinzi@lmu.de

[1] J. Itatani, J. Levesque, D. Zeidler, H. Niikura, H. Pepin, J. C. Kieffer, P. B. Corkum, and D. M. Villeneuve, Nature (London) **432**, 867 (2004).
[2] P. Salières, A. Maquet, S. Haessler, J. Caillat, and R. Taïeb, Rep. Prog. Phys. **75**, 062401 (2012).
[3] M. Spanner, O. Smirnova, P. B. Corkum, and M. Y. Ivanov, J. Phys. B **37**, L243 (2004).
[4] J. Xu, C. I. Blaga, K. Zhang, Y. H. Lai, C. D. Lin, T. A. Miller, P. Agostini, and L. F. DiMauro, Nat. Commun. **5**, 4635 (2014).
[5] O. Smirnova, Y. Mairesse, S. Patchkovskii, N. Dudovich, D. Villeneuve, P. Corkum, and M. Y. Ivanov, Nature (London) **460**, 972 (2009).
[6] D. Pavičić, K. F. Lee, D. M. Rayner, P. B. Corkum, and D. M. Villeneuve, Phys. Rev. Lett. **98**, 243001 (2007).
[7] I. Thomann, R. Lock, V. Sharma, E. Gagnon, S. T. Pratt, H. C. Kapteyn, M. M. Murnane, and W. Li, J. Phys. Chem. A **112**, 9382 (2008).
[8] M. Ammosov, N. Delone, and V. Krainov, Sov. Phys. JETP **64**, 1191 (1986).
[9] X. M. Tong, Z. X. Zhao, and C. D. Lin, Phys. Rev. A **66**, 033402 (2002).
[10] A. Ferr *et al.*, Nat. Commun. **6**, 5952 (2015).
[11] S. Petretti, Y. V. Vanne, A. Saenz, A. Castro, and P. Decleva, Phys. Rev. Lett. **104**, 223001 (2010).
[12] S.-K. Son and Shih-I. Chu, Phys. Rev. A **80**, 011403 (2009).
[13] M. Abu-samha and L. B. Madsen, Phys. Rev. A **80**, 023401 (2009).
[14] M. Spanner and S. Patchkovskii, Phys. Rev. A **80**, 063411 (2009).
[15] P. Krause and H. B. Schlegel, J. Phys. Chem. Lett. **6**, 2140 (2015).
[16] R. Murray, M. Spanner, S. Patchkovskii, and M. Y. Ivanov, Phys. Rev. Lett. **106**, 173001 (2011).
[17] M. D. Śpiewanowski and L. B. Madsen, Phys. Rev. A **91**, 043406 (2015).
[18] V. P. Majety, A. Zielinski, and A. Scrinzi, New J. Phys. **17**, 063002 (2015).
[19] H. Lischka, T. Müller, P. G. Szalay, I. Shavitt, R. M. Pitzer, and R. Shepard, WIREs Comput. Mol. Sci. **1**, 191 (2011).
[20] S.-F. Zhao, C. Jin, A.-T. Le, T. F. Jiang, and C. D. Lin, Phys. Rev. A **80**, 051402 (2009).
[21] B. Simon, Phys. Lett. A **71**, 211 (1979).
[22] W. P. Reinhardt, Annu. Rev. Phys. Chem. **33**, 223 (1982).
[23] A. Scrinzi, M. Geissler, and T. Brabec, Phys. Rev. Lett. **83**, 706 (1999).
[24] M. Ehara and H. Nakatsuji, Spectrochim. Acta, Part A **55**, 487 (1999).

4

Conclusions and outlook

Conclusions

In this work, a new ab-initio method called the hybrid anti-symmetrized coupled channels method was developed and applied to study strong field single ionization of multi-electron atoms and molecules. The calculations helped resolve several discrepancies between theory and experiments.

Discretizing a multi-electron wavefunction using a coupled channels basis has several advantages: (i) The size of the discretization is independent of the number of electrons. (ii) It is engineer-able. Any pre-existing knowledge can be used to keep the basis compact. For example, correlated states that are known to play a role in the process can be included as neutral states in the basis. (iii) It can be used to systematically turn-on or off the multi-electron effects. For example, core polarization can be systematically improved by including excited ionic channels.

The important realization of the work is the new multi-electron Schrödinger equation solver itself that has many potential applications in the context of studying photo-ionization of multi-electron systems. Prior to this work, there existed a number of numerical approaches to study strong field ionization of one- and two-electron systems on the one hand and a number of elaborate quantum chemical techniques to obtain field-free electronic structure of atoms and molecules on the other. This works brings together a set of techniques in both the fields, thereby significantly advancing the theoretical capabilities that exist in the field of strong field physics. The overall method is composed of several key techniques: configuration interaction theory, finite element methods, infinite range exterior complex scaling technique, mixed gauge representations and the time dependent surface flux method.

The implementation of the method includes an interface to `COLUMBUS` quantum chemistry code that provides a great flexibility to the method in terms of choosing ionic and neutral states computed from various levels of quantum chemical theory. Notable issues that had to be tackled in the development of the method are linear dependency issues and computation of electron-electron integrals. The linear dependencies in the basis are handled by using a modified Woodbury formula for the inversion of the overlap matrix and

the two-electron integrals are computed using a multi-pole expansion.

An important off-shoot from the development of the haCC method is the development of the mixed gauge approach for solving the TDSE. The popular gauges - velocity and length gauges were found to be incompatible with the overall haCC scheme. Therefore, a mixed gauge that uses length gauge in the region encompassing the ionic states and a velocity gauge thereafter was developed. This proved to be a numerically very efficient solution. The general idea of mixed gauges can be used in other restricted basis set methods as well. It essentially involves identifying that particular representation of the wavefunction which can be most efficiently described by the basis of choice.

The important application of the haCC method studied here is the angle dependent strong field ionization of small molecules. For the first time, static field ionization rates for molecules were computed from a multi-electron method where a systematic convergence study is possible. The calculations revealed the importance of polarization and the importance of imposing the correct exchange symmetry during strong field ionization dynamics. They resolve the long standing discrepancies between theory and experiment in the angle dependent strong field ionization of molecules O_2, CO_2 and CO, thereby removing a hurdle in the long term goal of strong field ionization based ultrafast imaging of molecules.

Outlook

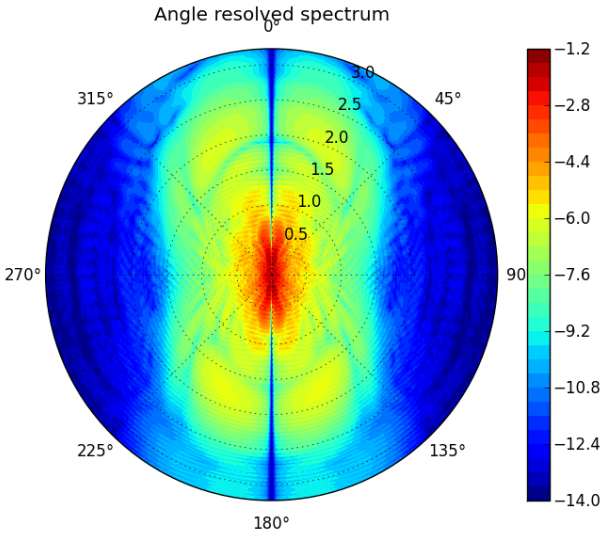

Figure 4.1: Angle resolved photo-electron spectra for CO_2 with ground state channel ansatz. The colorbar is scaled logarithmically. Pulse parameters: 3-cycle, $\cos^2$ envelope 800nm laser pulse with a peak intensity of 10^{14} W cm^{-2}.

Future applications: The haCC method, being a general TDSE solver, has many potential applications. Recently, the method was applied to study Fano resonances in Helium

atom, where it was shown that in the presence of external fields Fano resonances acquire a complex q parameter [88]. Other potential applications of the method include computation of fully differential photo-electron spectra and high harmonic spectra for small molecules.

Figure 4.1 shows angle resolved photo-electron spectra from CO_2 with a 3 cycle, 800nm laser pulse with a peak intensity of 10^{14} W cm^{-2}. This preliminary computation was done with the ground state channel ansatz. The spectra show that the nodal structure of the highest occupied molecular orbital is translated into the photo-electron spectra.

These spectra can be used to analyze re-collision imaging experiments or for several other topical problems in attosecond physics like time delays in photo-emission [18].

Possible structural extensions: A number of structural improvements to the method are possible. Two of the possible extensions are: (i) Using symmetry adapted spherical harmonics in the one-electron basis to increase the blocking of the Hamiltonian matrix for molecules with lower symmetry. (ii) The hybrid nature in the current basis comes from atom centered Gaussian orbitals and the single center expansion. This choice however is not sufficient when hard re-collisions during ionization become important. The spatial structure of the molecule imposed on the re-colliding continuum wavepacket cannot be easily described with Gaussians. For these problems, an addition of a small atom-centered numerical finite-element basis could be useful.

At present, the haCC method can be only applied to atoms and linear molecules and the computations presented here were run on standard 8 core machines. Implementation of the above features along with a large scale parallelization of the code would allow us to apply the current method to larger molecules and molecules with lesser symmetry.

Other possible extensions could be to include effects of nuclear motion in molecules which however is not a simple extension of the current formalism.

5

Technical appendices

5.1 Derivation of matrix elements

The haCC basis with the neutral bound states ($|\mathcal{N}\rangle$) and the single ionic channel functions ($\mathcal{A}[|I\rangle|\alpha\rangle]$) is expressed as:

$$|\Psi\rangle = \frac{1}{\sqrt{N}} \sum_{I,\alpha} \mathcal{A}[|I,\alpha\rangle] C_{I\alpha} + \sum_{\mathcal{N}} |\mathcal{N}\rangle C_{\mathcal{N}} \tag{5.1}$$

To avoid confusion, the single electron basis is represented using Greek letters: $|\alpha\rangle$ and $|\beta\rangle$ and the normalization factor is explicitly written. For the sake of simplicity, the ionic and neutral configuration interaction functions composed of Hartree Fock orbitals, $|\phi_k\rangle$ are denoted as:

$$|I\rangle = \frac{1}{\sqrt{(N-1)!}} \sum_{i_1 i_2 \cdots i_{N-1}} |\phi_{i_1}\phi_{i_2}\cdots\phi_{i_{N-1}}\rangle a_{i_1\cdots,i_{N-1}} := \frac{1}{\sqrt{(N-1)!}} \sum_{i_1\cdots i_{N-1}} |i_1\cdots i_{N-1}\rangle a_{i_1\cdots,i_{N-1}} \tag{5.2}$$

$$|\mathcal{N}\rangle = \frac{1}{\sqrt{N!}} \sum_{n_1\cdots n_N} |\phi_{n_1}\phi_{n_2}\cdots\phi_{n_N}\rangle d_{n_1\cdots n_N} := \frac{1}{\sqrt{N!}} \sum_{n_1\cdots n_N} |n_1\cdots n_N\rangle d_{n_1\cdots n_N} \tag{5.3}$$

with the coefficients $a_{i_1\cdots i_{N-1}}$ and $d_{i_1\cdots i_N}$ satisfying the required anti-symmetry property. The ionic channels functions

$$\mathcal{A}|I,\alpha\rangle = \sum_{i_1\cdots i_{N-1}} \mathcal{A}|i_1\cdots i_{N-1}\alpha\rangle a_{i_1\cdots i_{N-1}} \tag{5.4}$$

can be explicitly expanded as:

$$\mathcal{A}|i_1\cdots i_{N-1}\alpha\rangle = |i_1\cdots i_{N-1}\alpha\rangle + \cdots + (-1)^{N-k}|i_1\cdots i_{k-1}\alpha i_k\cdots i_{N-1}\rangle + \cdots \tag{5.5}$$

Introducing a convenient notation:

$$A_k = \sum_{i_1\cdots i_{N-1}} (-1)^{N-k}|i_1\cdots i_{k-1}\alpha i_k\cdots i_{N-1}\rangle a_{i_1\cdots i_{N-1}} \tag{5.6}$$

the channel function can be written as:

$$\mathcal{A}|I,\alpha\rangle = \sum_{k=1}^{N} A_k \tag{5.7}$$

where A_k denotes the term with α at the kth position.

The ionic and neutral states are orthonormal to each other, that is $\langle I|J\rangle = \delta_{IJ}$ and $\langle \mathcal{N}|\mathcal{N}'\rangle = \delta_{\mathcal{N}\mathcal{N}'}$. The Hartree-Fock orbitals are also orthonormal $\langle \phi_i|\phi_j\rangle = \delta_{ij}$. The anti-symmetrization satisfies the property $\mathcal{A}\mathcal{A} = N\mathcal{A}$.

Finally, the generalized reduced density matrices between two N-particle wavefunctions are defined as:

$$\rho^{IJ}_{i_1\cdots i_k j_1\cdots j_k} = \frac{N\,!}{(N-k)\,!} \sum_{i_{k+1}\cdots i_N} \sum_{j_{k+1}\cdots j_N} a^*_{i_1\cdots i_k i_{k+1}\cdots i_N} b_{j_1\cdots j_k j_{k+1}\cdots j_N} \tag{5.8}$$

and the non-standard generalized reduced density matrices between an N-particle function and an N-1 particle function as:

$$\eta^{\mathcal{N}J}_{i_{N-k}\cdots i_N j_{N-k}\cdots j_{N-1}} = \frac{\sqrt{N}(N-1)\,!}{(N-k)\,!} \sum_{i_1\cdots i_{N-k}\cdots i_N} \sum_{j_1\cdots j_{N-k}\cdots j_{N-1}} d^*_{i_1\cdots i_N} b_{j_1\cdots j_{N-1}} \tag{5.9}$$

5.1.1 Overlap

Between neutrals

The overlap matrix between neutral states satisfy the orthonormality condition:

$$\boxed{\langle \mathcal{N}|\mathcal{N}'\rangle = \delta_{\mathcal{N}\mathcal{N}'}} \tag{5.10}$$

Between neutral and channel function

The overlap between neutral and a channel functions can be evaluated as:

$$\begin{aligned}
\frac{1}{\sqrt{N}}\langle \mathcal{N}|\mathcal{A}|J\beta\rangle &= \sqrt{N}\cdot\langle \mathcal{N}|J\beta\rangle \qquad [\mathcal{N} \text{ is anti-symmetric}] \\
&= \sqrt{N}\cdot \sum_{n_1\cdots n_N} \sum_{j_1\cdots j_{N-1}} \langle n_1 n_2\cdots n_N|j_1\cdots j_{N-1}\beta\rangle d^*_{n_1\cdots n_N} b_{j_1\cdots j_{N-1}} \\
&= \sqrt{N}\cdot \sum_{n_1\cdots n_N} \langle n_N|\beta\rangle d^*_{n_1\cdots n_N} b_{n_1\cdots n_{N-1}} \\
[\text{Renaming indices}] &= \sum_i \langle i|\beta\rangle \eta^{\mathcal{N}J}_i
\end{aligned}$$

$$\boxed{\frac{1}{\sqrt{N}}\langle \mathcal{N}|\mathcal{A}|J\beta\rangle = \langle i|\beta\rangle \eta^{\mathcal{N}J}_i}$$

Between channel functions

The overlap matrices between channel functions can be computed as:

$$\begin{aligned}\frac{1}{N}\langle I\alpha|\mathcal{A}\mathcal{A}|J\beta\rangle = \langle I\alpha|\mathcal{A}|J\beta\rangle &= \sum_{k=1}^{N}\langle A_N|B_k\rangle \\ &= \langle A_N|B_N\rangle + \sum_{k=1}^{N-1}\langle A_N|B_k\rangle \\ \text{[Identical N-1 terms]} &= \langle A_N|B_N\rangle + (N-1)\langle A_N|B_1\rangle\end{aligned}$$

The equivalence of the terms in each of the summations can be proved through a simple interchange and renaming of indices.

$$\langle A_N|B_N\rangle = \langle I|J\rangle\langle\alpha|\beta\rangle$$

$$\begin{aligned}\langle A_N|B_1\rangle &= \sum_{i_1\cdots i_{N-1}}\sum_{j_1\cdots j_{N-1}}(-1)^{N-1}\langle i_1\cdots i_{N-1}\alpha|\beta j_1\cdots j_{N-1}\rangle a^*_{i_1\cdots i_{N-1}}b_{j_1\cdots j_{N-1}} \\ &= \sum_{i_1\cdots i_{N-1}}\sum_{j_{N-1}}(-1)^{N-1}\langle i_1|\beta\rangle\langle\alpha|j_{N-1}\rangle a^*_{i_1\cdots i_{N-1}}b_{i_2\cdots i_{N-1}j_{N-1}} \\ \text{[Reordering indices]} &= \sum_{i_1\cdots i_{N-1}}\sum_{j_{N-1}}-\langle i_1|\beta\rangle\langle\alpha|j_{N-1}\rangle a^*_{i_2\cdots i_{N-1}i_1}b_{i_2\cdots i_{N-1}j_{N-1}} \\ \text{[Renaming indices]} &= \sum_{i_2\cdots i_{N-1}ij}-\langle i|\beta\rangle\langle\alpha|j\rangle a^*_{i_2\cdots i_{N-1}i}b_{i_2\cdots i_{N-1}j}\end{aligned}$$

$$(N-1)\langle A_N|B_1\rangle = \sum_{ij}-\langle\alpha|j\rangle\rho^{IJ}_{ij}\langle i|\beta\rangle$$

Hence,

$$\boxed{\frac{1}{N}\langle I\alpha|\mathcal{A}\mathcal{A}|J\beta\rangle = \langle I|J\rangle\langle\alpha|\beta\rangle - \langle\alpha|j\rangle\rho^{IJ}_{ij}\langle i|\beta\rangle}$$

5.1.2 Single particle operators

The single particle operator for an N-particle system is defined as:

$$\hat{S} = \sum_{l=1}^{N} s_l \tag{5.11}$$

where s_l is the single particle operator that acts on the l^{th} coordinate. Note, in the following treatment the subscript is dropped when not essential. As the operators are symmetric with respect to coordinate exchange $\frac{1}{N}\mathcal{A}\hat{S}\mathcal{A} = \hat{S}\mathcal{A}$

Between neutrals

The single particle matrix elements between two neutral states can be computed as:

$$\boxed{\langle \mathcal{N}|\hat{S}|\mathcal{N}'\rangle = \langle i|s|j\rangle \rho_{ij}^{\mathcal{N}\mathcal{N}'}} \tag{5.12}$$

Between neutral and channel function

The single particle matrix elements between a neutral and an ionic channel functions are evaluated as:

$$\begin{aligned}
\frac{1}{\sqrt{N}}\langle \mathcal{N}|\hat{S}\mathcal{A}|J\beta\rangle = \sqrt{N}\cdot\langle \mathcal{N}|\hat{S}|J\beta\rangle &= \sqrt{N}\cdot\sum_{l=1}^{N}\langle \mathcal{N}|s_l|B_N\rangle \\
&= \sqrt{N}\cdot\langle \mathcal{N}|s_N|B_N\rangle + \sqrt{N}\cdot\sum_{l=1}^{N-1}\langle \mathcal{N}|s_l|B_N\rangle \\
&= \sqrt{N}\cdot\langle \mathcal{N}|s_N|B_N\rangle + \sqrt{N}\cdot(N-1)\langle \mathcal{N}|s_1|B_N\rangle.
\end{aligned}$$

Evaluating term-wise:

Term 1:

$$\begin{aligned}
\langle \mathcal{N}|s_N|B_N\rangle &= \sum_{n_1\cdots n_N}\sum_{j_1\cdots j_{N-1}}\langle n_1\cdots n_N|s_N|j_1\cdots j_{N-1}\beta\rangle d^*_{n_1\cdots n_N} b_{j_1\cdots j_{N-1}} \\
&= \sum_{n_1\cdots n_N}\langle n_N|s_N|\beta\rangle d^*_{n_1\cdots n_N} b_{n_1\cdots n_{N-1}} \\
&= \sum_i \langle i|s_N|\beta\rangle \eta_i^{\mathcal{N}J}/\sqrt{N}
\end{aligned}$$

Term 2:

$$\begin{aligned}
\langle \mathcal{N}|s_1|B_N\rangle &= \sum_{n_1\cdots n_N}\sum_{j_1\cdots j_{N-1}}\langle n_1\cdots n_N|s_1|j_1\cdots j_{N-1}\beta\rangle d^*_{n_1\cdots n_N} b_{j_1\cdots j_{N-1}} \\
&= \sum_{n_1\cdots n_N}\sum_{j_1}\langle n_1|s_1|j_1\rangle\langle n_N|\beta\rangle d^*_{n_1\cdots n_N} b_{j_1 n_2\cdots n_{N-1}} \\
\text{[Reordering indices]} &= \sum_{n_1\cdots n_N}\sum_{j_1}\langle n_1|s_1|j_1\rangle\langle n_N|\beta\rangle d^*_{n_2\cdots n_{N-1}n_1n_N} b_{n_2\cdots n_{N-1}j_1} \\
\text{[Renaming indices]} &= \sum_{n_1 n_2 j_1}\langle n_1|s_1|j_1\rangle\langle n_2|\beta\rangle \eta^{\mathcal{N}J}_{n_1n_2j_1}/\left[\sqrt{N}(N-1)\right]
\end{aligned}$$

The total single particle operator between the neutral and the ionic channel functions is:

$$\boxed{\frac{1}{\sqrt{N}}\langle\mathcal{N}|\hat{S}\mathcal{A}|J\beta\rangle = \langle i|s|\beta\rangle\eta_i^{\mathcal{N}J} + \langle n_1|s|j_1\rangle\langle n_2|\beta\rangle\eta_{n_1n_2j_1}^{\mathcal{N}I}} \tag{5.13}$$

Between channel functions

The single particle matrix elements between two ionic channel functions are evaluated as:

$$\begin{aligned}
\frac{1}{N}\langle I\alpha|\mathcal{A}\hat{S}\mathcal{A}|J\beta\rangle &= \langle I\alpha|\hat{S}\mathcal{A}|J\beta\rangle \\
&= \sum_{k=1}^{N}\sum_{l=1}^{N}\langle A_N|s_l|B_k\rangle \\
&= \langle A_N|s_N|B_N\rangle + \sum_{l=1}^{N-1}\langle A_N|s_l|B_N\rangle + \sum_{k=1}^{N-1}\langle A_N|s_N|B_k\rangle \\
&\quad + \sum_{k=1}^{N-1}\langle A_N|s_k|B_k\rangle + \sum_{k=1}^{N-1}\sum_{l=1,l\neq k}^{N-1}\langle A_N|s_l|B_k\rangle \\
\text{[Equivalent terms]} &= \langle A_N|s_N|B_N\rangle + (N-1)\langle A_N|s_1|B_N\rangle + (N-1)\langle A_N|s_N|B_1\rangle \\
&\quad + (N-1)\langle A_N|s_1|B_1\rangle + (N-1)(N-2)\langle A_N|s_2|B_1\rangle
\end{aligned}$$

Evaluating term-wise:

Term 1:

$$\langle A_N|s_N|B_N\rangle = \langle I\alpha|s_N|J\beta\rangle = \langle I|J\rangle\langle\alpha|s_N|\beta\rangle$$

Term 2:

$$\begin{aligned}
\langle A_N|s_1|B_N\rangle &= \langle I\alpha|s_1|J\beta\rangle \\
&= \sum_{i_1\cdots i_{N-1}}\sum_{j_1\cdots j_{N-1}}\langle i_1\cdots i_{N-1}\alpha|s_1|j_1\cdots j_{N-1}\beta\rangle a^*_{i_1\cdots i_{N-1}}b_{j_1\cdots j_{N-1}} \\
&= \sum_{i_1j_1}\langle i_1|s_1|j_1\rangle\rho^{IJ}_{i_1j_1}\langle\alpha|\beta\rangle/(N-1)
\end{aligned}$$

Term 3:

$$\langle A_N|s_N|B_1\rangle = \sum_{i_1\cdots i_{N-1}}\sum_{j_1\cdots j_{N-1}}(-1)^{N-1}\langle i_1\cdots i_{N-1}\alpha|s_N|\beta j_1\cdots j_{N-1}\rangle a^*_{i_1\cdots i_{N-1}}b_{j_1\cdots j_{N-1}}$$

$$
\begin{aligned}
&= \sum_{i_1\cdots i_{N-1}} \sum_{j_{N-1}} (-1)^{N-1} \langle i_1|\beta\rangle\langle\alpha|s_N|j_{N-1}\rangle a^*_{i_1\cdots i_{N-1}} b_{i_2\cdots i_{N-2} j_{N-1}} \\
\text{[Reordering indices]} &= \sum_{i_1\cdots i_{N-1}} \sum_{j_{N-1}} -\langle i_1|\beta\rangle\langle\alpha|s_N|j_{N-1}\rangle a^*_{i_1\cdots i_{N-1}} b_{j_{N-1} i_2\cdots i_{N-2}} \\
&= \sum_{ij} -\langle i|\beta\rangle\langle\alpha|s_N|j\rangle \rho^{IJ}_{ij}/(N-1)
\end{aligned}
$$

Term 4:

$$
\begin{aligned}
\langle A_N|s_1|B_1\rangle &= \sum_{i_1\cdots i_{N-1}} \sum_{j_1\cdots j_{N-1}} (-1)^{N-1} \langle i_1\cdots i_{N-1}\alpha|s_1|\beta j_1\cdots j_{N-1}\rangle a^*_{i_1\cdots i_{N-1}} b_{j_1\cdots j_{N-1}} \\
&= \sum_{i_1\cdots i_{N-1}} \sum_{j_{N-1}} (-1)^{N-1} \langle i_1|s_1|\beta\rangle\langle\alpha|j_{N-1}\rangle a^*_{i_1\cdots i_{N-1}} b_{i_2\cdots i_{N-1} j_{N-1}} \\
\text{[Reordering indices]} &= \sum_{i_1\cdots i_{N-1}} \sum_{j_{N-1}} -\langle i_1|s_1|\beta\rangle\langle\alpha|j_{N-1}\rangle a^*_{i_1\cdots j_{N-1}} b_{j_{N-1} i_2\cdots i_{N-1}} \\
&= \sum_{ij} -\langle i|s_1|\beta\rangle\langle\alpha|j\rangle \rho^{IJ}_{ij}/(N-1)
\end{aligned}
$$

Term 5:

$$
\begin{aligned}
\langle A_N|s_2|B_1\rangle &= \sum_{i_1\cdots i_{N-1}} \sum_{j_1\cdots j_{N-1}} (-1)^{N-1} \langle i_1\cdots i_{N-1}\alpha|s_2|\beta j_1\cdots j_{N-1}\rangle a^*_{i_1\cdots i_{N-1}} b_{j_1\cdots j_{N-1}} \\
&= \sum_{i_1\cdots i_{N-1}} \sum_{j_2 j_{N-1}} (-1)^{N-1} \langle i_1|\beta\rangle\langle i_2|s_2|j_1\rangle\langle\alpha|j_{N-1}\rangle a^*_{i_1\cdots i_{N-1}} b_{j_1 i_3\cdots i_{N-1} j_{N-1}} \\
\text{[Reordering indices]} &= \sum_{i_1\cdots i_{N-1}} \sum_{j_2 j_{N-1}} -\langle i_1|\beta\rangle\langle i_2|s_2|j_1\rangle\langle\alpha|j_{N-1}\rangle a^*_{i_1 i_2 i_3\cdots i_{N-1}} b_{j_{N-1} j_1 i_3\cdots i_{N-1}} \\
\text{[Renaming indices]} &= \sum_{i_3\cdots i_{N-1}} \sum_{i_1 i_2 j_1 j_2} -\langle i_1|\beta\rangle\langle i_2|s_2|j_2\rangle\langle\alpha|j_1\rangle a^*_{i_1 i_2 i_3\cdots i_{N-1}} b_{j_1 j_2 i_3\cdots i_{N-1}} \\
&= \sum_{i_1 i_2 j_1 j_2} -\langle i_1|\beta\rangle\langle i_2|s_2|j_2\rangle\langle\alpha|j_1\rangle \rho^{IJ}_{i_1 i_2 j_1 j_2}/\left[(N-1)(N-2)\right]
\end{aligned}
$$

Hence, the overall one particle operator between the ionic channel functions takes the form:

$$
\boxed{
\begin{aligned}
\frac{1}{N}\langle I\alpha|\mathcal{A}\hat{S}\mathcal{A}|J\beta\rangle = &\langle I|J\rangle\langle\alpha|s|\beta\rangle + \langle\alpha|\beta\rangle\langle i|s|j\rangle\rho^{IJ}_{ij} \\
&- \langle\alpha|s|j\rangle\rho^{IJ}_{ij}\langle i|\beta\rangle - \langle\alpha|j\rangle\rho^{IJ}_{ij}\langle j|s|\beta\rangle \\
&- \langle\alpha|j_1\rangle\langle i_1|\beta\rangle\langle i_2|s|j_2\rangle\rho^{IJ}_{i_1 i_2 j_1 j_2}
\end{aligned}
} \tag{5.14}
$$

5.1.3 Two particle operators

A general two particle operator can be written as

$$\hat{T} = \sum_{m=1}^{N} \sum_{n=m+1}^{N} t_{mn} \tag{5.15}$$

where t_{mn} acts on the m, n coordinates. Note, that the subscripts are dropped in the following treatment when not essential. Again, as the operators are symmetric with respect to coordinate exchange $\frac{1}{N}\mathcal{A}\hat{T}\mathcal{A} = \hat{T}\mathcal{A}$

Between neutrals

The two particle operators between two neutrals can be evaluated as:

$$\boxed{\langle \mathcal{N}|\hat{T}|\mathcal{N}'\rangle = \frac{1}{2}\langle n_1 n_2|t|n_1' n_2'\rangle \rho^{\mathcal{N}\mathcal{N}'}_{n_1 n_2 n_1' n_2'}} \tag{5.16}$$

Between neutral and channel function

The two particle operator between a neutral and a channel function can be computed as:

$$\begin{aligned}
\frac{1}{\sqrt{N}}\langle \mathcal{N}|\hat{T}\mathcal{A}|J\beta\rangle &= \sqrt{N}\langle \mathcal{N}|\hat{T}|J\beta\rangle \\
&= \sqrt{N}\cdot \sum_{p=1}^{N}\sum_{q=p+1}^{N} \langle \mathcal{N}|t_{pq}|B_N\rangle \\
&= \sqrt{N}\cdot \left[\sum_{p=1}^{N-1}\langle \mathcal{N}|t_{pN}|B_N\rangle + \sum_{p=1}^{N-1}\sum_{q=p+1}^{N-1}\langle \mathcal{N}|t_{pq}|B_N\rangle\right] \\
&= \sqrt{N}(N-1)\langle \mathcal{N}|t_{1N}|B_N\rangle + \frac{\sqrt{N}(N-1)(N-2)}{2}\langle \mathcal{N}|t_{12}|B_N\rangle
\end{aligned}$$

Evaluating term-wise:

Term 1:

$$\begin{aligned}
\langle \mathcal{N}|t_{1N}|B_n\rangle &= \sum_{n_1\cdots n_N}\sum_{j_1\cdots j_{N-1}} \langle n_1\cdots n_N|t_{1N}|j_1\cdots j_{N-1}\beta\rangle d^*_{n_1\cdots n_N} b_{j_1\cdots j_{N-1}} \\
&= \sum_{n_1\cdots n_N}\sum_{j_1} \langle n_1 n_N|t_{12}|j_1\beta\rangle d^*_{n_1\cdots n_N} b_{j_1 n_2\cdots n_{N-1}} \\
\text{[Reordering indices]} &= \sum_{n_1\cdots n_N}\sum_{j_1} \langle n_1 n_2|t_{12}|j_1\beta\rangle d^*_{n_2\cdots n_{N-1} n_1 n_N} b_{n_2\cdots n_{N-1} j_1}
\end{aligned}$$

$$\begin{aligned}[\text{Renaming indices}] &= \sum_{n_1\cdots n_N}\sum_{j_1}\langle n_2 n_1|t_{12}|j_1\beta\rangle d^*_{n_3\cdots n_N n_1 n_2} b_{n_3\cdots n_N j_1} \\ &= \sum_{n_1 n_2 j_1}\langle n_1 n_2|t|j_1\beta\rangle \eta^{\mathcal{N}J}_{n_1 n_2 j_1} / \left[\sqrt{N}(N-1)\right]\end{aligned}$$

Term 2:

$$\begin{aligned}\langle\mathcal{N}|t_{12}|B_N\rangle &= \sum_{n_1\cdots n_N}\sum_{j_1\cdots j_{N-1}}\langle n_1\cdots n_N|t_{12}|j_1\cdots j_{N-1}\beta\rangle d^*_{n_1\cdots n_N} b_{j_1\cdots j_{N-1}} \\ &= \sum_{n_1\cdots n_N}\sum_{j_1 j_2}\langle n_N|\beta\rangle\langle n_1 n_2|t_{12}|j_1 j_2\rangle d^*_{n_1\cdots n_N} b_{j_1\cdots j_{N-1}} \\ &= \sum_{n_1 n_2 n_3 j_1 j_2}\langle n_1 n_2|t|j_1 j_2\rangle\langle n_3|\beta\rangle \eta^{\mathcal{N}J}_{n_1 n_2 n_3 j_1 j_2} / \left[\sqrt{N}(N-1)(N-2)\right]\end{aligned}$$

The overall matrix element looks as:

$$\boxed{\frac{1}{\sqrt{N}}\langle\mathcal{N}|\hat{T}\mathcal{A}|J\beta\rangle = \langle n_1 n_2|t|j_1\beta\rangle\eta^{\mathcal{N}J}_{n_1 n_2 j_1} + \frac{1}{2}\langle n_1 n_2|t|j_1 j_2\rangle\langle n_3|\beta\rangle\eta^{\mathcal{N}J}_{n_1 n_2 n_3 j_1 j_2}} \tag{5.17}$$

Between channel functions

The two particle matrix elements between two ionic channel functions can be evaluated as:

$$\begin{aligned}&\frac{1}{N}\langle I\alpha|\mathcal{A}\hat{T}\mathcal{A}|J\beta\rangle = \langle I\alpha|\hat{T}\mathcal{A}|J\beta\rangle \\ =\ & \sum_{k=1}^{N}\sum_{m=1}^{N}\sum_{n=m+1}^{N}\langle A_N|t_{mn}|B_k\rangle \\ =\ & \sum_{m=1}^{N}\sum_{n=m+1}^{N}\langle A_N|t_{mn}|B_N\rangle + \sum_{k=1}^{N-1}\sum_{m=1}^{N}\sum_{n=m+1}^{N}\langle A_N|t_{mn}|B_k\rangle \\ =\ & \sum_{m=1}^{N-1}\sum_{n=m+1}^{N-1}\langle A_N|t_{mn}|B_N\rangle + \sum_{m=1}^{N-1}\langle A_N|t_{mN}|B_N\rangle + \sum_{k=1}^{N-1}\sum_{m=1}^{N-1}\langle A_N|t_{mN}|B_k\rangle + \sum_{k=1}^{N-1}\sum_{m=1}^{N-1}\sum_{n=m+1}^{N-1}\langle A_N|t_{mn}|B_k\rangle \\ =\ & \sum_{m=1}^{N-1}\sum_{n=m+1}^{N-1}\langle A_N|t_{mn}|B_N\rangle + \sum_{m=1}^{N-1}\langle A_N|t_{mN}|B_N\rangle + \sum_{k=1}^{N-1}\langle A_N|t_{kN}|B_k\rangle + \sum_{k=1}^{N-1}\sum_{m=1,m\neq k}^{N-1}\langle A_N|t_{mN}|B_k\rangle \\ &+\sum_{m=1}^{N-1}\sum_{n=m+1}^{N-1}\langle A_N|t_{mn}|B_n\rangle + \sum_{m=1}^{N-1}\sum_{n=m+1}^{N-1}\langle A_N|t_{mn}|B_m\rangle + \sum_{m=1}^{N-1}\sum_{n=m+1}^{N-1}\sum_{k=1,k\neq m,n}^{N-1}\langle A_N|t_{mn}|B_k\rangle \\ =\ & \frac{(N-1)(N-2)}{2}\langle A_N|t_{12}|B_N\rangle + (N-1)\langle A_N|t_{1N}|B_N\rangle + (N-1)\langle A_N|t_{1N}|B_1\rangle \\ &+(N-1)(N-2)\langle A_N|t_{2N}|B_1\rangle + \frac{(N-1)(N-2)}{2}\langle A_N|t_{12}|B_2\rangle\end{aligned}$$

$$
\begin{aligned}
&+\frac{(N-1)(N-2)}{2}\langle A_N|t_{12}|B_1\rangle + \frac{(N-1)(N-2)(N-3)}{2}\langle A_N|t_{23}|B_1\rangle \\
= \;& \frac{(N-1)(N-2)}{2}\langle A_N|t_{12}|B_N\rangle + (N-1)\langle A_N|t_{1N}|B_N\rangle + (N-1)\langle A_N|t_{1N}|B_1\rangle \\
&+(N-1)(N-2)\langle A_N|t_{2N}|B_1\rangle + (N-1)(N-2)\langle A_N|t_{12}|B_1\rangle \\
&+\frac{(N-1)(N-2)(N-3)}{2}\langle A_N|t_{23}|B_1\rangle
\end{aligned}
$$

There are 6 terms in the above expression which can be evaluated as:

Term 1:

$$
\frac{(N-1)(N-2)}{2}\langle A_N|t_{12}|B_N\rangle = \frac{1}{2}\langle i_1 i_2|t|j_1 j_2\rangle \rho^{IJ}_{i_1 i_2 j_1 j_2}\langle\alpha|\beta\rangle
$$

Term 2:

$$
\begin{aligned}
\langle A_N|t_{1N}|B_N\rangle &= \sum_{i_1\cdots i_{N-1}}\sum_{j_1\cdots j_{N-1}}\langle i_1\cdots i_{N-1}\alpha|t_{1N}|j_1\cdots j_{N-1}\beta\rangle a^*_{i_1\cdots i_{N-1}} b_{j_1\cdots j_{N-1}} \\
&= \sum_{i_1\cdots i_{N-1}}\sum_{j_1}\langle i_1\alpha|t_{1N}|j_1\beta\rangle a^*_{i_1\cdots i_{N-1}} b_{j_1 i_2\cdots i_{N-1}} \\
&= \sum_{ij}\langle i\alpha|t|j\beta\rangle \rho^{IJ}_{ij}/(N-1)
\end{aligned}
$$

Term 3:

$$
\begin{aligned}
\langle A_N|t_{1N}|B_1\rangle &= \sum_{i_1\cdots i_{N-1}}\sum_{j_1\cdots j_{N-1}}(-1)^{N-1}\langle i_1\cdots i_{N-1}\alpha|t_{1N}|\beta j_1\cdots j_{N-1}\rangle a^*_{i_1\cdots i_{N-1}} b_{j_1\cdots j_{N-1}} \\
&= \sum_{i_1\cdots i_{N-1}}\sum_{j_{N-1}}(-1)^{N-1}\langle i_1\alpha|t_{1N}|\beta j_{N-1}\rangle a^*_{i_1\cdots i_{N-1}} b_{i_2\cdots i_{N-1} j_{N-1}} \\
&= \sum_{i_1\cdots i_{N-1}}\sum_{j_{N-1}}-\langle i_1\alpha|t_{1N}|\beta j_{N-1}\rangle a^*_{i_1\cdots i_{N-1}} b_{j_{N-1} i_2\cdots i_{N-1}} \\
&= \sum_{ij}-\langle i\alpha|t|\beta j\rangle \rho^{IJ}_{ij}/(N-1)
\end{aligned}
$$

Term 4:

$$
\begin{aligned}
\langle A_N|t_{2N}|B_1\rangle &= \sum_{i_1\cdots i_{N-1}}\sum_{j_1\cdots j_{N-1}}(-1)^{N-1}\langle i_1\cdots i_{N-1}\alpha|t_{2N}|\beta j_1\cdots j_{N-1}\rangle a^*_{i_1\cdots i_{N-1}} b_{j_1\cdots j_{N-1}} \\
&= \sum_{i_1\cdots i_{N-1}}\sum_{j_1 j_{N-1}}(-1)^{N-1}\langle i_1|\beta\rangle\langle i_2\alpha|t_{2N}|j_1 j_{N-1}\rangle a^*_{i_1\cdots i_{N-1}} b_{j_1 i_3\cdots i_{N-1} j_{N-1}}
\end{aligned}
$$

$$
\begin{aligned}
&= \sum_{i_1\cdots i_{N-1}} \sum_{j_1 j_{N-1}} -\langle i_1|\beta\rangle\langle i_2\alpha|t_{2N}|j_1 j_{N-1}\rangle a^*_{i_1\cdots i_{N-1}} b_{j_{N-1} j_1 i_3\cdots i_{N-1}} \\
\text{[Renaming indices]} \quad &= \sum_{i_1\cdots i_{N-1}} \sum_{j_1 j_2} -\langle i_1|\beta\rangle\langle i_2\alpha|t_{2N}|j_2 j_1\rangle a^*_{i_1\cdots i_{N-1}} b_{j_1 j_2 i_3\cdots i_{N-1}} \\
&= \sum_{i_1 i_2 j_1 j_2} -\langle i_1|\beta\rangle\langle i_2\alpha|t_{2N}|j_2 j_1\rangle \rho^{IJ}_{i_1 i_2 j_1 j_2} \\
&= \sum_{i_1 i_2 j_1 j_2} -\langle i_1|\beta\rangle\langle \alpha i_2|t|j_1 j_2\rangle \rho^{IJ}_{i_1 i_2 j_1 j_2} / \left[(N-1)(N-2)\right]
\end{aligned}
$$

Term 5:

$$
\begin{aligned}
\langle A_N|t_{12}|B_1\rangle &= \sum_{i_1\cdots i_{N-1}} \sum_{j_1\cdots j_{N-1}} (-1)^{N-1}\langle i_1\cdots i_{N-1}\alpha|t_{12}|\beta j_1\cdots j_{N-1}\rangle a^*_{i_1\cdots i_{N-1}} b_{j_1\cdots j_{N-1}} \\
&= \sum_{i_1\cdots i_{N-1}} \sum_{j_1 j_{N-1}} (-1)^{N-1}\langle i_1 i_2|t_{12}|\beta j_1\rangle\langle \alpha|j_{N-1}\rangle a^*_{i_1\cdots i_{N-1}} b_{j_1 i_3\cdots i_{N-1} j_{N-1}} \\
&= \sum_{i_1\cdots i_{N-1}} \sum_{j_1 j_{N-1}} -\langle i_1 i_2|t_{12}|\beta j_1\rangle\langle \alpha|j_{N-1}\rangle a^*_{i_1\cdots i_{N-1}} b_{j_{N-1} j_1 i_3\cdots i_{N-1}} \\
\text{[Renaming indices]} \quad &= \sum_{i_1\cdots i_{N-1}} \sum_{j_1 j_2} -\langle i_1 i_2|t_{12}|\beta j_2\rangle\langle \alpha|j_1\rangle a^*_{i_1\cdots i_{N-1}} b_{j_1 j_2 i_3\cdots i_{N-1}} \\
&= \sum_{i_1 i_2 j_1 j_3} -\langle i_1 i_2|t|\beta j_2\rangle\langle \alpha|j_1\rangle \rho^{IJ}_{i_1 i_2 j_1 j_2} / \left[(N-1)(N-2)\right]
\end{aligned}
$$

Term 6:

$$
\begin{aligned}
\langle A_N|t_{23}|B_1\rangle &= \sum_{i_1\cdots i_{N-1}} \sum_{j_1\cdots j_{N-1}} (-1)^{N-1}\langle i_1\cdots i_{N-1}\alpha|t_{23}|\beta j_1\cdots j_{N-1}\rangle a^*_{i_1\cdots i_{N-1}} b_{j_1\cdots j_{N-1}} \\
&= \sum_{i_1\cdots i_{N-1}} \sum_{j_1 j_2 j_{N-1}} (-1)^{N-1}\langle i_1|\beta\rangle\langle i_2 i_3|t_{23}|j_1 j_2\rangle\langle \alpha|j_{N-1}\rangle a^*_{i_1\cdots i_{N-1}} b_{j_1 j_2 i_4\cdots i_{N-1} j_{N-1}} \\
&= \sum_{i_1\cdots i_{N-1}} \sum_{j_1 j_2 j_{N-1}} -\langle i_1|\beta\rangle\langle i_2 i_3|t_{23}|j_1 j_2\rangle\langle \alpha|j_{N-1}\rangle a^*_{i_1\cdots i_{N-1}} b_{j_{N-1} j_1 j_2 i_4\cdots i_{N-1}} \\
\text{[Renaming indices]} \quad &= \sum_{i_1\cdots i_{N-1}} \sum_{j_1 j_2 j_3} -\langle i_1|\beta\rangle\langle i_2 i_3|t|j_2 j_3\rangle\langle \alpha|j_1\rangle a^*_{i_1\cdots i_{N-1}} b_{j_1 j_2 j_3 i_4\cdots j_{N-1}} \\
&= \sum_{i_1 i_2 i_3 j_1 j_2 j_3} -\langle i_1|\beta\rangle\langle i_2 i_3|t|j_2 j_3\rangle\langle \alpha|j_1\rangle \rho^{IJ}_{i_1 i_2 i_3 j_1 j_2 j_3} \frac{(N-4)!}{(N-1)!}
\end{aligned}
$$

Finally, the two particle matrix elements between two ionic channel functions look as:

$$\begin{aligned}
&\frac{1}{N}\langle I\alpha|\mathcal{A}\hat{T}\mathcal{A}|J\beta\rangle \\
&= \frac{1}{2}\langle i_1 i_2|t|j_1 j_2\rangle \rho^{IJ}_{i_1 i_2 j_1 j_2}\langle\alpha|\beta\rangle + \langle i\alpha|t|j\beta\rangle\rho^{IJ}_{ij} - \langle i\alpha|t|\beta j\rangle\rho^{IJ}_{ij} \\
&- \langle i_1|\beta\rangle\langle\alpha i_2|t|j_1 j_2\rangle\rho^{IJ}_{i_1 i_2 j_1 j_2} - \langle i_1 i_2|t|\beta j_2\rangle\langle\alpha|j_1\rangle\rho^{IJ}_{i_1 i_2 j_1 j_2} \\
&- \frac{1}{2}\langle i_1|\beta\rangle\langle i_2 i_3|t|j_2 j_3\rangle\langle\alpha|j_1\rangle\rho^{IJ}_{i_1 i_2 i_3 j_1 j_2 j_3}.
\end{aligned} \tag{5.18}$$

Note: The current treatment needs upto three particle reduced density matrices. The non-orthogonality of the single electron basis, α, with respect to the Hartree-Fock (HF) basis, ϕ_k, leads to a significant complexity in the matrix elements. Explicit orthogonalization of the single electron basis with respect to HF orbitals is not a solution because: the ionic and neutral states are treated on the configuration interaction level and each ionic state is composed of several Slater determinants.

5.2 Two electron integrals

The two electron integrals are the computationally most intensive parts in the setting up of the Hamiltonian. In the current implementation of these integrals, they are evaluated using a multi-pole expansion, where the electron-electron interaction operator is expanded as:

$$\frac{1}{|\vec{r}_1 - \vec{r}_2|} = \sum_{L=0}^{\infty} \frac{4\pi}{2L+1}\frac{r_<^L}{r_>^{L+1}} \sum_{M=-L}^{L} Y_{LM}(\Omega_1)Y^*_{LM}(\Omega_2) \tag{5.19}$$

where $r_< = \min(r_1, r_2)$ and $r_> = \max(r_1, r_2)$. The infinite multi-pole expansion is truncated by the angular momentum content in the basis and the limits are denoted using symbols $L_{min}, L_{max}, M_{min}$ and M_{max}.

The radial part of the operator, $\frac{r_<^L}{r_>^{L+1}}$, is evaluated with a polynomial basis and the matrix elements obtained are transformed to a corresponding quadrature grid representation. The quadrature grid has the same order as the polynomial basis. This matrix is denoted as $V^L_{qq'}$. The molecular orbitals, ϕ_k are expressed in a single centered expansion which can be written as:

$$\phi_i = \sum_{q l_i m_i} c^i_{q l_i m_i} Y_{l_i m_i}. \tag{5.20}$$

Since a multi-centered atomic orbital needs an infinite angular momenta, the above expansion is truncated by defining a tolerance and this tolerance is a convergence parameter in the calculations. The resulting limits for the angular momentum expansion for the molecular orbitals are denoted as l^g_{max} and m^g_{max}. The single-electron numerical basis can also

be expressed on a quadrature grid as:

$$\alpha(\vec{r}) = \sum_q \alpha_q Y_{l_\alpha m_\alpha}. \tag{5.21}$$

The largest angular momenta in this one-electron expansion is denoted using symbols l_{max} and m_{max}.

There are four types of two-electron integrals that appear in the haCC scheme: $\langle\alpha\phi_i|V^{\{2\}}|\beta\phi_j\rangle\rho_{ij}^{IJ}$, $\langle\alpha\phi_i|V^{\{2\}}|\phi_j\beta\rangle\rho_{ij}^{IJ}$, $\langle\alpha\phi_m|V^{\{2\}}|\phi_l\phi_n\rangle\rho_{klmn}^{IJ}$ and $\langle\alpha\phi_l|V^{\{2\}}|\phi_m\phi_k\rangle\eta_{klm}^{IN}$ (See section (5.1.3)). Outline of the steps following to compute them in the current implementation is presented in the following subsections. There exists a trade-off between the storage requirements and the operations count while designing a suitable algorithm.

5.2.1 Hartree term

The Hartree term: $\langle\alpha\phi_i|V^{\{2\}}|\beta\phi_j\rangle\rho_{ij}^{IJ}$, is the easiest of the all the four varieties as the integral over the molecular orbitals yields an effective potential for the second electron coordinate. Denoting the matrix element as $M_{\alpha\beta}^{IJ}$:

$$\begin{aligned} M_{\alpha\beta}^{IJ} &= \sum_{ij}\langle\alpha\phi_i|V^{\{2\}}|\beta\phi_j\rangle\rho_{ij}^{IJ} \\ &= \sum_{ij}\rho_{ij}^{IJ}\sum_{qq'}\sum_{LM}\frac{4\pi}{2L+1}\alpha_q^*\beta_q V_{qq'}^L\sum_{l_im_i}c_{q'l_im_i}^{i*}\sum_{l_jm_j}c_{q'l_jm_j}^{j}\langle Y_{l_\alpha m_\alpha}Y_{LM}|Y_{l_\beta m_\beta}\rangle\langle Y_{l_im_i}|Y_{LM}Y_{l_jm_j}\rangle \end{aligned} \tag{5.22}$$

the integral evaluation is performed using the following steps:

1. First, an effective potential object R_{LMq}^{IJ} is defined as follows:

$$R_{LMq}^{IJ} = \frac{4\pi}{2L+1}\sum_{ij}\rho_{ij}^{IJ}\sum_{q'}V_{qq'}^L\sum_{l_im_i}c_{q'l_im_i}^{i*}\sum_{\langle_jm_j}c_{q'l_jm_j}^{j}\langle Y_{l_im_i}|Y_{LM}Y_{l_jm_j}\rangle \tag{5.23}$$

   which is computed at the start and stored. The next steps are done on the fly.

2. For each I, J, α, β the vector T_q is computed as:

$$T_q = \sum_{LM}R_{LMq}^{IJ}\langle Y_{l_\alpha m_\alpha}Y_{LM}|Y_{l_\beta m_\beta}\rangle \tag{5.24}$$

3. This yields the required integral

$$M_{\alpha\beta}^{IJ} = \sum_q \alpha_q^* T_q \beta_q \tag{5.25}$$

The limits of LM expansion define the required storage and this can be obtained by examining equations 5.23 and 5.24. The needed LM are:

$$\begin{aligned} L_{min} &= 0 \\ L_{max} &= 2\min(l_{max}, l^g_{max}) \\ M_{min}(L) &= \max(\max(-2m^g_{max}, -2m_{max}), -L) \\ M_{max}(L) &= \min(\min(2m^g_{max}, 2m_{max}), L) \end{aligned}$$

5.2.2 Standard exchange term

The standard exchange term which is the most expensive of all can be expressed as:

$$\begin{aligned} M^{IJ}_{\alpha\beta} &= \sum_{ij} \langle \alpha\phi_i | V^{\{2\}} | \phi_j \beta \rangle \rho^{IJ}_{ij} \\ &= \sum_{ij} \rho^{IJ}_{ij} \sum_{qq'} \sum_{LM} \frac{4\pi}{2L+1} \alpha^*_q \beta_{q'} V^L_{qq'} \sum_{l_i m_i} c^{i*}_{q' l_i m_i} \langle Y_{l_i m_i} Y_{LM} | Y_{l_\beta m_\beta} \rangle \sum_{l_j m_j} c^j_{q l_j m_j} \langle Y_{l_\alpha m_\alpha} | Y_{LM} Y_{l_j m_j} \rangle \end{aligned} \tag{5.26}$$

which can be recast as:

$$M^{IJ}_{\alpha\beta} = \sum_{qq'} \alpha^*_q \beta_q \sum_{LM} \frac{4\pi}{2L+1} V^L_{qq'} \sum_{ij} R^{LM}_{\alpha j q} \rho^{IJ}_{ij} R^{\dagger LM}_{\beta i q'} \tag{5.27}$$

where

$$R^{LM}_{\alpha j q} = \sum_{l_j m_j} c^j_{q l_j m_j} \langle Y_{l_\alpha m_\alpha} | Y_{LM} Y_{l_j m_j} \rangle \tag{5.28}$$

The expression within the ij summation can be simplified by performing a singular value decomposition or in other words by transforming from the molecular orbital basis to natural orbital basis. In the natural orbital basis ρ^{IJ}_{ij} is a diagonal matrix. Using the singular value decomposition $\rho^{IJ}_{ji} = U^{IJ}_{jx} V^{IJ\dagger}_{xi}$,

$$\sum_{ij} R^{LM}_{\alpha j q} \rho^{IJ}_{ij} R^{\dagger LM}_{\beta i q'} = \sum_{ij} R^{LM}_{\alpha j q} U^{IJ}_{jx} V^{IJ\dagger}_{xi} R^{\dagger LM}_{\beta i q'} = \sum_x T^{IJLM}_{\alpha x q} T^{\dagger IJLM}_{\beta x q'} \tag{5.29}$$

This reduces the number of required floating point operations when the number of natural orbitals is smaller than the number of Hartree-Fock orbitals. The reduction in the double summation ij to single summation is compensated by the fact that T is also a function of IJ unlike R.

The original expression for the exchange integral can be re-written as:

$$M^{IJ}_{\alpha\beta} = \sum_{qq'} \alpha^*_q \beta_q \sum_{LM} \frac{4\pi}{2L+1} V^L_{qq'} \sum_x T^{IJLM}_{\alpha x q} T^{\dagger IJLM}_{\beta x q'} \tag{5.30}$$

The integrals are computed using the following steps:

1. The objects T are computed and stored. This is possible for atomic case. In the molecular case due to the large angular momentum requirements, storing these may not be possible.

2. The next steps are done on the fly. An object $S^{IJ}_{qq'\alpha\beta}$ is evaluated as:

$$S^{IJ}_{qq'\alpha\beta} = \sum_{LM} \frac{4\pi}{2L+1} V^L_{qq'} \sum_x T^{IJLM}_{\alpha xq} T^{\dagger IJLM}_{\beta xq'} \tag{5.31}$$

3. This leads to the required integral:

$$M^{IJ}_{\alpha\beta} = \sum_{qq'} \alpha^*_q S^{IJ}_{qq'\alpha\beta} \beta_q \tag{5.32}$$

The multipole expansion truncations can be obtained by examining the integrals between the spherical harmonics. In the current case the LM truncation limits are:

$$\begin{aligned} L_{min} &= \max(0, l_a - l^g_{max}) \\ L_{max} &= l_a + l^g_{max} \\ M_{min} &= \min(\max(-L, m_a - m^g_{max}), L) \\ M_{max} &= \max(\min(L, m_a + m^g_{max}), -L) \end{aligned}$$

5.2.3 Non-standard two-electron integral: $\langle\alpha\phi_b|V^{\{2\}}|\phi_c\phi_d\rangle\rho^{IJ}_{abcd}$

There are other non-standard exchange terms that appear in the two-particle operator due to non-orthogonality of the molecular orbitals from quantum chemistry with respect to the single electron finite element basis. The integral

$$\begin{aligned} M^{IJ}_{\alpha a} &= \sum_{bcd} \langle\alpha\phi_b|V^{\{2\}}|\phi_c\phi_d\rangle\rho^{IJ}_{abcd} \\ &= \sum_{bdc} \rho^{IJ}_{abcd} \sum_{qq'} \sum_{LM} \frac{4\pi}{2L+1} \alpha^*_q V^L_{qq'} \sum_{l_b m_b} c^{b*}_{q' l_b m_b} \sum_{l_c m_c} c^c_{q l_c m_c} \sum_{l_d m_d} c^d_{q' l_d m_d} \langle Y_{l_b m_b}|Y_{LM} Y_{l_d m_d}\rangle \langle Y_{l_\alpha m_\alpha} Y_{LM}|Y_{l_c m_c}\rangle \end{aligned} \tag{5.33}$$

is evaluated using the following steps:

1. A direct potential like object P^{bd}_{LMq} is first constructed:

$$P^{bd}_{LMq} = \frac{4\pi}{2L+1} \sum_{q'} V^L_{qq'} \sum_{l_b m_b} c^{b*}_{q' l_b m_b} \sum_{l_d m_d} c^d_{q' l_d m_d} \langle Y_{l_b m_b}|Y_{LM} Y_{l_d m_d}\rangle \tag{5.34}$$

2. For each l_α, m_α an intermediate object Q^{cq}_{bd}

$$Q^{cq}_{bd} = \sum_{l_c m_c} c^c_{q l_c m_c} \sum_{LM} \langle Y_{l_\alpha m_\alpha} Y_{LM}|Y_{l_c m_c}\rangle P^{bd}_{LMq} \tag{5.35}$$

3. Using the object Q, an object T_{qa}^{IJ} is constructed as:

$$T_{qa}^{IJ} = \sum_{bcd} Q_{bd}^{cq} \rho_{abcd}^{IJ} \tag{5.36}$$

which is computed and stored.

4. This leads to the required result:

$$M_{\alpha a}^{IJ} = \sum_{q} T_{qa}^{IJ} \alpha_q^* \tag{5.37}$$

The multipole expansions are truncated as:

$$\begin{aligned} L_{min} &= 0 \\ L_{max} &= \min(2l_{max}^g, l_{max} + l_{max}^g) \\ M_{min} &= \max(-L, -2m_{max}^g, -m_{max} - m_{max}^g) \\ M_{max} &= \min(L, 2m_{max}^g, m_{max} + m_{max}^g) \end{aligned}$$

5.2.4 Non-standard two-electron integral: $\langle\phi_a\phi_b|V^{\{2\}}|\phi_d\beta\rangle\eta_{abd}^{\mathcal{N}J}$

The steps followed for this integral is very similar to the previous one. The integral can be expanded using the multi-pole expansion as:

$$\begin{aligned} M_\beta^{\mathcal{N}J} &= \sum_{abd} \langle\phi_a\phi_b|V^{\{2\}}|\phi_d\beta\rangle\eta_{abd}^{\mathcal{N}J} \\ &= \sum_{abd} \eta_{abd}^{\mathcal{N}J} \sum_{qq'} \sum_{LM} \frac{4\pi}{2L+1} \beta_{q'} V_{qq'}^L \sum_{l_a m_a} c_{ql_a m_a}^{a*} \sum_{l_b m_b} c_{q'l_b m_b}^{b*} \sum_{l_d m_d} c_{ql_d m_d}^{d} \langle Y_{l_a m_a}|Y_{LM} Y_{l_d m_d}\rangle \langle Y_{l_b m_b} Y_{LM}|Y_{l_\beta m_\beta}\rangle \end{aligned} \tag{5.38}$$

which is evaluated using the following steps.

1. Construct the potential $P_{LMq'}^{ad}$

$$P_{LMq'}^{ad} = \frac{4\pi}{2L+1} \sum_{q} V_{qq'}^L \sum_{l_a m_a} c_{ql_a m_a}^{a*} \sum_{l_d m_d} c_{ql_d m_d}^{d} \langle Y_{l_a m_a}|Y_{LM} Y_{l_d m_d}\rangle \tag{5.39}$$

2. For each l_β and m_β construct an intermediate object $Q_{ab}^{bq'}$ as:

$$Q_{ab}^{bq'} = \sum_{l_b m_b} c_{q'l_b m_b}^{b*} \sum_{LM} \langle Y_{l_b m_b} Y_{LM}|Y_{l_\beta m_\beta}\rangle P_{lmq'}^{ad} \tag{5.40}$$

3. Construct object $T_{q'}$ as:
$$T_{q'}^{\mathcal{N}J} = \sum_{abd} Q_{ad}^{bq'} \eta_{abd}^{\mathcal{N}J} \tag{5.41}$$
This object is computed initially for each l_β and m_β and stored.

4. Finally, the required matrix element is computed on the fly using the stored object T as:
$$M_\beta^{\mathcal{N}J} = \sum_{q'} T_{q'}^{\mathcal{N}J} \beta_{q'} \tag{5.42}$$

The multi-pole expansions are truncated as:

$$\begin{aligned} L_{min} &= 0 \\ L_{max} &= \min(2l_{max}^g, l_{max} + l_{max}^g) \\ M_{min} &= \max(-L, -2m_{max}^g, -m_{max} - m_{max}^g) \\ M_{max} &= \min(L, 2m_{max}^g, m_{max} + m_{max}^g) \end{aligned}$$

Note: As finite elements are used, the angular momentum limits can also be made a function of the finite element number.

5.3 Interfacing with quantum chemistry

A major feature of this work is the setting up of a direct interface with an established quantum chemistry package `COLUMBUS` for ionic and neutral states required in the haCC ansatz. This was a non-trivial task due to several reasons. The standard outputs of these codes typically give only the observables and not the complete definition of CI wavefunctions. Hence modification of some routines was needed that would give access to the complete CI wavefunction. These quantum chemistry codes are a fruition of several decades of programming and development of algorithms and they lack coherent documentation that allows easy implementation of changes.

The construction of the interface that reads the complete CI wavefunction was achieved with the help of several `COLUMBUS` authors.

A Configuration interaction wavefunction describing an N-electron wavefunction can be written in general as follows:

$$|\Psi_{CI}\rangle = \sum_I c_I |I\rangle \tag{5.43}$$

where the slater determinants $|I\rangle$ can be expressed as:

$$|I\rangle = \mathcal{A}[\phi_1 \phi_2 ... \phi_N] \tag{5.44}$$

using Hartree-Fock (HF) orbital ϕ_k. The HF orbitals or molecular orbitals are constructed from symmetrized atomic orbitals

$$\phi_m(x,y,z) = \left[T^{MS}\right]_{mn} S_n(x,y,z) \tag{5.45}$$

which in-turn are constructed from atomic orbitals

$$S_n(x,y,z) = \left[T^{SA}\right]_{np} A_p(x,y,z). \tag{5.46}$$

Finally, the atomic orbitals are a linear combination of atom centered primitive Gaussian orbitals:

$$A_p(x,y,z) = \left[T^{AP}\right]_{pq} G_q(x,y,z) \tag{5.47}$$

which are defined as:

$$G_q(x,y,z) = (x-x_q)^{d_q}\ (y-y_q)^{e_q}\ (z-z_q)^{f_q}\ e^{-\alpha_q\left[(x-x_q)^2+(y-y_q)^2+(z-z_q)^2\right]} \tag{5.48}$$

where (x_q, y_q, z_q) are the coordinates on which the Gaussian is based, which is one of the atomic coordinates.

Construction of `COLUMBUS` interface consisted of reading the entire CI wavefunction obtained from the quantum chemistry calculation and storing it in a form that is suitable for performing various operations needed by the haCC method. As seen from the above construction of a typical CI wavefunction, reading it essentially means extracting the coefficients c_I, the list of Slater determinants, various transformation matrices T^{MS}, T^{SA}, T^{AP} and definitions of primitive Gaussian functions: the exponents α_q, coordinates (x_q, y_q, z_q) and powers (d_q, e_q, f_q).

5.4 The haCC code

The code development for the haCC method was associated with a larger code development project called the tRecX project. The code development was done in `C++` language using concepts of object oriented programming. The haCC code is broadly based on three pieces of code:

- tRecX: A general PDE solver.
- CI wavefunction reconstruction code.
- Implementations of all the matrix elements for the haCC method which includes high dimensional integrals like the two-electron integrals and the calculation of the generalized reduced density matrices.

The contributions of this thesis are the complete implementation of the last two components and parts of the tRecX code and the application of the overall tRecX package to the haCC problem. Two important aspects of any long term usable code is the good structure

that allows readability and easier debugging, and efficient algorithmic design for certain computationally intensive parts of the code. The algorithms used for the computation of the electron-electron integrals have already been presented in appendix 5.2. In the following sections, a brief overview of the tRecX code and the CI wavefunction interface is presented.

5.4.1 tRecX: a general pde solver

tRecX, the acronym for time dependent recursive indexing structure, is a general partial differential equation solver package. It employs recursive schemes to construct discretizations: basis set as well as grid type, with arbitrary dimensionality and arbitrary truncation schemes. The core classes that the package provides are: `Discretization`, `Wavefunction`, `Coefficients` and `Operator`.

Class `Discretization` allows one to create any arbitrary multi-index discretization of interest for solving a particular PDE. It provides a framework to impose arbitrary truncation schemes between various dimensions of the discretization. For example, consider a two index discretization denoted as $|ab\rangle$. With the Class `Discretization`, it is easy to define truncation schemes as $b_{min} = f(a)$ and $b_{max} = g(a)$.

The `wavefunction` class contains the time parameter and a `Coefficients` class object that stores the coefficients corresponding to the defined discretization. Apart from storage, the `Coefficients` class also defines operations like conjugation, inner product and so on.

Finally, the various operators evaluated in the basis defined by the discretization object are stored and handled by the class `Operator`. It also defines the most important operation `axpy`:

$$\texttt{axpy} : Y \leftarrow AX + Y.$$

The code takes into account the blocked nature of various operators and avoids unnecessary multiplication with zeros, thereby keeping the operations count to minimum.

The specific problem at hand, the haCC discretization, is a five dimensional ansatz that can be denoted as $|lmInk\rangle$ with the five indices: ionic index (I), angular momentum indices (l, m) and finite element indices (n, k). The ordering chosen in the current implementation is $lmInk$ which leads to an optimal blocking of operators for the case of atoms and to some extent for linear molecules. The set of neutral states that are included in haCC ansatz are treated as a special case in the hierarchy, given as $|00n_I0k\rangle$, with n_I the number of ionic states and k index running over the number of neutral states. A schematic describing the haCC discretization is given in figure 5.1.

Apart from these core classes, tRecX also provides supporting classes like time propagation class, basis functions classes and tRecX matrix class which wraps up several available linear algebra packages like the lapack solvers. It also provides a wrapper to the arpack solver that allows root tracing and imaginary time propagation to find the ground state of the system. The code is also parallelizable.

A very useful feature of the tRecX package is its implementation of the exterior complex scaling absorption (ECS), the most efficient absorption technique in the context of the

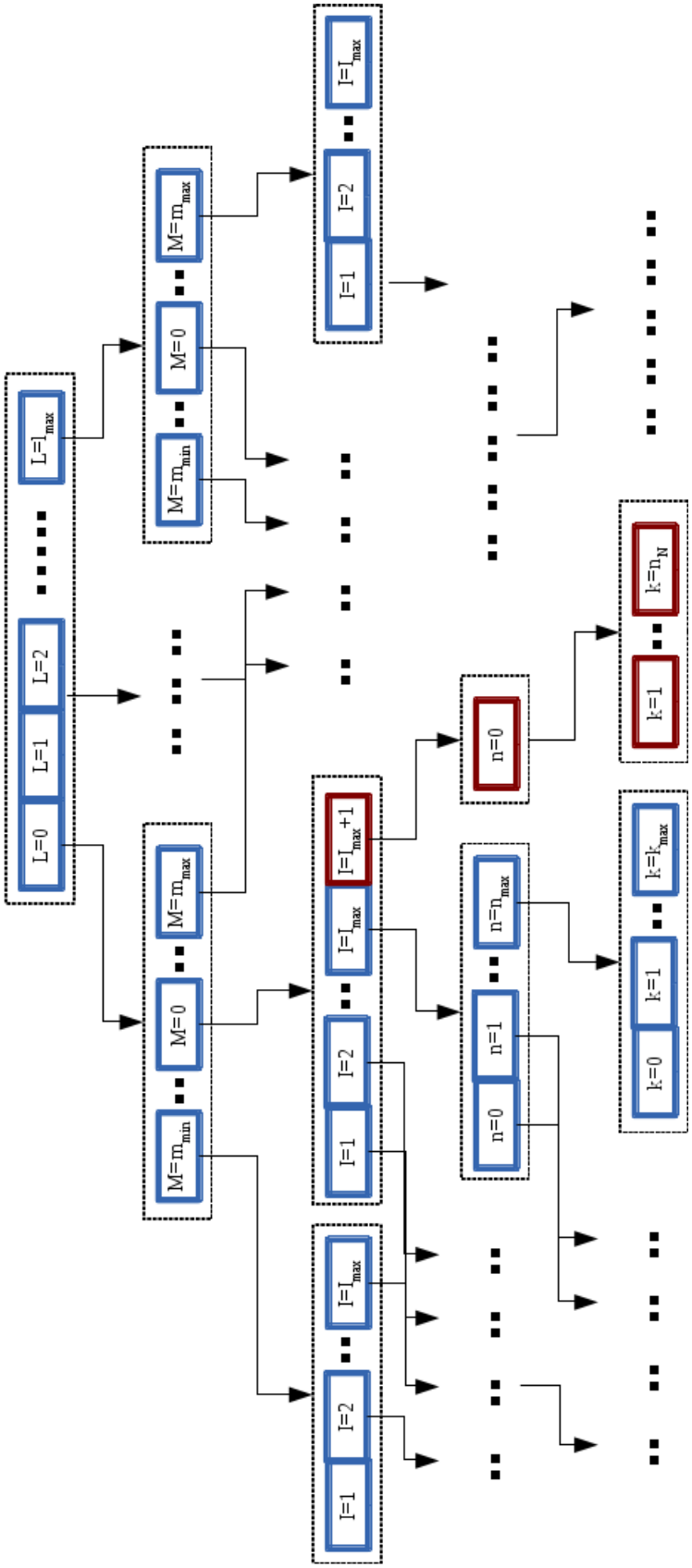

Figure 5.1: A schematic showing the hierarchy of haCC discretization $|lmlnk\rangle$.

Schrödinger equation and the implementation of the tSURFF spectral analysis which is an extremely efficient spectral analysis method to obtain photo-electron spectrum.

5.4.2 Reconstructing the CI wavefunctions

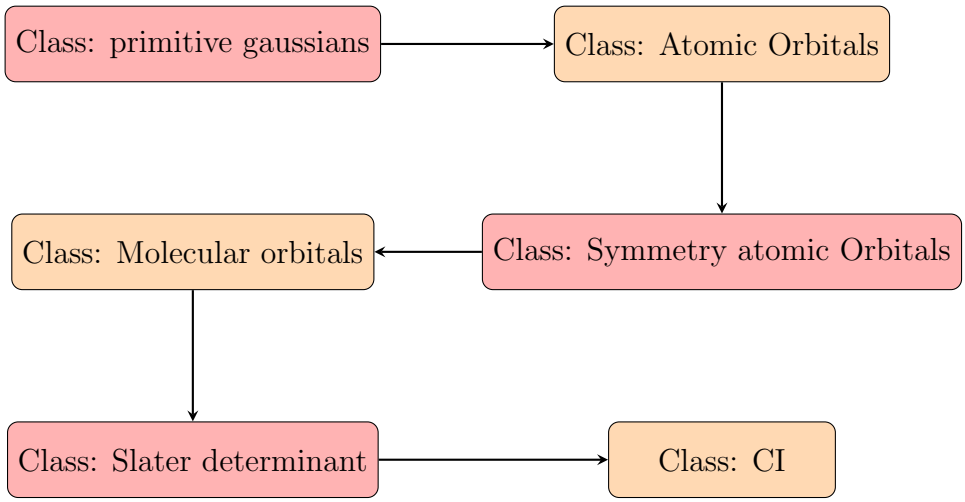

Figure 5.2: A schematic showing the series of classes implemented to store and manipulate the configuration interaction (CI) wavefunctions from quantum chemistry. Each class has an object of the previous class and the necessary transformations.

The code that reads the CI wavefunction from `COLUMBUS` preserves the hierarchy seen in the mathematical formulation presented in section 5.3. This allows for easier manipulations and implementation of checks at various levels. Figure 5.2 shows the construction of CI wavefunction using various class objects: primitive gaussians, atomic orbitals, symmetry atomic orbitals, molecular orbitals, Slater determinants and the CI wavefunction. Each class has an object of the previous class and the associated transformation matrix. All the single particle operators are evaluated at the level of primitive gaussians, which are then multiplied by respective transformation matrices to evaluate operators at higher levels of the hierarchy. The CI class in addition defines functions to compute the generalized reduced density matrices.

Bibliography

[1] Ferenc Krausz and Misha Ivanov. Attosecond physics. *Rev. Mod. Phys.*, 81:163–234, Feb 2009.

[2] Pierre Agostini and Louis F DiMauro. The physics of attosecond light pulses. *Reports on Progress in Physics*, 67(6):813, 2004.

[3] A Scrinzi, M Yu Ivanov, R Kienberger, and D M Villeneuve. Attosecond physics. *Journal of Physics B: Atomic, Molecular and Optical Physics*, 39(1):R1, 2006.

[4] P. B. Corkum and Ferenc Krausz. Attosecond science. *Nat Phys*, 3(6):381–387, June 2007.

[5] M Ferray, A L'Huillier, X F Li, L A Lompre, G Mainfray, and C Manus. Multiple-harmonic conversion of 1064 nm radiation in rare gases. *Journal of Physics B: Atomic, Molecular and Optical Physics*, 21(3):L31, 1988.

[6] Jeffrey L. Krause, Kenneth J. Schafer, and Kenneth C. Kulander. High-order harmonic generation from atoms and ions in the high intensity regime. *Phys. Rev. Lett.*, 68:3535–3538, Jun 1992.

[7] P. B. Corkum. Plasma perspective on strong field multiphoton ionization. *Phys. Rev. Lett.*, 71:1994–1997, Sep 1993.

[8] P. Agostini, F. Fabre, G. Mainfray, G. Petite, and N. K. Rahman. Free-free transitions following six-photon ionization of xenon atoms. *Phys. Rev. Lett.*, 42:1127–1130, Apr 1979.

[9] U. Mohideen, M. H. Sher, H. W. K. Tom, G. D. Aumiller, O. R. Wood, R. R. Freeman, J. Boker, and P. H. Bucksbaum. High intensity above-threshold ionization of he. *Phys. Rev. Lett.*, 71:509–512, Jul 1993.

[10] G. G. Paulus, W. Nicklich, Huale Xu, P. Lambropoulos, and H. Walther. Plateau in above threshold ionization spectra. *Phys. Rev. Lett.*, 72:2851–2854, May 1994.

[11] Katsumi Midorikawa. Ultrafast dynamic imaging. *Nat Photon*, 5(11):640–641, November 2011.

[12] A. D. Shiner, C. Trallero-Herrero, N. Kajumba, H.-C. Bandulet, D. Comtois, F. Légaré, M. Giguère, J-C. Kieffer, P. B. Corkum, and D. M. Villeneuve. Wavelength scaling of high harmonic generation efficiency. *Phys. Rev. Lett.*, 103:073902, Aug 2009.

[13] Bruno E Schmidt, Andrew D Shiner, Mathieu Gigure, Philippe Lassonde, Carlos A Trallero-Herrero, J-C Kieffer, P B Corkum, D M Villeneuve, and Franois Lgar. High harmonic generation with long-wavelength few-cycle laser pulses. *Journal of Physics B: Atomic, Molecular and Optical Physics*, 45(7):074008, 2012.

[14] Misha Yu Ivanov, Michael Spanner, and Olga Smirnova. Anatomy of strong field ionization. *Journal of Modern Optics*, 52(2-3):165–184, 2005.

[15] P. M. Paul, E. S. Toma, P. Breger, G. Mullot, F. Aug, Ph. Balcou, H. G. Muller, and P. Agostini. Observation of a train of attosecond pulses from high harmonic generation. *Science*, 292(5522):1689–1692, 2001.

[16] P. A. Carpeggiani, P. Tzallas, A. Palacios, D. Gray, F. Martín, and D. Charalambidis. Disclosing intrinsic molecular dynamics on the 1-fs scale through extreme-ultraviolet pump-probe measurements. *Phys. Rev. A*, 89:023420, Feb 2014.

[17] M. Holler, F. Schapper, L. Gallmann, and U. Keller. Attosecond electron wave-packet interference observed by transient absorption. *Phys. Rev. Lett.*, 106:123601, Mar 2011.

[18] M. Schultze, M. Fieß, N. Karpowicz, J. Gagnon, M. Korbman, M. Hofstetter, S. Neppl, A. L. Cavalieri, Y. Komninos, Th. Mercouris, C. A. Nicolaides, R. Pazourek, S. Nagele, J. Feist, J. Burgdörfer, A. M. Azzeer, R. Ernstorfer, R. Kienberger, U. Kleineberg, E. Goulielmakis, F. Krausz, and V. S. Yakovlev. Delay in photoemission. *Science*, 328(5986):1658–1662, 2010.

[19] Pierre Agostini and Louis F. DiMauro. Chapter 3 - atomic and molecular ionization dynamics in strong laser fields: From optical to x-rays. In Ennio Arimondo Paul Berman and Chun Lin, editors, *Advances in Atomic, Molecular, and Optical Physics*, volume 61 of *Advances In Atomic, Molecular, and Optical Physics*, pages 117 – 158. Academic Press, 2012.

[20] S Haessler, J Caillat, and P Salires. Self-probing of molecules with high harmonic generation. *Journal of Physics B: Atomic, Molecular and Optical Physics*, 44(20):203001, 2011.

[21] Michael Spanner, Olga Smirnova, Paul B Corkum, and Misha Yu Ivanov. Reading diffraction images in strong field ionization of diatomic molecules. *Journal of Physics B: Atomic, Molecular and Optical Physics*, 37(12):L243, 2004.

[22] M. Meckel, D. Comtois, D. Zeidler, A. Staudte, D. Pavii, H. C. Bandulet, H. Ppin, J. C. Kieffer, R. Drner, D. M. Villeneuve, and P. B. Corkum. Laser-induced electron tunneling and diffraction. *Science*, 320(5882):1478–1482, 2008.

[23] Cosmin I. Blaga, Junliang Xu, Anthony D. DiChiara, Emily Sistrunk, Kaikai Zhang, Pierre Agostini, Terry A. Miller, Louis F. DiMauro, and C. D. Lin. Imaging ultrafast molecular dynamics with laser-induced electron diffraction. *Nature*, 483(7388):194–197, March 2012.

[24] M. Lein, N. Hay, R. Velotta, J. P. Marangos, and P. L. Knight. Interference effects in high-order harmonic generation with molecules. *Phys. Rev. A*, 66:023805, Aug 2002.

[25] Manfred Lein. Attosecond probing of vibrational dynamics with high-harmonic generation. *Phys. Rev. Lett.*, 94:053004, Feb 2005.

[26] J. Itatani, J. Levesque, D. Zeidler, Hiromichi Niikura, H. Pepin, J. C. Kieffer, P. B. Corkum, and D. M. Villeneuve. Tomographic imaging of molecular orbitals. *Nature*, 432(7019):867–871, December 2004.

[27] S. Haessler, J. Caillat, W. Boutu, C. Giovanetti-Teixeira, T. Ruchon, T. Auguste, Z. Diveki, P. Breger, A. Maquet, B. Carre, R. Taieb, and P. Salieres. Attosecond imaging of molecular electronic wavepackets. *Nat Phys*, 6(3):200–206, March 2010.

[28] Olga Smirnova, Yann Mairesse, Serguei Patchkovskii, Nirit Dudovich, David Villeneuve, Paul Corkum, and Misha Yu. Ivanov. High harmonic interferometry of multi-electron dynamics in molecules. *Nature*, 460(7258):972–977, August 2009.

[29] A. Ferr, A. E. Boguslavskiy, M. Dagan, V. Blanchet, B. D. Bruner, F. Burgy, A. Camper, D. Descamps, B. Fabre, N. Fedorov, J. Gaudin, G. Geoffroy, J. Mikosch, S. Patchkovskii, S. Petit, T. Ruchon, H. Soifer, D. Staedter, I. Wilkinson, A. Stolow, N. Dudovich, and Y. Mairesse. Multi-channel electronic and vibrational dynamics in polyatomic resonant high-order harmonic generation. *Nat Commun*, 6:–, January 2015.

[30] P. Lambropoulos, P. Maragakis, and Jian Zhang. Two-electron atoms in strong fields. *Physics Reports*, 305(5):203 – 293, 1998.

[31] L. D. Landau and E. M. Lifshitz. *Quantum Mechanics.* Pergamon Press Oxford,, 1965.

[32] M.V. Ammosov, N.B Delone, and V.P. Krainov. Tunnel ionization of complex atoms and of atomic ions in an alternating electromagnetic field. *Sov. Phys. JETP*, page 1191, 1986.

[33] X. M. Tong, Z. X. Zhao, and C. D. Lin. Theory of molecular tunneling ionization. *Phys. Rev. A*, 66:033402, Sep 2002.

[34] X M Tong and C D Lin. Empirical formula for static field ionization rates of atoms and molecules by lasers in the barrier-suppression regime. *Journal of Physics B: Atomic, Molecular and Optical Physics*, 38(15):2593, 2005.

[35] L V Keldysh. Ionization in the field of a strong electromagnetic wave. *Sov. Phys. JETP (Engl. transl.)*, 20:1307, 1965.

[36] F H M Faisal. Multiple absorption of laser photons by atoms. *Journal of Physics B: Atomic and Molecular Physics*, 6(4):L89, 1973.

[37] Howard R. Reiss. Effect of an intense electromagnetic field on a weakly bound system. *Phys. Rev. A*, 22:1786–1813, Nov 1980.

[38] Liang Tao and Armin Scrinzi. Photo-electron momentum spectra from minimal volumes: the time-dependent surface flux method. *New Journal of Physics*, 14(1):013021–, 2012.

[39] Armin Scrinzi. t -surff: fully differential two-electron photo-emission spectra. *New Journal of Physics*, 14(8):085008–, 2012.

[40] J. Feist, S. Nagele, R. Pazourek, E. Persson, B. I. Schneider, L. A. Collins, and J. Burgdörfer. Nonsequential two-photon double ionization of helium. *Phys. Rev. A*, 77:043420, Apr 2008.

[41] A. Palacios, H. Bachau, and F. Martín. Enhancement and control of h2 dissociative ionization by femtosecond vuv laser pulses. *Phys. Rev. Lett.*, 96:143001, Apr 2006.

[42] M. Abu-samha and L. B. Madsen. Theory of strong-field ionization of aligned co_2. *Phys. Rev. A*, 80:023401, Aug 2009.

[43] M. Z. Milošević and N. S. Simonović. Calculations of rates for strong-field ionization of alkali-metal atoms in the quasistatic regime. *Phys. Rev. A*, 91:023424, Feb 2015.

[44] Simon Petretti, Yulian V. Vanne, Alejandro Saenz, Alberto Castro, and Piero Decleva. Alignment-dependent ionization of $\mathbf{n}_2$, $\mathbf{o}_2$, and co_2 in intense laser fields. *Phys. Rev. Lett.*, 104:223001, Jun 2010.

[45] Sang-Kil Son and Shih-I Chu. Multielectron effects on the orientation dependence and photoelectron angular distribution of multiphoton ionization of co_2 in strong laser fields. *Phys. Rev. A*, 80:011403, Jul 2009.

[46] M. Lewenstein, Ph. Balcou, M. Yu. Ivanov, Anne L'Huillier, and P. B. Corkum. Theory of high-harmonic generation by low-frequency laser fields. *Phys. Rev. A*, 49:2117–2132, Mar 1994.

[47] Anh-Thu Le, R. R. Lucchese, S. Tonzani, T. Morishita, and C. D. Lin. Quantitative rescattering theory for high-order harmonic generation from molecules. *Phys. Rev. A*, 80:013401, Jul 2009.

[48] Stefan Pabst and Robin Santra. Strong-field many-body physics and the giant enhancement in the high-harmonic spectrum of xenon. *Phys. Rev. Lett.*, 111:233005, Dec 2013.

[49] A. Staudte, S. Patchkovskii, D. Pavičić, H. Akagi, O. Smirnova, D. Zeidler, M. Meckel, D. M. Villeneuve, R. Dörner, M. Yu. Ivanov, and P. B. Corkum. Angular tunneling ionization probability of fixed-in-space h_2 molecules in intense laser pulses. *Phys. Rev. Lett.*, 102:033004, Jan 2009.

[50] J. Wu, L. Ph. H. Schmidt, M. Kunitski, M. Meckel, S. Voss, H. Sann, H. Kim, T. Jahnke, A. Czasch, and R. Dörner. Multiorbital tunneling ionization of the co molecule. *Phys. Rev. Lett.*, 108:183001, Apr 2012.

[51] H. Li, D. Ray, S. De, I. Znakovskaya, W. Cao, G. Laurent, Z. Wang, M. F. Kling, A. T. Le, and C. L. Cocke. Orientation dependence of the ionization of co and no in an intense femtosecond two-color laser field. *Phys. Rev. A*, 84:043429, Oct 2011.

[52] Domagoj Pavičić, Kevin F. Lee, D. M. Rayner, P. B. Corkum, and D. M. Villeneuve. Direct measurement of the angular dependence of ionization for n_2, o_2, and co_2 in intense laser fields. *Phys. Rev. Lett.*, 98:243001, Jun 2007.

[53] Ryan Murray, Michael Spanner, Serguei Patchkovskii, and Misha Yu. Ivanov. Tunnel ionization of molecules and orbital imaging. *Phys. Rev. Lett.*, 106:173001, Apr 2011.

[54] Kenneth C. Kulander. Time-dependent hartree-fock theory of multiphoton ionization: Helium. *Phys. Rev. A*, 36:2726–2738, Sep 1987.

[55] J. Caillat, J. Zanghellini, M. Kitzler, O. Koch, W. Kreuzer, and A. Scrinzi. Correlated multielectron systems in strong laser fields: A multiconfiguration time-dependent hartree-fock approach. *Phys. Rev. A*, 71:012712, Jan 2005.

[56] David Hochstuhl, Sebastian Bauch, and Michael Bonitz. Multiconfigurational time-dependent hartree-fock calculations for photoionization of one-dimensional helium. *Journal of Physics: Conference Series*, 220(1):012019, 2010.

[57] Loren Greenman, Phay J. Ho, Stefan Pabst, Eugene Kamarchik, David A. Mazziotti, and Robin Santra. Implementation of the time-dependent configuration-interaction singles method for atomic strong-field processes. *Phys. Rev. A*, 82:023406, Aug 2010.

[58] Yulian V Vanne and Alejandro Saenz. Numerical treatment of diatomic two-electron molecules using a b -spline based ci method. *Journal of Physics B: Atomic, Molecular and Optical Physics*, 37(20):4101–, 2004.

[59] Michael Spanner and Serguei Patchkovskii. One-electron ionization of multielectron systems in strong nonresonant laser fields. *Phys. Rev. A*, 80:063411, Dec 2009.

[60] Vinay Pramod Majety, Alejandro Zielinski, and Armin Scrinzi. Photoionization of few electron systems: a hybrid coupled channels approach. *New Journal of Physics*, 17(6):063002–, 2015.

[61] Takeshi Sato and Kenichi L. Ishikawa. Time-dependent complete-active-space self-consistent-field method for multielectron dynamics in intense laser fields. *Phys. Rev. A*, 88:023402, Aug 2013.

[62] David Hochstuhl and Michael Bonitz. Time-dependent restricted-active-space configuration-interaction method for the photoionization of many-electron atoms. *Phys. Rev. A*, 86:053424, Nov 2012.

[63] Haruhide Miyagi and Lars Bojer Madsen. Time-dependent restricted-active-space self-consistent-field theory for laser-driven many-electron dynamics. ii. extended formulation and numerical analysis. *Phys. Rev. A*, 89:063416, Jun 2014.

[64] Haruhide Miyagi and Lars Bojer Madsen. Time-dependent restricted-active-space self-consistent-field theory for laser-driven many-electron dynamics. *Phys. Rev. A*, 87:062511, Jun 2013.

[65] Daniel J. Haxton and C. William McCurdy. Two methods for restricted configuration spaces within the multiconfiguration time-dependent hartree-fock method. *Phys. Rev. A*, 91:012509, Jan 2015.

[66] M. A. Lysaght, H. W. van der Hart, and P. G. Burke. Time-dependent r-matrix theory for ultrafast atomic processes. *Phys. Rev. A*, 79:053411, May 2009.

[67] R G Parr. Density functional theory. *Annu. Rev. Phys. Chem.*, 34(1):631–656, October 1983.

[68] Neil S. Ostlund Attila Szabo. *Modern Quantum Chemistry: Introduction to Advanced Electronic Structure Theory.* McGraw-Hill Publishing Company, New York, 1989.

[69] Hans Lischka, Thomas Mller, Pter G. Szalay, Isaiah Shavitt, Russell M. Pitzer, and Ron Shepard. Columbus–a program system for advanced multireference theory calculations. *WIREs Comput Mol Sci*, 1(2):191–199, 2011.

[70] Armin Scrinzi. Infinite-range exterior complex scaling as a perfect absorber in time-dependent problems. *Phys. Rev. A*, 81:053845, May 2010.

[71] H Bachau, E Cormier, P Decleva, J E Hansen, and F Martn. Applications of b -splines in atomic and molecular physics. *Reports on Progress in Physics*, 64(12):1815, 2001.

[72] Armin Scrinzi. Ionization of multielectron atoms by strong static electric fields. *Phys. Rev. A*, 61:041402, Mar 2000.

[73] M. Woodbury. Inverting modified matrices. *Memorandum Rept., 42, Statistical Research Group, Princeton University, Princeton, NJ*, 1950.

[74] W P Reinhardt. Complex coordinates in the theory of atomic and molecular structure and dynamics. *Annual Review of Physical Chemistry*, 33(1):223–255, 1982.

[75] B. Simon. Definition of molecular resonance curves by the method of exterior complex scaling. *Phys. Lett. A*, 71:211–214, 1979.

[76] A D Bandrauk, F Fillion-Gourdeau, and E Lorin. Atoms and molecules in intense laser fields: gauge invariance of theory and models. *Journal of Physics B: Atomic, Molecular and Optical Physics*, 46(15):153001, 2013.

[77] Vinay Pramod Majety, Alejandro Zielinski, and Armin Scrinzi. Mixed gauge in strong laser-matter interaction. *arXiv:1408.6309*, Aug 2014.

[78] Robert R. Lucchese, Georges Raseev, and Vincent McKoy. Studies of differential and total photoionization cross sections of molecular nitrogen. *Phys. Rev. A*, 25:2572–2587, May 1982.

[79] Vinay Pramod Majety and Armin Scrinzi. Static field ionization rates for multi-electron atoms and small molecules. *Submitted to J Phys B.*, 2015.

[80] J S Parker, G S J Armstrong, M Boca, and K T Taylor. From the uv to the static-field limit: rates and scaling laws of intense-field ionization of helium. *Journal of Physics B: Atomic, Molecular and Optical Physics*, 42(13):134011, 2009.

[81] Armin Scrinzi, Michael Geissler, and Thomas Brabec. Ionization above the coulomb barrier. *Phys. Rev. Lett.*, 83:706–709, Jul 1999.

[82] Alejandro Zielinski, Vinay Pramod Majety, and Armin Scrinzi. A general solver for the time-dependent schorödinger equation of one and two particle systems. (Unpublished).

[83] Vinay Pramod Majety and Armin Scrinzi. Photo-ionization of noble gases: A demonstration of hybrid coupled channels approach. *Photonics*, 2(1):93–103, 2015.

[84] Vinay Pramod Majety and Armin Scrinzi. Dynamic exchange in the strong field ionization of molecules. *arxiv:1505.03349. Submitted to Phys Rev Lett.*, 2015.

[85] Isabell Thomann, Robynne Lock, Vandana Sharma, Etienne Gagnon, Stephen T. Pratt, Henry C. Kapteyn, Margaret M. Murnane, and Wen Li. Direct measurement of the angular dependence of the single-photon ionization of aligned n2 and co2. *J. Phys. Chem. A*, 112(39):9382–9386, August 2008.

[86] Maciej Dominik Śpiewanowski and Lars Bojer Madsen. Alignment- and orientation-dependent strong-field ionization of molecules: Field-induced orbital distortion effects. *Phys. Rev. A*, 91:043406, Apr 2015.

[87] Bin Zhang, Jianmin Yuan, and Zengxiu Zhao. Dynamic core polarization in strong-field ionization of co molecules. *Phys. Rev. Lett.*, 111:163001, Oct 2013.

[88] Alejandro Zielinski, Vinay Pramod Majety, Stefan Nagele, Renate Pazourek, Joachim Burgdrfer, and Armin Scrinzi. Anomalous fano profiles in external fields. *arXiv:1405.4279*, 2014.

Acknowledgements

Firstly, I would like to thank my PhD supervisor Prof. Armin Scrinzi for this opportunity to pursue my PhD in his group at Ludwig Maximilians University. I am grateful for all his time, guidance and support which helped me persevere specially during the nearly 3 year long method and code development.

I would like to thank my parents for being very supportive in this pursuit of a PhD in a far off country.

I am grateful for the generous financial support from the EU Marie Curie ITN CORINF and also support from the Munich advanced photonics and International Max Planck Research School for Advanced Photonics. The association with the CORINF and IMPRS-APS networks helped in broadening my knowledge and getting to know other researchers working in this field.

I would like to acknowledge the help from COLUMBUS authors - Prof. Hans Lischka, Dr. Thomas Müller, Dr. Jiri Pittner and Dr. Felix Plasser. Their support was essential in constructing the COLUMBUS interface. Special thanks to Dr. Thomas Müller for providing me a four day personalized training on COLUMBUS usage.

I am thankful to Prof. Saenz and Prof. Decleva for the opportunity to visit their groups in Berlin and Trieste respectively during the course of my PhD which definitely helped in widening my knowledge.

I would like to thank all my group members specially Alejandro for the many useful discussions. I would also like to thank Alejandro and Andreas for helping me with translating the summary to German.

I am thankful to Mrs. Tobiasch and Mrs. Wild for helping me with many bureaucratic issues during my PhD.

Last but not the least, I would like to thank all my friends specially Harish, Mahesh, Sudeepta, Anil and Vidya for making my stay in Munich more enjoyable.

Resume

Personal information

Name	**Naga Venkata Vinay Pramod, Majety**
Date of birth	15.02.1990
Nationality	Indian
Languages spoken	Telugu, English and Hindi

Contact

Email Vinay.Majety@physik.uni-muenchen.de

Education

July 2011 -	PhD candidate in Faculty of Physics. *Ludwig Maximilians University, Munich, Germany.*
2009 - 2011	Master of Science, Physics. *Sri Sathya Sai Institute of Higher Learning, Prasanthi Nilayam, India.*
Summer 2010	Internship at Center for ion beam applications. *National university of Singapore, Singapore.*
2009 - 2011	Bachelor of Science (Honours), Physics. *Sri Sathya Sai Institute of Higher Learning, Prasanthi Nilayam, India.*

Fellowships and scholarships

2011 - 2015	Fellow of IMPRS-APS. *International Max Planck Research School for Advanced Photon Science.* *MPI for Quantum Optics, Garching, Germany.*
2011 - 2014	Marie-Curie ITN CORINF fellowship.
Summer 2010	SIPIS scholarship, *National University of Singapore, Singapore.*

Research interests

AMO physics, Strong field physics, Photonics.

Computer skills

Languages	C, C++, Python.
VCS	git

Scientific publications

1. *V. P Majety and A. Scrinzi.* Dynamic exchange in the strong field ionization of molecules. **Phys. Rev. Lett.** 115, 103002 (2015).
2. *V. P. Majety, A. Zielinski and A. Scrinzi.* Photoionization of few electron systems: a hybrid coupled channels approach, **New J. Phys.** 17 (2015) 063002.
3. *A. Zielinski, V.P. Majety, S. Nagele, R. Pazourek, J. Burgdörfer, A. Scrinzi.* Anomalous Fano profiles in external fields. **arXiv:1405.4279, Submitted to Phys. Rev. Lett.** (2015).
4. *V. P. Majety, A. Zielinski and A. Scrinzi.* Mixed gauge in strong laser-matter interaction, **J. Phys. B:** At. Mol. Opt. Phys. 48 (2015) 025601.
5. *V. P Majety and A. Scrinzi.* Photoionization of noble gases: a demonstration of hybrid coupled channels approach. **Photonics** (2015), 2, 93-103.
6. *V. P Majety and A. Scrinzi.* Static field ionization rates for multi-electron atoms and small molecules. **Submitted to J Phys B.** (2015).

Conferences

Contributed talk	ATTO 2015, *Saint-Sauveur, Canada.* Dynamic exchange and polarization in strong field ionization of molecules.
Fellow talk	Joint XLIC-CORINF workshop 2013, *Madrid, Spain.* Photo-emission from atoms and diatomics.
IMPRS-APS	Talks at three annual meetings 2012-2014.
Poster presentations	ICPEAC 2015, *Toledo, Spain.* UDIM 2015, *Grindelwald, Switzerland.* GRC 2014: Photoionization and Photodetachment, *Galveston, USA.* ATTO 2013, *Paris, France.*